John Bacon; Stephen Dye; Claire Beraud (Hg.)

Proceedings of the XXVth TELEMAC-MASCARET User Conference, 9th to 11th October 2018, Norwich

Cefas
CCSUS
Collaborative Centre for Sustainable Use of the Seas

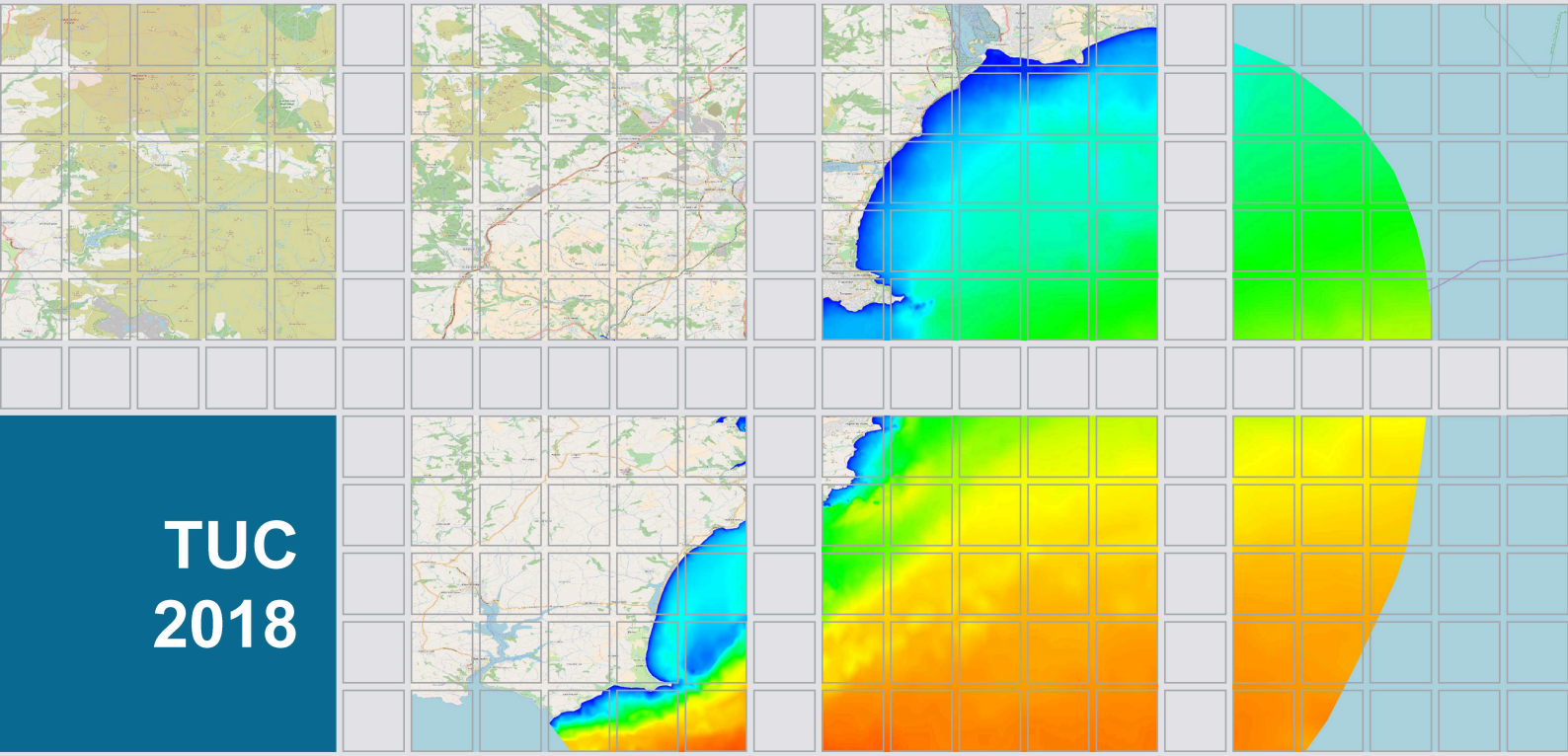

TUC 2018

Proceedings of the

XXVth TELEMAC-MASCARET User Conference

9th to 11th October 2018, Norwich

ARTELIA
BAW Bundesanstalt für Wasserbau
Cerema
Science & Technology Facilities Council
eDF
HR Wallingford Working with water
CERFACS

Proceedings of the 25th TELEMAC-MASCARET User Conference

9th-11th October, Norwich, UK

Organised by

Collaborative Centre for the Sustainable Use of the Seas (CCSUS)
Centre for Environment, Fisheries and Aquaculture Science (Cefas)
Pakefield Road,
Lowestoft, NR33 0HT, UK
Tel: +44 1502 562244
telemac2018@gmail.com
www.telemac2018.org.uk

Edited by

John Bacon, Stephen Dye and Claire Beraud

Design

Clemens Dorfmann, Stephen Dye and Luz Garcia

Published by

ISBN: 978 0 907545 75 0
DOI: 10.14465/2018.tucxxv.nrw

TELEMAC-MASCARET Core Group

Artelia
www.arteliagroup.com

Bundesanstalt für Wasserbau
Federal Waterways Engineering and Research Institute
www.baw.com

Centre d'études et d'expertise sur les risques, l'environment, la mobilité et l'aménagement
www.cerema.fr

Centre Européen de Recherche et de Formation Advancée en Calcul Scientifique
www.cerfacs.fr

Électricité de France
www.edf.com

HR Wallingford
www.hrwallingford.com

Science and Technology Facilities Council
Daresbury Laboratory
www.stfc.ac.uk

Organisation

International Scientific Committee

Olivier Bertrand	Artelia Eau & Environnement
Christophe Coulet	Artelia Eau & Environnement
Thomas Brudy-Zippelius	BAW
Frederik Folke	BAW
Boris Glander	BAW
Rebekka Kopmann	BAW
Sophie Ricci	CERFACS
Patrick Chasse	CEREMA
Vanessya Laborie	CEREMA
Riadh Ata	EDF R&D
Yoann Audouin	EDF R&D
Jacques Fontaine	EDF R&D
Thierry Fouquet	EDF R&D
Cédric Goeury	EDF R&D
Agnès Leroy	EDF R&D
Magali Jodeau	EDF R&D
Chi-Tuân Pham	EDF R&D
Pablo Tassi	EDF R&D
Sébastien Bourban	HR Wallingford
Noémie Durand	HR Wallingford
Michiel Knaapen	HR Wallingford
David Emerson	STFC
Charles Moulinec	STFC

Local Organising Committee

John Bacon (Chair)	Cefas
Claire Beraud	Cefas
Stephen Dye	Cefas
Liam Fernand	Cefas
David Haverson	Cefas

Centre for Environment Fisheries & Aquaculture Science

Cefas

CCSUS
Collaborative Centre for Sustainable Use of the Seas

Foreword to the 25th TELEMAC-MASCARET Users Conference 2018

October 2018

Dear TUC2018 delegates,

The Centre for Environment, Fisheries and Aquaculture Science (Cefas) and the Collaborative Centre for the Sustainable use of the Seas (CCSUS), a partnership with the University of East Anglia, are delighted to host the TELEMAC-MASCARET Users conference this year in Norwich, UK. We hope that your visit to Norwich is enjoyable and that the conference is interesting and memorable.

The huge advancement of the TELEMAC-MASCARET system during the period of these conferences is clear to see. Where the developers of our modular finite element system led, others have followed and the release of the open source code in 2010 had the desired impact of widening the involvement and input from users around the globe. The efforts of all contributors to the development and application of the system are now widely shared by all the users through the active forum and the TELEMAC-MASCARET "family" grows stronger by the day.

The User conferences have traditionally been the high point in the development year and more recently, being held on a wider geographical base, news of how versatile and widely applicable the modelling system is, have been broadly broadcast. New and ever more innovative applications are presented each year. The huge range of environmental and hydrodynamic conditions enveloped by the system are impacting the Blue Economy and driving significant advances in the development of integrated modelling and monitoring methods.

The ability to range between global, regional, coastal and fluvial scale problems, using the same system, makes the application of TELEMAC-MASCARET invaluable as one of the tools in the armoury of those monitoring and regulating environmental state in our seas, estuaries and coastlines.

The organising committee is grateful to the TELEMAC-MASCARET consortium for its support, to the many authors for the effort you have made to publish and present your work and of course, to the scientific committee for the publication reviews and support for the organisation of the conference.

We wish all of you attending the conference, whether to present, just to listen and learn, or most importantly, to meet old and new friends in this remarkable scientific family, a thoroughly enjoyable few days with us here in Norwich.

John Bacon

Chair of the Local Organising Committee
TELEMAC-MASCARET User Conference 2018

CONTENTS

Development of the EFFORS service for operational flood forecasting

S. Gegenleithner[1], C. Dorfmann[2], G. Zenz[1], F. Wölfelmaier[3]
[1] Institute of Hydraulic Engineering and Water Resources Management, Graz
[2] flussbüro OG, Graz
[3] Central Institute for Meteorology and Geodynamics (ZAMG), Wien
sebastian.gegenleithner@tugraz.at

***Abstract*—This article describes the development of a real-time flood forecasting system in Austria and southern Germany. The project Enhanced Flood Forecasting System for Critical Infrastructure Protection in Medium Size Alpine Catchments or short EFFORS [1] is partly financed by the European Space Agency (ESA) within the framework of the Integrated Applications Promotion (IAP) programs. The project brings together experts in the field of satellite communication, geographic information systems, meteorology, hydrology, computational engineering and hydraulics.**

Under operation, the EFFORS system produces 24-hour forecasts of heavy precipitation, discharge and flood inundation areas. The results are updated hourly making the system operate in near real-time. Due to the high computational costs, especially of the hydraulic part, EFFORS is operated on a High Performance Computing Cluster (HPC). The results are then displayed within an interactive web application.

The development of the system is intended to be finished in the end of 2018 and will then be operated by the ZAMG as service provider.

I. Introduction

Today's society is highly dependent on a steady supply of electricity, fresh water, transportation and telecommunication. It is thus necessary to ensure a resilient supply even during catastrophic events. However, it is not possible to protect all critical infrastructure by means of permanent measures like flood retention basins, etc. Therefore, alternative flood protection systems, like forecast models, gain importance.

The project Enhanced Flood Forecasting System for Critical Infrastructure Protection in Medium Size Alpine Catchments (EFFORS) aims at increasing the forecast quality by making use of real-time measurements, observations and numerical models. The developed forecast system will aid public authorities, emergency services, owners of critical infrastructure and also private persons at the task of flood protection and will thus decrease the risk of social, ecological and economical damages. For individual actions, the system has to be combined with risk assessment approaches.

Figure 1. *Pilot areas (source: Robert Stöffler, OSGH), modified*

II. DEMONSTRATION PHASE AND USER REQUIREMENTS

For the demonstration phase of the project three pilot catchments were defined. Two are located in Austria and one in the southern part of Germany (Fig. 1). Within the feasibility study of the project a wide range of potential users were identified within the three pilot catchments. Potential users were found to be owners and operators of critical infrastructure, public authorities and other stakeholders like insurance companies, consulting engineers, etc. In order to identify user requirements and needs a workshop was held in July 2014.

The aforementioned workshop showed that owners and operators of critical infrastructure had the following expectations of a real-time forecasting system:

- Sufficient lead time for warning of flood events
- Information of temporal evolution of discharge and water levels for given thresholds

Whereas public authorities and disaster management organizations would like the system to fulfil the following criteria:

- Improvement of existing flood forecasting systems for small and medium sized catchments
- Improvement of preparation before floods
- Fulfilling the goals of the EU Water Framework Directive
- Warning of communities and public authorities to increase the safety against damages caused by floods

III. METHODOLOGY

A. Model Chain

The core of the EFFORS system is a shell program, steering the individual models and interfaces. It is operated at the HPC of the service provider ZAMG (Austrian Central Institute for Meteorology and Geodynamics). The whole model chain, illustrated in Fig 2, is triggered in hourly intervals and processes the individual modules successively.

As a first step, the shell gathers and pre-processes the required dynamic data for the real-time forecast. The meteorological input data is acquired directly from the servers of the service provider, whereas other data, like gauge measurements, are obtained from the individual catchments respectively. The input data is stored in a central database and further feeds the hydrological model. After the hydrological simulation is finished the results are pushed back to the database and the input for the hydrodynamic model is built. As soon as the hydrodynamic simulation is completed and the result is stored in the database, the forecast can be post-processed. The results from the numerical models – meteorology, hydrology and hydraulic – are then visualized in an interactive web application. In case the forecast exceeds predefined thresholds, the shell automatically sends warnings via SMS or E-Mail to the users.

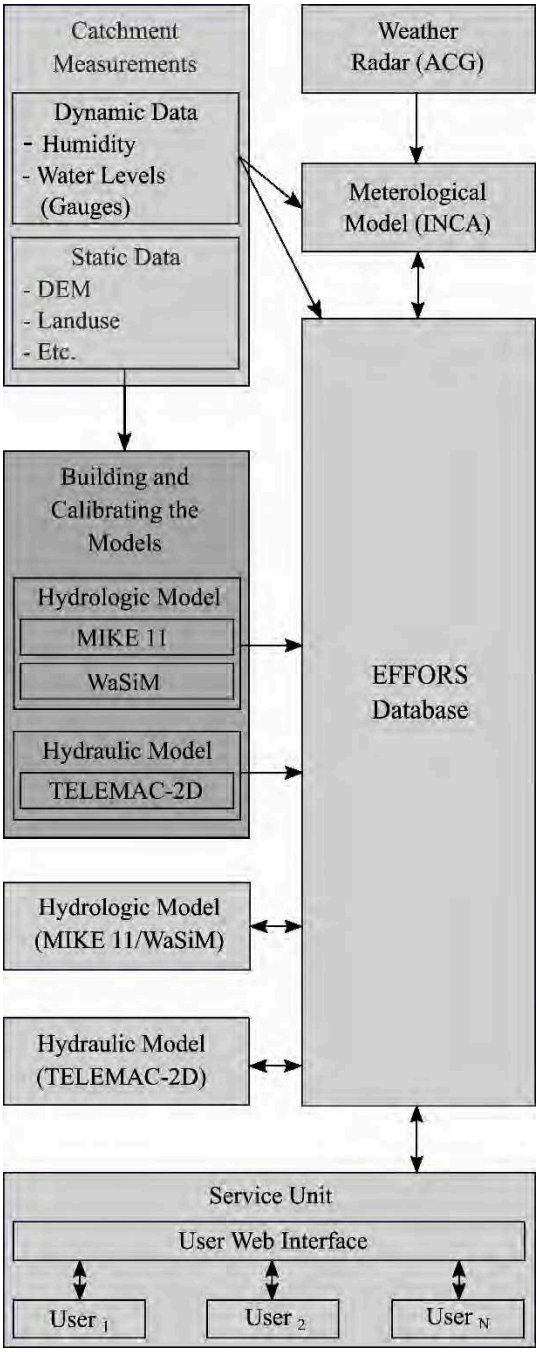

Figure 2. *Schematic model chain of the EFFORS service*

B. Data management

The data required to run the EFFORS service is located in a general database. The system distinguishes between static and dynamic components. Static data, for example model components like geometry, are constructed once and do not change under operation. This type of information is only modified when the system is updated and the models are recalibrated. However, EFFORS also requires a broad range of dynamic data, updated in an hourly interval. Examples are water level measurements of gauges, temperature, humidity, precipitation, etc.

The meteorological inputs, which represent a large part of the overall dynamic data, are already included in the portfolio of the service provider and are thus used directly in EFFORS. The water level measurements at the gauges, required for the hydrological model, are available for each catchment respectively. To provide a redundant system, the data is transferred via terrestrial- but also satellite communication technology.

C. *Meteorological Model*

The meteorological modelling is done with the Analyse and Nowcastingsystem INCA [2]. This system combines numerical forecast models with real-time measurements. The forecasted grid information but also measurements of temperature, precipitation, etc. are used to feed the hydrological model. The spatial and temporal resolutions of the INCA model are 1 km and 1 hour or 15 minutes respectively.

D. *Hydrological Model*

Due to preferences of the local authorities, two different hydrological models are required in the EFFORS service. In the southern part of Germany the WaSiM model [3] is preferred and thus, is used in the pilot area of Berchtesgaden (Fig. 1). In both Austrian catchments (Mürz and Kainach) the MIKE 11 model [4] is demanded.

Both hydrological models make use of the meteorological forecast to compute the discharges within the catchment. This data, with a temporal resolution of 1 hour, further serves as input for the hydraulic model.

E. *Hydraulic Model*

As for the hydraulic part of EFFORS, the TELEMAC-2D model [5] is chosen. TELEMAC-2D uses the discharge in the main stream but also the discharge of lateral tributaries as liquid boundaries. The computed velocities and water depths are further visualized in the EFFORS web portal [6].

Contrary to the hydrological model, the hydraulic model only operates if the forecasted discharge exceeds a certain threshold. This is necessary to safe computational resources. The threshold has to be set for each catchment beforehand.

F. *Post-processing of the results*

After the numerical models finished the forecast, the results are post-processed. Based on the evaluated user requirements (Section. II) three different packages are available within the web portal:

- **Heavy precipitation**: For the heavy precipitation package, the results of the meteorological forecast model are visualized. This service is already operated by the ZAMG and is integrated to the EFFORS service. Fig. 3 gives an impression how a cumulative rain forecast in the web portal may look like.
- **Discharge**: The discharge within the river can be extracted from the hydrological results. Users of this package can define their point of interest within the river and monitor a real-time forecast of its discharge. Fig. 4 shows how the EFFORS system visualizes the forecasted discharge for the red circle, representing a user point.
- **Flood inundation areas**: The hydrodynamic result file provides 2D data of velocities and water depths. Users of the flood inundation package are provided with contour plots of the 2D flood plains. Furthermore, it is possible to specify points of interest within the domain. At these points the user will receive linear interpolated water depth values over the forecast period. Fig. 5 gives an impression how the hydrodynamic results are visualized in the EFFORS web interface.

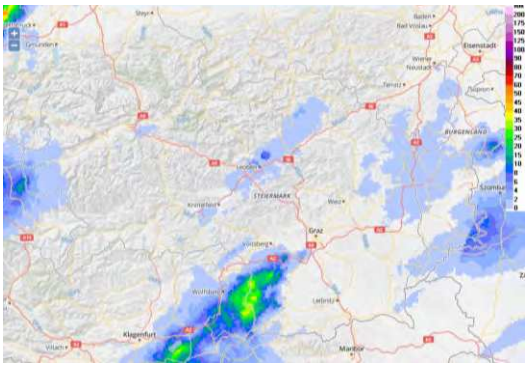

Figure 3. *EFFORS web portal – cummulative precipitation forecast*

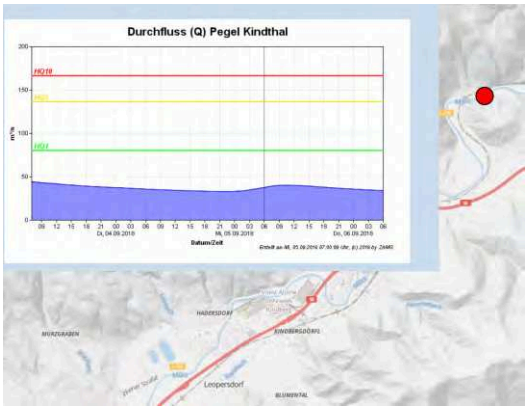

Figure 4. *EFFORS web portal – Discharge forecast at user point*

Figure 5. *EFFORS web portal – Visualization of 2D results, water depths*

G. *Progression in time of the forecast period*

The key of every forecast service is the progression in time. Even though the numerical models are calibrated, operating them with only forecasted data could lead to significant adding up of errors. It is thus necessary, that each forecast phase is followed by an analysis phase. This phase uses measured data to get the initial state of the variables right. This is especially important for the hydrological model. As for the hydraulic model, the correction is implicitly done by the liquid boundary conditions coming from the hydrological model.

To explain the progression in time, the start of the forecast is assumed to be t_0. The end of the forecast period is thus t_{24}. To get the initial conditions right, the hydrological model starts the numerical simulation at t_{-48}, wherein the period between t_{-48} and t_0 represents measured data. The measurements allow for the hydrological model to run with corrected hydrological forcing. Due to the high computational cost of the hydraulic model a similar lead time as for the hydrological model is not possible. Therefore, a lead time of one hour (t_{-1} until t_0) is used to improve the initial conditions at the start of the forecast. The scheme of a forecast at one point in time is illustrated in Fig 6.

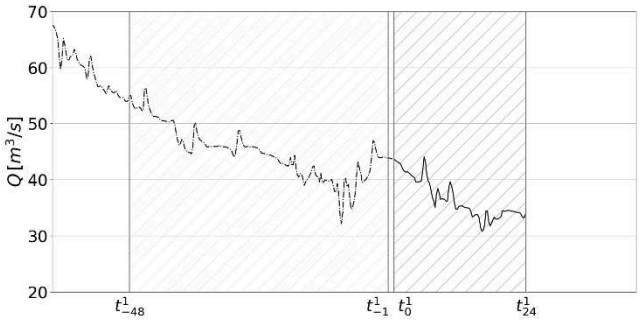

Figure 6. *Scheme of the forecast*

After the model chain (Fig. 2) finishes one run at a specific point in time, the shell moves 1 hour ahead. Fig 7 illustrates the same arbitrary hydrograph as Fig. 6 but already progressed n hours in time.

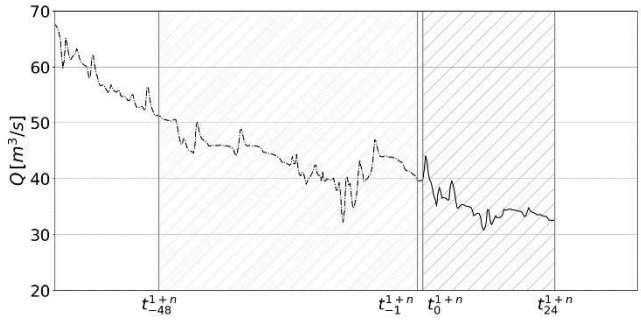

Figure 7. *Scheme of forecast; First simulation + n runs*

IV. THE ROLE OF TELEMAC WITHIN EFFORS

This section describes the application of the TELEMAC-2D model to the real-time flood forecasting service EFFORS. Since the shell program allows a modular treatment of individual catchments, only the implementation of one of the pilot catchments – the Mürz catchment (Fig. 1) – is explained in more detail.

A. *Study Catchment*

The study catchment is located in Austria in the province of Styria (Fig. 1). Its total area is about 1,500 km². Potential users are located between Mürzzuschlag and Bruck. a. d. Mur, spanning 40 km of river (Fig. 8).

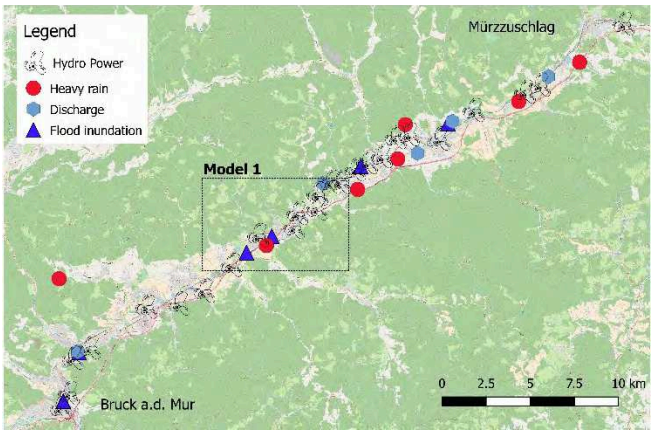

Figure 8. *Area of interest, © OpenStreetMap contributors*

The average annual discharge at the Mürz river is given with 14 m³/s. The characteristic flood discharges HQ30 and HQ100 are given with 215.0 m³/s and 275.0 m³/s respectively. Within the ~40 km of river reach 25 small run-off-river hydropower plants are located.

Potential users of the EFFORS system in the Mürz region, were identified within a workshop (Section II) and in several personal conversations. Stakeholders had the option to set markers on an interactive map to show their interest in one of the in Section III/F mentioned packages, available in the EFFORS system. The different markers, set by potential users, are illustrated in Fig. 8. A total number of 7 potential users set markers to show their interest in heavy rain warnings. The number of stakeholders interested in discharge warnings and flood inundation maps/warnings, are 5 and 6 respectively.

Due to the very limited available computation time, the area of interest had to be split in several parts. At the current state of the EFFORS system only the in Fig. 8 illustrated area (Model 1) is implemented. The splitting of the area of interest is done in such a way, that the inlet and the outlet lie in regions with well-defined hydraulic conditions.

B. *Numerical model*

Subtracting the time required for pre-processing, other numerical models and post-processing, leaves a total of 40 minutes (of 1 hour) available for the hydrodynamic model. Even though EFFORS is operated on a HPC, it is obligatory that not too many cores are assigned to one particular model. Therefore, there is a high requirement on mesh quality and optimization of numerical settings.

The final computational mesh features about 250,000 elements and 138,000 nodes. The mean element area is about 15 m² with an average edge length of about 5.5 m. The mesh

is more refined within the region of the river, at breaklines (e.g. streets) or houses. Further, there are 6 weirs located in the domain. First, the authors tried to model the weirs with internal boundary conditions, but it showed that the results improved by switching to a full geometrical implementation of the weirs. The computational mesh and its nodal elevations are visualized in Fig. 9.

The numerical model is calibrated by means of two historical flood events. For one of the flood events measurement points are available whereas for the second one only aerial photographs exist. After building and calibrating the hydrodynamic model it can be integrated to the EFFORS service.

As already mentioned, TELEMAC-2D should only run in flood scenarios – due to the high hardware costs. To define the discharge threshold several simulations were conducted and the steady discharge for whom close to now flooding occurs was chosen. For the Mürz catchment, this threshold is set to 50 m³/s. As soon as the hydrological model forecasts that this threshold is exceeded within the next 24 hours, the TELEMAC-2D model starts operating.

Since the TELEMAC-2D model does not consider evaporation, water remains in the model as the hydrograph decreases. Therefore, if the hydraulic model would be operated in the same manner as the hydrological model, a consecutive error would be introduced. Within the EFFORS system this is prohibited by using two different TELEMAC steering files, representing different initial conditions. In the following part the structure of the TELEMAC-2D model will be explained in more detail. The individual files are separated in static and dynamic components and are given in Tab. 1.

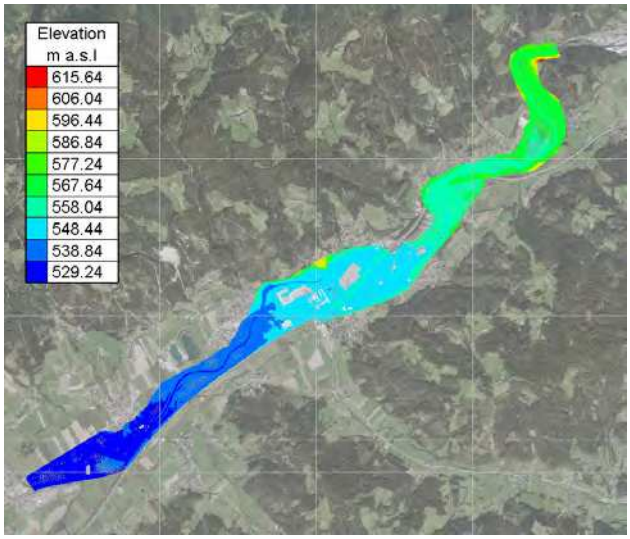

Figure 9. *Computational Mesh, Model 1*

TABLE 1: MODEL COMPONENTS

Description	**Type**	**Purpose**
Mesh	Static	Contains the computational mesh
Boundary conditions	Static	Sets the boundary conditions for the numerical model
Initial conditions	Static	The initial conditions file represents average annual water conditions within the river
Inlet boundary	Dynamic	The inlet boundary condition file represents the results of the hydrological model at the inlet
Outlet boundary	Static	The outlet boundary condition file defines a stage discharge curve at the outlet
Sources	Dynamic	In the source file all the lateral water sources to the domain are specified. The points given in the domain represent larger tributaries or several smaller ones. The input is also created from the hydrological model
Result file	Dynamic	The result file is the solution of velocities and water depths within the next forecast period
Steering file MQ	Static	TELEMAC steering file for average water level conditions
Steering file continuous	Static	TELEMAC steering file for continuous simulation

The model components (Tab. 1) contain three dynamic files. Furthermore, as already mentioned before, the model is operated with two different TELEMAC-2D steering files. The steering file MQ is only called by the EFFORS shell program when the threshold of the forecasted discharge is exceeded for the first time (for one hydrograph). In this case, the initial conditions file is used, representing average annual discharge conditions in the river. As the forecast progresses in time the program calls the continuous steering file. In this, the result file of the previous computation is used as initial conditions for the next TELEMAC-2D run. EFFORS continues operating with the continuous steering file as long as the threshold is exceeded. As soon as every discharge value within the forecast period is below the threshold, the shell program will not start TELEMAC-2D. For the next hydrograph exceeding the defined threshold the steering file MQ is used again, which allows resetting the model.

V. Discussion

Climate change, increasing population, further regulations of rivers, etc. will make it necessary to review existing flood protection and catastrophe management strategies. The newly developed EFFORS system for near real-time flood forecasting will go into operation at the end of 2018 and will take a leap in the improvement of non-intrusive flood protection measures in Austria and Germany. The positive feedback of the different stakeholders shows the potential of the service.

To be able to guarantee sufficient lead time, it is still state of the art to operate scenario based flood forecasting systems. Despite the fast availability of results, scenario based forecasts come along with major downsides like inflexibility. The newly developed EFFORS system offers hourly updated 24 hour forecasts of precipitation, discharge and flood inundation areas, making it competitive to scenario based approaches.

The user-friendly web portal as well as sophisticated distribution of warnings – via E-mail or SMS – will make the EFFORS system a powerful tool to aid different stakeholders in their task of flood protection.

Acknowledgements

The authors want to thank all the contributing project partners: Ingenieurbüro für Umweltmanagement und Wasserwesen (UWM), JOANNEUM RESEARCH (JR), Hydrographical Service of Styria (OSGH) and SLU. Furthermore, we express our gratitude to the European Space Agency (ESA) for partly financing this project.

References

[1] EFFORS: Enhanced Flood Forecasting System for critical Infrastructure Protection in Medium Size Alpine Catchments, https://business.esa.int/projects/effors

[2] INCA: Analyse- and Nowcasting system, https://www.zamg.ac.at/cms/de/forschung/wetter/inca

[3] J. Schulla, “Model Description WaSiM”, Technical report, pp. 347., 2017

[4] DHI, “MIKE 11, A modelling system for Rivers and Channels”, User Guide, 2003

[5] J-M. Hervouet, “Hydrodynamics of free surface flows: modelling with the finite element method”, John Wiley & Sons, 2007

[6] EFFORS web portal (only available for users)

Recent numerical models for engineering studies in open channels of power plants

Victor Winckler[1], Thomas Viard[1], Grégory Guyot[1], Matthieu Breysse[1], Olivier Garbe[1]
[1] Hydro Engineering Centre (CIH), EDF, Le Bourget du Lac, France
victor.winckler@edf.fr, thomas.viard@edf.fr, gregory.guyot@edf.fr, matthieu.breysse@edf.fr, olivier.garbe@edf.fr

***Abstract*— In studies performed by EDF's Hydro Engineering Centre, Mascaret software is widely used to model the water waves in channels. This paper presents several recent models developed for Hermillon scheme, the "Grand Canal d'Alsace" and Line 4 of the Durance scheme, which totals 7 models and 15 branches. These models include a variety of areas, confluences, and pressurized galleries.**

The aims of these studies are to determine the maximum water level produced by a load rejection of the power plants, or to define the gradient of the increase in the water level, which is then used in protection alarms.

When it was possible, tests on site were realized and the results of the calculation were compared to the measurements. The paper also presents some numerical issues which occurred with Mascaret software.

I. HERMILLON SCHEME

A. *Aim of the study*

The aim of the study is to determine the hydraulic behaviour of Hermillon channel, operating at a flow 20 % greater than the design flow and to check that there is no overflow during load rejection of the power plant.

Fig. 1 Layout of the channel

B. *Characteristics of the model*

The scheme is modelled from the intake of Saint Martin la Porte dam to the entrance of the power plant tunnel, by a single branch.

Design flow (1974)	80 m^3/s
Design flow + 20%	96 m3/s
Fudaa-Mascaret version	3.5 (2015)
Calculation core	unsteady subcritical

C. *Limits of the model*

The pressurized flows that occur in the reinforced concrete tunnel (940 m), and in the siphon of the Rieu Sec (140 m), have been modelled using a Preissman slot, which is not a satisfactory representation, as the lengths of these tunnels are significant relative to the channel's length (2250 m). However, a comparison between computed and measured values shows that this assumption is acceptable in this particular configuration.

The model does not take the channel's bends into consideration. The head difference produced by the channel bend or lateral banking, however, is very slight, less than 1 cm, considering the channel's curvature.

D. *Modelling parameters*

The surface width being about 10 to 30 m, the spacing between the design profiles was set at 20 m.

The height of the water being around 4 to 6 m, the planimetric step in a profile section was set at 10 cm.

After checking its influence on the water level calculations, the calculation time step was set at 2 s.

As flow in the channel is subcritical, the unsteady subcritical core was chosen and a water level would usually be imposed downstream and a flow upstream. However, the transient state simulations were done with a flow downstream and a constant level upstream because there is some measurement of the flow at the downstream extremity of the channel.

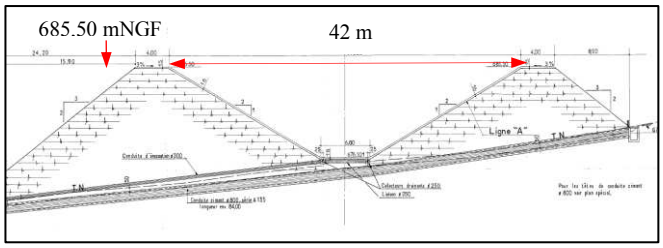

Fig. 2 Cross section of the channel

Fig. 3 Measuring flow and water level using a radar sensor at the downstream extremity of the channel

E. Main results

The values of the Strickler coefficients (Ks) were determined using two tests carried out on site in April 2015

TABLE 1: STRICKLER COEFFICIENTS (KS) FOR THE DIFFERENT PARTS OF THE CHANNEL

Parts of the channel	Ks
Reinforced concrete tunnel	81
Channel upstream	55
Rieu Sec siphon	75
Channel downstream	70

Fig. 4 Wave propagation going to the upstream, observed during the tests carried out in April 2015

The measurements gave a wave speed of 5 to 6 m/s.

The comparison between the model predictions and the measurements was satisfactory for the period of oscillation and the maximum water level values that occur in transients. However, the initial state or steady state showed a significant difference of 30 cm, which was one of the issues encountered in this study.

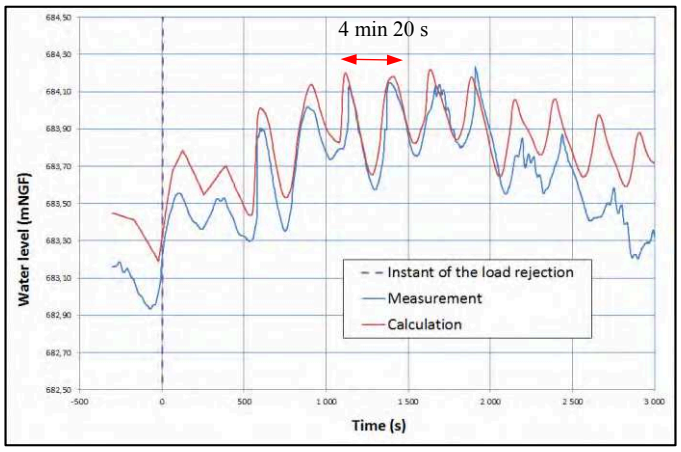

Fig. 5 Predicted and measured water level at the downstream extremity of the channel (test D5)

The simulation of a start up at the dam's high level, followed by a simultaneous load rejection of both units gives a maximum level that is reached at the downstream extremity of the channel and which leaves a freeboard of 1.10 m relative to the bank crest.

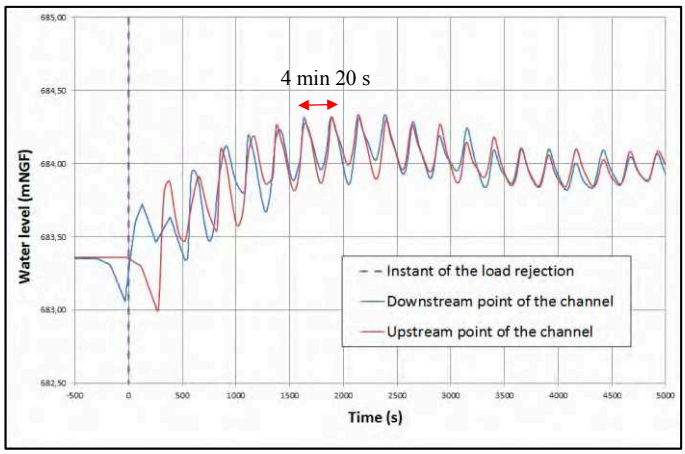

Fig.6 Result of a start up followed by a load rejection at the two extremities of the channel (calculation D6P)

The Mascaret code therefore fulfilled the aim of the study and the physical phenomena measured during the on-site tests were confirmed by calculations.

F. Difficulties encountered

It later appeared that, during the tests in steady state, the flow was stabilised but the water levels were not. The calibration of the Ks coefficients is therefore not optimum and can vary according to the simulations.

An analysis of the physical phenomena showed that the maximum water level in the channel is obtained not at the first group of oscillations, but after a rise of the water level towards the static level corresponding to the level in Saint Martin La Porte reservoir.

This maximum water level is therefore dominated in the first order by the filling of the channels (60 min period) and

only in the second order by the amplitude of the wave propagation. Considering the filling phenomenon described above, we can deduce that the channel's load losses only have a slight influence on this maximum level.

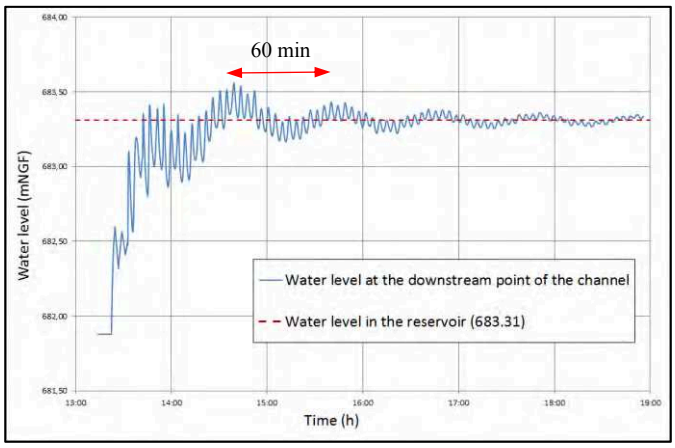

Fig. 7 Oscillations during the filling of the channel (D2)

II. "GRAND CANAL D'ALSACE"

A. *Aim of the study*

The aim of the study is to determine the variations in water levels produced by a load rejection in the headrace canals of Kembs, Ottmarsheim, Fessenheim and Vogelgrün power plants situated on the Grand Canal d'Alsace (GCA), without using the discharge elements.

These level variations have been drawn for a few specific points of the channels, corresponding to the locations of water level measurements and security weirs. They allow to determine the gradients of the rising water levels, to set the automatic operation system so that it does not deactivate them in case of the discharge elements stay closed (feedback on the incident at Marckolsheim scheme). They were also used to calculate the arrival times of the wave at the different security weirs.

Only the Kembs and Ottmarsheim models are detailed in this article.

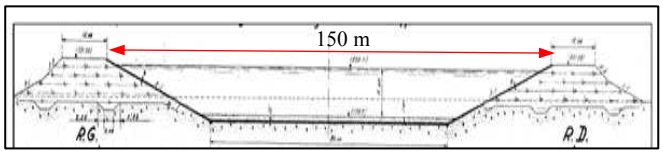

Fig.8 Cross section of the Grand Canal d'Alsace

B. *Characteristics of the models*

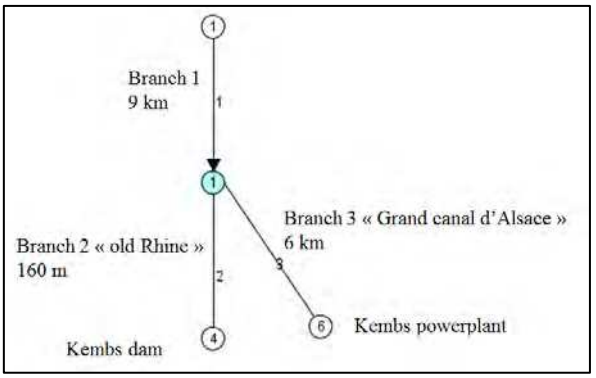

Fig. 9 Kembs model

TABLE 2: STRICKLER COEFFICIENTS (KS) IN THE DIFFERENT BRANCHES

Branch no.	Ks
1	25 - 40
2	39
3	49

Computation core unsteady subcritical

The transcritical core was used in that case, because the calculations are more complex with the diffluence.

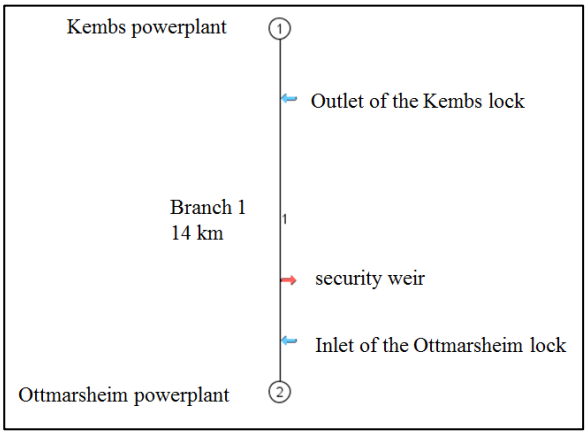

Fig. 10 Ottmarsheim model

Strickler coefficient	46
Computation core	transcritical
Use of non-hydrostatic terms	yes

These models were not calibrated and the Strickler coefficients are those used in the Mascaret models developed during earlier studies by EDF's Laboratoire National de l'Hydraulique et de l'Environnement (LNHE).

C. *Modelling Parameters*

For all simulations, the flow cutoff is triggered 5 min after the start of the simulation to check the model's stability in steady state.

A 0.25 s time step was used for Ottmarsheim, Fessenheim and Vogelgrün.

For Kembs, a 1 s time step was chosen to reduce the digital oscillations that only appeared for this model with 3 branches.

For the four models, a 10 m mesh size was chosen so that the sudden variations of the reservoir would be correctly reproduced by the model, although this size is much lower than the recommended rule of two to three times the width of the branch.

For the four models, a planimetric step value of 20 cm was chosen. 50 cm and 20 cm values were tested and the influence between these two values is negligible. This value of 20 cm respects the guideline of taking the elevation difference between the profile's lowest point and the water line's highest point, divided by 50.

Based on a water line initialised as steady state, the transient state uses the following limit conditions:

Upstream flow (1932) constant equal to 1400 m^3/s

Downstream flow cut from 1400 to 0 m^3/s in 10 s

D. *Main results*

The maximum level is not produced by the first intumescence since the channel continues to fill with a constant upstream flow, simulating a loss of the load rejection information from Kembs or Ottmarsheim power plants.

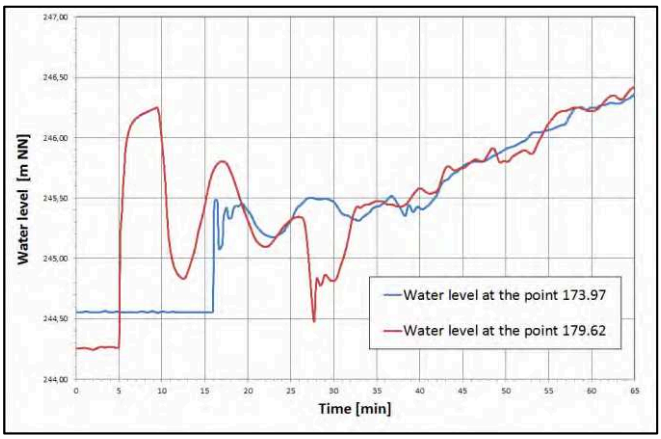

Fig. 11 Variation of water levels at Kembs in two different points

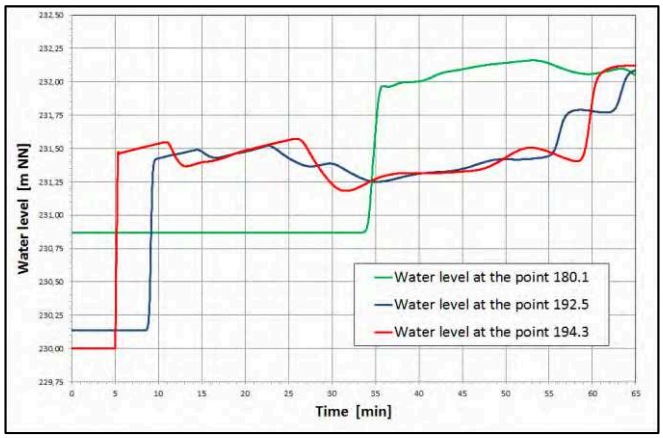

Fig. 12 Variation of water levels at Ottmarsheim in three different points

For Ottmarsheim (there is no security weir at Kembs) the time between load rejection and the start of overflow at the two extremities of the security weir is 11 min and 13 min. This corresponds to a speed of 8.5 m/s.

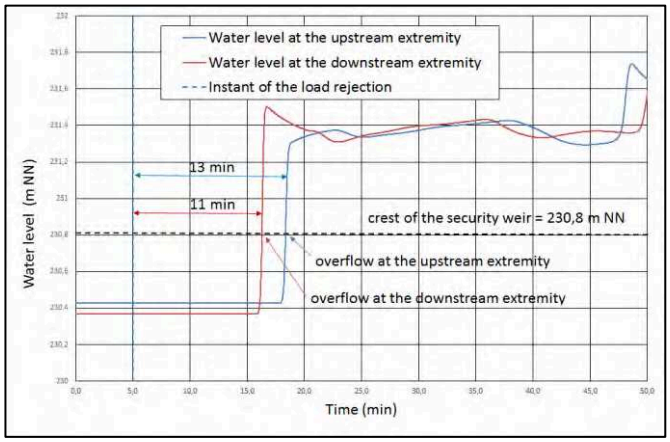

Fig. 13 Evolution of the level at Ottmarsheim security weir (D=5.6 km, L=1 km)

D = distance between the powerplant and the downstream extremity of the weir

L = length of the weir

The Mascaret code allowed the water level gradients and the transit time of the wave propagations required for the operation of the Rhine power plants to be predicted. These predictions avoided having to carry out on-site tests for each plant.

E. *Difficulties encountered*

Between two simulations carried out with mesh of 20 m and 10 m, the maximum level of the first oscillation shows a difference of 25 cm. The gradient of the rise in water level is unchanged, but this result is presently unexplained.

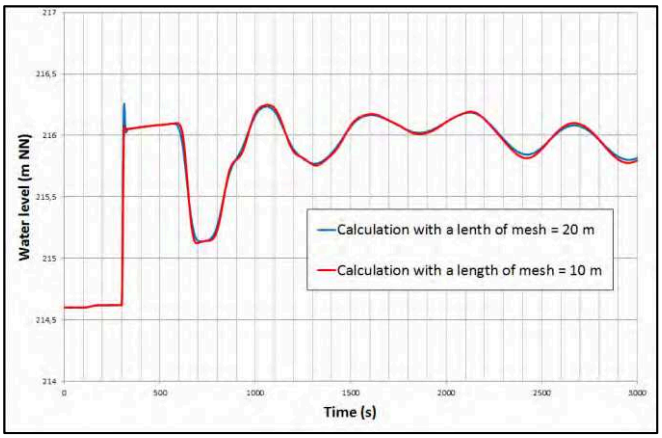

Fig. 14 Influence of the mesh

III. Line 4 of the Durance scheme - Manosque powerplant

The studied Line 4 is made up of six hydropower plants linked by 8 EDF channels parallel to the Durance river. To calculate the wave propagation, the line was separated into two parts, to refocus on the headrace canals of Manosque and Sainte Tulle 2 power plants.

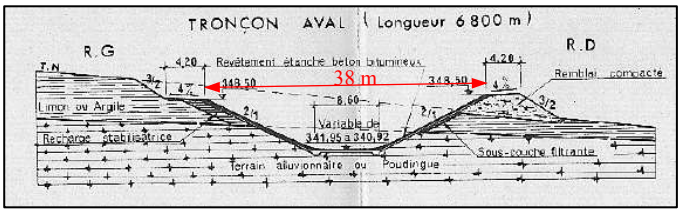

Fig. 15 Cross-section of Manosque headrace canal

A. Aim of the study

The aim of the study was to check the impact of an increase in flow from 140 to 168 m^3/s at Manosque power plant on the safety of the scheme's channels. The main check was that the water level variations produced by the plant's load rejection did not produce any overflow or loading of the bridges crossing the channel.

B. Characteristics of the model of Manosque

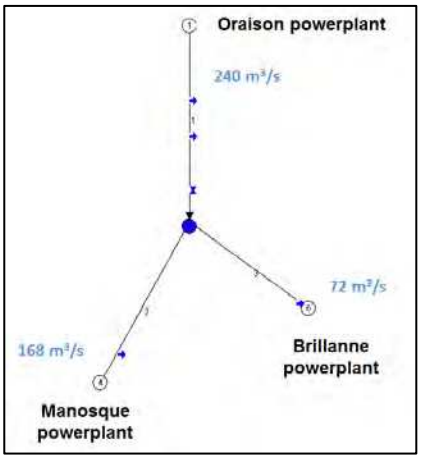

Fig. 16 Model of Manosque

The model is made up of three branches and three power plants: Oraison, Manosque and La Brillanne, linked by a junction called the Saint Saturnin diffluence.

Design flow (1969)	140 m^3/s
Design flow + 20 %	168 m^3/s
Fudaa-Mascaret version	3.5 (2015)
Calculation core	unsteady subcritical

Fig. 17 Saint Saturnin diffluence (view from upstream with a drone)

C. Tests realized in October 2017

The water level and flow measurements taken during the tests in October 2017 were done with a discharge of 140 m^3/s. They showed that the Favre waves observed on site did not produce maximum level in Manosque headrace canal.

For this reason, the "transcritical" core which allows the option "considering the non-hydrostatic terms" to be used, was not used.

Fig. 18 Wavefront and Favre waves in Manosque headrace canal (test D6)

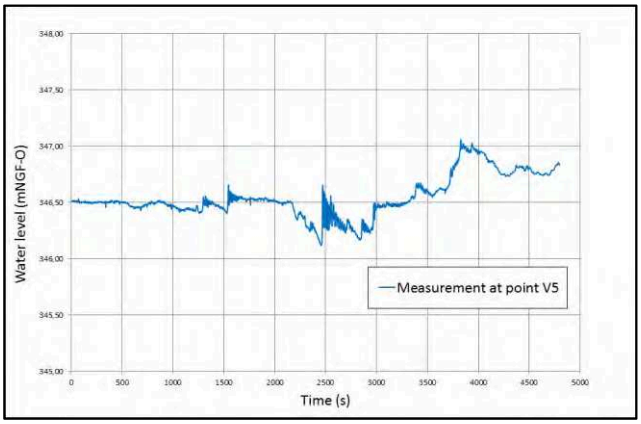

Fig. 19 Measurement in Manosque headrace canal (sensor V5 - test D6)

D. *Calculations parameters*

The numerical simulations have to be carried out at the highest level in the power plant's headrace canal, as well as with the highest flow. The operating constraints in steady states must therefore be considered, to avoid overflow at the security weirs and to respect the level laws set by the power plants controllers.

The main simulations are either a load rejection, or start up followed by a load rejection.

In steady state, as the flow regimes are subcritical, the simulations are done using the limit conditions upstream flow – downstream elevation.

In transient state, the simulations are done using the limit conditions upstream flow - downstream flow, based on the water lines in the channels determined by the steady state.

Since the watch officer of the Hydro Control Centre (CCH) can control the plants' operation, it was decided to use the flow variations measured during the on-site tests in October 2017 and adapted for the simulations at 168 m^3/s.

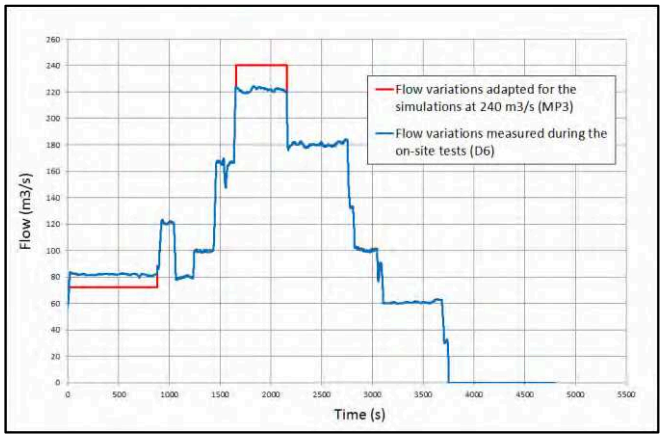

Fig. 20 Oraison flow laws

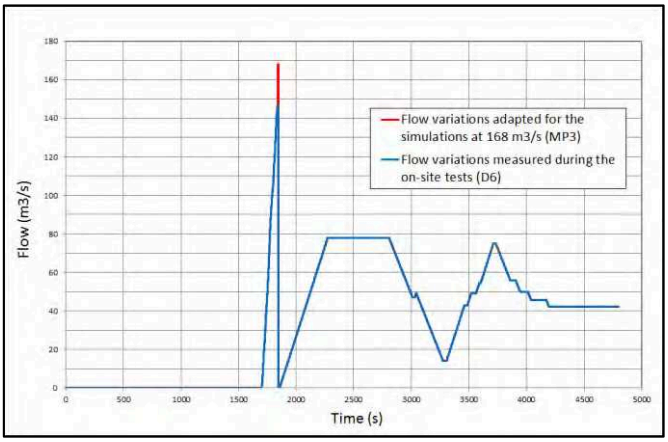

Fig. 21 Manosque flow laws (turbine + unloader)

E. *Main results*

The calibration of the model was based on tests carried out in 2012 to determine the Strickler coefficient values

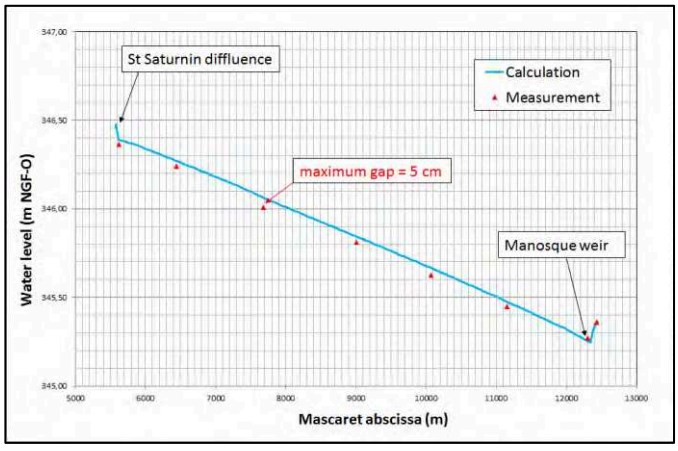

Fig. 22 Calibration of the Strickler coefficients

TABLE 3: STRICKLER COEFFICIENTS (KS) FOR THE DIFFERENT BRANCHES

Branch number	Abscissa of branches	Ks
1	0 – 403	60
1	403 – 2 220	62
1	2 220 – 3 899	70
1	3 899 – 4 257	68
1	4 257 – 4 292	60
1	4 292 – 5 527	65
2	5 566 – 12 448	65
3	12 603 – 14 205	52
3	14 205 – 15 054	54

The head losses that are specific to Saint Saturnin diffluence were not modelled. In steady state, they are included in the regular head losses by the Strickler coefficients.

In transient state, the maximum difference between the calculations and the measurements taken in October 2017 is 15 cm. It was decided to give the results with no uncertainty, because the numerical model tends to increase the levels measured during tests.

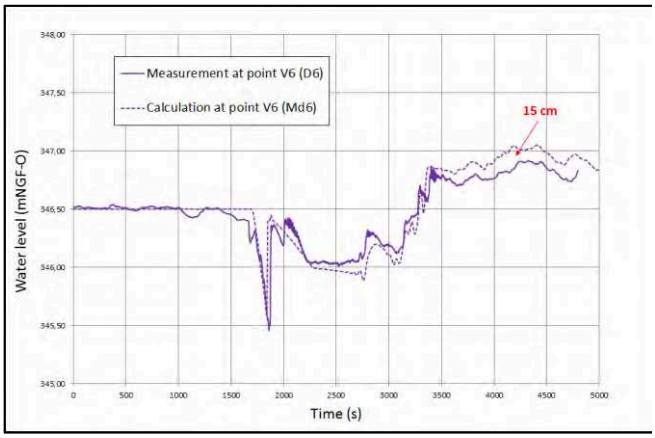

Fig. 23 Measurement calculation comparison for test D6

The maximum level reached for all the simulations at 168 m^3/s is at the upstream extremity of Manosque channel. The corresponding minimum freeboard is 1.10 m relative to the banks crest (348.50 m NGF-O) and no bridge is loaded.

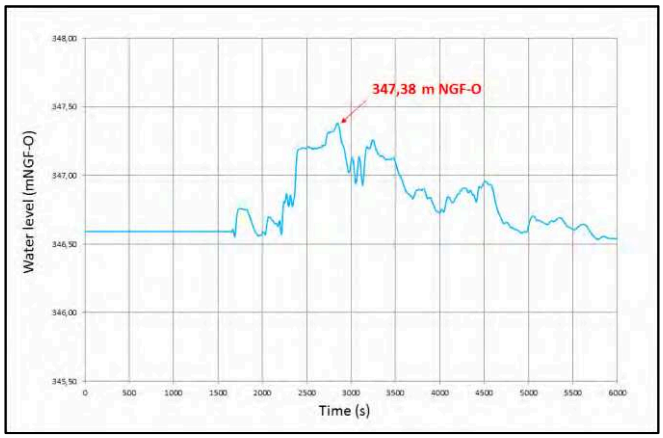

Fig. 24 Water level at the upstream extremity of Manosque channel during loading followed by a load rejection (MP3)

Thanks to Mascaret, it was possible to model this fairly complex scheme, after a number of simplifications, justified by the results of the tests of October 2017 and by the freeboard determined by the calculations, aim of the study.

F. Difficulties encountered

The calculation core used is "unsteady subcritical" because the initial water line calculations using the "transcritical" core do not converge easily and take too much calculation time, which was unsuitable for the time frame of this study.

Moreover, the initial water line calculated using the "unsteady subcritical" core is not compatible with a transient state calculation using the "transcritical" core.

Indeed, when we go back to the calculation, the "transcritical" core lacks information on the condition of the confluences, causing a systematic numerical instability at the start of the calculation.

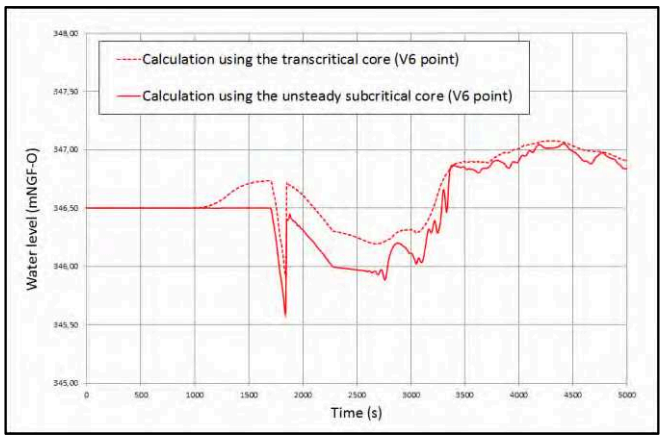

Fig. 25 Difference between the unsteady subcritical and transcritical cores

REFERENCES

User Guide Fudaa-Mascaret 3.0. Centre d'Etudes Techniques Maritimes et Fluviales (CETMEF) 2007

Numerical modelling of scale effects

Frederik Folke, Angela Haehne and Rebekka Kopmann
Department of Hydraulic Engineering
Federal Waterways Engineering and Research Institute
76187 Karlsruhe, Germany
frederik.folke@baw.de

***Abstract*— There is a long tradition of using hydraulic and morphodynamic models for river engineering purposes. Beside numerical models laboratory scale models play a crucial role, both to gain deeper insight into physical mechanisms and to study complex system behaviour and site-specific issues.**

In terms of river engineering all laboratory models are scaled in space and, thus, in time. One generally accepted method in scale models is to use different scaling factors in length and height resulting in exaggerated river geometry to ensure the similitudes of the main physical processes and to consider limitations of laboratory space. The exaggeration factor ranges typically from 1 to 2.5 for hydraulic laboratory models at the BAW, but 8 times larger factors can be found in literature.

In the present paper the scale effects, in particular the exaggeration, of a long fluvial model (Froude scaling) of the Middle Rhine with an exaggeration of n=1.2 are estimated numerically. A three-dimensional hydrodynamic-numerical (3D-HN) model of the laboratory model is set up and calibrated to the laboratory model measurements. The 3D-HN model is resized to nature-scale and to laboratory scale without exaggeration. The numerical results are analysed. Beside the global water level the secondary currents are of particular interest. The scale effects are estimated both qualitatively and quantitatively. The study has shown that the light exaggeration of the laboratory scales improves the results, but the improvement is small compared to the errors due to the scaling from nature-scale to laboratory scale.

I. INTRODUCTION

There is a long tradition of using hydraulic and morphodynamic models for river engineering purposes. Beside numerical models laboratory scale models play a crucial role, both to gain deeper insight into physical mechanisms and to study complex system behaviours and site-specific issues. In terms of river engineering all laboratory models are scaled in space and, thus, in time. This scaling results in so-called scaling effects. Additionally the force ratios have to be scaled using dimensionless numbers, such as the Reynolds number (ratio of inertial forces to viscous forces) or the Froude number (ratio of inertial and gravitational forces). It has to be taken into account that only two similitudes, e.g. the geometrical and the Reynolds number or the Froude number, can be fulfilled in a laboratory scale model using the same fluid and the same gravitational acceleration. For the other force ratios it has to be checked, that both systems are in the same regime, e.g. subcritical or fully turbulent. Other effects such as the surface tension (Weber number) can typically be neglected.

One generally accepted method in scale models is to use different scaling factors in length and height resulting in exaggerated river geometry to ensure the similitudes of the main physical processes and to consider limitations of laboratory space. This is quantified by the ratio, n, of the vertical length scaling factor, M_{Lv}, to the horizontal length scaling factor, M_{Lh},

$$n = \frac{M_{Lv}}{M_{Lh}}. \quad (1)$$

This ratio ranges typically from 1 to 2.5 for hydraulic laboratory models at the BAW. In literature, higher values can be found, such as 20, as applied in the Mississippi River Basin Model [1]. Besides the downsizing from real-world to laboratory scale also the exaggeration of laboratory models has an impact on the hydraulic and/or morphodynamic system ([2]). It must be considered, that it is impossible to keep in a scaled model all relevant force ratios constant ([3]).

In the present paper the scale effects, both from nature scale to laboratory scale and the exaggeration, of a long fluvial model (Froude scaling) of the Middle Rhine with an exaggeration of n=1.2 are investigated numerically. The scale of the laboratory model is 1:50 vertical and 1:60 horizontal. To account for the highly jointed bedrock topography a new manufacturing process for the laboratory model was developed. The final laboratory model bottom consist of plane concrete parts (traditional steel profile method), highly-resolved concrete blocks (using CNC processing method), and fixed gravel material. Furthermore, additional roughness elements were introduced during the calibration of the laboratory model.

A three-dimensional hydrodynamic-numerical (3D-HN) model of the laboratory model is set up on a scale 1:1. Each surface material and structure is represented in the numerical model by an individual roughness zone characterized by an equivalent sand roughness, ks. Not all geometrical details are captured by the numerical mesh, in particular the part of the highly-resolved concrete blocks. The calibrated 3D-HN model of the laboratory river model is resized to nature-scale and to laboratory scale without exaggeration.

The underlying scaling laws are described in section II. The laboratory and numerical models applied in this study

are presented in section III. In section IV the results are shown and the scale effects are analysed. The final conclusions and some ideas for further investigations are presented in section V.

II. SCALING LAWS

As mentioned above only a single force can be reproduced correctly in a scale model using the same fluid and with the same occurring gravitational force. In most river engineering purposes hydraulic laboratory models are scaled using the Froude similarity. It is applied when the dominant controlling force is gravity. The Froude scaling results in lower flow velocities in the model compared to nature. Consequently the Reynolds number is reduced, both due to the lower flow velocities and due to the smaller length scale. For a proper modelling it has to be checked that the turbulent regime (in general fully-turbulent) is the same in the model and in nature.

In Table 1 different factors for Froude and Reynolds scaling are summarized based on the geometrical scaling factor, M_L, and the exaggeration, n. For the Froude scaling it is distinguished between unexaggerated and exaggerated models. For detailed information see e.g. [4].

TABLE 1: FROUDE AND REYNOLDS SCALING FACTORS

Physical parameter		**Model law scale factor of**		
	Unit	**Froude**		**Reynolds**
		original	**exaggerated**	
Length / width	m	M_L	M_L (= M_{Lh})	M_L
Height	m	M_L	M_L/n (= M_{Lv})	M_L
Flow time, experiment duration	s	$M_L^{1/2}$	$(M_L\ n)^{1/2}$	M_L^2
Velocity	m/s	$M_L^{1/2}$	$(M_L/n)^{1/2}$	$1/M_L$
Acceleration	m/s^2	1	1/n	M_L^{-3}
Discharge	m^3/s	$M_L^{5/2}$	$(M_L^5/n^3)^{1/2}$	M_L
Relative slope	m/m	1	1/n	1

A common technique is to use different geometrical scaling factors in horizontal and vertical direction, resulting in an exaggerated model. This method makes it possible to use larger (horizontal) scaling factors, thus reducing the spatial extent of a laboratory model, without violating the Reynolds similarity. Furthermore, problems of to low water depths can be avoided, e.g. concerning the surface tension.

The exaggeration of a Froude scaled model has an impact on several hydraulic phenomena. Depending on the specific case and the amount of the exaggeration this effects might be more or less distinct. In Figure 1 three different aspects are highlighted. Exaggerated models are leading to a higher water level slope. To achieve similar velocities the bottom roughness has to be increased compared to unexaggerated nature (a). You also have to bear in mind, that vortex structures are not exaggerated in the model resulting in different proportions between the channel geometry and the vortex in the model with and without exaggeration (b). Furthermore, the exaggeration of a model results in different angles of inclination of non-horizontal structures. In the wake of these structures separations might occur resulting in higher energy losses compared to the unexaggerated model (c).

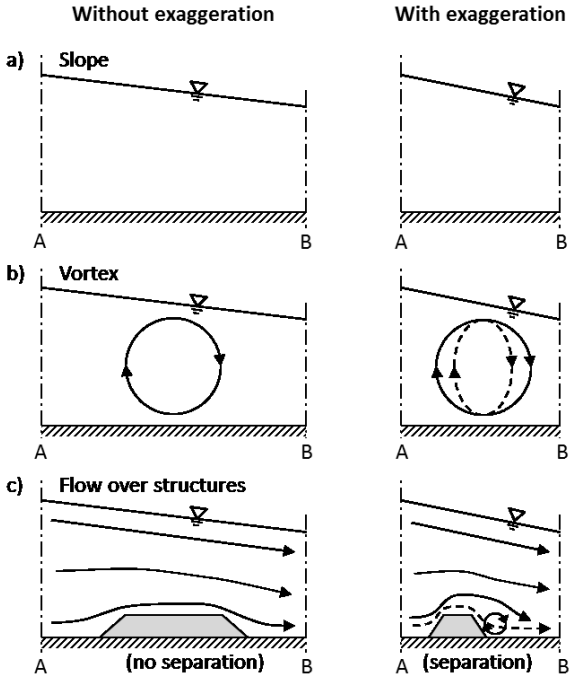

Figure 1: Influences of model exaggeration on a flume (a), a vortex (c) and an overflowed structure (d) after [5]

The roughness in scaled models is usually found by calibration. For this study the 3D-HN model of the laboratory river model is calibrated via experimentally derived roughness values from literature for the individual surface materials (concrete and gravel) and structures. For the scaled models– to nature-scale and to an unexaggerated model – two different methods are used to scale the roughness coefficient.

Firstly, the equivalent sand roughness of the Nikuradse friction law, k_s, is interpreted as a geometrical height. Thus, the same scaling as for the height is used (cf. Table 1), hereafter referred to as *geometrical scaling*.

Secondly, a scaling factor is derived based on the empirical Chézy equation

$$\bar{u} = C \cdot \sqrt{R_h \cdot S}, \tag{2}$$

with the cross-sectional averaged velocity, $\bar{u}$, the Chézy coefficient, C, the hydraulic radius, R_h, and the bottom slope, S (for steady and uniform flow). With the assumption of a wide channel ($R_h \approx h$, with the flow depth, h) and the Froude scaling factors for an exaggerated model a scaling factor of $\sqrt{n}$ can be derived; called *Chézy scaling* in the

following. For hydraulically rough flow the Colebrook-White formula correlates the Chézy coefficient and the ratio of the Nikuradse coefficient to the flow depth,

$$C = 18 \cdot \log_{10}\left(12 \cdot \frac{h}{k_s}\right). \quad (3)$$

For the scaling of the Nikuradse roughness – e.g. form the exaggerated laboratory model to nature-scale – based on the Chézy scaling and the Colebrook-White formula the flow depth must be known.

III. MODELS

A. Laboratory scale model

The laboratory model is 73 m long and represents a 4.4 km long stretch of the Middle Rhine. The central part of the investigation is a sharp 90° bend with a gravel bar on the inner bend and a rock island on the outer bend. It is designed as a long fluvial model (Froude scaling) with an exaggeration of n=1.2. The scale was defined 1:50 in vertical and 1:60 in horizontal direction. The bathymetry is presented in Figure 2.

To account for the highly jointed bedrock topography in the area of investigation a new manufacturing method was developed. By the use of CNC milling machines highly resolved concrete cast moulds were manufactured. This technique enables an extremely exact reproduction of the river bottom topography. Therefore most of the form roughness is incorporated in the model. During the calibration process different additional roughness elements were introduced (see Figure 3). For a detailed description of the laboratory model and the manufacturing process see [6].

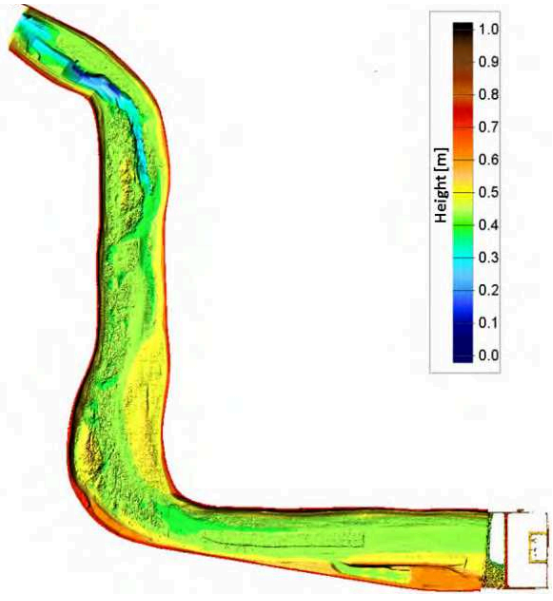

Figure 2: Bathymetry of the laboratory model

B. Numerical model

For the investigations of the scale effects three numerical models were built. The *reference model* (Lab_n12) has the same dimensions as the laboratory scale model. It is 73 m long and its bathymetry represents the laboratory model (Figure 2). Due to the used mesh size not all details of the topography are resolved, especially parts of the highly-resolved concrete blocks. This model was calibrated to velocity and water level measurements of the laboratory model. The same roughness zones as in the laboratory model (see Figure 3) were applied.

The *unexaggerated model* (Lab_n10) is the same as the reference model without the vertical exaggeration. Consequently, the slopes are the same as the slopes in nature.

The *nature-scale model* (Nat_n10) has nature dimensions, which means that the reference model is scaled by 60 in horizontal direction and by 50 in vertical direction.

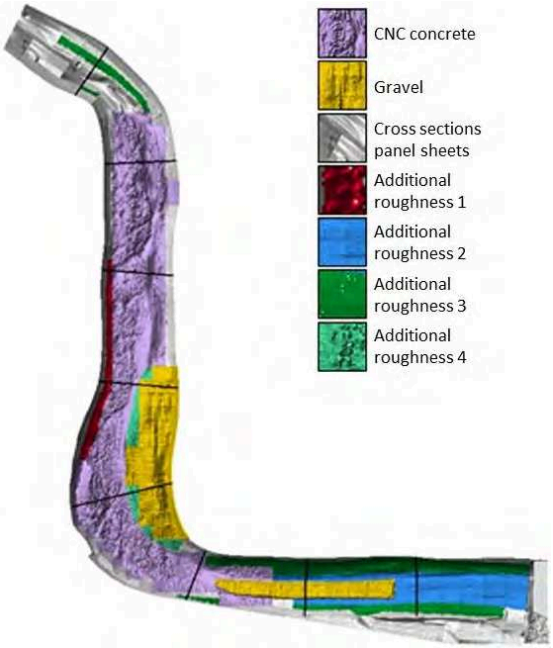

Figure 3: Roughness zones of the laboratory model

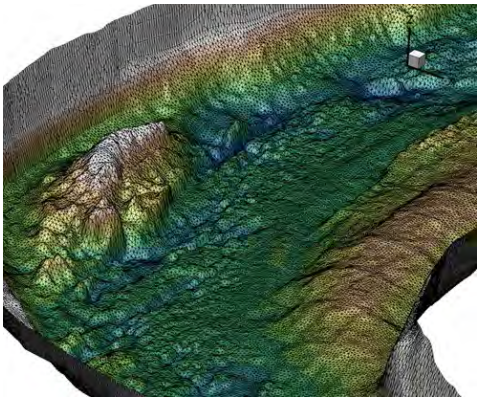

Figure 4: Grid structure of the numerical model at the 90° bend (figure exaggerated 5 times)

In Table 2 the characteristics of the three used numerical models are summarized. In the present paper all simulations were set up using stationary boundary conditions – constant

volume flux at the inlet and constant water level at the outlet. For the roughness-scaling the two above mentioned methods were used: geometrical scaling and Chézy scaling. For both methods a single value per roughness zone was used (cf. Figure 3). Only results for mean water level +1 m and the corresponding discharge are shown. Further information and results for other discharges can be found in [7].

TABLE 2: CHARACTERISTICS OF USED NUMERICAL MODELS

	Reference model (Lab_n12)	Unexaggerated model (Lab_n10)	Nature-scale model (Nat_n10)
Length / width scale	1:60	1:60	1:1
Height scale	1:50	1:60	1:1
Number of nodes	26370	26370	26370
Mean horizontal node distance	44 mm (bend: 38 mm)	44 mm (bend: 38 mm)	2640 mm (b.: 2280 mm.)
Vertical discretization	15 layers	15 layers	15 layers
Roughness coefficients	Calibrated to the lab model	geometrical (1:1.2) and Chézy scaling	geometrical (1:50) and Chézy scaling

IV. RESULTS

In Figure 5 the differences of the free surface from the unexaggerated model (Lab_n10, blue line) and the nature-scale model (Nat_n19, grey line) to the reference model (Lab_n12) are shown in nature-scale. The Chezy scaling (solid lines) results in lower Nikuradse roughness values than the geometrical scaling (dotted lines). The agreement of the water levels between all three models using the Chézy scaling of the roughness is fairly good. The maximum differences are within a 5 cm range. Using the geometrical scaling of the roughness, the water level shows show higher discrepancies between the unexaggerated model (Lab_n10) and the reference model (Lab_n12).

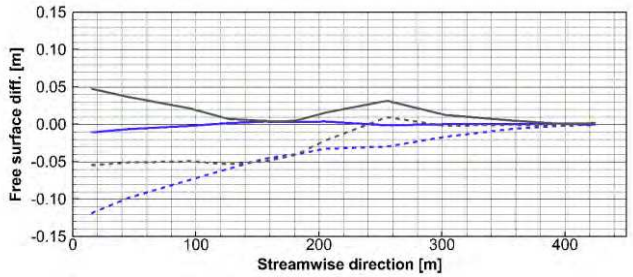

Figure 5: Differences of the free surface (blue: Lab_n10-Lab_n12, grey: Nat_n10- Lab_n12; solid: Chézy scaled, dotted: geometrical scaled

For Froude scaled models the assumption of the same laminar / turbulent regime in the prototype and in the model has to be verified. In this context a local Reynolds number is introduced,

$$Re = \frac{u \cdot h}{\nu}. \qquad (4)$$

based on local depth-averaged velocity, u, the local water depth, h, and the kinematic viscosity, ν. The critical Reynolds number for open-channel flow is 2320. For laboratory investigations it is recommended to be greater than 5000 to prevent Reynolds induced scaling effects ([2]). In the following we assume a laminar flow for 0<Re<2320, a partially turbulent flow for 2320<Re<5000 and a fully-turbulent regime for Re>5000.

In Figure 6 the local Reynolds number is shown for the reference model (left) and the unexaggerated model (middle) and for the nature-scale model (right), both using the Chézy scaling for the roughness. The geometrical scaling shows almost identical results (not shown in here). In the vicinity of the 90° bend deviations in the turbulent regime can be observed at the inner bend and at the outer bend. Especially in the area of the gravel bar at the inner bend the scaling from nature-scale (Nat_n10) to laboratory scale (Lab_n12 and Lab_n10) has a crucial effect. This is due to the lower water depth in this area. In the reference model (Lab_n12) the area of laminar and partially turbulent flow is reduced compared to the unexaggerated model. The influence of the scaling effects on the flow field is evaluated in the following.

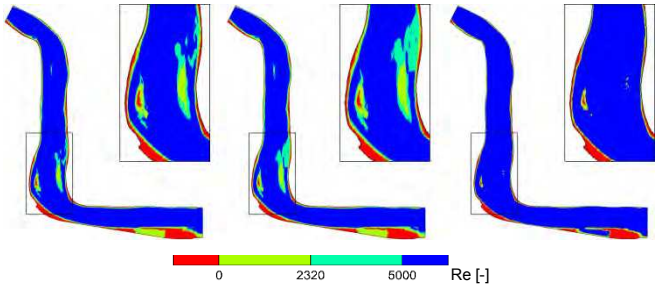

Figure 6: Local Reynolds number (left: Lab_n12, middle: Lab_n10 Chézy scaled, right: Nat_n10 Chézy scaled)

The velocity and discharge distribution is analysed at three different cross-sections for the three different models as shown in Figure 7. At the entrance of the bend (A-A) both the velocity distribution and the distribution of the specific discharge are similar in all three models (Figure 8 top). Only close to the right bank the velocities in the nature-scale model (Nat_n10, grey solid line) are smaller compared to models in laboratory scale (Lab_n10, blue solid line and Lab_n12, green solid line).

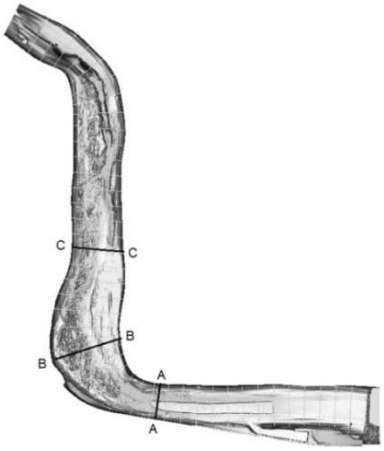

Figure 7: Cross-sections before (A-A), in (B-B) and after (C-C) the 90° bend

The distributions of the specific discharge show also in the bend (B-B) a good matching between the models (Figure 8 middle). The depth-averaged velocity shows differences in the range of the inner bend gravel bar. At a distance from 300 to 440 m to the left bank the flow velocities are in the nature-scale model (Nat_n10, grey solid line) significantly lower than in the models in laboratory scale (Lab_n10, blue solid line and Lab_n12, green solid line). Furthermore, in this part the distribution of the depth-averaged velocity differs, whereas the specific discharge (dashed lines) is similar in all models. With 70 % the maximum relative deviation of the specific discharge occurs at around 370 m to the left bank.

After the bend (C-C) both the velocity and discharge distribution show a slightly different distribution between the left and the right part of the channel (Figure 8 bottom). In the nature-scale model (Nat_n10, grey dashed line) the discharge is higher (up to 13 %) in the left part than in the models with laboratory scale and lower in the right part (up to 50 %). The reference model (Lab_n12, green lines) shows less deviation from the nature-scale model (Nat_n10, grey lines) than the unexaggerated model (Lab_n10, blue lines). This behaviour is similar to the differences of the laminar / turbulent regime as shown above in Figure 6. Violating the requirement of a fully turbulent regime, especially in the area of the gravel bar, leads to a less exact reproduction of the discharge distribution.

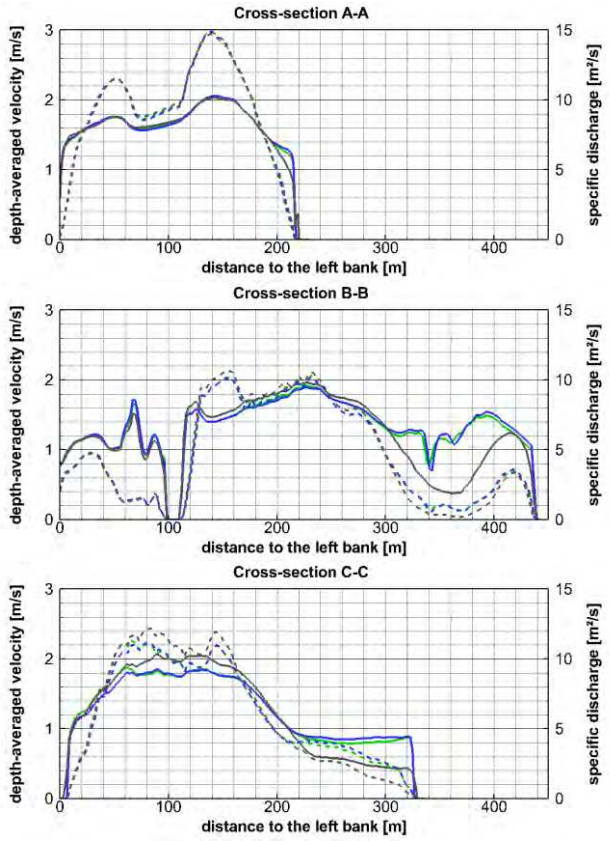

Figure 8: Depth-averaged velocity (solid) and specific discharge (dashed) distribution in three cross-sections (top: A-A, middle: B-B, bottom: C-C) for all three models (green: Lab_n12, blue: Lab_n10 Chézy scaled, grey: Nat_n10 Chézy scaled)

The differences of the specific discharge between the geometrical scaling and the Chézy scaling of the roughness are shown in Figure 9, both for the unexaggerated model (Lab_n10, blue lines) and the nature-scale model (Nat_n10, grey lines). The maximum deviations are in the order of 10 %, except in regions with very low specific discharges. In the cross-sections B-B and C-C the differences between nature-scale model and the two laboratory-scale models at least on order of magnitude larger than the differences between the two roughness scaling methods. Thus, in the specific case the influence of the roughness scaling is smaller than the geometrical (length-) scaling with a factor of 60.

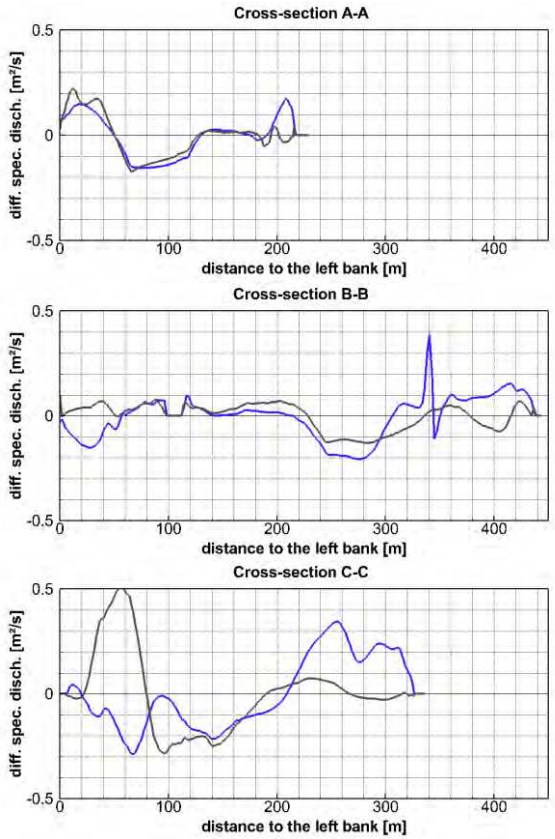

Figure 9: Differences of the specific discharge between the Chézy scaled roughness and the geometrical scaled roughness (blue: Lab_n10, grey: Nat_n10)

Beside the distribution of the velocity and the discharge the secondary flow in the 90° bend plays a crucial role for the evaluation of the scaling effects. In this context streamlines close to the bottom (near-bottom), at the height of the first cell, and on the free surface are compared. The starting line for the streamlines is located above the 90° bend slightly left of the channel centre line. This location is chosen as it is potentially on the main path of the sediments depositing at the inner bend.

In Figure 10 the streamlines in the nature-scale model are shown based on the depth-averaged velocity, the velocity at the free surface and the near-bottom velocity. Due to the occurring secondary flow induced by the channel curvature the fluid close to the bottom flows in the direction of the

inner bend and at the free surface in direction of the outer bend. This separation shows the highly three-dimensional character of the occurring flow field at the 90° bend section.

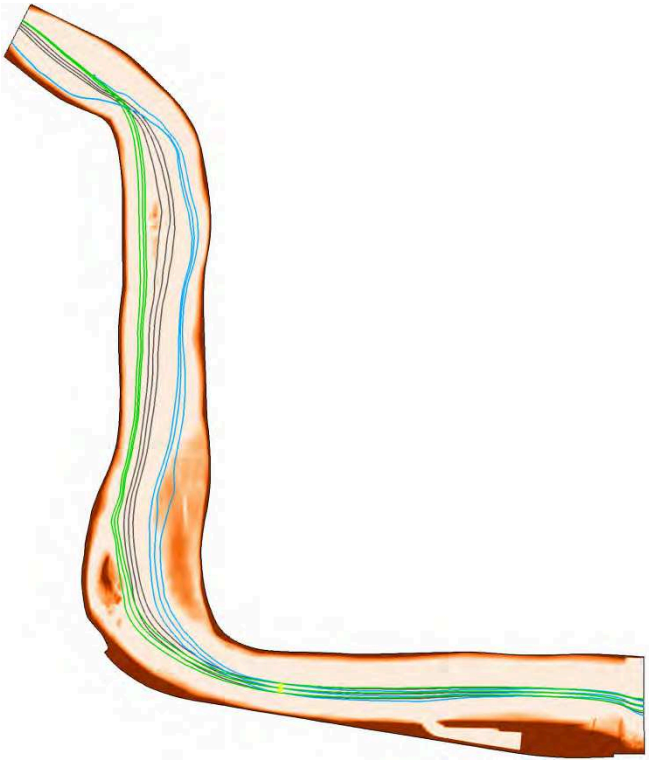

Figure 10: Streamlines nature-scale model, Nat_n10 Chézy scaled (grey: depth-averaged velocity, green: velocity at the free surface, blue: near-bottom velocity)

In Figure 11 the near-bottom streamlines and the streamlines at the free surface are compared for the nature-scale model (Nat_n10, black lines) and the reference model (Lab_n12, blue lines). In the zoom on the channel bend very small differences can be observed. In the nature-scale model the effect of secondary flow seems to be slightly higher. Due to the small differences the streamlines for the unexaggerated model (Lab_n10) are not shown here.

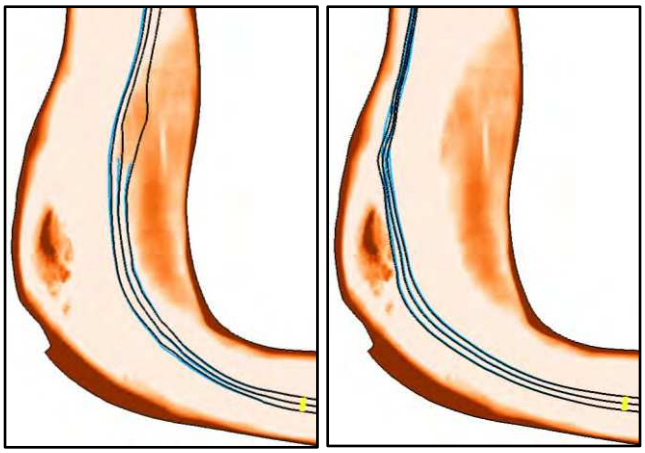

Figure 11: Left: near-bottom streamlines, right: free-surface streamlines (blue: Lab_n12 Chézy scaled, black: Nat_n10 Chézy scaled)

Despite the discrepancies of the velocity and discharge distribution the secondary flow effect on the separation of the flow field is only slightly affected. Due to the very small differences between the two roughness-scaling methods, the streamlines for the geometrical scaling case are not shown in here.

V. CONCLUSIONS AND OUTLOOK

The influence of scaling effects using laboratory scale models are highlighted and analysed for a specific laboratory model of the Middle Rhine. Due to scaling limitations using the same fluid (water) in the laboratory model and in nature and the same gravitational force, scaling effects are always occurring.

In the present case both the velocity distribution and the distribution of the specific discharge is affected by not fully ensuring Reynolds similarity. At the inner bend partially not fully-turbulent flow occurs at laboratory scale due to the low water depth in this part. This limitation is also not compensated by the used exaggeration factor of 1.2 – even though the results show less deviation to the nature-scale model than the unexaggerated model. Regarding the important effect of the secondary flow – resulting in a separation of the near-bottom flow and the flow at the free surface – only slight deviations between the nature-scale model and the reference model can be observed.

The two roughness-scaling methods showed only slight differences in the discharge distribution in the three cross-sections. The roughness-scaling based on the Chézy equation showed for the presented discharge less deviations of the water level compared to the reference case. The Chézy-scaling method is recommended for further investigations.

Depending on the problem formulation and the area of interest the laboratory scale models show good agreement to the investigated nature-scale model. The exaggeration of the model seems to have lower impact than the scaling from nature-scale to laboratory scale, which is the basis for laboratory investigations.

For future studies it is planned to perform a scale series to investigate the scaling effects with increasing / decreasing horizontal and vertical scaling factors. The aim is to identify a critical exaggeration factor which might significantly influence results.

In general, for laboratory investigations in river engineering it is of great importance to understand the influence of the occurring scaling effects. The presented method shows a cost-effective approach and the great value of hybrid modelling while working on river engineering challenges.

Nevertheless one has to bear in mind that the current investigation is performed only numerically. The influence of possible effects originated from this method, like numerical diffusion, was not evaluated in detail in the present study. It is assumed that the findings presented in this paper are not affected crucially by these artefacts, because all conclusions are based on comparative analysis.

REFERENCES

[1] K. D. Cheramie, “The Scale of Nature: Modeling the Mississippi River”, Places Journal.

[2] H. Dorer, “Similitude of Fluvial Models” (in German), Mitteilungsblatt der BAW, 54, 1984.

[3] V. Heller, “Scale effect in physical hydraulic engineering models”, J. Hydr. Res., Vol. 49, No. 3, 2001, pp. 293-306.

[4] H. Martin and R. Pohl, “Technical hydromechanics” (in German), Verlag für Bauwesen, Berlin, 2000.

[5] DVWK 1984, “Wasserbauliches Versuchswesen”, Heft 39.

[6] S. Wurms, T. Hüsener, F. Folke, N. P. Huber and A. Schmidt, “Growing challenges in river engineering – What contribution can hybrid modeling make?”, E-proceedings of the 2nd International Symposium on Hydraulic Modeling and Measuring Technology Congress, Nanjing, China, 2018.

[7] A. Haehne, “Numerical Modeling (3D-HN) of a highly resolved laboratory model in laboratory scale and nature-scale” (in German), Master Thesis, KIT Karlsruhe, 2018.

Introducing KHIONE – (Eulerian) Part I of the ice modelling component of TELEMAC

Sébastien E. Bourban[1], Fengbin Huang[2], Hung Tao Shen[2], Riadh Ata[3]
[1]Coasts and Ocean Group, HR Wallingford, Howbery Park, Wallingford, UK
[2]Department of Civil and Environmental Engineering, Clarkson University, Potsdam, NY 13699-5710, USA
[3]Laboratoire National d'Hydraulique et Environnement, EDF R&D, 6 Quai Watier, 78400 Chatou, France
s.bourban@hrwallingford.com

Abstract — **With a view to expand the applicability of the TELEMAC system to cold waters around the world, EDF R&D and HR Wallingford jointly financed the development of a new ice modelling component in collaboration with the ice modelling experts from Clarkson University, USA. This collaboration has seen years of experience and ice modelling capabilities of the Clarkson's team introduced into the TELEMAC system.**
Various ice processes can occur in cold regions during winter periods. These include complex interactions between thermal-ice processes and ice dynamics coupled with hydrodynamics. This Part I article introduces those based on the Eulerian assumption. Part II will later introduce processes based on the Lagrangian assumption.
Some of the validation cases developed to demonstrate KHIONE's capabilities are presented.

I. INTRODUCTION

The state of the art knowledge and modelling capabilities in ice processes resides in northern countries that have major infrastructures recurrently subject to ice for long periods of time. To name only a few, several industries in Canada, the USA, Northern Europe and Russia, Japan, and China are influenced by ice processes over water bodies. The presence of ice in waters affects the design and operation of coastal and riverine infrastructure and projects in addition to impacts on ecological and environmental conditions of water bodies. For instance, the St. Lawrence River is a major transportation route between the Atlantic and the Great Lakes for both the USA and Canada. It also serves the hydropower industry in those countries. Great portions of the St. Lawrence River freeze-up during the winter months. Similarly, the Yellow River is essential for China's very existence while being the cause of devastating floods. Amongst those floods, the breakup of ice jams in Inner Mongolia has caused extreme loss of life and property in the past century.

With a view to expand the use of the TELEMAC system to these waters and other cold regions around the world, EDF R&D and HR Wallingford jointly financed the development of a new ice modelling component in collaboration with the experts of the Department of Civil and Environmental Engineering, Clarkson University, USA. Years of experience and of development of ice modelling capabilities within the Clarkson's team were introduced into the TELEMAC system to produce KHIONE.

Somewhat in line with the naming tradition of TELEMAC, the new component was named KHIONE, from the Greek goddess of snow and ice, daughter of Borea (god of the northern wind), and who had a son with Poseidon (god of the sea).

This article is Part I of two parts, focusing on the ice processes based on the Eulerian assumption. Part II, anticipated for the XXVIth TELEMAC User Conference will later introduce processes based on the Lagrangian assumption. These processes have been integrated in the version v8p0 (released later in 2018) and are therefore documented and available in parallel.

II. POSITIONING OF KHIONE

A. ... within the ice modelling history

Numerical modelling studies have played an important role in river and coastal engineering, even more so when related to ice modelling. The requirement to work in an environment with air temperature below freezing to accurately represent exchanges at the air-ice-water interfaces has restricted physical modelling studies to idealised experiments in relatively small flumes in frigorific rooms. Additionally, it is very difficult to scale ice dynamic processes (see [1] and [2]) rendering the growth of frazil ice or the formation and evolution of an ice cover and their interaction with the hydrodynamics, the bathymetry, and the banks or any manmade structures virtually impossible.

Contrarily, numerical models can be a useful tool to investigate the numerous processes that interact under different flow, level, weather, and operational conditions. Thermal-ice processes have been considered in numerical models with increasing complexity in the past couple of decades (see [2]). For instance, in 1991, [2] developed a 1D river ice model, RICE, further improved by [3] and [4], capable of simulating unsteady flow and ice processes in channel networks over a long winter period. In 2000, [6] developed a 2D river ice dynamics model, DynaRICE, enable the modeling of the formation of ice jams, which could not be done with the conventional static ice jam theory (see [2] and [11] for instance). The DynaRICE models were further extended in 2006 by [6] to incorporate thermal-ice processes. Simulation of water temperature with super-cooling, frazil ice concentration, surface ice transport, ice cover progression, undercover ice transport, thermal growth and decay of ice covers, and ice-cover stability were included. Later this was further refined to include the treatment of trans-critical flows and wetting and drying bed transitions [9].

B. ... within the TELEMAC system

The KHIONE component is now part of TELEMAC, an open source suite of scientific codes enabling mathematical modelling of all free surface hydraulics including water levels,

currents, waves, transport of tracers and sediments as well as geomorphology and water quality.

Because ice processes are intertwined with hydrodynamic processes, a simulation using KHIONE is carried out through TELEMAC-2D (coupling with TELEMAC-3D to be completed at a later stage). KHIONE cannot be run in standalone mode. Furthermore, since ice processes are also dependent upon temperature and heat exchanges with the atmosphere, a coupling with the water quality component WAQTEL is also necessary. This is done through the TELEMAC-2D keyword `COUPLING WITH = "KHIONE;WAQTEL"`.

Once coupling is activated, individual ice processes are triggered by setting the keyword `ICE PROCESSES` to a multiplicative combination of prime numbers, with each prime number being associated to a particular process. For instance, `ICE PROCESSES = 2` turns on the surface heat exchanges with the atmosphere, and only that process. When water is allowed to cool slightly below freezing temperature, super-cooling can produce frazil ice. With `ICE PROCESSES = 14` (where 14 is 7 times 2), not only the surface heat exchange process is turned on, but the formation of static border ice is also made possible. The effect of surface ice dynamics and ice cover on the hydrodynamics uses the prime number 3, thus setting `ICE PROCESSES = 42` (where 42 is 7 times 3 times 2) would trigger a combination of all 3 processes. It is noted that 1 is not a prime number and would switch off all processes.

For consistency and possible interaction between KHIONE and WAQTEL, a number of changes were also implemented in WAQTEL. In particular, the TELEMAC-2D keyword `WATER QUALITY PROCESS` is now also based on a combination of prime numbers, with 1 switching all water quality processes off.

III. THEORETICAL ASPECTS

This section presents the first part of the theoretical aspects of the developments made for KHIONE. These include modules relating to the heat budget, the interaction between water temperature and frazil concentration, the freeze up processes and the formation of static and dynamic border ice cover, in addition to the effects ice has on the hydrodynamics or on structures such has clogging of frazil ice on intake grids or undercover flows. Surface ice dynamics and evolution, ice jam and breakup will be presented at a later stage.

A. Energy Budget (exchange with the atmosphere)

A dominant part of the heat exchanges occurs at the surface in contact with the atmosphere and includes short and long wave radiation, evaporation / condensation, sensible heat exchange, and precipitation (see [1] and [7]). There are two options provided to the user depending on the availability of atmospheric data: a linearized formulation, the parameters of which should be calibrated and a comprehensive thermal budget (based on humidity, winds, solar radiation, precipitation, cloud cover, etc.).

For the linearized option, the total surface heat loss rate, ϕ^*, may be written:

$$\phi^* = -\phi_R + \alpha' + \beta'(T_s - T_a) \quad (1)$$

in which, α' and β' are user defined parameters and ϕ_R is the net short wave radiation, the difference between the incoming solar radiation and the solar radiation reflected back to the atmosphere, a function of the cloud cover, the optical air mass, the day of the year and the solar latitude and declination, the atmospheric pressure, the eccentricity correction factor of the earth's orbit the albedo and a solar constant of 1,300 [W/m^2]. These are detailed in the user manual. If α' and the solar constant are set to zero, then the total surface heat loss rate is a direct function of the difference between the surface and the air temperature.

For the comprehensive option, the total surface heat loss rate, ϕ^*, may be written:

$$\phi^* = -\phi_R + \phi_B + \phi_E + \phi_H + \phi_P \quad (2)$$

in which, ϕ_B is the effective back radiation or terrestrial radiation, also the net balance of the atmospheric long-wave radiation reaching the surface water, the fraction of the atmospheric radiation reflected back by the surface water, and the long wave radiation emitted by the surface water, ϕ_E is the evaporation heat transfer, ϕ_H is the conductive or sensible heat transfer, and ϕ_P is the heat transfer due to precipitation. Saturated vapour pressure, wind, emissivity, relative humidity, air and surface temperatures, cloud cover, visibility or even the snow or rain fall make up the principal parameters of these additional fluxes. These are detailed in the user manual.

B. Supercooling and suspended frazil concentration

When the water is super-cooled, suspended frazil ice particles start to form. The continuous heat loss from the water body promotes the increase in size and concentration of the frazil ice. Depending on the turbulent intensity, the entrained frazil ice may either float to the water surface contributing to the surface ice sheet or remain entrained in the fast flows.

The change of suspended frazil ice concentration can be caused by both creation of particles (thermal growth) and by settling (mass exchange with surface ice). Separating the two terms, the source / sink term of the frazil equation is:

$$\frac{DF}{Dt} = \frac{DF^g}{Dt} + E \quad (3)$$

in which F is the frazil concentration and E represents the mass exchanges (settling) with the surface ice. Ice production due thermal growth of frazil can then be computed as:

$$\frac{DF^g}{Dt} = -\frac{1}{\rho_i L_i}\frac{N_u^f K_w}{d_e} a_0 T_w N_f \quad (4)$$

in which ρ_i is the mas density of ice, L_i is the latent heat of fusion, d_e is the frazil crystal thickness, N_u^f is the Nusselt number, K_w is the thermal conductivity of water, a_0 is the surface area of a frazil particle normal to the a-axis of frazil crystal, N_f is the number of crystal per unit volume, and T_w is the water temperature.

With that said, we note that the conservation of the thermal energy of the ice-water mixture is solved (as opposed to the conservation of frazil concentration) and is written:

$$\frac{De_T}{Dt} = (\phi_{ss} - \phi_{sk}) + \rho_i L_i E \quad (5)$$

where the thermal energy $e_T = \rho_w C_p (1 - F) T_w - \rho_i L_i F$

in which ϕ_{ss} and ϕ_{sk} are the rates of heat gain and loss respectively. Combining the above equations and re-arranging in an effort to extract the source and sink terms for the water temperature equation, leads to:

$$\frac{DT_w}{Dt} = \frac{(\phi_{ss}-\phi_{sk})}{\rho_w c_p(1-F)} - \frac{T_w E}{(1-F)} + \frac{\rho_i L_i}{\rho_w C_p(1-F)}\frac{DF^g}{Dt} + \frac{T_w}{(1-F)}\frac{DF^g}{Dt} \quad (6)$$

in which, on the right side of the above equation the first term denotes the water temperature change due to the heat loss and gain through the water surface; the second term denotes the water temperature change due to mass exchange of suspended frazil between the suspended layer and the surface ice layer; and the third and fourth terms denote the water temperature changes due to the heat transfer from suspended frazil to water or due to frazil thermal growth. The first term is included in the water temperature conservation equation, the second term is an order of magnitude smaller than the other terms and can be neglected. Additional details are provided within the user manual.

C. Border ice cover formation

Border ice can be divided into two types: static border ice and dynamic border ice. Static border ice is usually the first ice to appear on the surface. It is essentially the skim ice formation along the banks. Dynamic border ice is due to the accumulation of surface ice floes along the edge of static border ice. The growth of dynamic border ice is subjected to a mechanical condition where the adherence of the surface ice floes balances the drag and gravity component on the ice floes. The formulation for the static and dynamic border ice growth in KHIONE is detailed in [3].

1) Static border ice

Static border ice growth is computed by proximity to border edges of the finite element mesh (either mesh boundaries or by accumulation of border ice where border ice has formed already). If the thermal and hydrodynamic conditions for static border ice growth are met on a node adjacent to the border ice boundary, ice growth will proceed from the boundary toward that node. The growth continues from node to node until the conditions exceed the thresholds for static border ice growth.

The following thresholds for static border ice formation follow the work of [7]:

- The water surface temperature (computed from the depth-averaged water temperature based on [7] and [8]) is less than a critical value for static border ice formation (set by default to -1.1°C based on data from River Ohre, Germany);
- The buoyant velocity of frazil is greater than the vertical turbulence velocity (including the effect of wind-generated turbulence) computed by [3]; and
- The local depth-averaged velocity is less than the critical velocity for static border ice formation.

Additional details are provided within the user manual.

2) Dynamic border ice

The formulation implemented within KHIONE follows the work of [2], with modifications on the value of the critical velocity. A dimensionless relationship for the lateral growth rate of dynamic border ice is expressed as:

$$\rho_w L_i \frac{\Delta W}{\Delta \phi} = 14.1\, V_*^{-0.93} C_a^{1.08} \quad (7)$$

in which ΔW is the growth rate of dynamic border ice, $\Delta\phi$ the heat loss through the water-air interface, $V_* = u/V_c$ is the velocity criteria for dynamic border ice growth with u the flow velocity and V_c the maximum flow velocity where ice parcels can adhere to existing border ice, and C_a the surface ice area.

The critical velocity for dynamic border ice formation was found to be (see [12]) $V_c = 0.4$ [m/s] for the upper St. Lawrence River. Additionally, [2] found that equation (7) is valid for $0.167 < V_* < 1.0$. When $V_* < 0.167$ static border ice or skim ice will grow and $1.0 < V_*$ no border ice will grow. The lower limit is used for the limiting condition for static border ice growth, where $u \le V_* V_c = 0.167 * 0.4 = 0.07$ [m/s]. Dynamic border ice growth is also limited by areal concentration of surface ice (see [2]). Only static border ice can grow if $C_a < 0.1$ and only equation (7) should be used for dynamic border ice growth otherwise.

D. Ice cover impact on the hydrodynamics

The conventional St. Venant equations for free surface flow have been extended to include the surface ice effects (see [10]).

1) The continuity equation

The continuity equation for the total water discharge can be written as:

$$\frac{\partial \eta}{\partial t} + \frac{\partial q_{tx}}{\partial x} + \frac{\partial q_{ty}}{\partial y} = \frac{\partial}{\partial t}(C_a t_i') \quad (8)$$

in which $q_{tx} = q_{lx} + q_{ux}$ and $q_{ty} = q_{ly} + q_{uy}$ are the components of total unit width water discharge, q_{lx} and q_{ly} are the components of unit width water discharge beneath the ice layer (lower), $q_{ux} = q_{ix} + q_{sx}$ and $q_{uy} = q_{iy} + q_{sy}$ are the components of unit width water discharge in the upper layer, $q_{ix} = u_i(\eta - \eta')(1 - C_a)$ and $q_{iy} = v_i(\eta - \eta')(1 - C_a)$ are the components of unit width water discharge carried by the ice, q_{sx} and q_{sy} are the components of unit width water discharge in the ice layer relative to the moving surface ice, or seepage discharge through the ice cover, η the water surface elevation and η' the the bottom of the ice cover, C_a is the surface ice area.

2) The momentum equations

The momentum equations are modified as follows:

$$\begin{aligned} &\frac{\partial q_{tx}}{\partial t} + \frac{\partial}{\partial x}\frac{q_{tx}^2}{H_t} + \frac{\partial}{\partial x}\frac{q_{tx}q_{ty}}{H_t} = \\ &\qquad \frac{1}{\rho}(\tau_{sx} - \tau_{bx}) + \frac{1}{\rho}\left(\frac{\partial T_{xx}}{\partial x} + \frac{\partial T_{yx}}{\partial y}\right) - gH_t\frac{\partial \eta}{\partial x} \\ &\frac{\partial q_{ty}}{\partial t} + \frac{\partial}{\partial x}\frac{q_{tx}q_{ty}}{H_t} + \frac{\partial}{\partial y}\frac{q_{ty}^2}{H_t} = \\ &\qquad \frac{1}{\rho}(\tau_{sy} - \tau_{by}) + \frac{1}{\rho}\left(\frac{\partial T_{xy}}{\partial x} + \frac{\partial T_{yy}}{\partial y}\right) - gH_t\frac{\partial \eta}{\partial y} \end{aligned} \quad (9)$$

in which one can write $T_{xy} = \epsilon_{xy}(\partial q_{tx}/\partial y + \partial q_{ty}/\partial x)$ and ϵ_{xy} are the eddy viscosity coefficients, τ_s and τ_b are the shear stresses at the ice-water interface and the bed respectively, and H_t is the water depth underneath an equivalent ice-water interface computed from $H_t/H = (q_t/q_l)^{3/5}$, with H the water depth beneath the ice layer.

E. Frazil ice clogging on a set of bars

Figure 1 below shows the anticipated stages of frazil ice clogging on a rack made of regularly spaced bars. First, one observes the initial frazil ice adhesion, followed by the frazil ice deposition on the leading edge. Then the accumulated ice bridges between bars and start blocking the flow. Still ice

accumulates between bars due to the head difference across the rack and carry on pilling up for as long as there is frazil ice in suspension in the water.

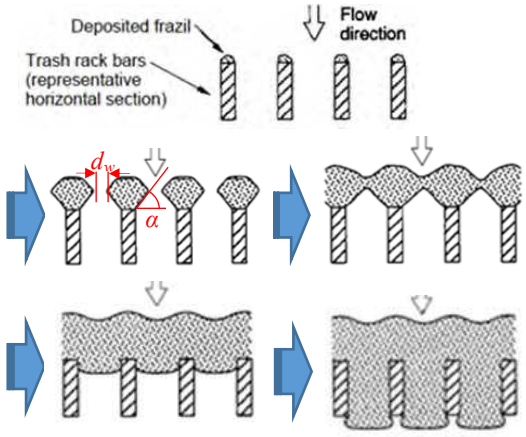

Figure 1 - Stages of frazil accretion on a rack of vertical bars

It is estimated from (see Figure 1) that the angle α between the edge of frazil accumulation and the transverse direction is about 55 deg. The width of the gap between two bars with gradual ice accumulation is noted d_w and is computed by KHIONE as a function of frazil ice concentration, the discharge through the bars, a deposition coefficient and the porosity of ice, assumed to be 0.67 (see [1]).

IV. Examples of Applications

In this section, a few of the validation test cases developed through the collaborative research project are presented to highlight practical applications of the theoretical aspects presented in the previous section. Again, these cases focus on the Eulerian part of KHIONE, with other validation test cases being currently tested for the Lagrangian part of KHIONE.

A. Energy Budget (contact with the atmosphere)

This first test case compares various uses of the two heat exchange models implemented within KHIONE, namely the full thermal budget model and a linearized model, with and without solar radiation.

1) Model setup

The domain is a simple square box (4x4 m) surrounded by solid boundary with no hydrodynamics, no friction and no diffusion of tracer. The still water depth is initially set to 1 m and the water temperature set at 10.59°C. The model is run for 288 steps of 300 s (i.e. a duration of 1 day).

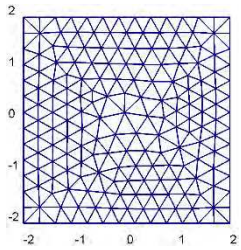

Although only one tracer is used (temperature), frazil is also activated by KHIONE when `ICE PROCESSES = 2`, and would appear if the air temperature was sufficiently cold.

2) Model drivers

There are no external drivers to the model other than the atmospheric exchanges. This is where the four variations of the same test case differ, with values of α' and β' of (1) set through the keywords `WATER-AIR HEAT EXCHANGE CONSTANT` and `WATER-AIR HEAT EXCHANGE COEFFICIENT` respectively. By default, $\alpha' = 50$ and $\beta' = 20$. These values are unrealistic in the test case provided and only serve for illustrative purpose.

- Linear model: the model is first driven by a constant air temperature and no solar radiation nor any other atmospheric heat fluxes.
  The essential keywords for KHIONE are:
  ```
  AIR TEMPERATURE = -6.0
  WATER-AIR HEAT EXCHANGE COEFFICIENT = 14.0
  SOLAR CONSTANT = 0.
  ```
  The essential keyword for WAQTEL is
  ```
  ATMOSPHERE-WATER EXCHANGE MODEL = 3
  ```

- Linear model with solar radiation: second, the linear model driven by a constant air temperature and the solar radiation is left default.
  The essential keyword for KHIONE is:
  ```
  AIR TEMPERATURE = -6.0
  WATER-AIR HEAT EXCHANGE CONSTANT = 70.0
  ```
  The essential keyword for WAQTEL is
  ```
  ATMOSPHERE-WATER EXCHANGE MODEL = 3
  ```

- Linear model with varying air temperature: third, the linear model driven by a varying air temperature and the solar radiation is left default.
  The essential keyword for KHIONE is:
  ```
  AIR TEMPERATURE = -6.0
  WATER-AIR HEAT EXCHANGE CONSTANT = 0.0
  WATER-AIR HEAT EXCHANGE COEFFICIENT = 25.0
  ```
  The essential keyword for WAQTEL is
  ```
  ATMOSPHERE-WATER EXCHANGE MODEL = 3
  ```
  The essential keyword for TELEMAC-2D is:
  ```
  ASCII ATMOSPHERIC DATA FILE = 't2d_meteo.lqd'
  ```

- Full thermal budget model: last but not least, variations in air temperature, cloud cover, dew temperature, visibility, snow, rain and wind speed are provided through the ASCII file within the TELEMAC-2 D steering file. The heat exchange model is now set to 4, one of two options available within KHIONE.
  The essential keyword for WAQTEL is
  ```
  ATMOSPHERE-WATER EXCHANGE MODEL = 4
  ```
  The essential keyword for TELEMAC-2D is:
  ```
  ASCII ATMOSPHERIC DATA FILE = 't2d_meteo.lqd'
  ```

The input dataset for the full thermal budget model (also used with varying air temperature) is taken from the Wanjiazhai reservoir, China, on the Yellow River.

3) Model results

Figure 2 shows the resulting water temperature in the box under the influence of the atmospheric conditions for all four approaches, whether weather data are provided or not. On a secondary axis (right) it also shows the air temperature (red dots).

This test case shows the importance of calibrating the α' and β' parameters of equation (1), corresponding to the keywords `WATER-AIR HEAT EXCHANGE CONSTANT` and `COEFFICIENT` respectively.

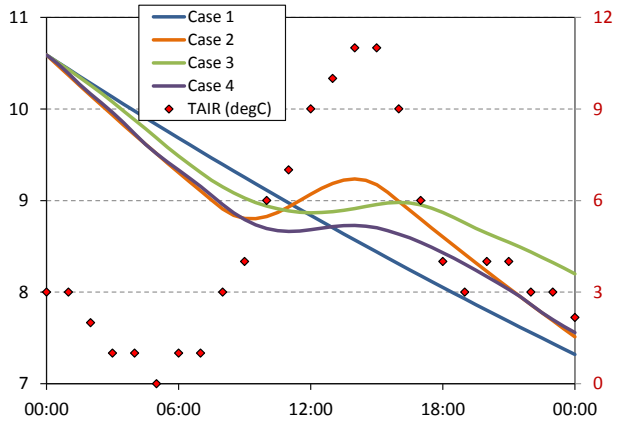

Figure 2 – Water temperature under atmospheric drivers

Comparing results for case 3 and 4, Figure 2 also shows the importance of the other weather parameters (cloud cover, humidity, wind, etc.).

B. *Supercooling and suspended frazil concentration*

Frazil ice forms in supercooled turbulent water whenever the water temperature is slightly below zero, usually only a few hundredths of a degree. This second test case demonstrates KHIONE ability to represent the typical evolution of the water temperature with time, as frazil develop.

1) *Model setup*

The domain is 10 km long flume, 150 m wide, with a mild slope of 1:10,000 between the elevation 5 m (upstream boundary) and 4 m (downstream boundary). Figure 3 below shows the bottom elevation as coloured contour and the mesh.

A hydrodynamic-only simulation is carried out first to reach steady state conditions based on a constant discharge of 300 m^3/s at the upstream boundary and a constant water level set to 6.6265 m at the downstream boundary (water depth of 2.6265 m). A Manning's n value of 0.025 is used.

Subsequently, a second simulation is carried out with both water temperature and frazil concentration, with the activation of the surface heat exchange (`ICE PROCESSES = 2`). Initial and upstream boundary temperature are set to 0.05°C and the frazil concentration to 0. The model is run for 10 hours, or 18,000 steps of 2 s.

2) *Model drivers*

There are no external drivers to the model other than the atmospheric exchanges. This is where the four variations of the same test case differ. The linear model is used based on a constant air temperature and no solar radiation nor any other atmospheric heat fluxes.

The essential keywords for KHIONE are:

```
WATER-AIR HEAT EXCHANGE CONSTANT = 200.
WATER-AIR HEAT EXCHANGE COEFFICIENT = 0.0
SOLAR CONSTANT = 0.
```

The essential keyword for WAQTEL is

```
ATMOSPHERE-WATER EXCHANGE MODEL = 3
```

3) *Model results*

Profiles of water temperature and frazil concentration are extracted along the length of the flume. These also represent how long the upstream water (entering the domain at 0.05°C) has been in contact with the atmosphere. These are shown in Figure 4, with temperature on the primary axis (left) and frazil concentration on the secondary axis (right, $x10^{-3}$).

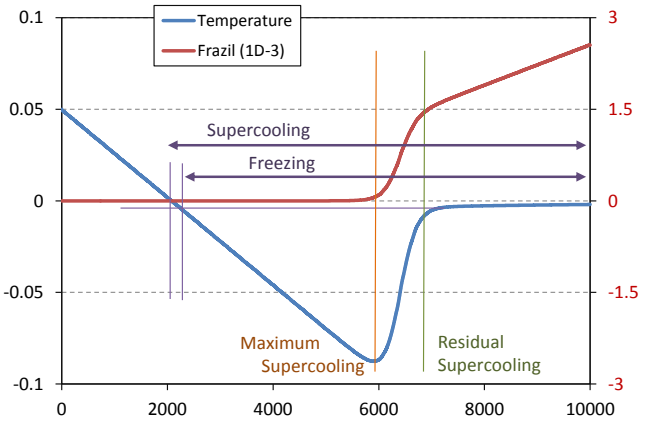

Figure 4 – Frazil growth as temperature gets supercooled

For a constant rate of heat loss, the temperature decreases linearly and reaches the freezing point. Further atmospheric cooling results in supercooling and frazil ice begins to form – although not visible here because of small amount. This process is accompanied by a release of latent heat due to frazil production. The maximum amount of supercooling is then reached and a balance between released latent heat and heat loss through the water surface occurs at that time. Where the frazil growth is faster with the increase in frazil concentration, the release of latent heat is larger than the heat loss to the atmosphere. The temperature thus increases until thermal equilibrium is reached. After that, the temperature is virtually constant, and if the temperature is less than 0° C, residual supercooling take place.

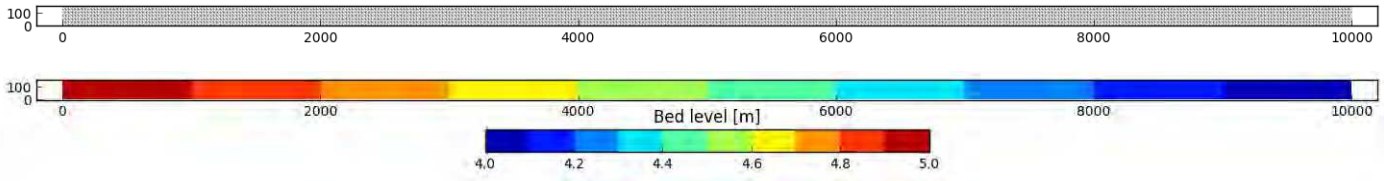

Figure 3 – Model gemetry (bathymetry and mesh) for the supercooling and frazil growth test case

C. *Border ice cover formation*

As described in the previous section, static border ice will form in areas where both the thermal and hydrodynamic threshold conditions are met, including in calmer areas of river bends, for instance.

1) *Model setup*

For this reason, the domain used in this case has been build based on a meandering channel following a sine curve, the cross section of which is of trapezoidal shape. The whole channel also follow a gentle slope of 1:10,000. The length of the meandering channel is about 400 m, while its width is about 25 m. The top inset of Figure 5 below shows the bottom elevation of the model.

A hydrodynamic-only simulation is carried out first to reach steady state conditions based on a constant discharge of 5 m^3/s set at the upstream and downstream boundary with an initial water level set at 2.5 m (water depth ranging from 0.5 m on the banks to 4.5 m in the middle of the channel). The simulation is first run without any friction. The second inset of the Figure 5 below shows the resulting current speed. The flow tends to overshoot each bend creating areas of calmer waters.

Subsequently, a second simulation is carried out, coupled with KHIONE, activating the surface heat budget, the effect of the ice cover on the hydrodynamics and the formation of border ice: `ICE PROCESSES = 42`, (`=2x3x7`).

Initial and upstream boundary temperature are purposefully set to -0.05°C, already in the range of supercooling, and the frazil concentration to 0.005. The model is run for 2 hours, or 7,200 steps of 1 s. A Manning's n value of 0.025 is used, so as to gradually change the steady state solution within this second simulation.

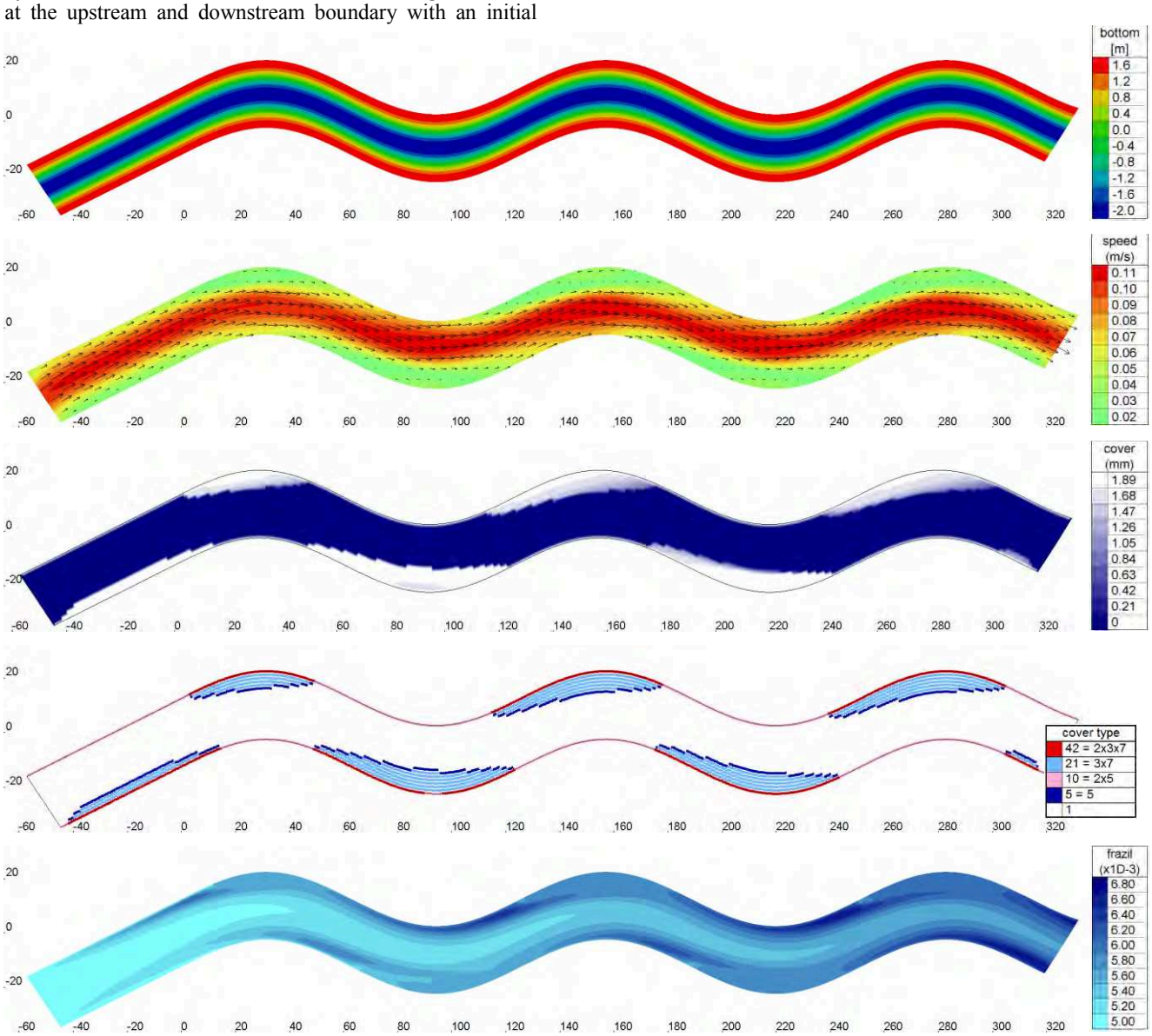

Figure 5 – Formation of static and dynamic border ice cover within a meandering channel (bottom, speed, ice cover, ice type)

2) Model drivers

There are no external drivers to the model other than the atmospheric exchanges. The linear model is used based on a constant air temperature and no solar radiation nor any other atmospheric heat fluxes.
The essential keywords for KHIONE are:

```
AIR TEMPERATURE = -10.0.
WATER-AIR HEAT EXCHANGE CONSTANT = 0.0
SOLAR CONSTANT = 0.
```

The essential keyword for WAQTEL is

```
ATMOSPHERE-WATER EXCHANGE MODEL = 3
```

3) Model results

The middle inset of Figure 5 above shows the ice cover formed after 2 hours. While it may only be a few millimetres thick (floating above the water), border ice forms extremely rapidly. Additionally, it prevents the water from being in direct contact with the atmosphere, providing an insulation layer where it forms. This is shown in the bottom inset of Figure 5, with darker blue area of frazil production, frazil is simply transported (and gradually melted) under the patches of ice cover.

The last inset of Figure 5 (second from the bottom up) shows a variable used by KHIONE to manage the various states and properties of the ice cover. This (integer) variable is set as a multiplicative combination of prime numbers, with each prime number associated to a particular ice cover type. It also shows that border ice expands from the border, while thickening from the surface down. Additional details can be found in the user manual.

D. Ice cover impact on the hydrodynamics

This test case demonstrates KHIONE's ability to affect the hydrodynamics – hence the coupling with TELEMAC-2D – in particular when an ice cover is produced. Four variations of the same test case are presented, each based on a different ice cover configuration.

1) Model setup

The model geometry is identical to the supercooling test case (see Section IV-B). The hydrodynamic regime is only different in its downstream boundary conditions, raised to 7.535 m (water depth of 3.535 m). A Manning's n value of 0.025 is used.

An ice cover is installed above the water surface at the start of the simulation, allowing TELEMAC-2D to adapt to its presence in term of static pressure and shear stress. Ice cover impact is activated with `ICE PROCESSES = 3`. It is noted that surface heat fluxes are not included here.

The model is run for 10 hours, or 7,200 steps of 5 s.

2) Model drivers

There are no external drivers to the model other than the initial cover, which if set through the keyword for KHIONE:

```
PREVIOUS ICE COVER COMPUTATION FILE = 'cv4.slf'
```

We note that KHIONE can have initial conditions distinct from the TELEMAC-2D initial conditions. Four variations are presented, whether the ice covers the entire flume, a portion of the upstream or the downstream, or represents an actual ice jam situation.

3) Model results

Steady state is reached fairly rapidly. Figure 6 below shows a cross sectional profile along the 10 km flume of the bed elevation (black), the top of the ice cover (red) the bottom of the ice cover (blue, also the interface with water) and the equivalent water surface level.

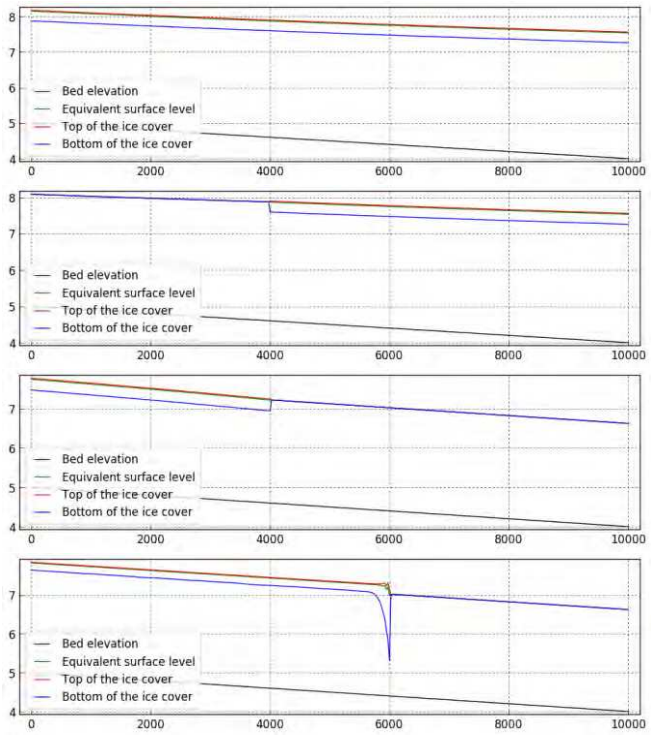

Figure 6 – Water surface affected by ice cover

This test case demonstrates the ability of KHIONE and TELEMAC-2D to interact with one another, with ice cover reaching either types of boundary conditions (imposed or free).

E. Frazil ice clogging on a set of bars

Ice formation on structures can cause serious difficulties in regions with cold climates, particularly so through frazil ice accretion. Frazil ice often blocks intakes to hydro or nuclear power plants, for instance.

1) Model setup

The model geometry is identical to the supercooling test case (see Section IV-B) except that the bottom elevation has a milder slope at 1:100,000 (from 4.0 m to 4.1 m). The hydrodynamic regime is slower with a prescribed upstream discharge value of 30 m^3/s and a downstream water elevation of 6.6265 m (water depth of 2.6265 m). A Manning's n value of 0.025 is used.

Surface heat fluxes is used to produce a supercooling within the channel, hence the formation of frazil ice, to which the clogging process is added. Both processes are activated with `ICE PROCESSES = 10`, (`=2x5`).

2) Model drivers

The linear model is used based on a constant air temperature and no solar radiation nor any other atmospheric heat fluxes. The essential keywords for KHIONE are:

```
AIR TEMPERATURE = -5.0
SOLAR CONSTANT = 0.
```

The essential keyword for WAQTEL is

```
ATMOSPHERE-WATER EXCHANGE MODEL = 3
```

Additionally, clogging is set at the downstream boundary as if it was an intake to a power station (150 m entrance width). The physical characteristics of the rack is defined through the thickness of the bars and the distance between two bars (from their centre axis). Either or both horizontal and vertical bars are allowed but only vertical bars are here tested to slow down the clogging process.

The essential keywords for KHIONE are:

```
CLOGGING RESULTS FILE = 'clg.prn'
CLOGGED BOUNDARY NUMBERS = 1
POROSITY OF ACCUMULATED ICE = 0.67
ANGLE OF ACCUMULATED ICE = 35.
PHYSICAL CHARACTERISTICS OF THE INTAKE RACK =
0.2; 0.00; 0.2;0.01
```

with an absence of transverse bars is set with the `0.00` value.

The model is run for 5 hours, or 600 steps of 30 s, which highlights the usually very rapid blockage of the intake once frazil ice are in suspension in the incoming water.

3) Model results

KHIONE writes a number of quantities to its ASCII result file, amongst which the remaining open area through which water continue to pass through and the total mass of ice accumulated on the grid. These are shown on Figure 7 below.

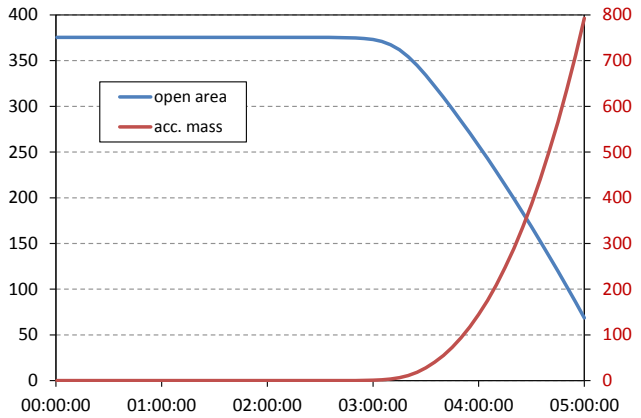

Figure 7 – Frazil ice accumulation on an intake

At this stage, KHIONE does not feedback the blockage of the rack to the hydrodynamics and assumed a uniform accumulation of ice throughout the length of the intake. HR Wallingford is currently expanding the clogging code to correct these.

CONCLUSIONS

Thanks to the important and sustained effort of the Department of Civil and Environmental Engineering of Clarkson University, technically and financially supported over the last two years by EDF R&D and HR Wallingford, ice modelling capabilities have now been added to the TELEMAC system, in the name of the Greek goddess KHIONE.

While this article presents, in this Part I, the capabilities of the Eulerian part of this ice modelling component, a Lagrangian part also exists to model the dynamics of surface / floating ice, ice jams and breakup phases. This second part will be presented at a future conferences.

KHIONE comes with its latex documentations, including a comprehensive user manual with extensive theoretical description and a validation manual based on a growing number of test cases. Of course, as it is always the case with scientific code, KHIONE is bound to be evolving rapidly in the next few years, and the TELEMAC consortium welcomes any feedback the open source community may have.

REFERENCES

[1] Andersson A. and Daly S.F. “Laboratory investigation of trash rack freezeup by frazil ice”. Technical Report CRREL Report 92-16, Army Cold Regions Research Laboratory, 1992.

[2] Fonseca F. Rivard G. Michel B., Marcotte N. “Formation of border ice in the st. anne river”. In Workshop on Hydraulics of Ice-Covered Rivers, 1980.

[3] Huang F. Shen H.T. and Knack I.M. “Modeling border ice formation and cover progression in rivers”. In 21th IAHR Ice Symposium, June 2012.

[4] Kandamby A., Jayasundara N., Shen H.T. and Deyhle C. “A numerical river ice model for elbe river”. In 20th IAHR International Symposium of Ice, 2010.

[5] Lazier S.S. Michel B. Kennedy, J.F. and R.R. Rumer. “Review of ice-hydraulic model studies”. Technical Report to U.S. Army Engineering District, 1981. 86p.

[6] Liu L., Li H., and Shen H.T. “A two-dimensional comprehensive river ice model”. In 18th IAHR International Symposium on Ice, Sapporo, Japan, 2006.

[7] Matousek V. “Types of ice run and conditions for their formation”. In 7th IAHR International Ice Symposium, 1984.

[8] Matousek V. “Regularity of the freezing-up of the water surface and heat exchange between water body and water surface”. In 7th IAHR International Ice Symposium, 1984.

[9] Shen H.T. “Mathematical modeling of river ice processes”. Cold Regions Science and Technology, 62:3–13, 2010.

[10] Shen H.T., Su J., Liu L. “SPH simulation of river ice dynamics”. Journal of Computational Physics, 165:752–771, 2000.

[11] Uzuner, M.S., Kennedy, J.F. “Theoretical model of river ice Jams”. ASCE Journal of the Hydraulics Division 102 (HY9), 1365–1383, 1976.

[12] Van Devalk W. A. Shen H. T. “Field investigation of St. Lawrence river hanging ice dam”. In 7th IAHR International Ice Symposium, 1984.

Improving simulations of extreme skew surges through waves' contributions

Cécile Lalanne[1], Roberto Frau[1], Marc Andreevsky[1], Chi-Tuan Pham[1], Cécile Raoult[2], Vanessya Laborie[3], Nathalie Giloy[4]

[1]Laboratoire National d'Hydraulique et Environnement, EDF R&D, Chatou, France
[2]Laboratoire d'Hydraulique Saint-Venant, Chatou, France
[3]Laboratoire d'Hydraulique Saint-Venant , Cerema EMF, Chatou, France
[4]IRSN, Fontenay-aux-roses, France
cecilemarion.lalanne@gmail.com, roberto.frau@edf.fr

***Abstract*—The coastal flood risk assessment is an overriding priority for EDF to ensure the nuclear safety. For this reason, statistical methods linked to Extreme Value Theory (EVT) are carried out to evaluate extreme events associated to high return periods (up to 10^3 years). Usually, these evaluations are applied to time series from 30 to 50 years and extreme estimations are not very accurate. A potential way to improve statistical estimations of extreme events is the use of historical data ([6], [7], [4]). Before to properly use them in a statistical analysis, the validation of historical records is needed.**

Numerical models may be complementary to historical values and they may even validate historical values recovered and reconstructed from several sources. Firstly, it is necessary to achieve a deep examination of the numerical models during several well-known extreme events in order to be able to validate historical events. In this study, extreme sea levels and, in particular, extreme skew surges simulated by a TELEMAC-2D model are considered.

TELEMAC-2D allows to simulate free-surface flows in two dimensions and to compute sea levels taking into account meteorological conditions during a storm. Unfortunately, not considering waves' contributions in simulations ([15], [14]) leads to non-accurate results. Waves' contributions can represent a significant part of skew surge [21]. In the present work, waves' contributions are taken into account in the computation of the surface drag coefficient C_D, using the Charnock relation, and the consideration of wave stresses. A sensitivity analysis of the Charnock coefficient is studied to find an optimal value.
Extreme skew surges are computed from simulations and these values are compared to measurements. Better results are obtained considering waves' contributions.
The model is tested for three of the well-known storms that impacted French coasts in 1987, 1999 and 2010, respectively The Great Storm of 1987, Lothar-Martin storms and Xynthia storm.

I. INTRODUCTION

The safety of nuclear power plants located along the coasts is one of the main priorities for EDF. Indeed, due to their proximity to the sea, coastal nuclear stations are subjected to the aggressions of extreme meteo-oceanic conditions such as sea levels, surges and waves. It is crucial to provide an accurate coastal risk assessment in order to be able to design effective protections. As part of the prevention of risks, numerical models allow to simulate storm events to study the different physical variables and processes involved. In this context, a lot of effort has been spent to improve simulations of extreme sea levels. The model has to be suitable for extreme events and effective at representing skew surges and in particular the maximum skew surge, our variable of interest in this study. The skew surge is the difference between the maximum observed sea level and the maximum predicted astronomical tide level during a tidal cycle ([22], [23], [6]). The risk of coastal flooding is bigger at high water conditions and justifies working with the maximum skew surge. Skew surge time series at several locations along French and British coasts can be obtained with the model.

At the Saint-Venant Hydraulics Laboratory (LHSV), a surge numerical model based on TELEMAC-2D software was built a few years ago [15] and then globally validated with additional tests [14]. The model showed relatively bad performances for the estimation of maximum skew surges along some regions such as Pays de la Loire or Nouvelle-Aquitaine. Waves' contributions had not been taken into account yet in [14] and at least for this reason, skew surges may have been underestimated for most of the study sites along the French coastline. Storm surges are generated by the meteorological forcing, in particular wind and pressure [8], and also by the waves. Waves' contributions can be divided into three components [17]: sea surface drag coefficient modification with the nature of waves, bottom friction and wave set-up. The positive relevance to use wave set-up and atmospheric effects in simulations, for instance, through a better surface drag parameterization, has been shown as part of the Previmer-Surcotes project [13].

The aim of this study is to improve the performances of the TELEMAC-2D model in South of the North Sea, English sea, and Biscay Bay and to provide the best simulated skew surge during an extreme event. As a first step, satisfactory results for maximum skew surges for some recent and well-known storms are expected. For this reason, a comparison between observed skew surges recorded by tide gauges and simulated skew surges has to be done in order to verify the numerical model. Finally, the model may be used to validate historical skew surges. Since historical data can be associated with considerable uncertainties, simulations generated by a reliable model can help us to determine if these skew surges likely happened in the past and so if they should be taken into account in the statistical of extreme events or not.

This paper presents the implementation of the waves' contributions in the TELEMAC-2D surge model through Charnock formulation and wave stresses. In addition, a validation part with three well-known storms The Great storm of 1987, Lothar-Martin (1999) and Xynthia (2010) is carried out. All the physical processes involved and their modelling are fully described in Sect.2. Sect.3 presents the results for the estimation of the maximum skew surges for each storm in different sites along the French coasts.

II. NUMERICAL MODEL AND SIMULATIONS

In this study, TELEMAC-2D (T2D) solves the Shallow Water Equations and some user FORTRAN sub-routines (for instance, prosou.f) are adapted to simulate skew storm surges. The numerical model is based on the one of [14] but a sub-routine has been changed and some input data have been added in order to consider waves' contributions. The TELEMAC-2D model extends from 10°W to 14°E and from 42°N to 64°N and includes French and British coasts (Fig. 2). The mesh (called mesh 2 in Fig. 3) is unstructured: it is particularly refined near the coastline, with one node per kilometer. Off the French coasts, the greatest distance between two nodes is around 40 km. The bathymetry "North East Atlantic Europe" (NEA) provided by the LEGOS is used. The data base for the harmonic constants is provided by the LEGOS [11] atlas to be consistent with the bathymetry. Initial water level and tidal currents are computed from the Atlantic Ocean solution of TPXO [12] database by OSU. The bottom friction is parametrized by the Chézy formulation with a constant coefficient of 70 $m^{1/2}/s$.

The meteorological forcing is provided by The National Centers for Environmental Prediction (NCEP) Climate Forecast System Reanalysis (CFSR) [20]. In our study, mean level atmospheric pressure at the sea level and horizontal components of wind (at 10 m) are used. Selected hourly time-series variables are available from January 1979 to December 2010. Besides a great temporal resolution, the fine spatial resolution ($0.301° \times 0.301°$) is necessary to represent precisely the atmospheric phenomena. Using a Python program, CFSR data are interpolated and a single SELAFIN file containing pressures and wind velocities data is obtained. To compute simulated skew surges, two simulations are achieved (Fig. 3): the first with meteorological forcing, the second one without (only tide propagation is used). Tidal simulations have been validated previously for several French harbours [14]. However, for some sites, an error up to 30 cm has been found during high tide. In our study, skew surges are considered and particularly the maximum skew surge as extreme values are sought. Substracting maximum predicted astronomical tide level to maximum observed water levels, potentially occurring with a time lag, leads to skew surge levels. The results are compared to those observed by the French Navy Hydrographic and Oceanographic (SHOM). For each storm event, a simulation, beginning seven days before the date of the storm and ending four days after, is run. The simulation time step is 30 s, according to [15].

III. IMPROVEMENT ON EXTREME EVENTS SIMULATIONS

The quality of a storm surge model depends on the accuracy of the input data, being the meteorological forcing, the spatial and temporal resolution and also the physical processes modelled. Storm surges were not properly modelled so far because at least waves' contributions were not taken into account: only the tide and the surge induced by the atmospheric forcing were integrated in the model. In order to improve skew surges estimations using waves' contributions in our model, the parametrization of the sea surface drag coefficient has to be firstly modified. This allows to describe more precisely the air-sea interaction. Secondly, wave stresses have to be considered during the simulations.

A. Sea surface drag coefficient

The wind influence is represented by a dimensionless sea surface drag coefficient C_D. This coefficient can be calculated with several formulations and most of them depend on the wind magnitude velocity at 10 m, U_N. C_D models complex phenomena. In fact, the wind influence depends on U_N but also on the roughness of the sea surface, which is itself dependent on the wind and the distance over which it is applied (fetch) [10].

In TELEMAC-2D, the wind influence is represented by the following formulation of Flather (Fig. 1): $C_D = 0.565 \times 10^{-3} if\, U_N \leqslant 5\, m/s$

$$C_D = (-0.12 + 0.137 U_N) \times 10^{-3} if\, 5\, m/s \leqslant U_N \leqslant 19.22\, m/s$$

$$C_D = 2.513 \times 10^{-3} if\, U_N \geqslant 19.22\, m/s$$

With this formulation the coefficient only depends on U_N, whereas the wind influence may also depends on the roughness of the sea surface induced by the waves (characterized by the sea state). Charnock formulation suggests that the roughness length z_0 of the wind profile depends on the kinematic viscosity ν in the case of weak wind or on the Charnock relation (1) in the case of strong wind (above 20 m/s), for instance during a storm [9]:

$$z_0 = (\alpha_{CH} U_{STAR}^2)/g \quad (1)$$

where α_{CH} is the dimensionless Charnock coefficient; U_{STAR}, defined by $U_N/25$ [9], is the friction velocity (m/s) and g is the gravitational acceleration (m/s^2). z_0 is linked to the sea surface drag coefficient C_D according to the following relation (2):

$$C_D = \kappa^2 log(z/z_0)^{-2} \quad (2)$$

κ=0.4 is the Von Karman constant and z is the altitude (m).

The Charnock coefficient models the surface roughness of the ocean and varies in time and space. α_{CH} (usually between 0.01 and 0.04, 0.018 is a typical value) depends on the sea state and on the wage age [24]. A wave model should be used to obtain a Charnock coefficient which takes into account the sea state. For example, WaveWatchIII gives α_{CH} from 1990 to 2018, based on CFSR or ECMWF reanalysis, and those data can be read in TELEMAC-2D. The consideration of waves' contributions through this database allows to improve the estimation of surges [18]. For the purpose of studying historical storms, a database for the Charnock coefficient that goes back further in the past is needed. The spectral wave model used at the LNHE, TOMAWAC, does not allow the computation of α_{CH} for the moment. It would require some developments that is why, as a first step, the formulation of Charnock has been implemented in TELEMAC-2D with a α_{CH} as a parameter fixed by the user and thus constant in time and space. The Charnock formulation gives more flexibility for the range of value of the drag coefficient. Higher values can be reached for the higher wind speed (increasing α_{CH}) in comparison with the formulation of Flather (Fig. 1). Thus, the Charnock coefficient can be used to strengthen, or not, the wind influence, depending on the value of α_{CH}. However, recent studies ([19], [5]) have shown that for winds greater than 33 m/s, the drag coefficient starts to decrease (Fig. 1). Hence, the Charnock formulation is not correct anymore and other formulations like Makin [16] should be used instead. In this paper, the maximum wind measured during the three considered storms is below 33 m/s so Charnock formulation has been kept.

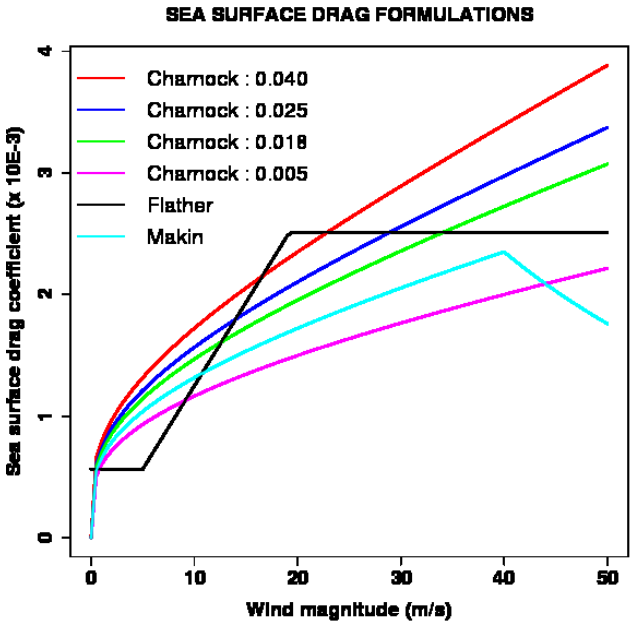

Figure 1. *Comparison between various formulations for the sea drag coefficient C_D and analysis of the influence of the Charnock parameter on this coefficient.*

Given that the performances of TELEMAC-2D were not homogeneous along the French coastline [14], a regional division (only determined by the latitude) based on French geographical areas is carried out. It is a first approach which has to be improved. Thus, four regions have been defined (Fig. 2): Hauts-de-France/Normandy, Brittany, Pays de la Loire and Nouvelle-Aquitaine. For each area, a different α_{CH} is applied, more appropriate locally, waiting to be able to calculate α_{CH} for each point of the mesh considering the sea state. The values for the Charnock coefficient have been chosen after several tests, depending on the results of our TELEMAC-2D model with the Flather formulation (if the maximum skew surge simulated by [14] was under the SHOM maximum skew surge, a high coefficient is fixed and conversely). In Sect. 3, details will be given about the α_{CH} used for each storm.

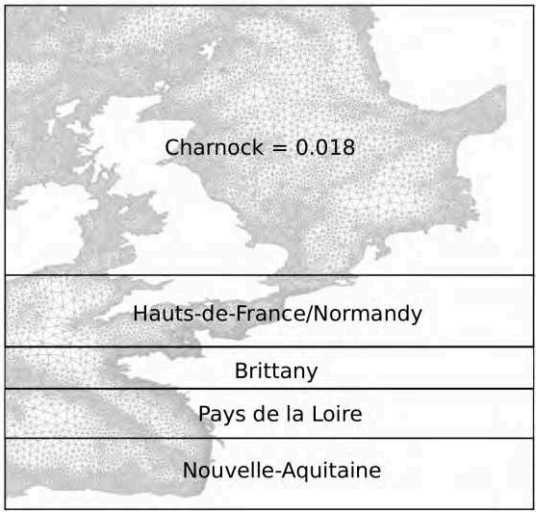

Figure 2. *Regional division for the adaptation of α_{CH}.*

B. Wave stresses

As TELEMAC-2D is used to simulate skew surges, waves are not taken into account. However, waves induce currents which may impact the surge and this effect can represent a significant part of the surge [21]. Those wave driven currents are calculated in TOMAWAC in the form of two forces F_u and F_v, called the wave stresses. The TOMAWAC software models wave propagation in coastal areas and estimates the mean characteristics of waves (water depth, direction, frequency). TELEMAC-2D is designed to be coupled with TOMAWAC but this requires to build a wave model on the same mesh as the one used for TELEMAC-2D (called mesh 2 in Fig. 3) with the determination of boundary conditions. Thus, for a first test of using wave stresses in the model, the data were taken from another project where a wave model is run with varying water level and currents due to tide (steps 1, 2 and 3 in Fig. 3). The same forcing conditions are used, but the computational domain is smaller and limited to close to the coast (called mesh 1 in Fig. 3). If the results are promising, a "real" 2-way-coupling will be implemented. With F_u and F_v as input data in

TELEMAC-2D, simulations with the contributions of wave induced currents are realized (step 4 in Fig. 3).

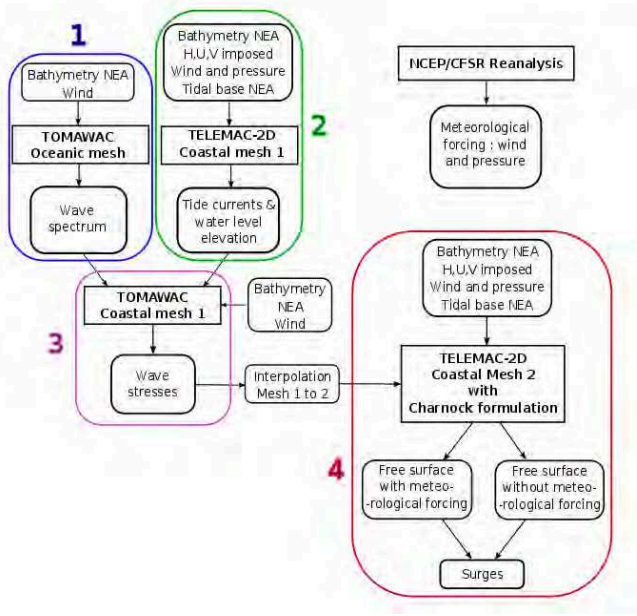

Figure 3. *Diagram of the chaining methodology to simulate surges.*

IV. RESULTS

A. Xynthia

Xynthia is a recent well-known storm for which the SHOM collected data in plenty of ports. This case study served to calibrate our TELEMAC-2D surge model and also to estimate the contributions linked to the Charnock formulation or the wave stresses.

Xynthia was a violent storm which crossed rapidly Western Europe between the 27th of February and the 1st of March 2010. The trajectory of the storm was quite unusual, from South-West to North-East and created a particular sea state in the Bay of Biscay [1]. The waves were really short and arched. This induced the effect of increasing the sea roughness and so the drag coefficient [2]. To model this phenomenon, a Charnock coefficient of 0.04 is applied in the region of Pays de la Loire and 0.018, the typical value, everywhere else. Nine harbours are concerned: Dunkerque, Dieppe, Le Havre, Saint-Malo, Roscoff, Saint-Nazaire, La Rochelle, Port-Bloc and Boucau. The results of the TELEMAC-2D model with or without waves' contributions are compared to the SHOM observations. For all the study sites, the maximum skew surge was underestimated by the model. Nevertheless, using the Charnock formulation rather than the Flather one (Fig. 1) permitted to reduce the error between the peak of the simulated skew surge and the peak of the observed skew surge (Table 1).

The wave stresses do not have positive influences on our results, except for Le Havre. The performances of the TELEMAC-2D model are still not homogenous between all harbours: for instance, at Port-Bloc, the correct numerical value for the peak of skew surge is simulated, whereas at Saint-Nazaire, it is clearly overestimated (Fig. 4). Further tests should be conducted with a lower value of α_{CH} in Pays de la Loire to approach the maximum skew surge recorded by the SHOM. At Boucau, regardless of the modifications of the model, the same result is obtained. We will see with the other storms that the region of Nouvelle-Aquitaine shows low sensitivity to the model parameters in general. The regional division should be modified: working with smaller regions could help to describe local effects.

TABLE 1: RESULTS OF ABSOLUTE RELATIVE ERROR FOR THE 9 SITES FOR THE MAXIMUM SKEW SURGES DURING XYNTHIA

Harbour	**Absolute relative error for the peak between the TELEMAC-2D model and the SHOM observations (%)**			
	Without waves' contri-butions	***With Charnock formulation only***	***With wave stresses only***	***With waves' contri-butions***
Dunkerque	16.05	1.23	17.28	1.23
Dieppe	12.63	2.11	14.74	1.05
Le Havre	35.64	25.74	7.92	1.98
Saint-Malo	16.47	4.71	17.65	4.71
Roscoff	31.67	28.33	33.33	30.0
Saint-Nazaire	19.81	26.42	33.96	24.52
La Rochelle	47.06	12.42	44.44	13.07
Port-Bloc	23.15	0.00	24.07	0.93
Boucau	43.90	39.04	46.34	41.46

In conclusion, taking into account the wind influence, through Charnock formulation, and the wave stresses helps to improve the estimation of the maximum skew surge for all sites for the Xynthia storm. To improve the results, the change of bathymetry database and the mesh refinement are prominent possibilities to take into account for future improvements. Of course, those promising results will lead to a complete coupling between TOMAWAC and TELEMAC-2D. The calibration of α_{CH} has to be refined eventually with a calculation directly in TOMAWAC.

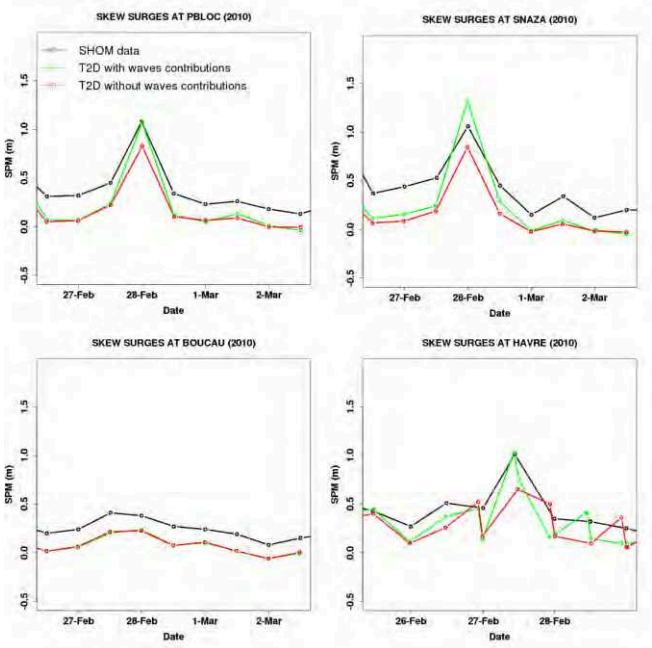

Figure 4. *Comparison between simulated skew surge (SPM) with (in green) or without (in red) the waves 'contributions with data recorded from tide gauge station (in black) during Xynthia storm.*

B. *Lothar-Martin*

Storm Lothar crossed Europe following a West-East track and peaked during the high tide of a moderate tidal range. It occurred on the December 26th, 1999. Less than 36 hours later, a second storm, called Martin, crossed France, a little further south, and affected almost of the same sites. This is quite unusual and during the tests of [15], the 1999 events were not correctly represented by the TELEMAC-2D model. Five tide gauges recorded the water level during both Lothar and Martin: Boucau, Cherbourg, Le Havre, Roscoff and Saint-Nazaire. La Rochelle tide gauge was not operating during those storms because of a general power failure. [3] simulated a skew surge value of 2.17 m for December 27th for storm Martin at La Rochelle so our results are compared with it (Fig. 5).

After some tests, the following values for the Charnock coefficient were chosen:

- 0.001 for Hauts-de-France/Normandy and Brittany,
- 0.04 for Pays de la Loire and Nouvelle-Aquitaine.

Indeed, the model used in [14] overestimated the peak of the skew surge in northern France, so a very small α_{CH} is used to reduce the wind influence and conversely for the South of France. For Cherbourg, Le Havre, Saint-Nazaire and Boucau, we manage to improve the results of the TELEMAC-2D model through waves' contributions (Fig. 5) but the numerical value of the maximum skew surge cannot be validated, except at Cherbourg. Finally, for La Rochelle, the waves' contributions lead to two skew surge peaks rather than three (Fig. 5). It could be more coherent as there is two really close storms but the simulated values are still far from measurements and the temporal occurrence is not quite exact.

To conclude, in this case, the implementation of the waves' contributions does not allow our model to describe correctly the 1999 events in all harbours. Results have been enhanced for some sites which encourages us to continue our work. As for storm Xynthia, a bathymetry and a mesh with a better resolution should have a benefit on our skew surge estimations as a precision of the geographical regions.

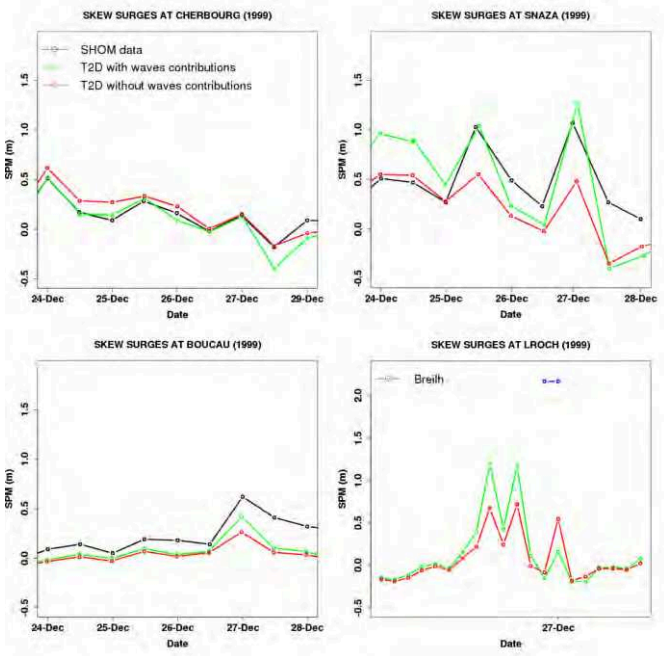

Figure 5. *Comparison between simulated skew surge (SPM) with (in green) or without (in red) the waves 'contributions with data recorded from tide gauge station (in black) during Lothar-Martin storms. Comparison with [3] (in blue) for La Rochelle.*

C. *The Great Storm of 1987*

This storm occurred in the middle of October 1987: a depression originated on the Bay of Biscay on the 15th and moved North-East. The Great Storm of 1987 impacted Brittany and then England. Eight French tide gauges recorded the sea level during this event: Dieppe, Le Havre, Cherbourg, Roscoff, Le Conquet, Port-Tudy, Verdon and Saint-Jean-de-Luz. For this study, we choose α_{CH} = 0.04 for Hauts-de-France/Normandy, α_{CH} = 0.35 for Brittany and α_{CH} = 0.018 for the other regions as the storm mainly affected the North of France.

Estimations of the maximum skew surge are improved only for six harbours. In fact, this storm does not strongly impact the sites of Le Verdon and Saint-Jean-de-Luz in which time series of skew surges are available. In addition, the Nouvelle Aquitaine region, to which these two sites belong, is poorly sensitive to the parameters of the TELEMAC-2D model. Results at Cherbourg and Roscoff (Fig. 6) allow us to get few ameliorations for the maximum skew surge. On the contrary, for Le Havre and for Port-Tudy (Fig. 6), the waves' contributions have a clear positive influence.

This case study needs a careful work especially for the regions of Hauts-de-France/Normandy and Brittany where the storm had the strongest impact. As the Great Storm of 1987 affected the English coasts too, skew surges simulations should be done for British harbours. As for the 2010 and 1999 storm events, the TELEMAC-2D model should be enhanced with more refined bathymetry and mesh. In addition, a coupling with TOMAWAC could be considered, rather than a chaining.

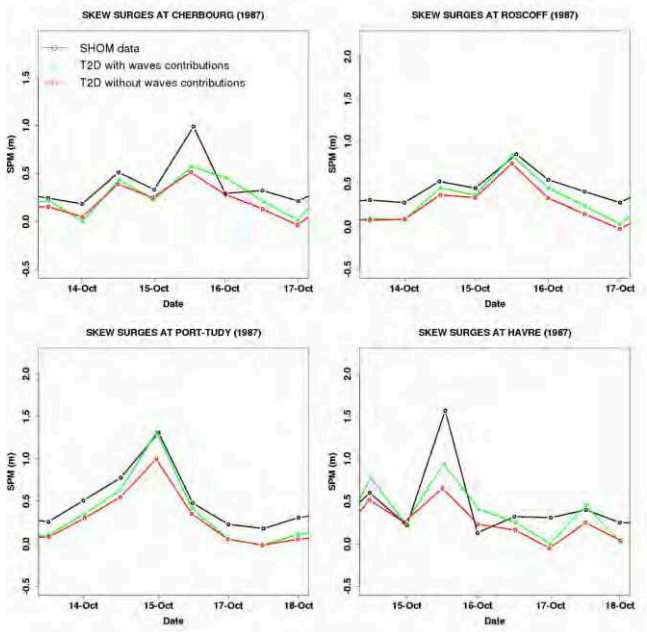

Figure 6. *Comparison between simulated skew surge (SPM) with (in green) or without (in red) the waves 'contributions with data recorded from tide gauge station (in black) during The Great Storm of 1987.*

CONCLUSIONS AND PERSPECTIVES

The storm surges model based on TELEMAC-2D built and validated a few years ago ([15], [14]) has been improved through the implementation of the waves' contributions. The formulation for the sea surface drag coefficient which translates the wind influence has been modified with the Charnock formulation. A regional division has been settled to affect a particular Charnock coefficient for each area. In addition, the wave stresses are now taken into account in our simulation thanks to a chaining with TOMAWAC. For the three storms studied, an improvement, nevertheless sometime small, of our estimations of the maximum skew surge is observed in most of the sites. The examination of the TELEMAC-2D model for several well-known storms is essential to be able to study extreme historical events later and thus validate historical values.

Work is still in progress at the LNHE. A new bathymetry from the SHOM with a resolution of 100 m should be tested and a new mesh will be soon developed. Indeed, all tide gauges are located in ports so there are influenced by local effects. A coupling between TOMAWAC and TELEMAC-2D could be considered as a promising way to still improve results. The Charnock formulation is valid for winds below 33 m/s, we may change for the Makin formulation [16] for other storms. Moreover, the geographic division has to be precise and the Charnock coefficient needs to be calculated for each node of the mesh, updated at each time step. This could be possible with the calculation of the coefficient directly in TOMAWAC. One advantage will be that our model would not be dependent anymore on a database such IOWAGA from WaveWatchIII and therefore it will ensure coherence between all the data used in our storm surges simulations. In addition, British ports should be studied to complete this work, especially for The Great Storm of 1987.

REFERENCES

[1] Bertin, X., Bruneau, N., Breilh, J. F., Fortunato, A. B., & Karpytchev, M. (2012). Importance of wave age and resonance in storm surges: The case Xynthia, Bay of Biscay. Ocean Modelling, 42, 16-30.

[2] Bertin, X., Li, K., Roland, A., Breilh, J. F., & Chaumillon, E. (2012). Contributions des vagues dans la surcote associée à la tempête Xynthia, février 2010. XIIèmes Journées Nationales Génie Côtier–Génie Civil.

[3] Breilh, J. F., Bertin, X., Chaumillon, É., Giloy, N., & Sauzeau, T. (2014). How frequent is storm-induced flooding in the central part of the Bay of Biscay?. Global and Planetary change, 122, 161-175.

[4] Bulteau, T., Idier, D., Lambert, J., & Garcin, M. (2015). How historical information can improve estimation and prediction of extreme coastal water levels: application to the Xynthia event at La Rochelle (France). Natural Hazards and Earth System Sciences, 15(6), 1135-1147.

[5] Donelan, M. A., et al. (2004). On the limiting aerodynamic roughness of the ocean in very strong winds. Geophysical Research Letters, 31(18).

[6] Frau, R., Andreewsky, M., & Bernardara, P. (2018). The use of historical information for regional frequency analysis of extreme skew surge. Natural Hazards and Earth System Sciences, 18(3), 949-962.

[7] Hamdi, Y., Bardet, L., Duluc, C. M., & Rebour, V. (2015). Use of historical information in extreme-surge frequency estimation: the case of marine flooding on the La Rochelle site in France. Natural Hazards and Earth System Sciences, 15(7), 1515-1531.

[8] Heaps, N. S. (1983). Storm surges, 1967–1982. *Geophysical Journal of the Royal Astronomical Society*, *74*(1), 331-376.

[9] Hersbach, H. (2011). Sea Surface Roughness and Drag Coefficient as Functions of Neutral Wind Speed. Journal of Physical Oceanography, 41(1), 247-251.

[10] Hervouet, J. M. (2007). Hydrodynamics of Free Surface Flows: modelling with the finite element method. John Wiley & Sons.

[11] http://sirocco.omp.obs-mip.fr/outils/Tugo/Produits/TugoProduits.htm

[12] http://volkov.oce.orst.edu/tides/

[13] Idier, D., et al. (2012). Modélisation des surcotes sur les côtes françaises, Manche et Atlantique. In Congrès SHF: Evènements extrêmes fluviaux et maritimes).

[14] Laborie, V., Sergent, P., Levy, F., Frau, R., & Weiss, J. (2015). The hydrodynamic, sea-state and infrastructures platform developed by Saint-Venant Hydraulics Laboratory and Cerema: a special focus on the TELEMAC2D surge levels numerical model of the Atlantic Ocean, the Channel and the North Sea. In 22nd TELEMAC-MASCARET User Conference 2015 (pp. 172-181).

[15] Levy, F. "Modélisation des surcotes avec Telemac 2D", internal report, 24 pages, April 2013

[16] Muller, H., Pineau-Guillou, L., Idier, D., & Ardhuin, F. (2014). Atmospheric storm surge modeling methodology along the French (Atlantic and English Channel) coast. Ocean Dynamics, 64(11), 1671-1692.

[17] Nicolle, A., Karpytchev, M., & Benoit, M. (2009). Amplification of the storm surges in shallow waters of the Pertuis Charentais (Bay of Biscay, France). Ocean Dynamics, 59(6), 921-935.

[18] Pineau-Guillou, L., Theetten, S., Dumas, F., Lecornu, F., & Idier, D. (2012, June). Prévision opérationnelle des niveaux de la mer, surcotes et décotes sur les côtes de la Manche et de l'Atlantique. In XIIèmes Journées Nationales Génie Côtier–Génie Civil, Cherbourg, 12-14 juin 2012.

[19] Powell, M. D., Vickery, P. J., & Reinhold, T. A. (2003). Reduced drag coefficient for high wind speeds in tropical cyclones. Nature, 422(6929), 279-283.

[20] Saha, S., et al. (2010). The NCEP climate forecast system reanalysis. Bulletin of the American Meteorological Society, 91(8), 1015-1058.

[21] Sheng, Y. P., Alymov, V., & Paramygin, V. A. (2010). Simulation of storm surge, wave, currents, and inundation in the Outer Banks and Chesapeake Bay during Hurricane Isabel in 2003: The importance of waves. Journal of Geophysical Research: Oceans, 115(C4).

[22] Simon, B., & Gonella, J. (2007). La marée océanique côtière. Institut océanographique.

[23] Weiss, J., Bernardara, P., Andreewsky, M., & Benoit, M. (2012). Seasonal autoregressive modeling of a skew storm surge series. Ocean Modelling, 47, 41-54.

[24] Zhou, L., Wang, A., Guo, P., & Wang, Z. (2008). Effect of surface waves on air–sea momentum flux in high wind conditions for typhoons in the South China Sea. Progress in Natural Science, 18(9), 1107-1113.

Modification of TELEMAC 2D for Storm Surge Use

D. M. Kelly[1,*], R. Ata[2] and Y. Li[3]
[1.] W.F. Baird & Associates, Oakville, ON., Canada.
*dkelly@baird.com
[2.] EDF R&D, National Laboratory for Hydraulics and Environment (LNHE) & Saint Venant Laboratory for Hydraulics, Chatou, France
[3.] International Hurricane Research Center, Miami, FL 33119, USA.

***Abstract*—Despite the *ad-hoc* use of TELEMAC 2D to predict storm surge over recent years, to-date no coherent effort has been made to develop TELEMAC 2D into a useable, off-the-shelf, storm surge model released via the openTELEMAC website. This has motivated the work presented here in which two distinct parametric wind models and a large variety of drag laws have been introduced into TELEMAC2D. The ability to read both time and space varying wind and rain data is also added. The resulting numerical model is particularly powerful as it can be combined with the existing, curve number-based, rainfall runoff model in TELEMAC in order to provide storm tide simulations that parameterize the effects of hurricane wind, tide, shortwaves (via the spectral wave model TOMAWAC), rainfall and runoff. In order to validate the model in the paper we present results for the forecast mode simulation of the surge due to a number of recent hurricanes in both Puerto Rico and South Florida. The South Florida model includes street level flooding around the City of Miami Beach.**

I. INTRODUCTION

The TELEMAC 2D model has previously been used to simulate storm surges, see for example the work presented in [1] in which cyclone Yasi was simulated using the Holland (1980) wind model. In their paper Cooper et al. [1] reported good agreement between simulated results and the available data. Despite the fact that there has been previous promising storm, and combined storm tide modelling, utilising TELEMAC 2D, this has been undertaken in a somewhat *ad-hoc* manner, and the capacity to simulate storm surges has not yet been formally included within the open source release version of TELEMAC. It is with this in mind that a concerted effort has been made to introduce state-of-the-art parametric wind and drag models into TELEMAC2D. This has been combined with the ability to employ time and space varying rain data within the TELEMAC2D model. The aim of this paper is to serve as a brief summary of this work. The structure of the paper is as follows: In Section II we outline the two parametric wind models that have been introduced into TELEMAC2D and also provide an overview of some of the additional wind drag formulations that have also been introduced into TELEMAC2D. In Section III the implementation of these parametric wind models within the TELEMAC framework is briefly outlined. This section also includes details on newly introduced keywords and how to use the newly implemented storm surge model. Finally, in Section IV, results for two distinct example cases are presented, namely the surges due to hurricane Maria (2017) in Puerto Rico and hurricanes Frances (2004), Wilma (2005), Matthew (2016) and Irma (2017) in South Florida. The South Florida model that is presented also includes rainfall, obtained from satellite data, and the associated run-off. Comparisons of model results and NOAA co-ops gauge data as well as contour plots of the maximum surge are presented.

II. WIND AND DRAG MODELS

TELEMAC 2D has been modified to include two parametric wind models. The first wind model is the well known Holland (1980) model [3]. This simple model has been used in TELEMAC before by other researchers, see for example [1], although it has never been included as part of the official open TELEMAC suite. The second parameteric wind model introduced into TELEMAC in this work is the Myers & Malkin (1961) model [9] which is used by the US National Hurricane Center (NHC) Sea, Lakes and Overland Surges from Hurricanes (SLOSH) model [5]. This model is more complex than the simple algebraic Holland (1980) model.

A. The Holland (1980) Parametric Wind Model

The Holland (1980) wind model [3], referred to from hereonin as H80 wind, is the best known of the parametric wind models. Defining the radius of maximum winds as r_{mw}, and the surface pressure at radius r by p_s, the H80 wind is based on a modified rectangular hyperbola to approximate the radial surface pressure profile giving the surface pressure as:

$$p_s = p_{cs} + \Delta p_s e^{-\left(\frac{r_{mw}}{r}\right)^b}$$

The pressure drop from the defined external pressure is denoted by Δp_s. Scaling is achieved via the exponent b which relates the ratio of maximum wind for a given pressure drop to the maximum wind speed [3]. This is then introduced into the cyclostrophic wind equation to give the cyclostrophic wind speed V_c as:

$$V_c = V_m\left[\Psi e^{(1-\Psi)}\right]^{0.5}$$

where:

$$\Psi = \left(\frac{r_{mw}}{r}\right)^b$$

V_m is the maximum wind speed that must be provided in a hurricane track file. Other parameters that must be provided in the same hurricane track file are the centre loction, the pressure drop and the radius of maximum winds. An asymmetric version of the Holland model, accounting for the hurricane forward speed, has also been coded and is available to the user.

B. Myers & Malkin (1961) or SLOSH parametric wind

The Myers and Malkin (1961) model [9], which was adapted for the NHC SLOSH model by Jelesnianski et al. [5], has been added to the TELEMAC model in the form proposed by [5]. The Myers & Malkin (1961) wind model, referred to from here-on-in as the MM61, model is less well known than the H80 model; perhaps because it is more complex to implement. The wind and atmospheric pressure fields are generated based on the parameters of atmospheric pressure drop and radius of maximum wind speed. The pressure, wind speed, and wind direction are computed from a stationary, circularly symmetric storm using the balance of forces along a surface wind trajectory and normal to a surface wind trajectory. The governing equations for the adapted MM61 wind model are [5]:

$$\frac{1}{\rho}\frac{dp}{dr} = \frac{k_s V^2}{sin\phi} - V\frac{dV}{dr}$$

and

$$\frac{1}{\rho_a}\frac{dp}{dr}cos\phi = f_c V\frac{V^2}{r}cos\phi - V^2\frac{d\phi}{dr}sin\phi + k_n V^2$$

where ρ is the air density, r is the distance from the storm center, p is the pressure, φ is the inflow angle across circular isobars toward the storm center, and V is the wind speed. The values of k_s and k_n are empirically determined coefficients and f_c is the Coriolis force. The two equations can be solved for p and φ if the form of wind speed profile V is supplied. The TELEMAC2D-based model follows the same approach employed in the SLOSH model and uses the following wind speed profile for a stationary storm:

$$V(r) = V_R\frac{2RMW\cdot r}{RMW^2 + r^2}$$

where *RMW* is the radius of maximum wind. Solution of the equations is effected in *SLOSHWINDFIELD.f* via a Runge Kutta approach. The MM61 model requires an identical track file to that required by the H80 wind model.

C. Using Reanalysis Wind Field Data

If the user has access to reanalysis wind data the TELEMAC2D model is now able to employ a time and space varying wind field as model input to provide the wind forcing. A typical example of such renalysis wind data would be that provided by the NOAA Hurricane Research Wind Analysis System (H*WIND) [12]. Currently, the input wind field must be converted from its native format into the SELAFIN format.

D. Drag Models for Wind Shear Stress

A number of well-known, and not so well-known, wind drag formulations have been coded into TELEMAC2D for use in storm surge simulation. A small selection of the newly introduced drag models that have been coded is outlined below. The models are defined in terms of the 10-m neutral values for the drag coefficient, C_{10}.

Garratt (1977) [2] – The linear version of the Garratt drag formulation is included:

$$C_{10}x10^3 = 0.75 + 0.067U_{10}, 4ms^{-1} < U_{10} < 21ms^{-1}$$

this is a popular formulation often used in the NHC SLOSH model and the ADCIRC model [15].

Large & Pond (1981) [6]:

$$C_{10}x10^3 = \begin{cases} 1.14 \\ 0.49 + 0.065U_{10}, 10ms^{-1} < U_{10} < 26ms^{-1} \end{cases}$$

Wu (1980,1982) [14]:

$$C_{10}x10^3 = 0.8 + 0.065U_{10}, U_{10} > 1ms^{-1}$$

Peng & Li (2015) [10]:

$$C_{10}x10^3 = -a(U_{10} - 33)^2 + c$$

where, for the South China Sea, *a=0.00215* and *c=2.797*. It should be noted that this is a typhoon model. A number of other wind drag models are included in the release and a full list will be provided in a future issue of the TELEMAC2D User Manual. Importantly, the more complex sector based model of Powell [11], often used in the ADCIRC model [15], has also been implemented. It should be noted that all of the above drag models employ an extinction depth below which the effect of the wind on the water is discounted. The extinction depth is typically taken to be *0.4m* although this is a user defined parameter.

III. IMPLEMENTATION WITHIN TELEMAC2D

A. New/Modified Subroutines

A number of the base TELEMAC2D subroutines were modified in order to allow for the inclusion of these two parametric hurricane wind and pressure models. New subroutines and functions were also introduced; a brief list of some of the key subroutines that were modified and the newly introduced subroutines is provided below. For reasons of brevity it is not possible to detail all the requisite modifications or new routines here. In TELEMAC-2D, the *METEO.f* subroutine is the place where external atmospheric pressure and wind forcing are handled. This subroutine has been modified to include the ability to read a hurricane track file, via a new subroutine called *SLOSHDAT.f*, and make the requisite calls to enable the parametric wind field to be computed via calls to either SLOSHWINDFIELD.f (for MM61) or *HOLLANDWINDFIELD.f* (for H80) which are both called from *SLOSHDAT.f*. The effect of wind extinction is also included in *METEO.f*.

In TELEMAC-2D, the wind forcing is included via the momentum equations in the subroutine *PROSOU.f* . This subroutine has been modified to allow for the inclusion of a number of different wind drag models (which are defined via

FORTRAN functions). Importantly, this subroutine, and the RUNOFF_*SCS_CN.f* subroutine, have been modified in order to allow for the inclusion of time and space varying rain. In addition to these primary modifications the *TELEMAC2D.dico* file and modules have also been made.

B. New Keywords

As part of the development several new keywords have been introduced into the TELEMAC 2D dico these are described in the text below. It should be noted that it is envisaged that, before the official release, this list of keywords is likely to change.

The keyword *TIME AND SPACE VARYING RAIN* has been introduced to allow for the read-in of this data from the *binary atmospheric data file*.

The keyword *OPTION FOR WIND* has been modified to include two new options:

3: Time and space varying wind read in from a binary input file (file format must be native SELAFIN). This data must be included in the *binary atmospheric data file*.

4: Parametric hurricane wind model. Two parametric hurricane wind models are avaiable. A: Holland (1980) model or B: Myers & Malkin (1961), also known as the SLOSH wind, parametric wind model.

The keyword *HURRICANE TRACK FILE* has been introduced. This is the hurricane track file that is used to generate the hurricane wind field internally.

The keyword *HURRICANE EXTINCTION DEPTH* has been introduced. This is the extinction depth (in m). For water shallower than this depth the wind does not impact the hydrodynmamics.

The keyword *HURRICANE RAMP-IN TIME* has been introduced. This is the time over which the shear stress due to the hurricane wind is ramped in to its true value. This is often necessary to stop the transients caused by an impulsive wind leading to numerical instability.

The keyword *HURRICANE RAIN OFFSET TIME* has been introduced. This is the time by which the rainfall will be offset with respect to the track file. This value is used to syncronise the hurricane track file and the input rainfall data file. NB: It is recommended that the huricane track and rainfall data files should be set-up such that they start at the same instant in time.

The keyword *HURRICANE PATH OFFSET X-DIR* has been introduced. The amount by which to offset all the track abscissae.

The keyword *HURRICANE PATH OFFSET Y-DIR* has been introduced. The amount by which to offset all the track ordinates.

The keyword *AIR DENSITY* has been introduced. The density of air used to compute the wind forcing source term.

The keyword *AIR PRESSURE* includes the effect of the air pressure drop due to the hurricane in the simulation. For storm surge simulations this should always be included or the surge will likely be underpredicted. The air pressure is included based on the internally generated parametric model output or the values provided in the input SELAFIN format file.

The keyword *INVERTED BAROMETER EFFECT* has been introduced. Include the inverted barometer effect in the calculation. This is a parameterization of the adjustment of sea level due to changes in barometric pressure A decrease in barometric pressure of 1 mb corresponds to a fall in sea level of 0.01 m. At the time of this paper this is not fully incorporated into the model (it should be included before release).

IV. EXAMPLE APPLICATIONS

A. Hurricane Maria (2017) at Puerto Rico

In the first application of the model we present the results from a simulation of the storm tide due to hurricane Maria (2017) at Puerto Rico. Maria made landfall on the East coast of Puerto Rico as a high-end Category 4 hurricane. For the results presented here the H80 wind model was employed, in asymmteric mode, and the Garratt [2] linear drag model was utilised. The computational grid was derived by triangulating the SLOSH v6 Puerto Rico basin to give ~450,000 computational nodes. For the bathymetry local to Puerto Rico and the U.S. Virgin Islands coastal regions we employed 1 arc-second and 1/3 arc-second digital elevation models (DEMs) developed by the US National Geophysical Data Center (NGDC), and NOAA, for the Pacific and Marine Environmental Laboratory (PMEL) and the NOAA Center for Tsunami Research. For the offshore areas the NGDC ETOPO1, 1 arc-minute, global relief model was used. The bathymetry was interpolated onto the grid from the data using a kernel-based approach. The TELEMAC2D model utilised spatially varying bottom friction which was obtained using the look-up table of Mattocks & Forbes [8] to convert the USGS landcover data into suitable Manning's *n* values. Figure 1 shows a comparison of the free surface time series obtained using TELEMAC2D with the NOAA co-ops data for all of the 9 available gauges. A comparison of the maximum envelope of observed water (MEOW) with the NOAA mean high water mark data is shown in Figure 2. For a forecast mode study the results are very promising and it is envisaged that the results would be improved by the use of re-analysis wind data or a better calibrated parametric wind field. The contribution of short waves, parameytrised via use the TOMAWAC spectral wave model, would likely also improve predictions due to the contribution of static set-up.

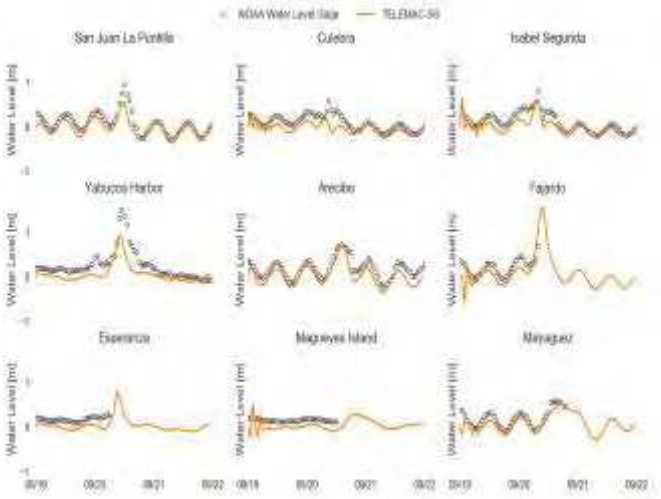

Fig. 1. Comparison of free surface time series at NOAA co-ops gauges at locations around the island of Puerto Rico for hurricane Maria (2017).

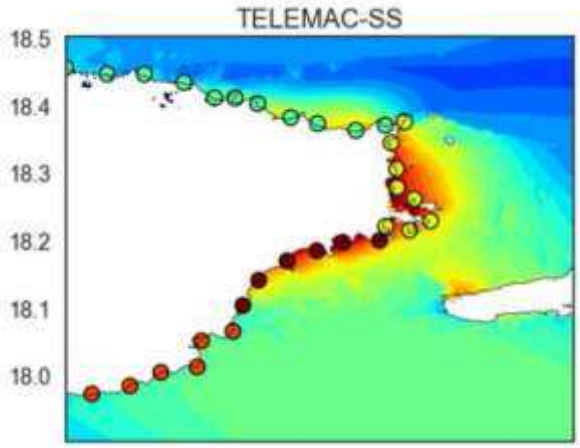

Fig. 2. Comparison of the predicted (contours) and observed (circles) MEOWs around the landfall site, East coast of Puerto Rico, for hurricane Maria (2017). The colour range is 0m(blue) - 2m(red).

B. Combined Tide, Surge and Rain around the City of Miami Beach

The model grid comprised approximately 750,000 computational nodes (~1.5M elements) with grid spacing ranging from O(5km) in the open ocean down to O(10m) around the focus area (City of Miami Beach). Figure 3 shows the model domain and hurricane tracks. The South Florida Water Management District (SFWMD) 5-m digital elevation model (DEM) data was used to derive the bottom elevation over the fine-resolution model grid wherever data was available for the study area. The Florida Geographic Data Library (FGDL) 5-m DEM data was used for areas without SFWMD DEM data. NOAA 2-minute Global Relief Model (ETOPO2), and the 3-arc-second Coastal Relief Model, were combined to obtain bathymetric data for the model grid. Rainfall data for the simulations presented here was obtained from the NOAA Integrated Multi-satellite Retrievals for GPM (IMERG) precipitation product [7]. The IMERG data is created by inter-calibrating, merging and interpolating all available satellite microwave precipitation estimates, together with microwave-calibrated infrared (IR) satellite estimates [7]. Wind fields were created via the asymmteric H80 model employing best track data created by experts at the International Hurricane Research Center, Miami. In Figure 4 we present time series results at Virginia Key (in Biscane Bay) for four historical hurricanes namely hurricane Frances (2004), Wilma (2005), Matthew (2016) and Irma (2017).

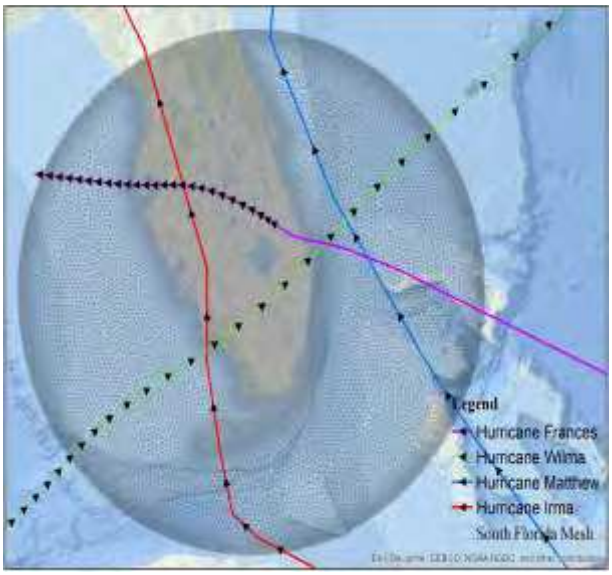

Fig. 3. South Florida mesh based on NOAA domain and comprising ~1.5M elements. Historical hurricane tracks are also shown.

Results shown include the combined effects of tides, wind and rain. We choose to present the reults at NOAA gauge 8723214 (Virginia Key) as this is the closest to the area of the City of Miami Beach which was the primary focus area of the study. In this area significant effort was expended to achieve good bathymetric representation; moreover, the mesh resolution was highest around the City of Miami Beach, with the grid resolution being 10m in this area. Figure 5 illustrates comparisons of the simulated and observed free surface time series. The agreement between the modelled results and observations is reasonable. Good results are obtained for hurricanes Wilma (2005) and Irma (2017) for which we had the best track data. It should be noted that the use of more accurate reanalysis wind data, alongside the fine tuning of bathymetry and friction coefficients, can be expected to improve the results; however, this would result in a hindcast mode simulation. Figure 6 shows an example of the combined maximum surge and street level flooding around the North Miami Beach area. Zoom-in contour plots are shown for hurricanes Frances, Wilma, Irma and Maria (clockwise from

top left). As well as the surge the street level flooding, due to the associated rainfall, is clearly evident.

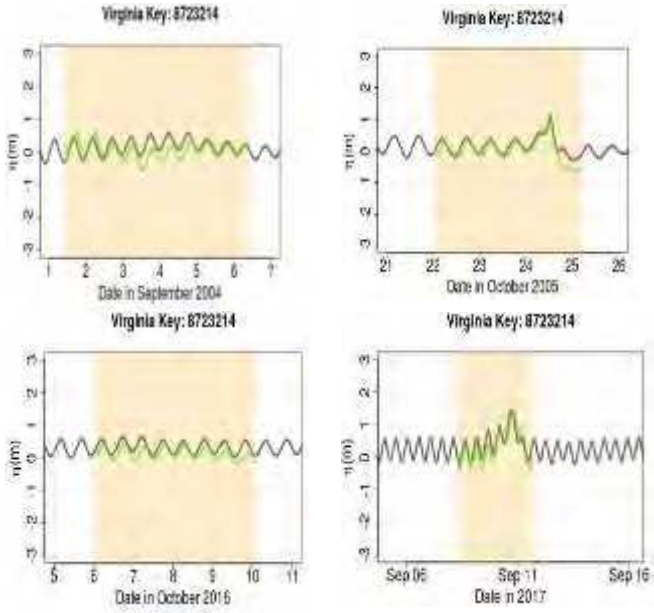

Fig. 4. Comparison of model predictions (green) vs the observed (grey) free surface time series at Vriginia Key in Biscane Bay, Miami (NOAA gauge 8723214) for hurricanes Frances (2004), Wilma (2005), Matthew (2016) and Irma (2017).

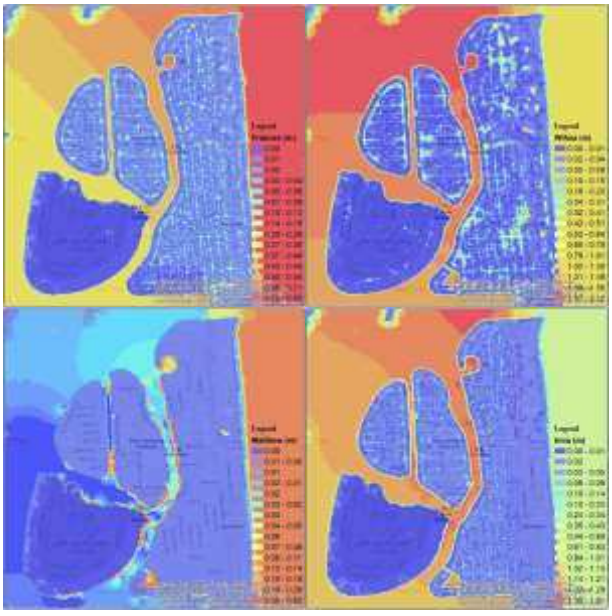

Fig. 5. Zoom-in of the maximum observed water level due to surge and flooding in the North Beach area of the City of Miami Beach, Florida. Refer to the main text for details.

V. CONCLUSIONS

Two distinct parametric wind models, as well as the capacity to read in time and space varying (reanalysis) hurricane wind and rain and a number of hurricane-type wind drag models have been implemented in TELEMAC2D. The introduction of these features, combined with the existing rainfall run-off and spectral wave model (TOMAWAC) makes the TELEMAC-MASCARET suite potentially very powerful for the simulation of storm surge and hurricane induced overland flooding. It is envisaged that this additional functionality will be formally included in the next release of the open TELEMAC-MASCARET suite.

ACKNOWLEDGEMENTS

This work was partitially supported by both the State of Florida Department of Emergency Management and W.F. Baird and Associates Ltd. The authors aknowledge the assistance of Mr. Yahia Kala (W.F. Baird & Assocs.) in producing the time series and HWM figures for hurricane Maria.

REFERENCES

[1] Cooper, A. Turnbull, M., Grey, S. Loilier, P. (2013) Tropical Cyclone Modelling with TELEMAC-2D. *Proc. XXth Telemac User Conf.*, Karlsruhe, Germany

[2] Garratt J.R. (1977) Review of drag coefficients over oceans and continents. *Mon Weather Rev*. 105:915–929

[3] Holland, G. J., 1980: An analytical model of the wind and pressure profiles in hurricanes. *Mon. Wea. Rev.*, 108, 1212–1218.

[4] Huffman, G. J., Bolvin, D. T., Braithwaite, D., Hsu, K., Joyce, R., Xie, P. & Yoo, S. H. (2015). NASA global precipitation measurement (GPM) integrated multi-satellite retrievals for GPM (IMERG). *Algorithm theoretical basis document*, version, 4, 30.

[5] Jelesnianski, C.P., Chen, J. and Shaffer, W.A., 1992. SLOSH: Sea, lake and overland surges from hurricanes, NOAA, Washington, D.C.

[6] Large, W. G. & Pond, S. (1981) Open ocean momentum fluxes in moderate to strong winds, *J. Phys. Oceanography* 11, 324–336.

[7] Liu, Z., 2016, Comparison of integrated multisatellite retrievals for GPM (IMERG) and TRMM multisatellite precipitation analysis (TMPA) monthly precipitation products: initial results. *Journal of Hydrometeorology*, 17(3), 777-790.

[8] Mattocks, C., Forbes, C., 2008. A real-time, event-triggered storm surge forecasting system for the state of North Carolina. *Ocean Modelling* 25, 95-119.

[9] Myers, V., & Malkin, W., 1961, Some Properties of Hurricane Wind Fields as Deduced from Trajectories. *National Hurricane Research Project Report* No. 49

[10] Peng, S., Li, Y. (2015) A parabolic model of drag coefficient for storm surge simulation in the South *China Sea. Sci. Rep.*, 5, 15496

[11] Powell, M.D (2006). Final Report to the National Oceanic and Atmospheric Administration (NOAA) Joint Hurricane Testbed (JHT) Program.

[12] Powell, M.D, Houston SH, Amat LR, Morisseau-Leroy N (1998) The HRD real-time hurricane wind analysis system. J Wind Eng Ind Aerodyn 77:53–64

[13] Sharifi, E., Steinacker, R. & Saghafian, B. (2016). Assessment of GPM-IMERG and other precipitation products against gauge data under different topographic and climatic conditions in Iran: Preliminary results. *Remote Sensing*, 8(2), 135.

[14] Westerink, J. J., Luettich, R. A., Feyen, J. C., Atkinson, J. H., Dawson, C., Roberts, H. J., Powell, M. D., Dunion, J. P., Kubatko, E. J. & Pourtaheri, H. (2008) A basin- to channel-scale unstructured grid hurricane storm surge model applied to southern Louisiana, *Mon. Weather Rev.* 136, 833–864.

Sediment dynamics of a nearshore sandbank: Results from TELEMAC-2D, TOMAWAC and SISYPHE modelling.

J.N. Aldridge, J. C. Bacon, T. Dolphin, A. Farcas

Centre for Environmental Fisheries and Aquaculture Science, Pakefield Road, Lowestoft, Suffolk, NR33 OHT, john.aldridge@cefas.co.uk

***Abstract*— Results are presented from a model study of the sediment transport regime and morphological evolution of the Sizewell-Dunwich Bank, a headland associated sandbank on the east coast of the UK North Sea. Offshore sandbanks play an important role in reducing storm wave energy at the shoreline and the Sizewell-Dunwich Bank may be of particular importance for the stability of the neighbouring shoreline. To gain insight into possible bank evolution, calculations of tides, waves and sediment transport were made using the finite element TELEMAC model suite, with the aim of understanding bank formation and maintenance mechanisms. The general pattern of tidally averaged total transport flux (bedload plus suspended load) indicated a zone of convergence at the location of the present Sizewell Bank and evidence of a weaker one at the location of the Dunwich Bank to the north. In common with previous studies tidal asymmetry was found to be oppositely oriented on the inshore and offshore sides of the banks. This suggest a plausible mechanism for the bank formation and maintenance with material from the north or the south having the potential to accumulate at the bank location.**

I. INTRODUCTION

Offshore sand banks can play an important role in influencing shoreline evolution and movement by attenuating the incident wave energy through the process of wave breaking and bed friction [1]–[6]. Assessing future shoreline stability in the vicinity of such sandbanks therefore requires taking account of possible changes to the sandbank position and morphology. Such a case study is presented here for the Sizewell–Dunwich bank located on the east coast of the UK North Sea. The working assumption is that the bank is a headland associated sandbank belonging to the nearby Thorpeness promontory. Explanations for the existence of headland associated sandbanks have focussed on the presence of tidal residual eddies [7]–[9], bedload convergences [10], and more generally with differing flood-ebb tidal asymmetry on the shoreward and seaward flanks of the bank [11]–[15]. Numerical modelling studies using idealised coastline geometry and tidal forcing typically show the formation of sandbanks on both sides of a headland [15], however in many cases sandbank formation is observed to be asymmetrical, with a larger bank forming preferentially on one side of the headland [11]. The Sizewell-Dunwich Bank is an extreme case with a substantial bank to the north of Thorpeness, but no bank observed to the south. The shape of the bank, pear shaped with the broader end pointed toward the headland and with steeper sides on the seaward flank at the broader end, is in remarkable accord with the description given in [13] for type 3A headland associated banner banks.

In this paper the mechanisms for formation and maintenance of the Sizewell-Dunwich Bank are investigated as a prelude to the eventual goal of predicting potential changes in bank morphology, evolution over decadal timescales. Results are presented for tidally averaged sediment transport fluxes both tidal and wave effects on the bedload and suspended load transport are considered and associated erosion and deposition patterns based on the recent bank configuration.

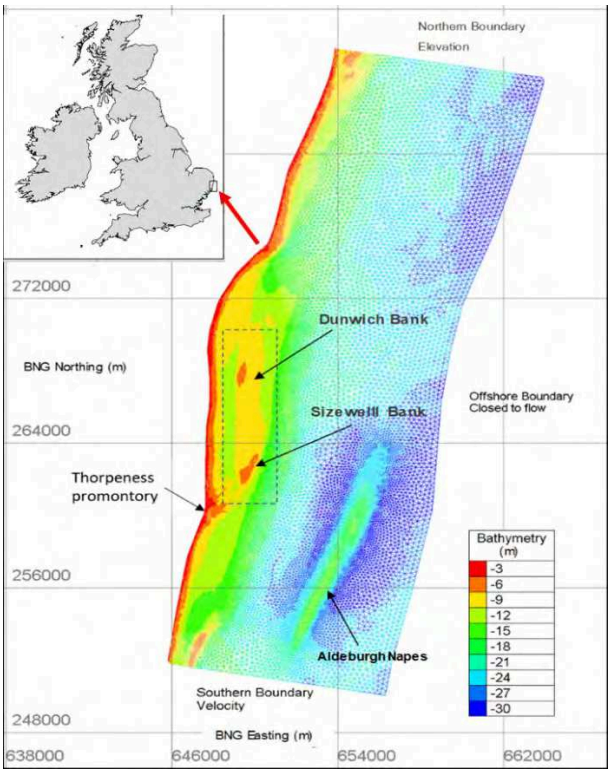

Figure 1: TELEMAC-2D model domain and mesh. The Sizewell-Dunwich Bank is indicated by the dashed box. Coordinate system is the British National Grid and elevations are in metres below ODN. Mesh resolution in the Sizewell-Dunwich Bank region is too high to discern individual elements but ranges from 30-50m elements on the bank increasing to 300m offshore.

II. METHODS

Modelling in this study used the TELEMAC suite of models consisting of TELEMAC-2D, TOMAWAC and SISYPHE to simulate tides, waves and sediment transport respectively [17], [18],[23]. TELEMAC-2D and SISYPHE were run in fully coupled mode, so that bed elevation change calculated in the sediment transport model SISYPHE was feed back to the hydrodynamic model. TOMAWAC was run separately in non-coupled mode to provide surface wave amplitude and period. All models were run on a common finite element mesh and associated bathymetry covering the greater

Sizewell embayment (Figure 1). Depth data covering the region from the mouth of the Blyth River to Thorpeness, were obtained from high resolution (better than 10m horizontal resolution) surveys carried out between 2007 and 2009 [19]. This survey data was integrated with data from the UK Hydrographic Office for the offshore region. The combined dataset was corrected to Ordnance Datum Newlyn (ODN) as an approximation to the local Mean Sea Level (MSL). The highest mesh resolution was approximately 50m in the shallow inshore region adjoining Thorpeness and the Sizewell-Dunwich Bank, increasing to around 300m for the offshore regions. Bathymetric smoothing was applied using a Fourier transform method [20] to the raw depth values. This procedure removed mesh scale noise in the calculated erosion/deposition patterns evident when calculations were performed on an unsmoothed bathymetry.

A. *Hydrodynamics*

Tidal forcing consisted of surface elevation specified at the northern boundary and depth average velocities at the southern boundary. The eastern offshore boundary was configured to follow the tidal stream and treated as a solid boundary with no transverse flow. TELEMAC-2D was run with a 10 second timestep and with a constant bed roughness coefficient corresponding to a rippled sand bed [21]. Measurements covering a 30-day period in November/December of 2013 provided the southern and northern hydrodynamic boundary forcing. A set of synthetic tidal forcing data was also generated from the measured velocity and elevations by applying a tidal analysis based on a least squares fit to a set of underlying harmonic constituent [22] to extract the M2 (largest semi-diurnal), M4 (first non-linear harmonic) and Z0 (residual) constituents. These generally provide the leading order components important for tidal sediment transport, namely: correct overall magnitude of tidal bed stress provided by the M2 constituent and the first order contributions to tidal asymmetry provided by M4 and Z0 constituents [23], [24]. This forcing allowed exact M2 tidal averages to be extracted in the simulations aimed at understanding the underlying transport processes.

Table 1: Wave forcing applied at the boundary of the TOMAWAC wave model. Hs values are those applied at the model boundary. Values measured at the bank are typically reduced by 20% compared to the boundary values due to attenuation by bed friction. Significant wave heights for given return periods were derived from a Weibull distribution fit to 30 years of hourly values at a location offshore of the Sizewell Dunwich bank taken from the UK Meteorological Office European Wave Model.

Case No	Wave direction (degrees from, North)	Hs (m)	Peak wave period (s)	Notes
1	40	0.9	5.0	Annual average NE[1]
2	40	2.2	7.7	1 week return NE[1]
4	153	0.94	4.0	Annual average SE[2]
5	153	2.2	6.0	1 week return SE[2]

[1] From northeast sector. [2] From southeast sector.

B. *Waves*

Significant wave height (Hs), peak wave period (Tp) and were calculated using the TOMAWAC spectral wave model run on the same mesh as the hydrodynamic calculation with a time step of 10 seconds, 22 frequency bins and 36 wave directions. Water depths in the wave model were fixed with respect to Mean Sea Level (MSL) and did not include tidal variations. Observations from a wave rider situated offshore of the bank showed a strongly bi-model distribution of wave directions clustered around north easterly and south easterly directions. A set of four wave model runs were created (Table 1) by applying constant wave height and direction boundary forcing using two different wave heights for each of the two dominant wave directions. The TOMAWAC wave model was then run to steady state and the final results stored for later input to the coupled TELEMAC2D-SISYPHE model. Within the coupled model, wave height, period and water depth were combined, using linear water wave theory, to estimate the near-bed orbital velocity for sediment transport calculations.

C. *Sediment transport*

Information on sediments in the region was obtained from grab samples (grid resolution approximately 250m on the Dunwich Sizewell Bank and 500m off the bank), collected during March to April 2008. Surficial sediments in the region were found to be heterogenous, with areas of soft and compacted mud, fine to medium sands, gravels and regions of bare rock [25]. In contrast, the surface sediments of the bank were remarkably homogenous, consisting of well-sorted sands with median diameter 150 – 250 µm, straddling the boundary between fine and medium sands. No attempt was made to model the multi-particle size sediment dynamics of the entire region, instead the focus was on modelling the sediment associated with the Sizewell-Dunwich Bank. Model runs used a single size class of 250 µm. Sediment transport calculations used the SISYPHE model [26], [27]. This model allows the choice of a number of bedload and total load transport formulations, together with an option to calculate suspended load via an advection-diffusion transport equation. In this study bedload was calculated using the bedload component of the total load formulation of Soulsby and Van Rijn [21]:

$$Q_b = k_1 \overline{\mathbf{U}}[(|\overline{\mathbf{U}}|^2 + c_2 U_w^2)^{0.5} - U_{cr}]^{2.4} \qquad (1)$$

where $\overline{\mathbf{U}}$ is the depth mean current vector, U_w is the bed orbital velocity amplitude, U_{cr} is a grain size dependent critical erosion velocity and k_1 is a grain size dependent coefficient, and $c_2 = 0.0036/C_D$ where C_D is the 2D quadratic drag coefficient (set at a value appropriate for rippled sand [21]). This formulation was chosen as it includes both wave and current contributions. Note, the bedload vector is assumed to be aligned with the depth mean velocity. No slope correction was included in the sediment transport calculations. Tests with and without a slope correction made only a small difference to the overall prediction of bedload transport and associated erosion and deposition patterns. The

suspended load transport was calculated with the depth-integrated advection-diffusion equation

$$\frac{\partial C}{\partial t} + \beta\, \bar{\mathbf{U}}.\nabla C + D = -w_s(C_b - C_{ref})/h \qquad (2)$$

where C is the depth mean suspended sediment concentration, $\bar{\mathbf{U}}$ is the depth mean current velocity, h is the local water depth, C_b is the predicted bed concentration derived from the depth mean concentration assuming a Rouse vertical profile. The factor $\beta < 1$ is a correction for the greater concentration of sediment near the bed and weights the advection velocity to be closer to a near-bed value. It is calculated at each time step assuming logarithmic and Rouse type profiles for velocity and sediment concentration respectively [31]. The reference concentration C_{ref} is calculated from the bedload transport rate as described in [28] with

$$C_{ref} = Q_b/(b\ Z_{ref}\ u_*) \qquad (3)$$

Here u_* is the bed friction velocity calculated from the skin friction component of the total stress derived from the sand grain roughness, the reference level Z_{ref} is taken equal to the ripple roughness ($Z_{ref} = k_r$) and b=6.34 is an empirical constant. Ripple roughness (k_r) is calculated dynamically by SISYPHE based on the formulations of [29], [30]. Since Q_b depends on both wave and current contributions (equation 1), the reference concentration and hence suspended load transport includes both wave and current forcing. Zero sediment flux for both bedload and suspended load was applied at the domain boundaries.

III. RESULTS

For the results reported in this section, hydrodynamic boundary forcing was based on a tidal decomposition containing M2, M4 and Z0 (residual) constituents as described in Section 3.A. The coupled model was run for seven M2 tidal cycles. Time series plots indicated the model had reached a steady repeating state after two tidal cycles. The first two tidal cycles were discarded, individual bedload and suspended load vectors were summed and the net total load vectors were obtained by summing over five complete M2 tidal cycles. Associated net erosion and deposition was calculated over the same period. Off bank, the model was started with a uniform 10cm layer of 250 µm sand above a rigid non-erodible base. A thicker (5m) layer was placed on the bank. This case corresponds to an unlimited supply scenario since, other than right at the shore, the 10 cm layer was generally not eroded down to the rigid bed and was available as a sediment source (limited only by hydrodynamic forcing) to other locations. Thus, for the given hydrodynamic forcing, the sediment transport vectors presented here represent the potential maximum rates.

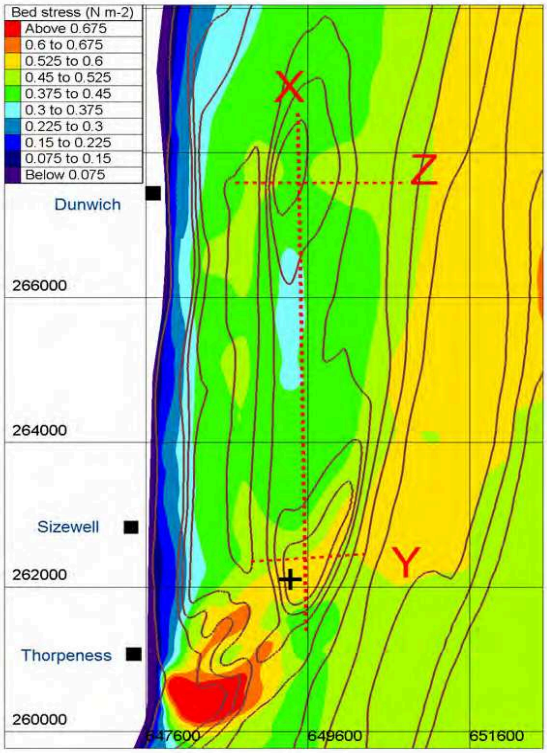

Figure 2: Tidally average bed stress values. Also indicated are the sections along which bed evolution is shown (Figure 12) and the position marked with cross (+) used to plot sediment flux and bed change over time (Figure 7).

A. *Bed stress*

The tidal bed stress distribution in vicinity of the Sizewell-Dunwich Bank show a maxima just offshore of Thorpeness on the shallow platform and crag ridges, with a band of enhanced tidal stress extending along the southern and eastern faces of the bank (Figure 2). In the results shown later, this region shows relatively large changes in bed level. A minimum in bed stress occurs in the deeper 'swale' region between the Dunwich and Sizewell Banks and associated with relatively small morphology changes (see next section).

B. *Erosion and deposition due to tidal forcing*

Model runs were carried out to assess the contributions of bedload, suspended load and wave-induced mobility to the modelled sediment flux and erosion/deposition patterns. Results are plotted as tidal averaged sediment flux vectors normalised (for display) to a uniform length to allow the net direction to be more easily discerned at smaller transport rates. Northward and southward pointing fluxes are coloured differently so that flood (south) and ebb (north) directed transport paths can be discerned.

The net bedload erosion and deposition are determined mathematically by the divergence of the net sediment transport flux vector. Although not exactly equivalent, broadly speaking deposition will occur when the average bedload magnitude decreases in the direction of net transport and erosion will occur when bedload magnitude increases in the direction of net transport.

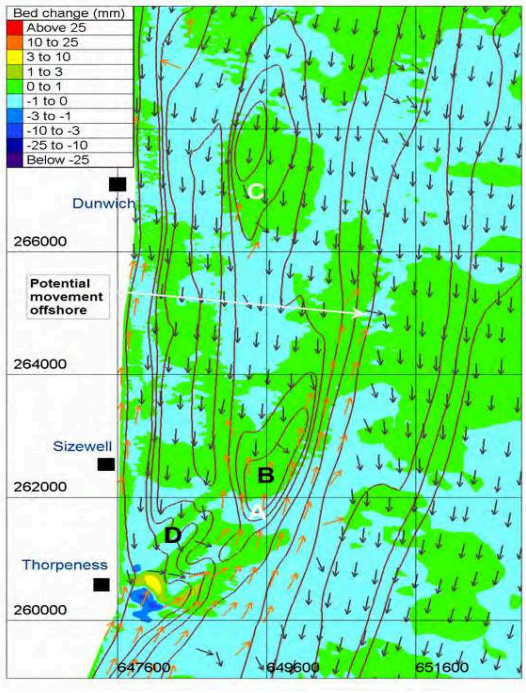

Figure 3: Bedload only with tidal forcing. Normalised tidal average transport vectors superimposed on erosion deposition patterns (mm) over five M2 tidal cycles for. Light coloured vectors represent net northerly (ebb) transport and dark vectors net southerly (flood) transport. Note, for clarity vector positions are sub-sampled and the plotted value is an average taken over the surrounding region. The actual mesh spacing is much denser.

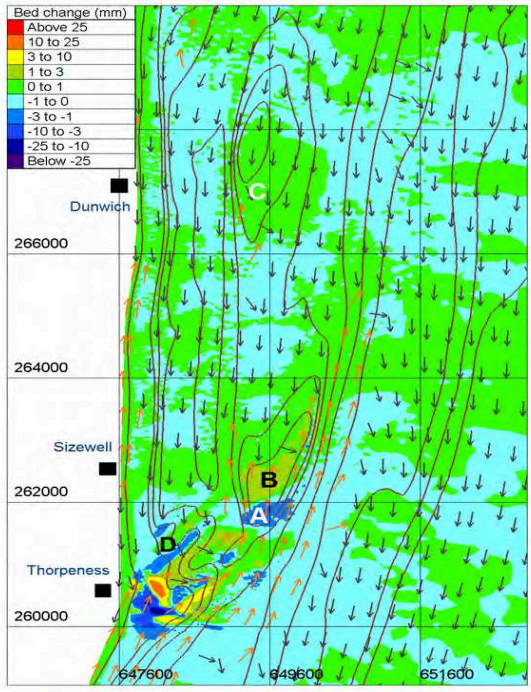

Figure 4: Bedload and Suspended load with tidal forcing. Normalised tidal average transport vectors superimposed on erosion deposition patterns (mm) over five M2 tidal cycles for. See Figure 3 for explanation of vectors.

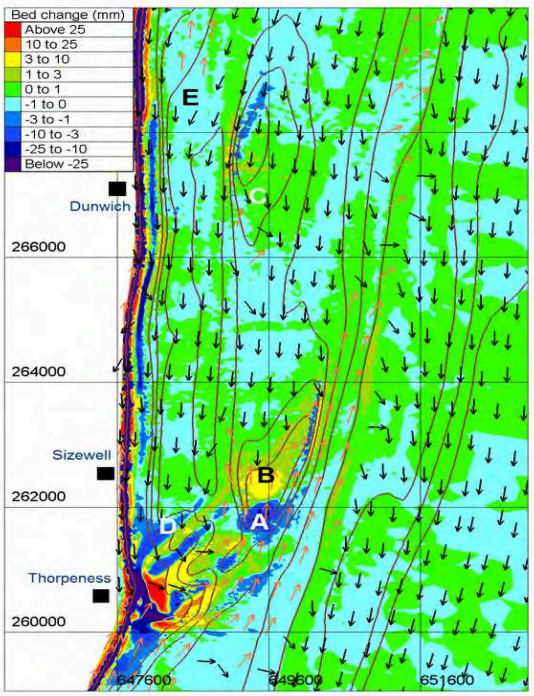

Figure 5: Bedload and suspended load with tidal forcing and annual average waves (Hs = 0.9 m) from north-east sector. Normalised tidal average transport vectors superimposed on erosion deposition patterns (mm) over five M2 tidal cycles. See Figure 3 for explanation of vectors.

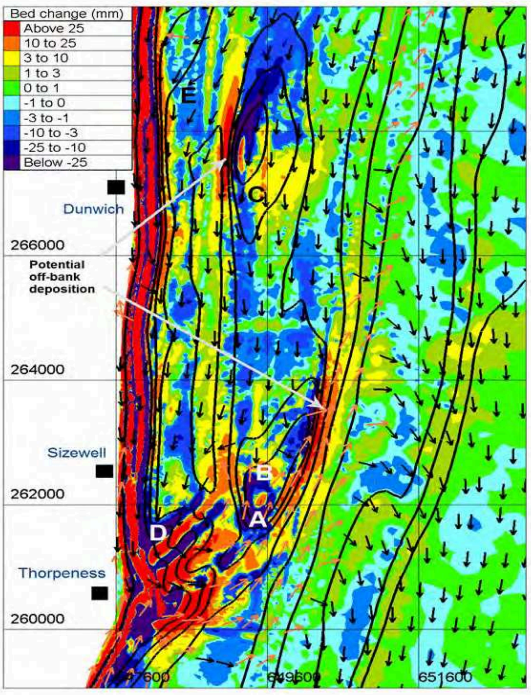

.

Figure 6: Bedload and suspended load with tidal forcing for 1 week return period waves (Hs = 2.2 m) from north-east sector. Normalised tidal average transport vectors superimposed on erosion deposition patterns (mm) over five M2 tidal cycles. See Figure 3 for explanation of vectors.

Calculations with bedload transport only, (Figure 3) showed deposition occurring at the top of the banks (locations B and C) and erosion on the south flank (location A). An interesting feature was the predicted convergence of opposing transport paths from the north and south at the top of the Sizewell Bank. Sediment moving inshore of the bank parallel to the shore was predicted to turn offshore at D, potentially joining material moving up from the south. Also marked is a possible path for material to move offshore from the eastern edge of the bank. Although not evident from the normalised vectors, this pathway is however very weak.

Calculations with bedload and suspended load gave a very similar distribution to the bedload-only case, but with a greater magnitude of erosion and deposition (Figure 4). As with the bedload case, erosion occurred on the southern face of the bank (location A) and the deposition at the top (location B) associated with the transport convergence in this region. As indicated by the normalised vectors, a second (weak) convergence zone is suggested at location C at the northern end of the Sizewell – Dunwich Bank. Thus, under tidal conditions the model yields southward (flood) directed sediment transport in the channel inshore of the Sizewell Bank and northward (ebb) directed transport along the seaward flank of the bank. Over five tidal cycles the magnitude of bed change due to bedload plus suspended load transport is generally in the range from 0-10mm. The similarity in general erosion/deposition pattern is not unexpected as both bedload and suspended load vectors are aligned with the depth mean current, and suspended load magnitude is closely related to the bedload via the reference concentration (3).

C. Erosion and deposition with tide and wave forcing

When a constant annual mean wave forcing was included (Table 1, case 1) the broad scale pattern of erosion and deposition did not change significantly from the tide only case, but magnitudes increased (Figure 5). Note, the inclusion of waves here was as a 'stirring mechanism' i.e. increasing the quantity of sediment being transported but with no modification to currents. Tidal erosion/deposition patterns identified previously were preserved, with erosion occurring on the southern flank (location A) and deposition on the top of the bank at locations B and C. With waves included, net erosion over five tidal cycles near location A for example, increased by a factor of four, from 2.5mm (tide only) to 10.5mm (tide and wave). Similar proportional changes were seen elsewhere. Extrapolation at location A of this magnitude of erosion over a year would give a very significant bed change of around 1.5 m. Bands of erosion and deposition associated with the Coralline Crag (location D) show erosion on the raised 'fingers' and deposition in-between. In this simulation, the start condition had the ridges covered in 10cm of sand, which was completely eroded. This is consistent with observed fluctuations in ridge elevation [16] that suggest that sediment can cover and uncover the ridges. There is also an indication of a bedload parting zone at E, that was present in the tide only calculations, but is more prominent when waves

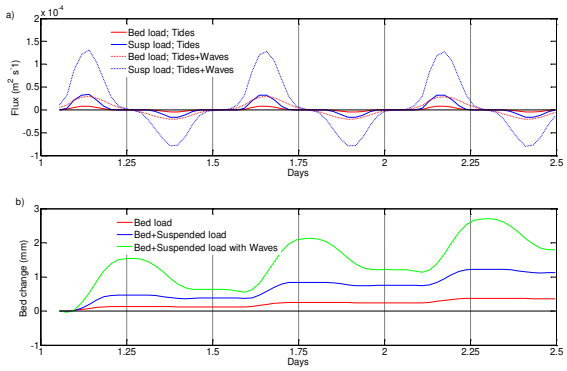

Figure 7: Time series near the top of Sizewell Bank (see Figure 9 for position marked with '+'). a) Sediment flux for bedload, suspended load with and without waves; b) Change in bed elevation. Note the time axis in both graphs is the same so the relationship between the flux and bed response can be discerned.

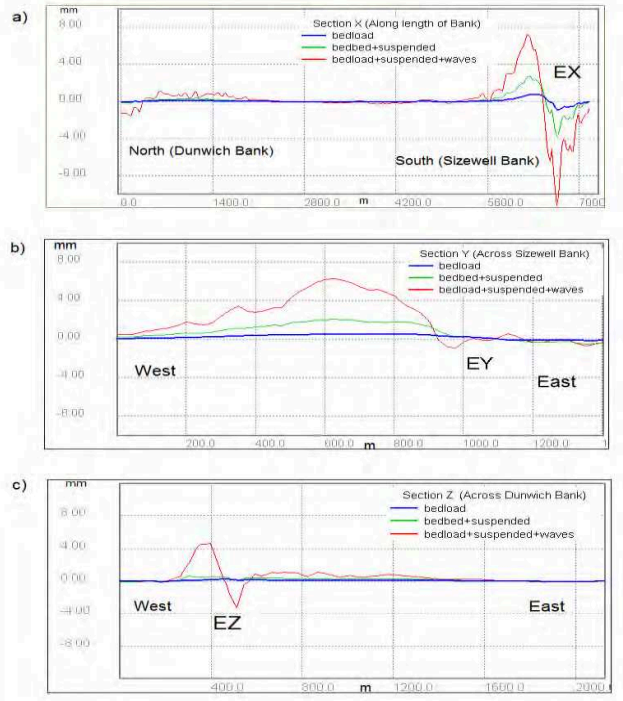

Figure 8: Change in bed elevation for 12 M2 tidal cycles along sections (see Figure 3). a) Section X, N-S along bank, with EX marking the south face of bank; b) section Y, E-W over the Sizewell Bank, with EY marking the east (seaward) face of the bank; c) Section Z, E-W over the Dunwich Bank, with EZ marking the western (shoreward) face of the bank.

are included. It is interesting to note the formation of erosion and deposition bands close to and parallel to the shore, suggestive of the longshore bar that occurs along this stretch of coast. Simulations with waves from the south east sector (Table 1, case 3) shows very similar patterns of erosion and deposition and are not shown here.

With larger waves (Table 1, case2) the overall patterns of erosion/accretion remained broadly similar but with erosion and deposition much intensified (Figure 6). However, the top of the Sizewell bank (location B) that previously showed

accumulation was eroded under stronger waves. Also evident are lateral regions of intense deposition/erosion seaward of the Sizewell Bank and shoreward of the Dunwich Bank. This appears to be a mechanism for removal of bank material in the model simulations. Simulations with waves from the south east sector (Table 1, case 4) showed very similar patterns of erosion and deposition and are not shown here. Note that these simulations neglect the effect of wave driven currents and these will be sensitive to wave direction.

D. Further analysis at specific locations along the Bank

The time series of transport flux magnitude and bed evolution at a location near the top of the Sizewell Bank (cross marked on Figure 2) shows suspended load flux to be about four times the magnitude of bedload flux (Figure 7). Including annual mean wave increased the absolute value of both suspended and bedload flux by approximately a factor of four. Without waves, the tidal transport flux was zero for almost half the tidal cycle, indicating that the average tidal M2 velocities were close to threshold conditions for movement of the sediment class used in the simulation (250 μm diameter). However, when the orbital velocity corresponding to an annual mean wave was included in the Soulsby van Rijn formulae (1), conditions were predicted to be above the transport threshold for most of the tidal cycle. For this location, accumulation of material occurs under both tidal and tide plus (average) wave conditions. Analysis based on the spatial plots (Figure 4 and Figure 5) would suggest the material deposited at the top of the Sizewell Bank is coming from erosion of the southern face.

To look in more detail at the individual effect of bedload, suspended load and wave stirring on bed morphology, the net changes in bed level after 5 tidal cycles were plotted along three transects (marked X, Y, Z Figure 2). Bed level change north-south along the Sizewell-Dunwich Bank system (transect X) in all cases showed erosion of the southern flank and accretion at the top of the Sizewell Bank (Figure 8a). Although hard to discern for the bedload and bedload + suspended load results, there is also some accumulation of material at the northern end on the Dunwich Bank. The effect of wave mobilisation was to enhance this general pattern. The wave-induced mobility also increased the rate of accretion at the Dunwich Bank, pushing it further to the south and removing material on the northern flank. The change in bed level east-west across the Sizewell Bank (transect Y) again shows the accumulation at the top of Sizewell Bank with average wave conditions significantly enhancing this (Figure 8b). However, the wave activity also leads to adjacent bands of erosion and deposition on the eastern (seaward) flank as marked at EY. A similar pattern is also evident in transect Z on the western (shoreward) flank of the Dunwich Bank (Figure 8c). These correspond to the deposition patterns noted in Figure 6 and associated with steep bathymetric gradients with erosion at the top and deposition at the bottom of the slope.

IV CONCLUSIONS

The bedload and suspended load sediment transport regime of the Sizewell Dunwich Bank on the UK east coast was simulated for a range of tidal and wave conditions using the coupled TELEMAC-2D and SISYPHE hydrodynamic and sediment transport model and TOMAWAC spectral wave model. Net sediment flux directions and patterns of erosion and deposition were obtained for the present bank configuration.

The general pattern of tidally averaged total transport flux (bedload plus suspended load) showed a well-defined convergence zone at the location of the present Sizewell Bank. This implies a likely mechanism for bank maintenance, with material moving from the north or the south having the potential to accumulate at the bank location. In particular, the model suggests that sediment transported southward by longshore drift could travel from the nearshore region at Thorpeness to the south end of the bank this providing a mechanism for bank maintenance.

ACKNOWLEDGEMENT

Funding under the British Energy Estuarine and Marine Studies (BEEMS) program and Cefas DP363A funding is gratefully acknowledged. We would also like to thank the many people associated with the BEEMS program who contributed to this work, including Liam Fernand who read the draft manuscript and whose comments helped improve the paper.

REFERENCES

[1] M. J. Tucker, A. P. Carr, and E. G. Pitt, “The effect of an offshore bank in attenuating waves,” Coast. Eng., vol. 7, no. 2, pp. 133–144, May 1983.

[2] N. J. MacDonald and B. A. O’Connor, “Influence of Offshore Banks on the Adjacent Coast.,” Proceedings 24th Coast. Eng. Conf., pp. 2311–2324, 1994.

[3] R. J. S. Whitehouse, N. W. Beech, J. A. Roelvink, and S. J. M. H. Hulscher, “Understanding the behaviour and engineering significance of offshore and coastal sand banks.” HR Wallingford Ltd., 1998.

[4] A. Hequette and D. Aernouts, “The influence of nearshore sand bank dynamics on shoreline evolution in a macrotidal coastal environment, Calais, northern France,” Cont. Shelf Res., vol. 30, no. 12, pp. 1349–1361, Jul. 2010.

[5] C. Coughlan, “Hydrodynamic Processes and Sediment Transport around a Headland-Associated Sandbank and Implications for the Neighbouring Shoreline,” 2008.

[6] A. P. Carr, “Evidence for the sediment circulation along the coast of East Anglia,” Mar. Geol., vol. 40, no. 3–4, pp. M9–M22, Apr. 1981.

[7] R. D. Pingree, “The Formation Of The Shambles And Other Banks By Tidal Stirring Of The Seas,” J. Mar. Biol. Assoc. United Kingdom, vol. 58, no. 01, p. 211, Feb. 1978.

[8] L. Maddock and R. D. Pingree, “Numerical simulation of the Portland tidal eddies,” Estuar. Coast. Mar. Sci., vol. 6, no. 4, pp. 353–363, Apr. 1978.

[9] R. D. Pingree and L. Maddock, “The tidal physics of headland flows and offshore tidal bank formation,” Mar. Geol., vol. 32, no. 3–4, pp. 269–289, Jul. 1979.
[10] A. C. Bastos, D. Paphitis, and M. B. Collins, “Short-term dynamics and maintenance processes of headland-associated sandbanks: Shambles Bank, English Channel, UK,” Estuar. Coast. Shelf Sci., vol. 59, no. 1, pp. 33–47, 2004.
[11] V. N. D. Caston, “Linear Sand Banks in the Southern North Sea,” Sedimentology, 1971.
[12] K. R. Dyer and D. A. Huntley, The origin, classification and modelling of sand banks and ridges, vol. 19, no. 10. 1999.
[14] A. Berthot, “Formation and maintenance of headland associated linear sandbanks,” 2005.
[15] A. Berthot and C. Pattiaratchi, “Mechanisms for the formation of headland-associated linear sandbanks,” Cont. Shelf Res., vol. 26, no. 8, pp. 987–1004, 2006.
[16] T. Dolphin, “Sizewell: Morphology of coastal sandbanks and impacts to adjacent shorelines. BEEMS Technical Report TR058, Cefas, Lowestoft.,” 2009.
[17] J. M. Hervouet, “TELEMAC modelling system: an overview,” Hydrol. Process., 2000.
[18] EDF, “TELEMAC Modelling System, 2D hydrodynamics TELEMAC-2D software. User Manual.,” 2014.
[19] K. Vanstaen, “Interpretation of BEEMS Sizewell Swath Bathymetry and Backscatter. BEEMS technical report TR087, Cefas, Lowestoft,” 2010.
[20] D. Garcia, “Robust smoothing of gridded data in one and higher dimensions with missing values,” Comput. Stat. Data Anal., 2010.
[21] R. Soulsby, Dynamics of marine sands : a manual for practical applications. Telford, 1997.
[22] J.-J. Shu, “Prediction and Analysis of Tides and Tidal Currents,” Int. Hydrogr. Rev., vol. 4, no. 2, pp. 57–64, 2003.
[23] R. D. Pingree and D. K. Griffiths, “Sand transport paths around the British Isles resulting from M2 and M4 tidal interactions,” J. Mar. Biol. Assoc. UK, vol. 59, no. 02, pp. 497–513, May 1979.
[24] J. Van Der Molen, “The influence of tides, wind and waves on the net sand transport in the North Sea,” vol. 22, pp. 2739–2762, 2002.
[25] K. Pye and S. J. Blott, “Sea bed sediment characteristics, bedforms and sediment transport pathways in the Sizewell area. BEEMS Technical Report TR107, Cefas, Lowestoft.,” 2011.
[26] EDF, “TELEMAC Modelling System, SYSYPHE, Version 6.3. User Manual.,” 2014.
[27] C. Villaret, J. M. Hervouet, R. Kopmann, U. Merkel, and A. G. Davies, “Morphodynamic modeling using the Telemac finite-element system,” Comput. Geosci., vol. 53, no. September 2014, pp. 105–113, 2013.
[28] E. W. Bijker, “Mechanics of Sediment Transport by the Combination of Waves and Current,” in Proceedings of the Short Course on Design and Reliability of Coastal Structures, 23rd International Conference on Coastal Engineering, 1992.
[29] P. L. Wiberg and C. K. Harris, “Ripple geometry in wave-dominated environments,” J. Geophys. Res., vol. 99, no. C1, p. 775, Jan. 1994.
[30] L. C. van Rijn, D.-J. R. Walstra, and M. van Ormondt, “Unified View of Sediment Transport by Currents and Waves. I: Initiation of Motion, Bed Roughness, and Bed-Load Transport,” J. Hydraul. Eng., vol. 133, no. 7, pp. 776–793, 2007.
[31] G. Galappatti and C. B. Vreugdenhil, “A depth-integrated model for suspended sediment transport,” J. Hydraul. Res., 1985.

Modelling Cohesive Sediments in the Scheldt Estuary (Belgium) with SEDI-3D

Sven Smolders, Qilong Bi, Tatiana Maximova and Joris Vanlede
Department of Mobility and public works, Flemish government
Flanders Hydraulics Research
Antwerp, Belgium
sven.smolders@mow.vlaanderen.be

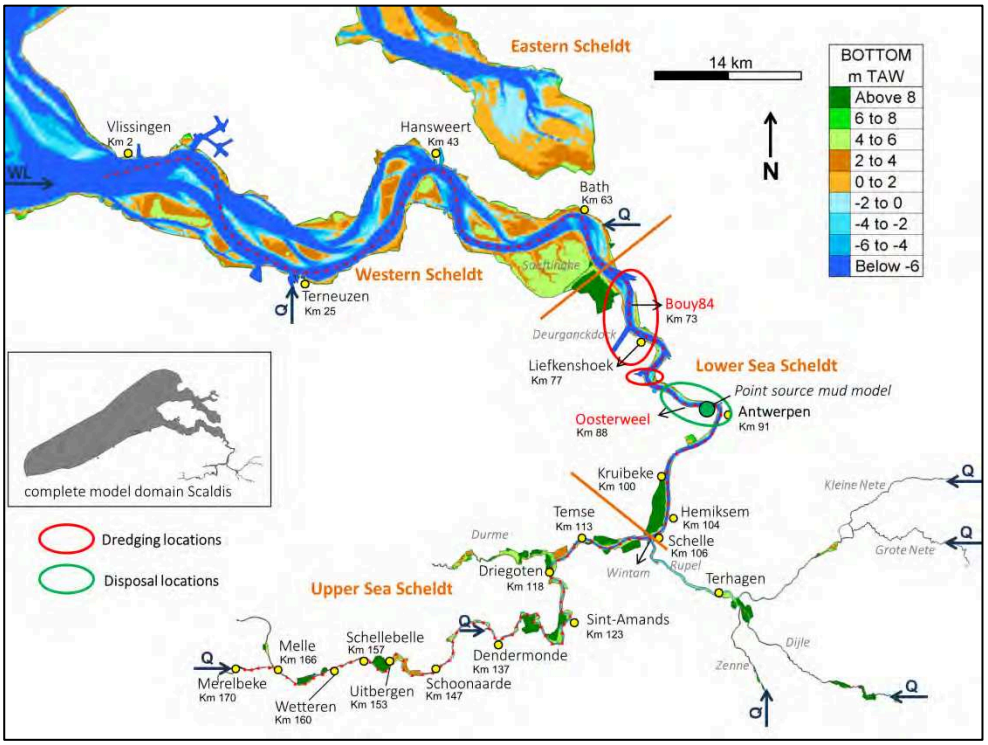

Figure 1- general overview of model domain and Scheldt estuary

***Abstract*—A new cohesive sediment transport model for the Scheldt Estuary is presented in this paper. The model is built in SEDI-3D, which itself is part of the TELEMAC-3D code. The 3D hydrodynamic Scheldt model, Scaldis, was used for hydrodynamics. One fraction of fine sediments is modelled as a tracer. The results show good agreement with point measurements and with estimated transport rates and directions. However the local turbidity maximum is dependent on a local sediment source and a fix for excessive deposition of mud in shallow areas needs a more elegant solution.**

I. INTRODUCTION

The implementation of the Seine-Scheldt connection will result in increased shipping traffic between France and Flanders. The Flemish Government wants to improve the navigability of the Upper Sea Scheldt. Within this framework, an integrated plan is being developed, in which navigability, safety and nature are the key elements.

At the moment, the upstream part of the Upper Sea Scheldt is a Class IV fairway (ships up to 85m long and 9.5m wide) and forms a bottleneck in the European network. The questions that need to be answered within the integrated plan pertain to the measures that need to be taken to upgrade the Upper Sea Scheldt to a Class Va fairway suitable for ships up to 2250 tons (ships up to 110m long and 11.4m wide), with respect for the other functions (safety, nature and recreation). It is of the utmost importance that the design of the morphological changes in the Upper Sea Scheldt leads to a multifunctional Scheldt Estuary with assets for navigability, guarantees for protection against flooding and a sustainable natural system.

A chain of models will be used to evaluate the different morphological scenarios. The mud model described in this paper is a part of that model chain. Cohesive sediments play a key role in aquatic ecosystems like the Scheldt estuary. They determine light penetration into the water column and hence

affect the primary production. They determine the layers of the bed supporting benthic life and the sediment's organic content forms food supply to filter feeders. Therefore the behavior of these cohesive sediments is important in the assessment of the impact of changes in bathymetry or management of the estuary and for this project, the Upper Sea Scheldt in particular. Results of the mud model will be used as input for models of project partners, e.g. cohesive sediment concentrations affect light penetration and this will affect algae growth, which is modeled in an ecosystem model of the University of Antwerp [1].

An existing mud model for the Scheldt Estuary was already developed in the framework of the Long Term Vision for the Scheldt estuary. This model was developed in DELWAQ [2, 3, 4, 5]. This model runs autonomous, but gets a spring/neap tidal cycle from a hydrodynamic model (SIMONA) as input and this input is repeated the longer the simulation time is set.

Within the integrated Plan Upper Sea Scheldt a 3D hydrodynamic model of the Scheldt Estuary was developed, named "Scaldis", in TELEMAC-3D. The model is described in detail in [6, 7, 8]. When coupling the hydrodynamics of this TELEMAC-3D model with DELWAQ it was not possible to simplify the model grid and decrease the number of computational nodes of the hydrodynamic model (which is possible in linking a SIMONA model with DELWAQ). This resulted in serious time constraints for running a simulation because DELWAQ could not run on multiple processors at that time and therefore a new mud model was made using SEDI-3D code that was already present within the TELEMAC-3D code.

In developing a new mud model in SEDI-3D some goals were set to reach a good quality model. The mud model should represent:

- the observed global spatial suspended sediment concentration (SSC) distribution, like the location of an estuarine turbidity maximum (ETM);
- a good intra-tidal SSC variation;
- a good spring/neap SSC variation;
- an overall mass balance in equilibrium;
- a good response to higher river discharges;
- good siltation rates of intertidal areas and salt marshes in the order of 1-2 cm/year, and siltation rates of harbor and docks according to dredging volumes.

II. TELEMAC-3D HYDRODYNAMIC MODEL: SCALDIS 3D

This chapter will briefly describe the TELEMAC-3D model, Scaldis 3D, which is presented in full detail in [6]. The model domain contains the Belgian coastal zone, extended to France in the South and The Netherlands in the north, the Eastern and the Western Scheldt in the Netherlands and the Sea Scheldt with its tributaries as far as the tidal influence reaches. The mesh resolution increases from 500 meters in the coastal zone to 120 meters in the Western Scheldt, to 60 meters in the Sea Scheldt further increasing upstream towards 5 meters at the upstream discharge boundaries. The horizontal grid contains 459,692 nodes. In the vertical there are five layers following a sigma transformation (0, 0.12, 0.30, 0.60 and 1). The bathymetry is interpolated from multi-beam measurements and lidar data for the shallow areas. Water level time series are imposed on the sea boundary and daily averaged discharges are imposed on 8 upstream liquid boundaries. Wind is assumed to be incorporated into the water level boundary downstream and is not taken into account further. The model was calibrated using a spatial varying Manning bottom friction coefficient. The friction coefficient varies from 0.026 s/m$^{1/3}$ in the downstream part and decreases to 0.014 s/m$^{1/3}$ in the upstream river part. Salinity is present as an active tracer and density effects are taken into account. The mixing length model of Nezu and Nakagawa is used for the vertical turbulence modelling. The horizontal turbulence model is the Smagorinski model. Tidal flats are present and equations are solved and corrected on tidal flats. Coriolis is taken into account.

III. SEDI-3D MUD MODEL: SCALDIS MUD

A. Theoretical background

Cohesive sediment transport occurs in water through the combination of advection and diffusion. In SEDI-3D, a 3D advection-diffusion equation is solved by considering the cohesive sediment particles moving at the same velocity as the fluid:

$$\frac{\partial C}{\partial t} + U_j \frac{\partial C}{\partial x_j} = \frac{\partial}{\partial x_i}\left(\frac{\nu_t}{\sigma_t}\frac{\partial C}{\partial x_i} + w_s C \delta_{i3}\right) \quad (1)$$

In this equation U is the mean flow velocity [m/s], t is the time [s], x_j represents the components of the coordinate vector [m], ν_t is the eddy viscosity [m2/s], σ_t is the turbulent Prandtl-Schmidt number (i.e. the ratio of ν_t to the eddy diffusivity of the sediment particles), C is the sediment concentration [g/L or kg/m³], w_s is the representative mean settling velocity [m/s], and δ_{ij} is the Kronecker delta.

At the interface between the water column and the bed layer, erosion processes happen due to the shear motion of the flow. The erosion flux is computed with the Partheniades formula. The erosion flux is the product of an erosion rate multiplied with a probability factor as a function of the shear stress in excess of a critical erosion shear stress:

$$E = \begin{cases} M\left(\frac{\tau_b}{\tau_{ce}} - 1\right) & if\ \tau_b > \tau_{ce} \\ 0 & otherwise \end{cases} \quad (2)$$

with M the Krone-Partheniades erosion constant [kg/m²/s], τ_b the bed shear stress and τ_{ce} the critical bed shear stress for erosion. So erosion only occurs when the bed shear stress is higher than the critical bed shear stress for erosion set by the user. The erosion constant M determines the intensity of the erosion. A larger value will mean more erosion if erosion occurs. The bed shear stress is given by:

$$\tau_b = \rho_w u_* |u_*| \quad (3)$$

with ρ_w the density of the water and u_* the friction velocity. In SEDI-3D, a quadratic friction law is used with a drag coefficient C_D to compute τ_b in a rough regime. When a Manning coefficient is used the equations look as follows:

$$\tau_b = \frac{1}{2}\rho_w C_D \overline{U}|\overline{U}| \quad (4)$$

With:

$$C_D = 2n^2 \frac{g}{h^{1/3}} \quad (5)$$

Where $\overline{U}$ is the depth-averaged velocity (which is also calculated in SEDI-3D), n is the Manning coefficient, g is gravitational constant and h is the water depth. After the calculation of this shear stress, the shear velocity is calculated and is then imposed at the bottom as a boundary condition for solving the momentum conservation equations of the flow.
The empirical deposition law from Krone is implemented in SEDI-3D to estimate sediment deposition. Here the deposition flux is approximated by the product of local sediment concentration with the settling velocity, multiplied with a deposition probability:

$$D = \begin{cases} w_s C\left(1 - \frac{\tau_b}{\tau_{cd}}\right) & if\ \tau_b < \tau_{cd} \\ 0 & otherwise \end{cases} \quad (6)$$

Where τ_{cd} is the critical shear stress for mud deposition , w_s is the settling velocity [m/s], and C is the sediment concentration in suspension [g/L] or [kg/m³]. If the bottom shear stress is smaller than the critical bottom shear stress for deposition, sediment is settling. Within this project the choice was made to model deposition D as a shear stress independent flux, following [10] and [11]. This is also in line with recent applications in modelling cohesive sediment transport [12, 13]. This is done by setting τ_{cd} to a large value of 1 000 Pa. The formula for the deposition flux, equation 6, then simplifies to:

$$D = w_s C \quad (7)$$

The bed evolution in SEDI-3D is calculated via the Exner equation:

$$(1 - \lambda)\frac{\partial z_b}{\partial t} + (E - D) = 0 \quad (8)$$

where λ is the bed porosity and z_b is the bed level.

B. Parameter choices

In this version of SEDI-3D (V7P2r1) only one fraction of cohesive sediment can be modelled. Based on [14, 15, 16] a characteristic mud particle diameter of 50 µm and a settling velocity of 0.5 mm/s was chosen. The sediment density was set to 2650 kg/m^3. Flocculation and hindered settling were not taken into account. Only one bed layer was chosen and this bed layer is initially empty. If mud deposits in this layer, the mud layer density was set to 500 kg/m^3. The critical shear stress for erosion was set to 0.05 Pa and the erosion coefficient was set to 1.0E-4 kg/m^2/s. These last two parameters are calibration parameters.

C. Boundary conditions

A simulation period of 42 days was chosen: two days for the hydrodynamic spin-up, 20 days for sediment spin-up and 20 days actual sediment run. The downstream water level boundary represents measured water levels from 29/07/2013 - 07/09/2013. The upstream discharges are kept constant with a long yearly averaged value and an rain event of five days, represented in the discharge time series as an event with a return period of 1/6.

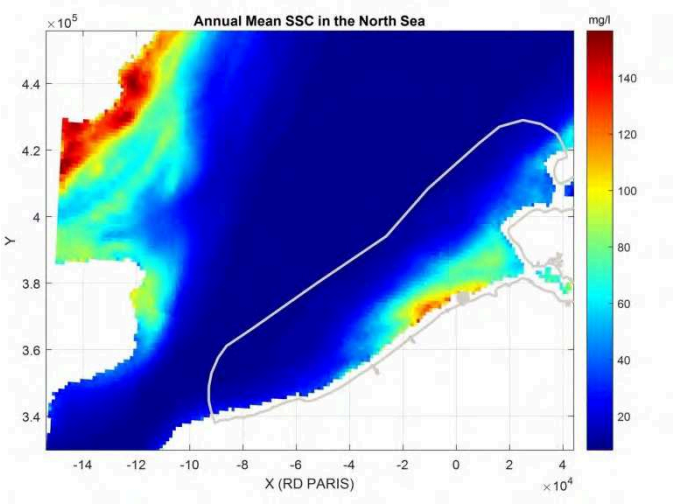

Figure 2 - Annual mean SSC in the North sea with the location of the Scaldis model sea boundary (source: KBIN – OD Natuur)

A constant sediment concentration is given to every liquid boundary. This concentration for the discharge boundaries represents the average annual total sediment load for the period 1971-2009 calculated by [17]. The order of magnitude of the contribution at each boundary varies between 0.04 g/L for the smallest tributary and 0.1 g/L for one of the larger upstream tributaries. For the downstream boundary satellite images were used from [18] (see Figure 2). The concentrations vary in space along the boundary, but one value was chosen, i.e. 0.013 g/L, for the entire downstream boundary because this boundary is far from the zone of interest of the project, i.e the Upper Sea Scheldt (see Figure 1).
The bottom layer is empty. The Bottom friction coefficient has a direct effect on the calculated shear stresses (equation 4). Normally the bottom friction coefficient of the hydrodynamic model is used for the calculations of the shear stresses for SEDI-3D, but since the spatial varying Manning bottom friction coefficient is the result of a calibration process and when calibrating it corrects more than only a different bottom friction in different parts of the estuary. In the Scaldis model unnaturally low Manning bottom friction values (see Figure 3) had to be used to get the water motion correct in most

upstream locations of the model. Therefore the subroutine clsedi.f was changed so that for the sediment model only a constant Manning bottom friction coefficient of 0.02 s/m$^{1/3}$ was used.

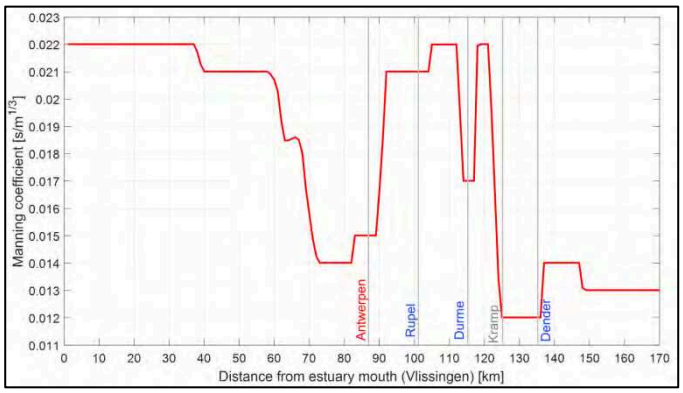

Figure 3 - Manning bottom roughness coefficient of Scaldis 3D 2013 along the estuary axis.

D. Initial conditions

A model simulation of two days is used to spin-up the hydrodynamics. This previous computation file is used to start a new 40 day simulation with sediment. The bed layer is empty at the start. Cohesive sediment is initiated in the water column as a concentration of 0.5 g/L. A sensitivity analysis showed that initialising a simulation with the same amount of sediment on the bed will give a similar result in an equilibrium situation. Putting an unlimited supply of sediment on the bed (bed layer with thickness of 100 m as default) gave much better results for SSC, but the erosion rates on the bottom were unrealistically high. Therefore it was chosen to initiate sediment in the water column as a concentration.

E. No feedback to hydrodynamic model

To keep the parallel with DELWAQ, the sediment module does not update the bottom of the hydrodynamics part. In the subroutine fonvas.f this update is commented. Also the effect of SSC on the water density is turned off in the subroutine drsurr.f by eliminating the sediment contribution to the relative density.

F. Reduced settling velocity in shallow areas using a logistic function

When the critical deposition shear stress is very high equation 6 becomes equation 7 and settling velocity is constant over the entire model domain. The first simulations showed that a lot of sediment is captured in shallow areas. In these areas deposition occurs, but the shear stresses are too low to bring sediment back into suspension, making these shallow areas sediment traps. Therefore a logistic function was added to equation 7 under the form of an alpha:

$$D = \alpha\, w_s\, C \tag{9}$$

with

$$\alpha = \frac{1}{1+e^{-k(d-d_0)}} \tag{10}$$

Where d is the water depth, d_0 is the water depth below which a significant reduction will take place and k determines the steepness of the slope in reducing alpha from 1 to 0. With k = 5 and d_0 = 1.5 m and 3.0 m two example are given in Figure 4.

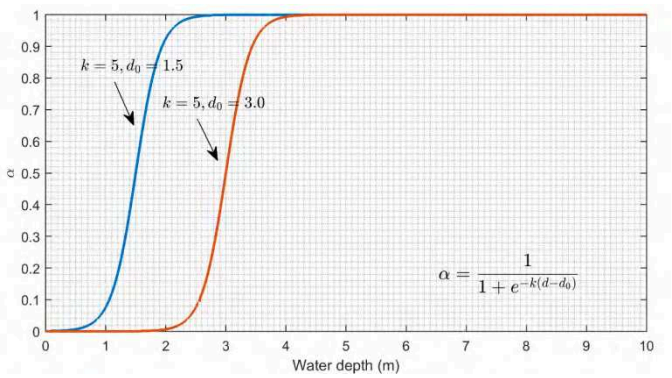

Figure 4 - sigmoid (logistic) curve alpha α in function of water depth.

For the mud model d_0 = 1.5 m proved to be very successful in keeping shallow areas becoming sediment traps. This alpha was added to the settling velocity calculated in the subroutine vitchu.f.

G. Dredging and disposal flux

As a first approximation of dredging and disposal of sediment, the total disposal flux of sediment is added as a point source of sediment to the simulation. The magnitude of the sediment concentration of this point source is determined based on reported disposals in recent years (2007-2015) [19]. On average 4.5 million tons dry solids (TDS) are deposited back in the estuary each year. In the Scaldis model a point source is added with coordinates (RD Paris): x=83430 m and y=361424 m. The sediment is released with a discharge of 0.1 m³/s and a concentration of 1441.53 g/L at -6 m TAW (Belgian reference level, where 0 m TAW corresponds to low water at the sea at the Belgian coast). This corresponds to a release of 4.5 million tons TDS per year. Because the bottom is not update to the hydrodynamics, no effort is done to dredge sediment from the estuary. The point source is located near the actual disposal sites in the estuary (big green dot in Figure 1).

IV. RESULTS

A. Spin-up time sediment

Using pure S2 harmonic boundary conditions for the water levels (programmed in subroutine sl3.f as SL3 = 1.89D0 * SIN(AT * (2.D0 * PI/43200.D0) + (PI/2)) + 2.68D0) and constant discharges upstream the sediment was initialised in

the model on the bed for one simulation and the same amount of sediment was initialised in the water column as a concentration in another identical simulation. The mass balance is plotted in Figure 5. The results show that both simulations tend to go the same solution and that after two days already both solutions come together. After 20 days the sediment in both simulations reaches a kind of equilibrium condition. This setup also shows that the closer to the final solution a simulation is started, the shorter the spin-up time needs to be.

B. Ensemble analysis

At three locations in the estuary SSC continuous point measurements are done. The measured values are compared with model results by performing an ensemble analysis. Every tide separately within a 14 day period is analysed for water level and SSC and time is expressed as hours relative to high water level. For every hour before and after (relative) high water average SSC concentrations with an uncertainty band are determined and plotted. This is done for the measured time series and the model results. In this way the time period of the measurement does not to coincide with the time period of the simulation. The three locations are called Bouy 84, Oosterweel and Driegoten. The three locations are situated at km 73, 89 and 118 from the estuary mouth at Vlissingen respectively. For Bouy 84 and Oosterweel measurements were done both near the surface and near the bottom (0.8 m and 3.3 m above the bottom). For both locations the results are very satisfying as can be seen in Figure 6 and Figure 7.

At Driegoten however the model showed no intra-tidal variation in SSC (figure not shown).

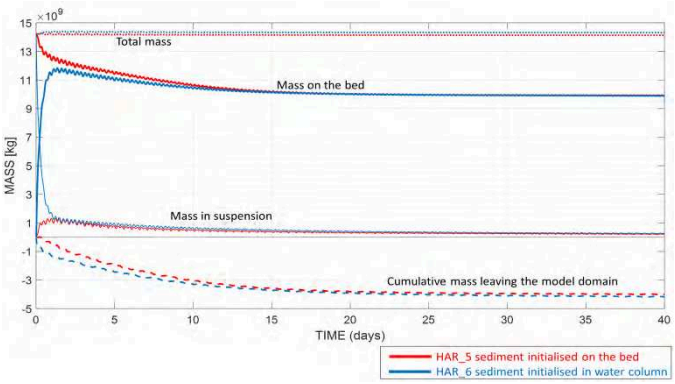

Figure 5 – Mass balance plot for simulation with sediment initialised on the bed and in the water column.

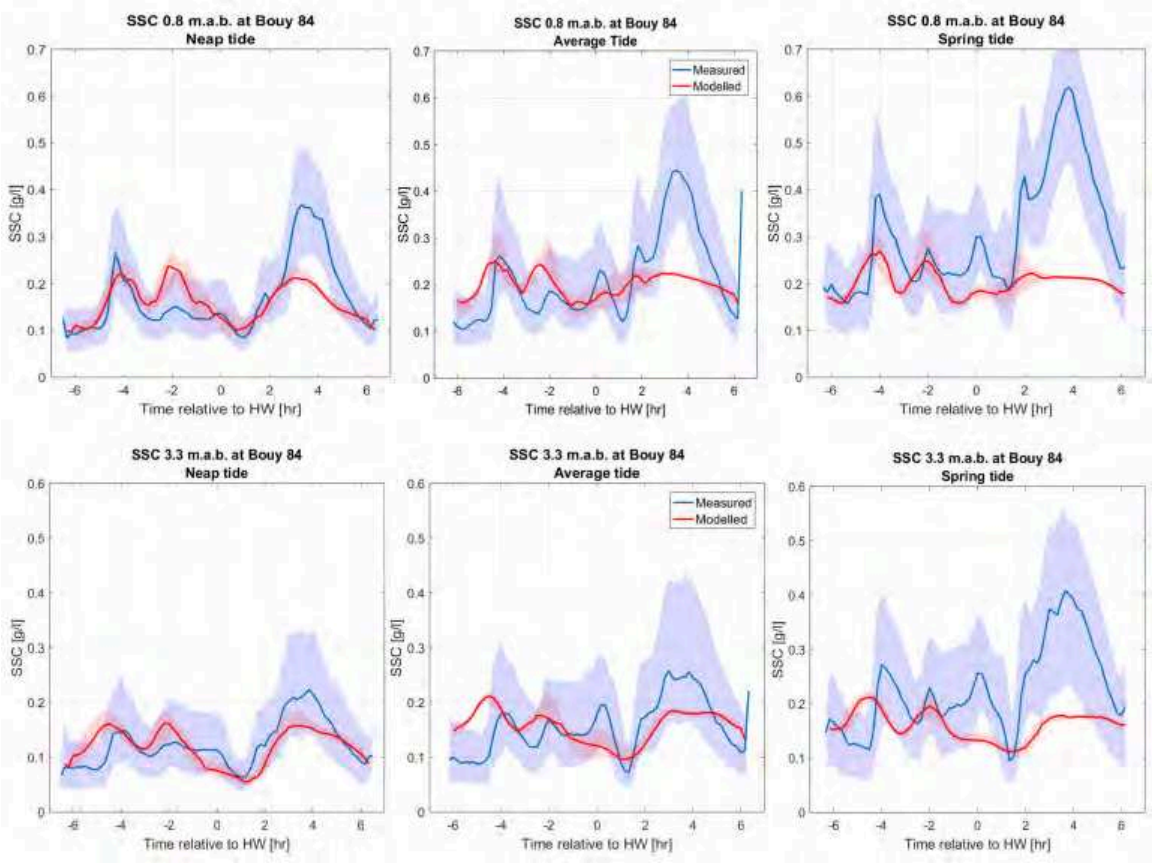

Figure 6 – Ensemble analysis results from model and measurements at Bouy 84

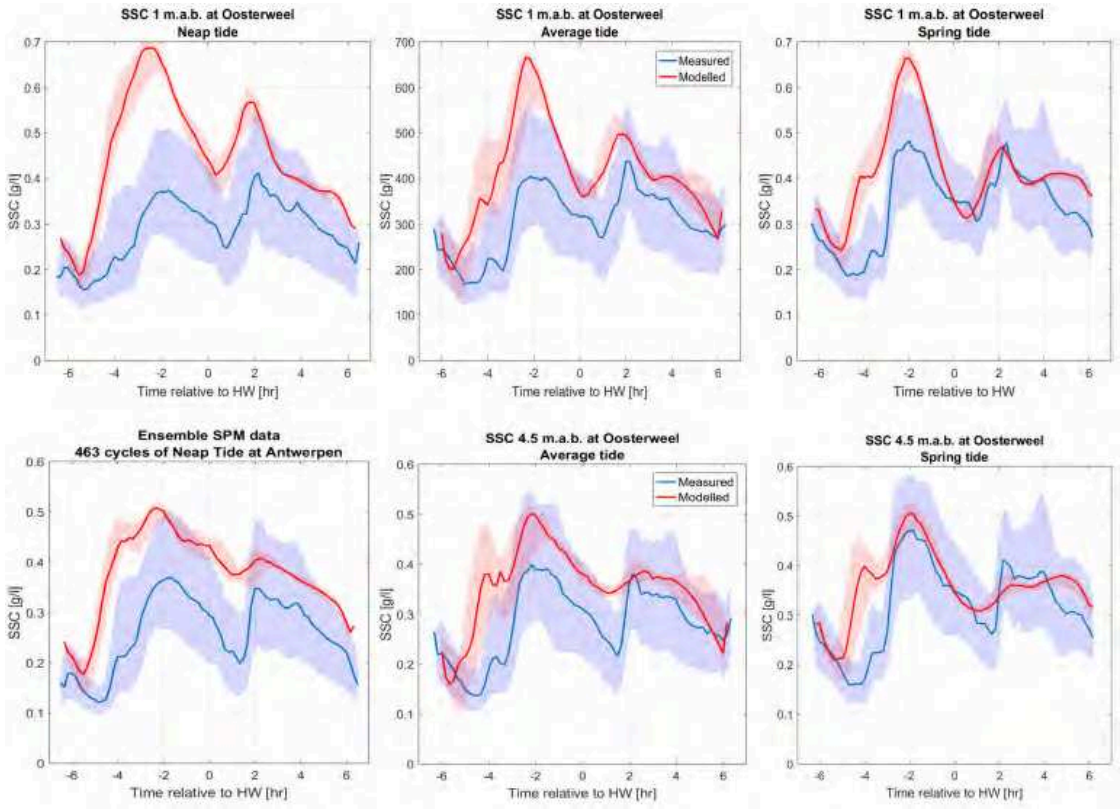

Figure 7 - Ensemble analysis results from model and measurements at Oosterweel

C. Estuarine turbidity maximum

When the results for SSC of the last 20 days of the simulation are averaged over time and over different cross sections and ETM is showing around Antwerp (km 80-90) (Figure 8). Depending on discharge events this location can be associated with higher SSC values in the real estuary.

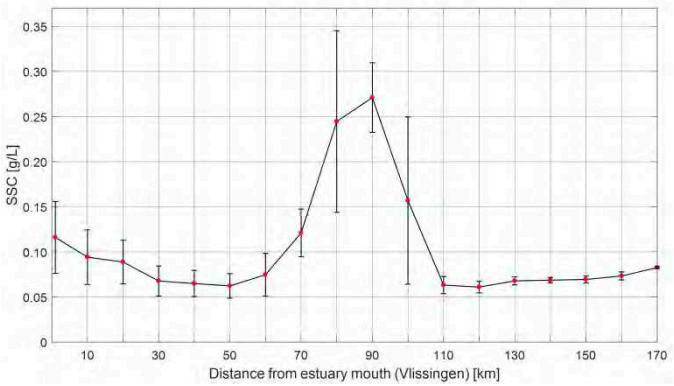

Figure 8 – cross sectional and time averaged SSC values along the Scheldt estuary showing an ETM

Figure 9 shows the same information as Figure 8 but with a higher spatial resolutions and for the different time steps of the simulation in the x-axis. This figure also shows the tide averaged location of the ETM and how it reacts on higher upstream discharge. In the lowest panel of the figure the tides on the boundary are given and the discharge over time of the most important discharge boundary upstream. The ETM moves a little downstream when the discharge upstream is increased.

D. Mass transfer map

Mud and sand transport over specific transect in the Sea Scheldt was estimated by [20] based on bathymetric surveys, lithological information of the bottom and dredging and dumping information. The estimated transports are values over a ten year period and here brought back to a one year averaged value. For the same transects the mud transport was calculated from the model results, i.e. for a full spring-neap tidal cycle. These results were then extrapolated to a one year period. Figure 10 shows the Sea Scheldt (Belgian part of the Scheldt Estuary) with the model results in yellow and transport directions over the transects indicated by yellow arrows. The grey values are the estimated values by [20]. For both the model and the estimated transport the directions over the specific transect was the same. But for most transects the model tends to overestimate the transport.

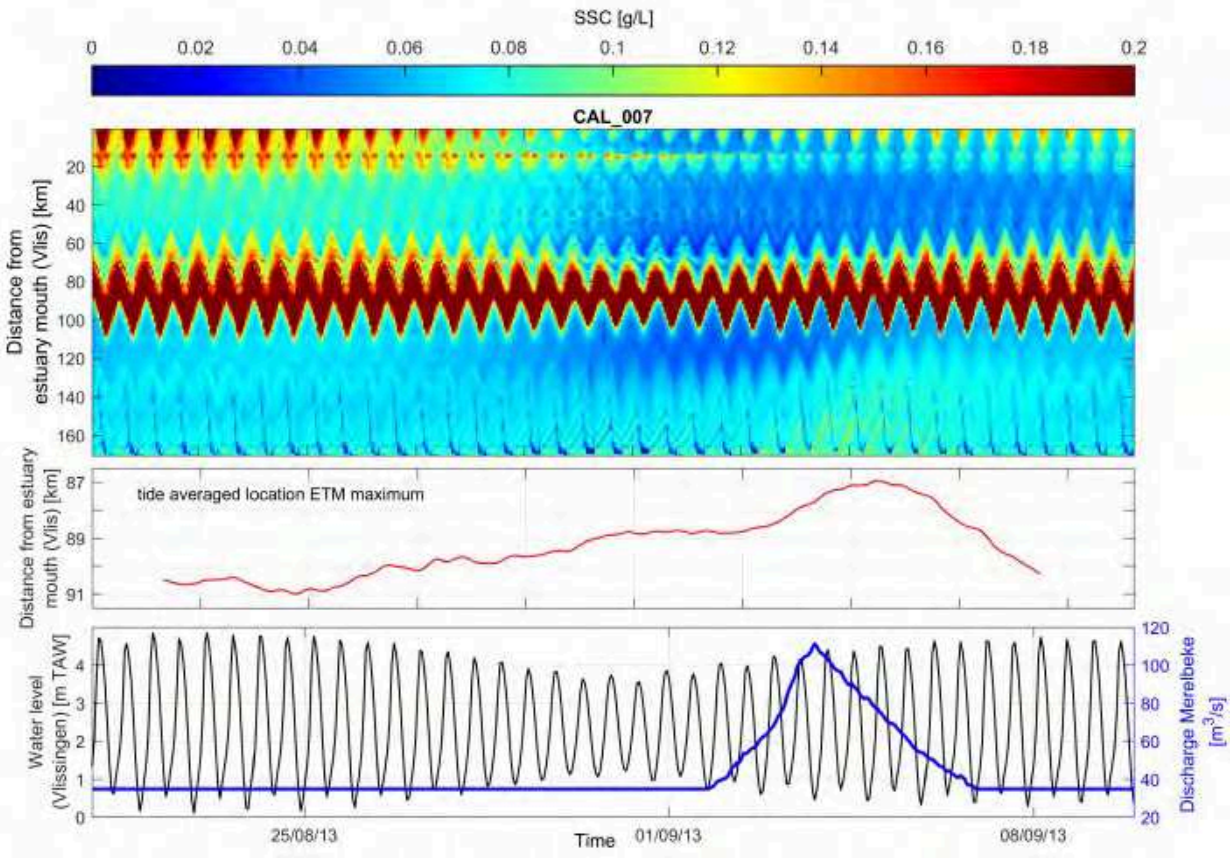

Figure 9 – Variation of SSC along the estuary in time.

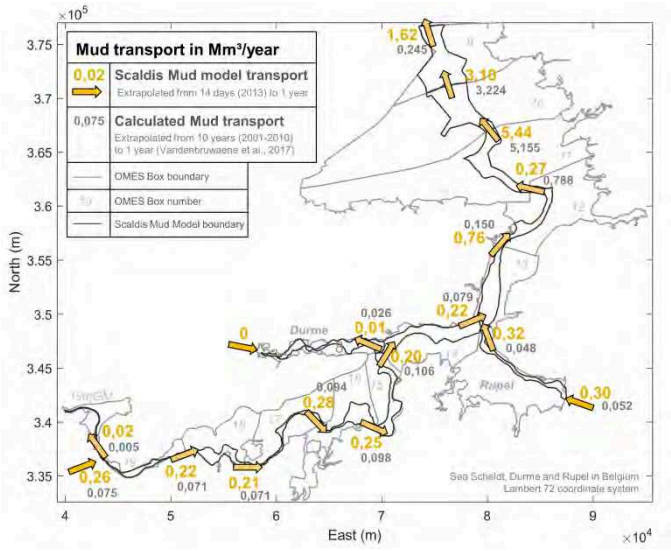

Figure 10 – Mud transport over specified transect in Mm³/year. Model results compared with estimated transports by [20]

E. Dredging and dumping number in the model

The model was able to reproduce similar amounts of sediments near lock entrances and tidal docks as dredged in reality.

V. DISCUSSION

A. Natural ETM

At first the results of the model look very good, but a sensitivity simulation without the sediment source (to compensate for dumping of dredged material) showed that the ETM is entirely dependent on this sediment source. Without this source the sediment coming in the estuary at the upstream boundaries is flushed out of the estuary. The local sediment source is also responsible for the weak response of this ETM on the increased discharge upstream. More work is needed to solve this issue. Probably the low settling velocity is the cause and maybe a second fraction of cohesive sediments with a higher settling velocity can improve the model. However higher settling velocities will increase the problem of excessive sedimentation in shallow areas.

B. Excessive sedimentation in shallow areas

In shallow areas the shear stress is too low to bring enough sediment back into suspension, resulting in excessive rate of deposition of sediment. using a sigmoid function to reduce the settling velocity in shallow areas fixed the problem of excessive deposition of cohesive sediment. The word "fixed" is deliberately used here, because it is not a solution to the problem, but a fix. The d_0 value in equation 10 is a modeller's choice and reduces settling velocity in water depths smaller than this d_0 value. However if circumstances change in the model, e.g. the concentrations increase a lot, excessive

deposition flux can be noticed in those location that have water depths just above d_0. In the existing mud model in DELWAQ this problem arose too and was fixed by adding extra shear stress caused by wind [2]. This shear stress is very high in shallow water and has less effect in the deep channel. More work is needed to find an correct solution for this problem.

VI. Conclusions

A first attempt was made to create a new cohesive sediment transport model for the Scheldt Estuary. The first results show good intra-tidal variation for some locations and almost no variation for other locations. An ETM was formed, but this was dependent on a local sediment source. The ETM had also a weak reaction on higher upstream discharges. Mud transport rates and transport directions over transect along the estuary is in agreement with earlier estimates. A problem with higher deposition than erosion flux in shallow areas was fixed by reducing the settling velocity in these areas. Further work is needed to find a more elegant solution for this problem.

For larger resolution and better figures the authors refer to [21], the report describing this mud model in full length and detail.

References

[1] van Engeland, T. and Buis K, "1D Ecosystem model of the Scheldt Estuary - Nutrient-Phytoplankton-Zooplankton dynamics in the pelagic - Description of the model and calibration for the reference situation", Report 018-R217, 2018, University of Antwerp, Antwerp, Belgium.

[2] van Kessel, T.; Vanlede, J.; Bruens, A. (2006). Development of a mud transport model for the Scheldt estuary in the framework of LTV: phases 1 and 2. Versie 1.0. Delft Hydraulics/Flanders Hydraulics Research: Delft. 79 + appendices pp.

[3] van Kessel, T.; Vanlede, J.; Kuijper, K.; de Kok, J. (2007). Further development and first application of a mud transport model for the Scheldt estuary: in the framework of LTV. Phase 2. Delft Hydraulics/Waterbouwkundig Laboratorium: Delft. 139 pp.

[4] van Kessel, T., J. Vanlede (2009). Impact of harbour basins on mud dynamics Scheldt estuary in the framework of LTV. Deltares & FHR report 1200253, Delft, The Netherlands.

[5] van Kessel, T.; Vanlede, J.; de Kok, J. (2011). Development of a mud transport model for the Scheldt estuary. Cont. Shelf Res. 31(10 SUPPL.). doi:10.1016/j.csr.2010.12.006

[6] Smolders, S.; Maximova, T.; Vanlede, J.; Plancke, Y.; Verwaest, T.; Mostaert, F. (2016). Integraal Plan Bovenzeeschelde: Subreport 1 – SCALDIS: a 3D Hydrodynamic Model for the Scheldt Estuary. Version 5.0. WL Rapporten, 13_131. Flanders Hydraulics Research: Antwerp, Belgium.

[7] Smolders, S.; Maximova, T.; Vandenbruwaene, W.; Coen, L.; Vanlede, J.; Verwaest, T.; Mostaert, F. (2017). Integraal Plan Bovenzeeschelde: Deelrapport 5 – Scaldis 2050. Version 4.0. FHR Reports, 13_131_5. Flanders Hydraulics Research: Antwerp.

[8] Smolders, S.; Maximova, T.; Vanlede, J.; Teles, M.J. (2014). Implementation of controlled reduced tide and flooding areas in the TELEMAC 3D model of the Scheldt Estuary, in: Bertrand, O. et al. (Ed.) Proceedings of the 21st TELEMAC-MASCARET User Conference,15th-17th October 2014, Grenoble – France. pp. 111-118

[9] Y. Yorozu, M. Hirano, K. Oka, and Y. Tagawa, "Electron spectroscopy studies on magneto-optical media and plastic substrate interface," IEEE Transl. J. Magn. Japan, vol. 2, pp. 740–741, August 1987 [Digests 9th Annual Conf. Magnetics Japan, p. 301, 1982].

[10] Sanford, L.P.; Halka, J.P. (1993). Assessing the paradigm of mutually exclusive erosion and deposition of mud, with examples from upper Chesapeake Bay. Mar. Geol. 114: 37–57

[11] Winterwerp, J.C. (2007). On the sedimentation rate of cohesive sediment. Proc. Mar. Sci. ISBN 9780444521637 209–226. doi:10.1016/S1568-2692(07)80014-3

[12] Le Hir, P.; Cayocca, F.; Waeles, B. (2011). Dynamics of sand and mud mixtures: A multiprocess-based modelling strategy. Cont. Shelf Res. ISBN 0278-4343 31(10 SUPPL.). doi:10.1016/j.csr.2010.12.009

[13] van Maren, D.S.; Winterwerp, J.C.; Vroom, J. (2015). Fine sediment transport into the hyper-turbid lower Ems River: the role of channel deepening and sediment-induced drag reduction. *Ocean Dyn.* ISBN 1023601508 *65*: 589–605. doi:10.1007/s10236-015-0821-2

[14] van Leussen, W., 1994. Estuarine Macroflocs: Their Role in Fine grained Sediment Transport. Universiteit van Utrecht, the Netherlands.

[15] Winterwerp, J., 2002. On the flocculation and settling velocity of estuarine mud. Continental Shelf Research 22, 1339-1360.

[16] Lee, B.J., Toorman, E., Molz, F.J. and Wang, J., 2011. A two-class population balance equation yielding bimodal flocculation of marine or estuarine sediments. Water research, 45(5), pp.2131-2145.

[17] Van Hoestenberghe, T.; Ferket, B.; De Boeck, K.; Vanlierde, E.; Vanlede, J.; Verwaest, T.; Mostaert, F. (2014). Slibbalans Zeeschelde: Deelrapport 2 – Sediment load for the river Scheldt and its main tributaries (1972-2009). Versie 5.0. WL Rapporten, 00_029. Waterbouwkundig Laboratorium & Antea Group. Antwerpen, België.

[18] Fettweis, M., Nechad, B., & Van den Eynde, D. (2007). An estimate of the suspended particulate matter (SPM) transport in the southern North Sea using SeaWiFS images, in situ measurements and numerical model results. Continental Shelf Research, 27(10-11), 1568-1583.

[19] Santermans, J. (IMDC). (2013). In Dutch: Maintaining navigation channels in the Scheldt Estuary; environmental licenses for disposal of dredged sediments. "Instandhouding Vaarpassen Schelde Milieuvergunningen terugstorten baggerspecie." LTV - Veiligheid en Toegankelijkheid. Baggeren en storten Achtergrondrapport A-31

[20] Vandenbruwaene, W.; Vanlede, J.; Plancke, Y.; Verwaest, T.; Mostaert, F. (2016). In Dutch: Mud balance for the Sea Scheldt: historical evolution of SSC. "Slibbalans Zeeschelde: Deelrapport 4 – Historische evolutie SSC." Versie 6.0. WL Rapporten, 00_029_4. Waterbouwkundig Laboratorium & Antea: Antwerpen.

[21] Smolders, S.; Bi, Q.; Vanlede, J.; De Maerschalck, B.; Plancke, Y.; Schramkowski, G.; Mostaert, F. (2018). Integraal plan Boven-Zeeschelde: Sub report 6 – Scaldis Mud: a Mud Transport model for the Scheldt Estuary. Version 4.0. FHR Reports, 13_131_6. Flanders Hydraulics Research: Antwerp.

Influence of the layer model on a 2D sediment transport model: Hirano-Ribberink versus C-VSM

Birgit Bleyel, Rebekka Kopmann
Hydraulic Engineering in Inland Areas, Bundesanstalt fuer Wasserbau (BAW), Karlsruhe, Germany
birgit.bleyel@baw.de; rebekka.kopmann@baw.de

Abstract— **With the possibilities introduced by the new C-VSM layer model, which provides continuous vertical grain sorting, it is essential to identify its impact on simulation results in comparison to the classical Hirano-Ribberink layer concept, which is the default layer model implemented in SISYPHE. To this goal, comparisons between field observations and numerical results obtained with both models are proposed.**

The comparisons were done with a two-dimensional sediment transport model consisting of a 46.5 km reach of the river Rhine. Numerical results using the Hirano-Ribberink layer model for a time period of six years (2000 – 2006) was not fully satisfying. Simulated evolutions were considerably underpredicted in comparison with the field measurements and the computed mean sediment diameter becomes coarser over time. Consequently, the transport rate prediction decreases.

Numerical results performed with the C-VSM model show no tendency to coarsen the mean grain diameter and the sediment transport is increased compared to the Hirano-Ribberink layer model. On the other hand, the computing time is quadrupled using C-VSM. This disadvantage could be damped by using twice as much parallel processors which leads to a doubled computing time.

I. Introduction

In morphodynamic modelling of inland rivers, the vertical distribution of the sediments influences the sediment transport behaviour. This is obvious in case of armouring, when coarse grains which cover the underlaying finer sediments prevent further erosion. Furthermore the sediment distribution in the uppermost sediment layer (the so called active layer) determines the current sediment transport. It is assumed that the hydrodynamic influences this active layer in such a way that it can be handled as fully mixed. A thinner active layer will speed up the process of armouring more than a thicker one. Several approaches calculating the active layer thickness are available e.g. [1]. Based on the authors' experience calculated active layer thicknesses often leads to numerical issues. Therefore constant values for the active layer thickness are preferred for practical applications. Furthermore active layer thickness is one of the most sensitive parameters behind the roughness parameter and the sediment grain sizes e.g. [2].

As morphodynamic is a slow process compared to hydrodynamics also the vertical distribution of sediment changes slowly. On the other hand the sediment distribution in the active layer adapts relatively fast to the simulated current hydrodynamics. The sediment distribution in the deeper layers also referred to as "sediment memory" stores the sediment distribution for a long time. Only in case of deep erosion the layers beyond the first two layers are modified. This means that the initial vertical sediment distribution influences the sediment transport significantly over a long period usually longer than the simulation period. So it is important to start with a best guessed initial distribution. The longer the simulation period the more decreases the influence of the initial vertical distribution and the more increases the influence of the numerically build vertical sediment distribution. Too much mixing processes or too less vertical resolution due to an insufficient modelling of the vertical sediment distribution can result in e.g. too coarse mean grain sizes. But modelling a proper vertical distribution is important especially for long term simulation.

In the following section, the two layer models available in SISYPHE (Hirano-Ribberink and C-VSM models), are presented briefly. In section III the 46.5 km Rhine model is introduced. This model was calibrated using Hirano-Ribberink model. The results are compared in section IV with simulations using the C-VSM model.

II. Vertical Layer Modelling in Sisyphe

A. Hirano-Ribberink model

The Hirano-Ribberink layer model [3], [4] is the default option in SISYPHE. The basic concept behind this model is a fully mixed top most active layer which interacts with the hydrodynamic. With the current sediment distribution a bed load discharge for each sediment class is calculated which can result in sedimentation or erosion per class. The sediment body below the active layer up to the rigid bed can be discretised by a selectable number of additional layers. The layer below the active layer is called stratum. The height of the active layer can be set as constant or it can be dynamically computed. The stratum is increasing or decreasing according to the sediment deposition or erosion processes. The underlaying layers are not involved in the sediment transport processes. If a layer is destroyed due to erosion processes it cannot be built again except for the active layer and the stratum.

In case of sediment deposit (Fig. 1) the new sediment is mixed into the active layer, which is temporarily enlarged by the height of the deposit. The newly mixed active layer is split into the height of the active layer and the enlarged part. The enlarged part is combined with the stratum. This procedure enlarges the stratum layer. In case of erosion (Figure 2) the eroded sediments are taken out of the active layer. This can result in a new sediment mixture of the active

layer. To restore the calculated or constant height of the active layer part of the stratum is mixed into it. If the cumulated erosion is larger than the stratum the former layer 3 becomes the new stratum.

B. Continuous Vertical Sorting model (C-VSM)

The C-VSM is based on the work of Astrid Blom et al. [5], [6] and was adapted and implemented in SISYPHE by Uwe Merkel. It is available since version V6P3. Detailed information can be found in [7], [8] and [1]. Each sediment class has its own continuous vertical grain sorting profile, which is discretised by a user defined maximum number of sections.

For the interaction with SISYPHE the current sediment distribution over the active layer thickness is temporarily mixed at every time step. As for the Hirano-Ribberink model bed load discharges per sediment class and sedimentation or erosion per class are calculated.

In case of sedimentation (Figure 3) the new sediment is added on top of the vertical sediment stratification. The vertical profile of each deposited class gets a new section on top. If the maximum number of section is reached sections are combined with a modified version of the line generalization algorithm proposed by Douglas and Peuker [9].

In case of erosion (Figure 4) the eroded classes are taken from the vertical sediment stratification.

An advantage to this model is that the only mixing process in the C-VSM model is the mixing of the active layer. But this mixing is only temporarily and does not modify the original vertical distribution. This is preserved and all sedimentation or erosion processes base upon this distribution.

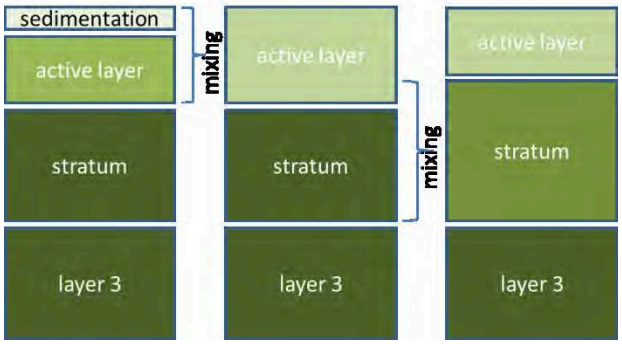

Figure 1: Sedimentation procedure for Hirano-Ribberink model in SISYPHE.

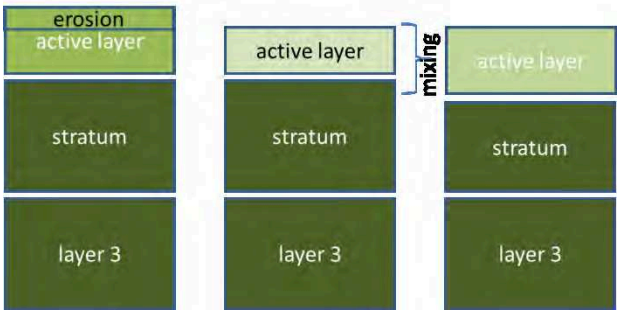

Figure 2: Erosion procedure for Hirano-Ribberink model in SISYPHE

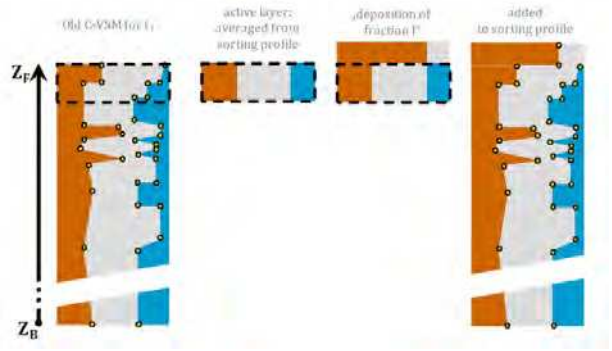

Figure 3: Sedimentation procedure for C-VSM model in SISYPHE. Figure taken from [7].

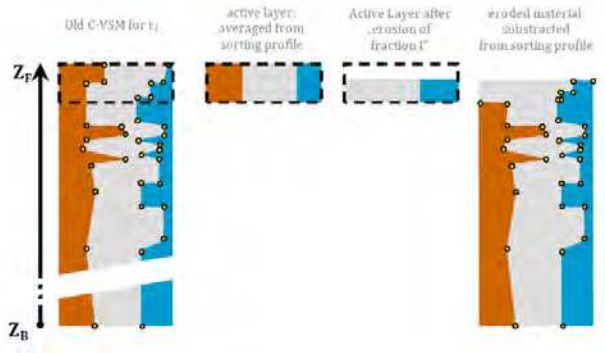

Figure 4: Erosion procedure for C-VSM in SISYPHE. Figure taken from [7]

III. RHINE MODEL

The comparison between the two layer models have been done with a 46.5 km long TELEMAC2D-SISYPHE model for the middle Lower Rhine from Rhine-km 730 near Neuss to 776.5 near Duisburg (see Figure 5). The model consists of about 260,000 nodes and was calibrated for a period of 6.5 years of the natural hydrograph 1.1.2000 - 22.6.2006. On a parallel cluster at BAW (Intel(R) Xeon(R) Gold 6138 CPU) the computing time is about 1.5 days for this simulation period using 160 processors respectively subdomains.

The grid resolution with node distances between 5-50 m allows a proper reproduction of the groyne geometry as well as the analysis of artificial bed load supply, bed evolution and bed-load transport.

The most important parameters for the hydrodynamic and morphodynamic simulations are listed below.

- Hydrodynamic time step: 4 s, morphological factor 4
- Nikuradse friction law, four different friction zones
- Elder turbulence model
- Multi-grain (10 sediment classes for bed load transport and if necessary 10 sediment classes to follow the artificial bed load supply), Hirano-Ribberink multi-layer model (3 layers, constant active layer thickness: 0.1 m)
- Meyer-Peter und Müller transport formula; Karim, Holly, Yang hiding exposure formulation
- Soulsby and Talmon slope effect formulation
- Secondary currents approach for hydrodynamics and morphodynamics, with the radius of curvature provided in an additional file
- Bed load management module NESTOR to consider artificial bed load supply and dredging procedures
- The sediment distribution is initialized by a pre-simulation over a period of 6.5 years starting with equal fractions for all sediment classes. The time averaged sediment distribution of the active layer is transferred to the other layers.

IV. Comparison Hirano-Ribberink vs C-VSM in SISYPHE

The Rhine model described in section III using the default layer model was taken as base scenario for the comparison between the Hirano-Ribberink model and the C-VSM model. The only difference between the two models is the choice of the layer model. The initial vertical distribution of the sediment body was the same for both models. For the C-VSM the influence of the vertical discretisation was investigated. A set of three different maximum sections numbers (25, 100 and 200) were tested. All are less or just even to the recommendation of 200 – 500 [1].

The smallest sections number produces instabilities of the bottom evolutions (peaks). The highest sections number took too much computation time for project needs. The results with 100 maximum sections number look plausible. Therefore this choice seems a good compromise between computation time and quality of results for this investigation.

No extra calibration was done for the C-VSM model even though the results are not in a good agreement with the measurements as this was not the aim of this study. Of course this must be done if the C-VSM model should be used instead of the Hirano-Ribberink model for project purposes.

Figure 5: Model area in the middle Lower Rhine. The flow direction is from South to North.

The hydrograph of the simulation period is shown in Figure 6. The annual averaged discharge (red line) illustrates that the years 2000 and especially 2001 - 2002 are wet years followed by four dry years 2003 - 2006.

In Figure 7 the simulated bottom evolution for the simulation period (2000 – 2006) is compared with field measurements. The simulated and measured bottom evolutions were averaged over the sounding width and along 1.1 km of the river stretch. The simulated bottom evolutions fit acceptable to the measurements considering measurement uncertainties and the comparably small changes. For the regions with bed load management actions (grey areas) the agreement is less satisfying as the simulated evolutions are mostly too big. Additionally the erosion area between Rh-km 755 and 765 which is the cause for the artificial bed load supply cannot be correctly represented in the numerical model.

A reason for that could be the coarsening tendency of the model which results in less erosion. Figure 8 shows the averaged grain size distribution in the active layer for the initial state and after 6.5 years simulation period. All

fractions for all sediment classes were initialized equally. But at some regions only the largest grain size was available due to scour protections measures. This leads to a slight increase of the averaged initial fractions for the coarsest sediment class.

The coarsening tendency after 6.5 years is clearly visible. The fractions of the smaller sediment classes were decreased while the coarser sediment classes were increased. The mean grain size in the active layer averaged over the bed load active area increased from 20.1 to 24.6 mm during the total simulation time.

Varying nearly every calibration parameter did not enhance the results significantly. E.g. a refined discretization of the vertical structure of the sediment body produced an even stronger coarsening effect. In Figure 9 the simulated annual solid discharges 2000 – 2006 with 3 and 5 layers using the Hirano-Ribberink model are compared. In both cases the active layer (constant 0.1 m) and the last layer (initially 98.9 m) are the same. For the 3-layer variant the stratum is about seven times larger (1 m instead of 0.15 m). The small thickness of the stratum promoted the coarsening effect. The layers 3 and 4 as possible new stratum layers if the original stratum is destroyed have also smaller thicknesses (0.3 and 0.55 m). With the refined vertical discretization of 5 layers the calculated annual solid discharges along the river stretch (dotted lines) were significantly smaller than for the 3-layer model (solid lines). Instead of enhancing the model the coarsening was increased by using more and finer layers.

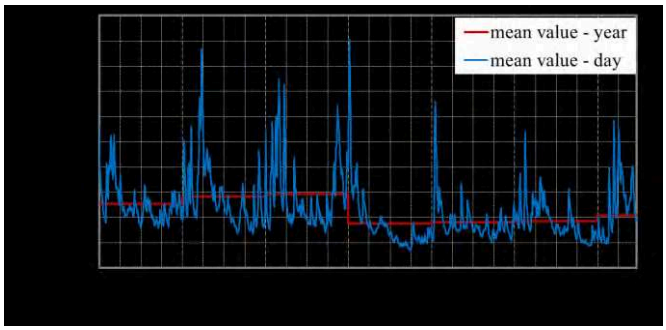

Figure 6: Hydrograph of simulation period

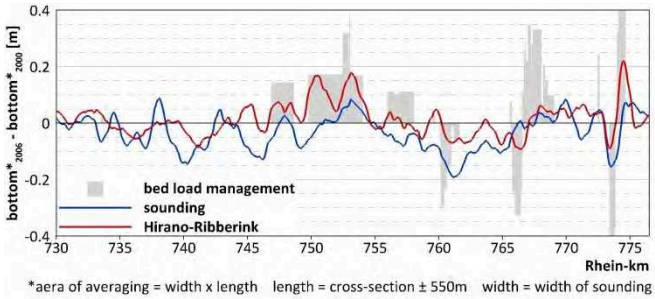

Figure 7: Measured and simulated bottom evolution for the simulation period (2000 – 2006) averaged for the width of the sounding and 1.1 km along river stretch.

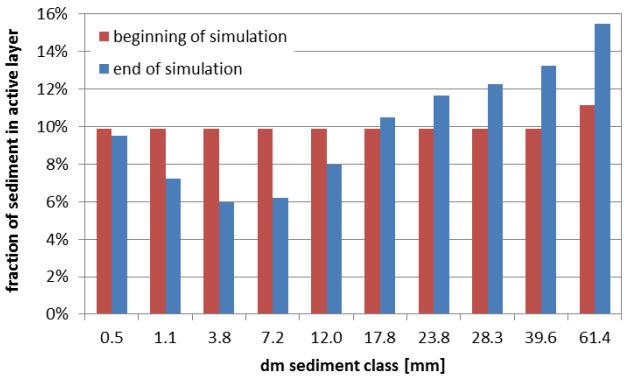

Figure 8: Simulated mean fraction of sediment classes for the active layer.

The development of the coarsening effect and the problem for long-term simulations can be seen in Figure 10. As expected the solid discharge is higher for wet years and smaller for dry years (compare the annual averaged discharges in Figure 6). A clear coarsening tendency due to simulation duration could not be proven. For better evidence the same hydrograph is used for a second simulation. This simulation is identical with the first run except for the sediment fractions in the beginning, which derive from the final vertical sediment distribution of the first run (dotted line). All annual discharges of the second hydrograph have smaller values. Also the variation of the solid discharge along the river stretch decreases with the simulation duration. These results confirm the coarsening tendency by simulation duration of the Hirano-Ribberink model.

This behavior of the Hirano-Ribberink model in SISYPHE hinders successful long-term simulation in the present project. For project studies simulation periods of 10 to 20 years or longer are needed. In order to solve this problem the second layer model C-VSM was tested.

With C-VSM a successful simulation run of the 6.5 years simulation period could be managed. Again the averaged grain size distribution in the active layer for the initial state and after 6.5 years simulation period was analyzed (Figure 11). The averaged fractions applying C-VSM doesn't change much within the simulation period. Instead of a coarsening as with Hirano-Ribberink the initial mean grain diameter of 20.1 mm decreases minimal to 19.7 mm during the 6.5 years.

Figure 12 shows the results of the first and second simulation period analogous to the simulations for Figure 10 with the C-VSM model. The annual solid discharges simulated with C-VSM but the same parameter set as the original model are generally higher than with the Hirano-Ribberink model. The annual solid discharges do not differ much between the first or second simulation run. The variation of the solid discharge along the river stretch is higher compared to the Hirano-Ribberink results. All three observations confirm that the C-VSM model has no coarsening tendency.

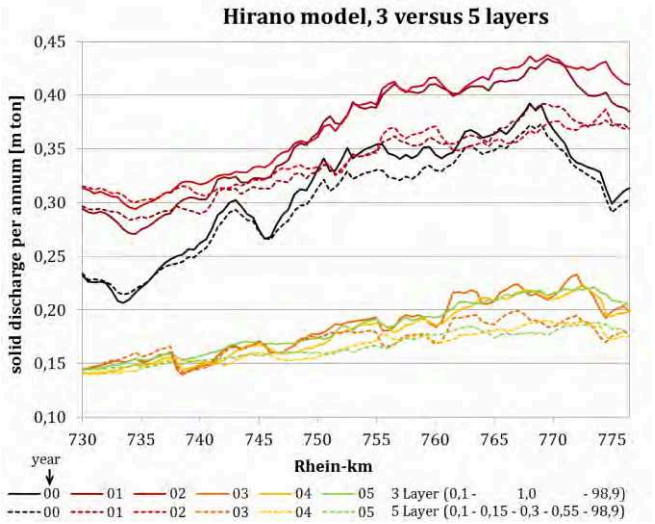

Figure 9:Comparison of simulated annual solid discharge with Hirano-Ribberink model using 3 and 5 vertical layers

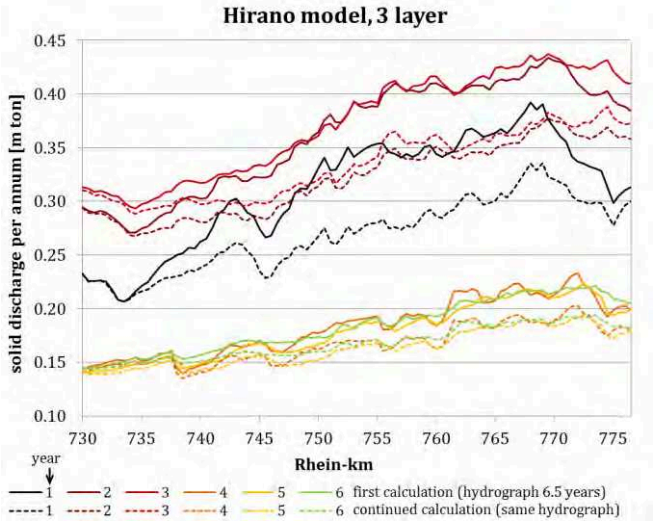

Figure 10: Simulated annual solid discharge with Hirano-Ribberink model (dotted lines: started with sediment fractions from the end of the first run).

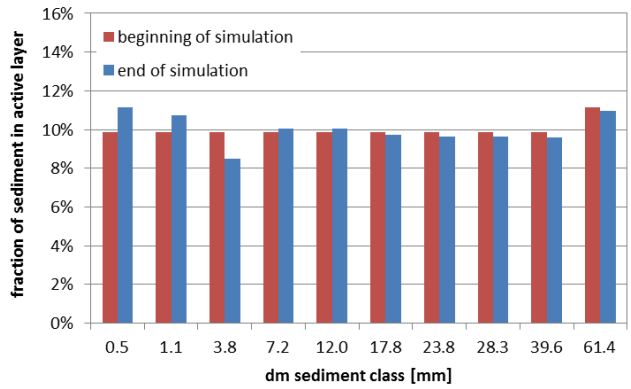

Figure 11: Simulated mean fraction of sediment classes for the active layer using C-VSM.

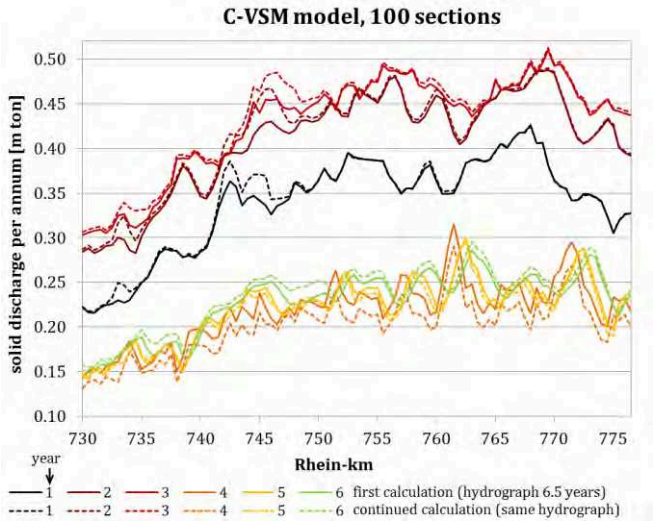

Figure 12: Simulated annual solid discharge with C-VSM model (dotted lines: started with sediment fractions from the end of the first run).

V. CONCLUSIONS AND OUTLOOK

The default layer model in Sisyphe (Hirano-Ribberink model) tends to coarsen the sediment distribution in time. Especially for long-time simulation the calculated mean grain sizes correspond not longer to the natural conditions and the sediment transport decreases in time. This tendency cannot be compensated by calibration.

First investigations with a 46.5 km Rhine model could not detect a coarsening tendency with the C-VSM model. So this model could be a better choice for long-term simulations in SISYPHE than the Hirano-Ribberink model. Nevertheless much more experiences have to be collected with the new layer model to verify its usability for project work. Next steps will be the calibration of the C-VSM model to the measurements. Even if there is no numerically driven coarsening there is no automatically mechanism that the C-VSM model is able to reproduce the erosion region between Rh-km 755 -765.

Furthermore the C-VSM model is computationally costly. It needs about four times more computing time than the Hirano-Ribberink model using a maximum sections number of 100. This could be reduced to two times if the number of processors is doubled. This increase in computation time is barely possible for long-time simulations. Further investigations are needed to proof that 100 maximum sections number produce comparable results than the recommended 200 – 500. The expected computation times can only be handled using restart functionality as the parallel cluster queues at BAW are limited.

VI.

ACKNOWLEDGEMENT

The authors thank Uwe Merkel for providing Figs. 3 and 4.

REFERENCES

[1] Merkel, U. “C-VSM-II: Large Scale and Long Time Simulations with Sisyphe’s Continuous Vertical Grain Sorting Model,” Proceedings 24thTelemac-Mascaret User Conference 17.-20.Oct. 2017, Graz, Austria, Eds.: Clemens Dorfmann, Gerald Zenz.

[2] Kopmann, R., Brudy-Zippelius, T. “Using reliability methods for quantifying uncertainties in a 2D-morphodynamic numerical model of river Rhine,” Water infinitely deformable but still limited. Proc. of the 2nd IAHR European Congress, 27. – 29.6.2012, TU München. Eds.: Rutschmann, P., Grünzner, M., Hötzl, S.. München: Eigenverlag, Lehrstuhl u. Versuchsanstalt f. Wasserbau u. Wasserwirtschaft d. TU München, 2012, USB-Stick, ISBN 978-3-943683-03-5; www.iahr2012.tum.de.

[3] Hirano, M. “River bed degradation with armouring,” Proceedings Japan Society of Civil. Engineers 195. 1971

[4] Ribberink, JS. “Mathematical modelling of one-dimensional morphological changes in rivers with non-uniform sediment,” Delft University of Technology. 1987

[5] Blom, A. “A vertical sorting model for rivers with non-uniform sediment and dunes”. Ph.D. thesis. University of Twente (NL). 2003

[6] Blom, A.,;Ribberink, J. S. ; Parker, G. “Vertical sorting and the morphodynamics of bed form – dominated rivers: A sorting evolution model”, J. Geophys. Res., doi:10.1029/2006JF000618. 2008

[7] Merkel, U., “A continuous sediment layer concept for Sisyphe,” 18thTelemac-Mascaret User Club 19.-21.10.2011, Chatou, France, Eds.: Violeau, D., Hervouet, J.-M., Razafindrakoto, E., Denis, C..

[8] Merkel, U. H.; Kopmann, R., “Continuous Vertical Grain Sorting for TELEMAC & SISYPHE v6p2,” Proceedings XIXth TELEMAC-MASCARET User Conference, Oxford, UK, October 18-19, 2012. Wallingford: HR Wallingford. S. 9-17, Eds.: Bourban, S., Durand, N., Hervouet, J.-M.

[9] Douglas, D., Peucker, T., “Algorithms for the reduction of the number of points required to represent a digitized line or its caricature,” In: The Canadian Cartographer. Bd. 10, Nr. 2, 1973, ISSN 0008-3127, S. 112–12

Sensitivity analysis of secondary currents in Telemac-2D: a study case at the Danube River

Audrey Valentine, Manuela Baron,
Guilherme Dalledonne
Department of Hydraulic Engineering
Federal Waterways Engineering and Research Institute (BAW)
76187 Karlsruhe, Germany
audrey.valentine@baw.de

***Abstract*—Numerical investigations using TELEMAC-2D on a German waterway section of the Danube River, have raised the question over the inclusion of secondary flow parameterization, in particular in the strongly-curved region known as the Mühlhamer Oxbow. Currently the secondary currents parameterization is not widely used, primarily due to lack of experience with the recommended values for the empirical parameters in (large) rivers. For this purpose, a study was performed to investigate result sensitivity in relation to the empirical constants' selected values from secondary flow parameterization in TELEMAC-2D.**

I. INTRODUCTION

In curved channels and river bends secondary flow effects introduce cross-channel water level gradients and flow circulation. This also has an important effect on the sediment transport and morphology in river bends. In depth-averaged (2D) models, these effects can only be included in a parameterized way, by modifying the streamwise velocity distribution and the bottom shear stress e.g. [1].

In a project at the Bundesanstalt für Wasserbau (BAW) on the Danube river a TELEMAC-2D model is used for predicting water levels, navigation depth, flow velocities and at a later stage also sediment transport and morphological changes (coupled with the module SISYPHE), with the aim to optimize ship navigability and sediment management. The river reach under consideration is the last free-flowing, without weirs and canal walls, German waterway section of the Danube River, which includes several strong bends, in particular in the region known as the Mühlhamer Oxbow. In comparison to measurements, it was found that the largest deviations occurring in the model are located in the strong bends. For this purpose, the question was raised whether the depth-averaged model could be improved by including the secondary-flow method, developed by [2]. In contrast to the already existing approach for secondary flow based on the Engelund model [3], this method does not only influence sediment transport processes but also the flow field.

The aim of this paper is two-fold: Firstly, to investigate whether the quality of the numerical model can be improved by incorporating the secondary currents (SC) parameterization. Secondly, to quantify how sensitive the model results are in regard to the two calibration parameters introduced by the method.

II. MATERIALS AND METHODS

In [2], Wang and Tassi describe the newly-implemented approach for including the effect of secondary flow in TELEMAC-2D, based on the method originally developed by [4].

In this method, the secondary flow effect is included in the governing equations as an additional force or acceleration, based on an enhanced shear stress which depends on the streamwise vorticity Ω. The vorticity is computed from a separate transport equation:

$$\frac{\partial \Omega}{\partial t} + u\frac{\partial \Omega}{\partial x} + v\frac{\partial \Omega}{\partial y} = \frac{A_s\sqrt{C_f}|\boldsymbol{u}|^2}{Rh\left(1+\frac{9h^2}{R^2}\right)} - D_s\sqrt{C_f}\Omega\frac{|\boldsymbol{u}|}{h} + \frac{1}{h}\nabla(\nu h\nabla\Omega) \quad (1)$$

where t represents time, u and v are the Cartesian components of the flow velocity vector u, h is the water depth, C_f is a friction coefficient, R is the local radius of flow curvature, ν is the (turbulent) viscosity and A_s and D_s are both empirical coefficients.

In (1), the second and third terms on the left-hand side correspond to the advection of vorticity, the first and second terms on the right-hand side correspond respectively to the production and dissipation of vorticity where the third term on the right encapsulates the (turbulent) diffusion of vorticity.

The local radius of curvature R is computed from, an approximation of the streamline [4]:

$$R = \frac{|\boldsymbol{u}|^3}{uv(v_y-u_x)+u^2v_x-v^2u_y} \quad (2)$$

Above v_y, u_x, v_x und u_y represent the spatial derivatives of u and v. After computation of the vorticity Ω from (1), the

enhanced bed shear stress (due to secondary flow) is computed as:

$$\tau_s = \varrho h|\boldsymbol{u}|\Omega\sqrt{C_f} \quad (3)$$

where ρ represents fluid density. Finally, the acceleration **S** that is used as additional 'forcing' in the momentum equations is computed (in a Cartesian coordinate system) as:

$$\boldsymbol{S} = (S_x, S_y) = \frac{1}{\varrho}\frac{\boldsymbol{u}}{|\boldsymbol{u}|}\left(\frac{v(h\tau_s)_x - u(h\tau_s)_y}{|\boldsymbol{u}|} + \frac{2h\tau_s}{R}\right) \quad (4)$$

Further details can be found in [2] and [4].

It can be seen that the vorticity equation contains a production and a dissipation term, with two empirical coefficients A_s and D_s, respectively. These coefficients have default values in TELEMAC-2D A_s = 7.071 and D_s = 0.5.

In Section III, the sensitivity to these empirical coefficients is investigated.

III. NUMERICAL TESTS AND SENSITIVITY ANALYSIS

For this study a pre-existing 70 km long 2D hydro-numerical model was used. The model applies the Elder turbulence model [5] and advection is computed using the MURD Scheme (*TYPE OF ADVECTION = 14*) [6]. A spatially-varying bed roughness is prescribed, based on an earlier model calibration, which did not include SC parameterization.

The river topography was integrated from sonar measurements dating from 2014. Two measurement campaigns were also selected from March and August 2014, corresponding respectively to low and high water levels. The water level and velocity distribution were evaluated at seven cross-sections. In this work, only three cross-sections at Danube-km 2272.9, 2270.3 and 2252.0 are shown.

The secondary flow option in TELEMAC-2D was switched on using the following changes to the steering file:

SECONDARY CURRENTS = YES
TYPE OF ADVECTION = 14; 5; 14

Here the third entry on the line of the *TYPE OF ADVECTION* keyword corresponds to the type of advection scheme used for the vorticity in (1).

Starting with the TELEMAC-2D default empirical values for secondary currents:

PRODUCTION COEFFICIENT FOR SECONDARY CURRENTS =7.071
DISSIPATION COEFFICIENT FOR SECONDARY CURRENTS = 0.5

a sensitivity analysis was carried out. The analysis was done in multiple steps. First, cross-sectional distribution of the streamwise velocity was adjusted to meet the distribution of the measured data. Next, the local roughness was adjusted to re-obtain a better agreement of simulated and measured water levels.

A comparison was carried out by calculating the normalized root-mean-square error (NRMSE) for the different velocity profiles obtained using the different settings. The NRMSE is calculated as the ratio of the RMSE and the standard deviation of measured data:

$$NRMSE = \frac{\sqrt{\sum(Y_i^{obs} - Y_i^{sim})^2}}{\sqrt{\sum(Y_i^{obs} - \overline{Y^{obs}})^2}} \quad (5)$$

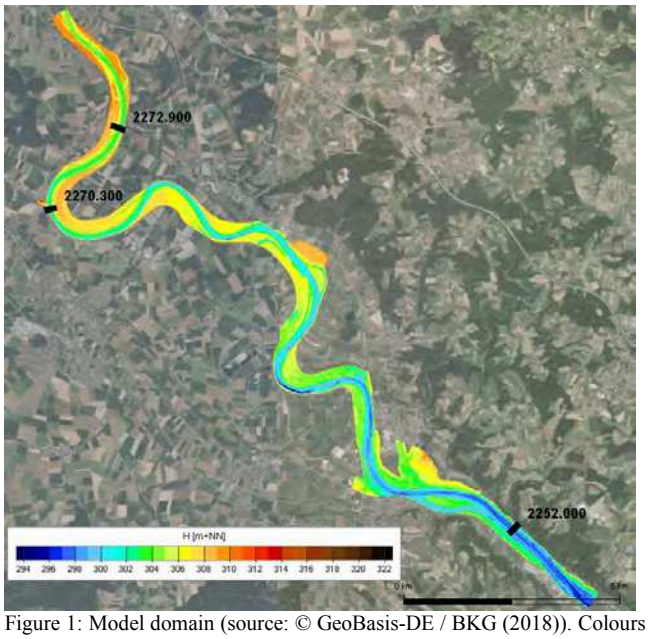

Figure 1: Model domain (source: © GeoBasis-DE / BKG (2018)). Colours indicate the water level (m+NN).

Sensitivity analysis of numerical models investigates the relationship between model outputs and model input parameters. This kind of analysis allows modellers to determine which input parameters contribute the most to output variability, which input parameters are less significant and can be neglected in the calibration process.

Although closely related, uncertainty analysis and sensitivity analysis are two different concepts. Sensitivity analysis is the systematic investigation of the reaction of model outputs to variations in model inputs. In uncertainty analysis the model inputs are sampled from certain

distributions to quantify the consequences of the uncertainties in the model inputs, for the model outputs.

In this study case the sensitivity analysis was carried out evaluating the sensitivity derivatives (S) by means of finite differences. That means, a small perturbation has been applied to each model input parameter (p) and the effects to each model output (M) have been independently analysed. Mathematically, S is given by:

$$S = \frac{\partial M}{\partial p} \approx \frac{\Delta M}{\Delta p}. \qquad (6)$$

IV. NUMERICAL RESULTS

A. *Influence of the secondary currents parameterization*

For this section the relationship between SC default values is investigated. Physical parameters such as friction coefficient and turbulence parameterization are kept constant during the numerical experiments.

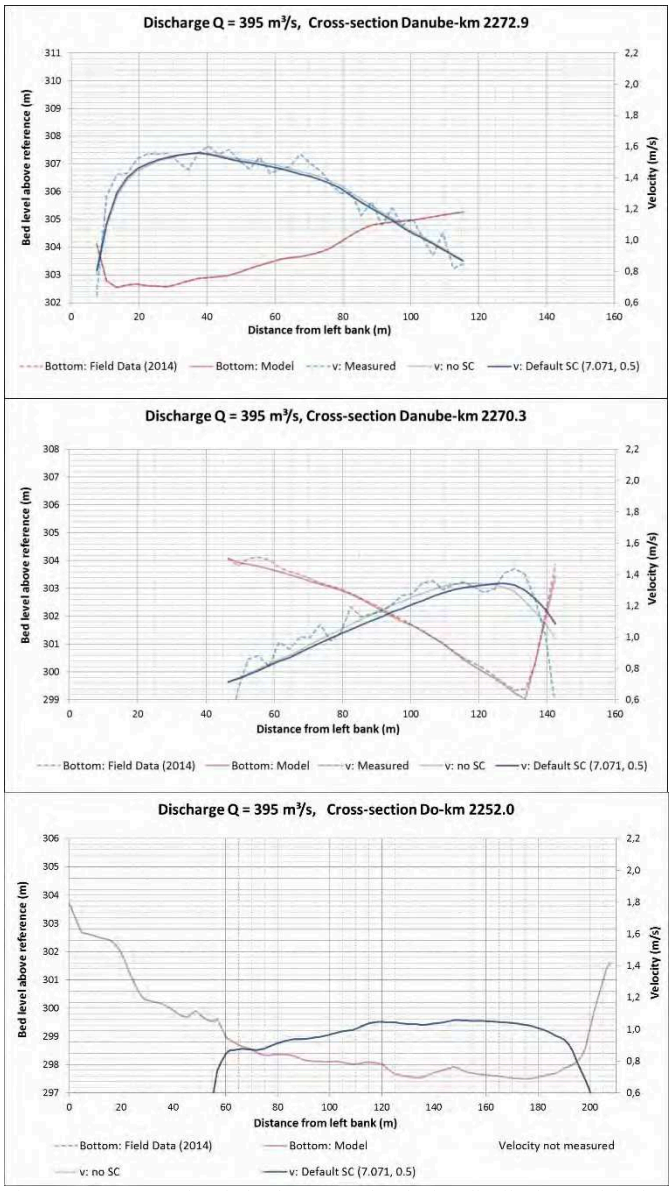

Figure 2: Cross-sectional depth averaged velocity distribution and bed level for discharge Q = 395 m^3/s. *bottom*: Danube-km 2252.0, *middle*: Danube-km 2270.3, *top*: Danube-km 2272.9.

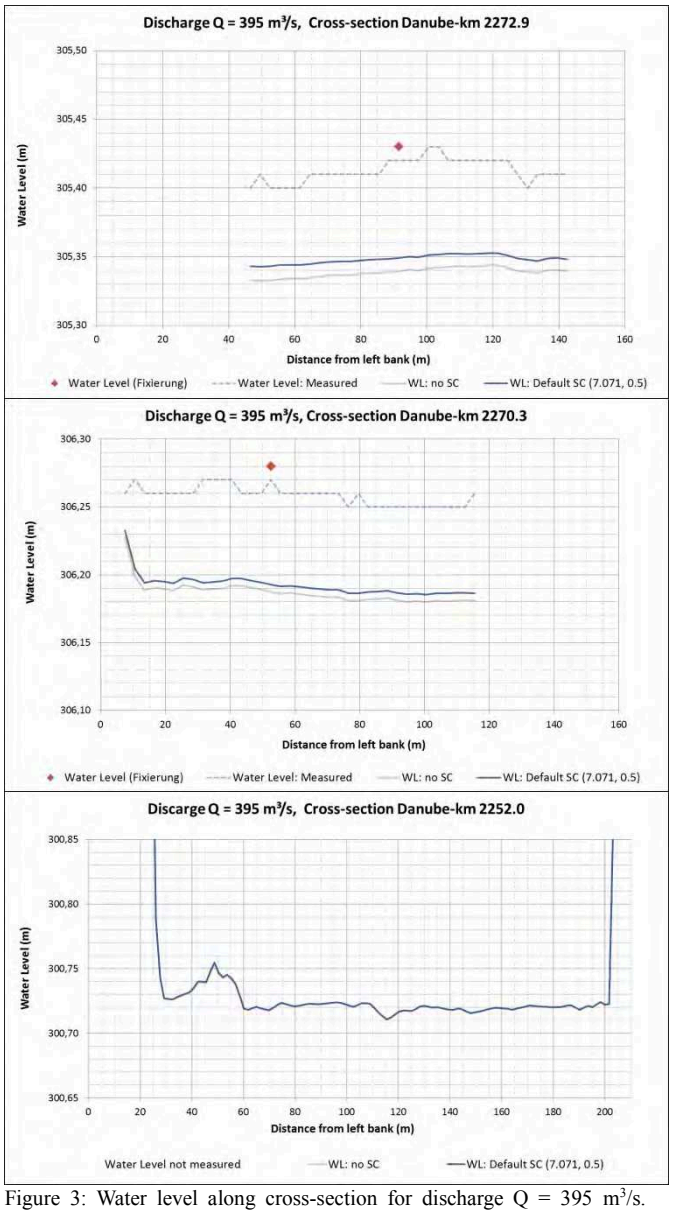

Figure 3: Water level along cross-section for discharge Q = 395 m^3/s. *bottom*: Danube-km 2252.0, *middle*: Danube-km 2270.3, *top*: Danube-km 2272.9.

In the present investigations, the measured and simulated water levels and depth averaged velocities were compared at a slightly curved section (Danube-km 2272.9) at the strongest bend (Danube-km 2270.3) and at a straight section (Danube-km 2252.0). Fig. 2 shows the simulation results for each case with and without SC and the measurements for a low water discharge (395 m^3/s). Fig. 4 presents the results for a bank-full discharge of 1146 m^3/s accordingly.

The agreement between simulated and measured velocities is generally good. The largest differences between the simulation results with and without SC are observed at the strongest bend (Danube-km 2270.3), then less in the slight bend (Danube-km 2272.9) and not at all in the straight section (Danube-km 2252.0). As expected the differences are higher for the bank-full discharge (Fig. 4). With SC the position of the maximum velocity (vertex) in the cross-section can be better reproduced.

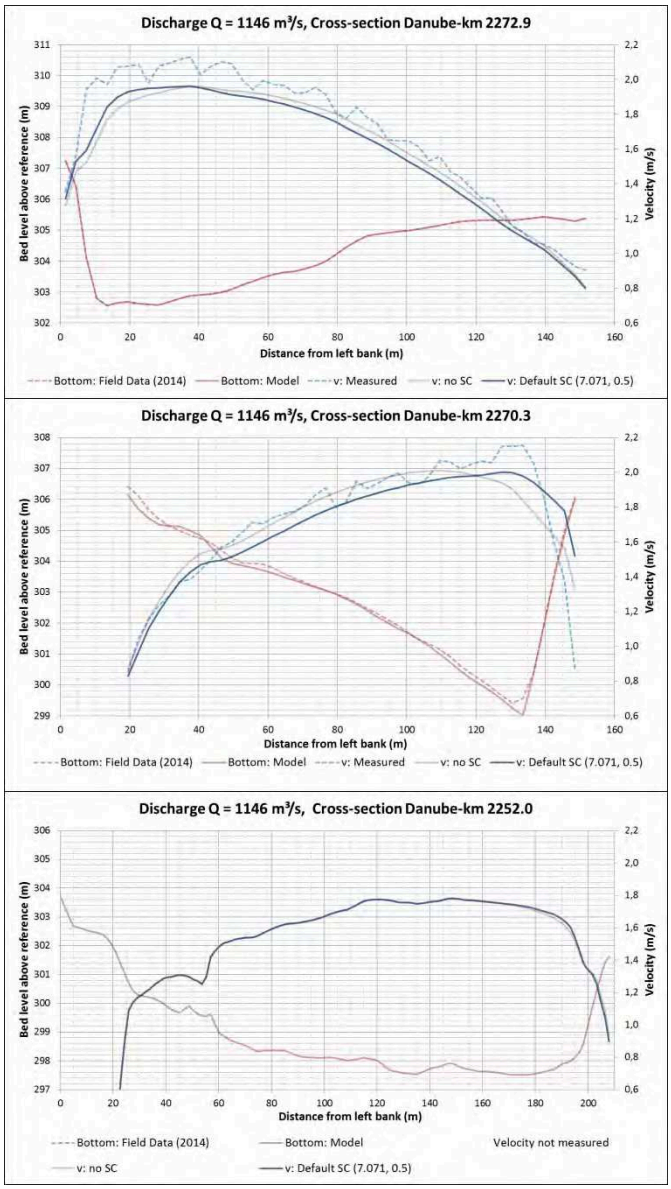

Figure 4: Cross-sectional depth averaged velocity distribution and bed level for discharge Q = 1146 m^3/s. *bottom*: Danube-km 2252.0, *middle*: Danube-km 2270.3, *top*: Danube-km 2272.9.

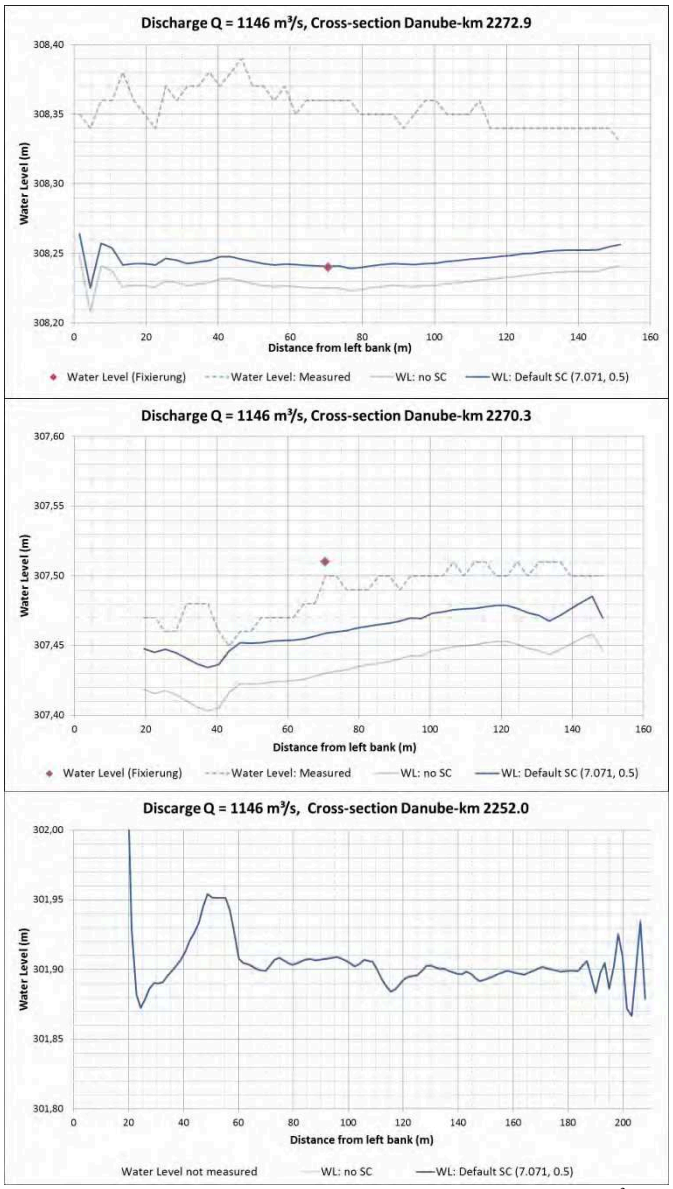

Figure 5: Water level along cross-section for discharge Q = 1146 m^3/s. *bottom*: Danube-km 2252.0, *middle*: Danube-km 2270.3, *top*: Danube-km 2272.9.

According to (1), the implemented secondary currents approach acts as an additional friction / loss term. Therefore an effect on the water levels is to be expected. Figures 3 and 5 visualise the simulated water levels for the three cross-sections Danube-km 2272.9, 2270.3 and 2252.0 and for the two discharges 395 and 1146 m^3/s with two different measurements (measurements were not available for Danube-km 2252.0). The dotted blue lines originate from the cross-sectional velocity measurements. The red dots come from water level measurements along the river stretch. The agreement fulfils the BAW requirements of +/- 5-10 cm for low water discharges and +/- 10-20 cm for high water discharges.

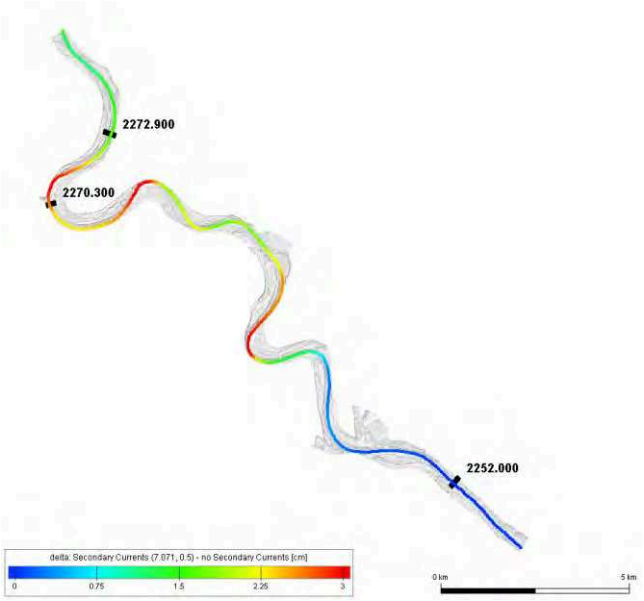

Figure 6. Difference in water level (cm) between results with and without secondary flow parameterization (Q=1146m³/s)

The comparison of the water levels for the simulations with and without the SC correction shows a similar behaviour as for the velocities. In contrast, the water levels including SC effects are higher in conjunction to river curves, as observed in the bends for a high discharge scenario.

In Fig. 6 the water level difference between model results with and without the SC correction is presented. The highest differences (up to a 3 cm) are located in the large-amplitude bends.

A statistical analysis of the current velocities is presented in Table 1. For each profile the normalised root mean square error (NRMSE) was calculated using (5), according to [7] values below 0.5 are considered to be very good. However, the default SC coefficients should be calibrated in order to improve the current model and roughness should be re-calibrated for the reasons already mentioned.

Profile	Num. results without SC correction [-]	Num. results with SC correction [-]
2270.30	0.3601	0.4293
2270.77	0.5089	0.5052
2271.15	0.2808	0.2851
2272.35	0.2780	0.3002
2272.90	0.3327	0.3247
2273.52	0.3441	0.3535
average	0.3508	0.3663

Table 1: NRMSE of the 6 measured velocity profiles, for the scenario with SC correction, where the default values of A_s and D_s were used.

B. Sensitivity Analysis

The sensitivity analysis on A_s and D_s coefficients was carried out by applying a variation of ±1.0 and ±0.1 respectively and then calculating the partial derivative of model results with respect to each parameter by means of central numerical difference, referenced as sensitivity derivative. Fig. 7 shows the sensitivity of the model related to free surface results. Fig. 8 shows the sensitivity of the model related to the current velocity magnitude.

In Fig. 7 it can be seen how each parameter significantly affects the free surface computation. For example, the sensitivity derivative of the free surface with regards to A_s presents a *positive* variation up to 0.005 m in the oxbow curve. On the other hand, in the same region the sensitivity derivative with regard to D_s varies negatively down to -0.08 m. While the model was calibrated before this study, the change in free surface caused by SC triggers the need to re-calibrate roughness such that the computed free surface elevation best fits the measured data.

In Fig. 8 the effect of each parameter on current velocities is presented. As expected, it affects only regions where the flow is deflected from its original direction i.e. river bends. At the bends it can be seen a *positive* variation up to 0.02 m/s for the sensitivity derivative of the current velocity with regard to A_s in the outer edges, and a *negative* variation in the same order of magnitude in the inner edges. A_s with D_s in Fig. 7, the sensitivity derivative shows an opposing effect with an absolute variation up to 0.3 m/s.

Based on the sensitivity results, it can be seen that the dissipation parameter D_s is one order of magnitude more sensitive than the production parameter A_s. It is not by coincidence that their default values also differ in one order of magnitude (7.071 and 0.5).

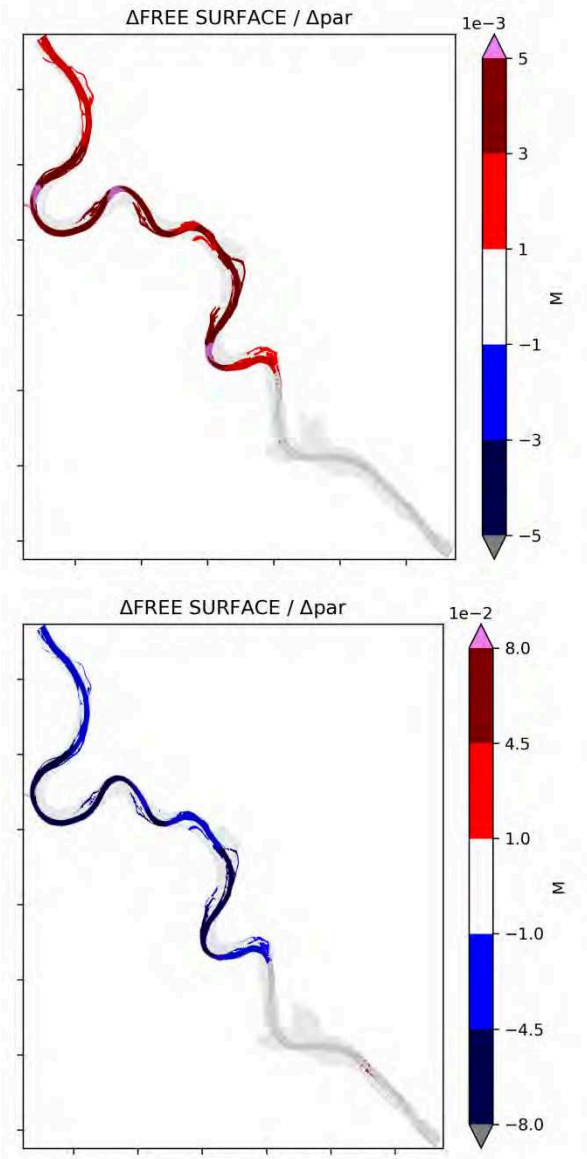

Figure 7. Sensitivity analysis of production A_s (top) and dissipation D_s (bottom) parameters w.r.t. free surface.

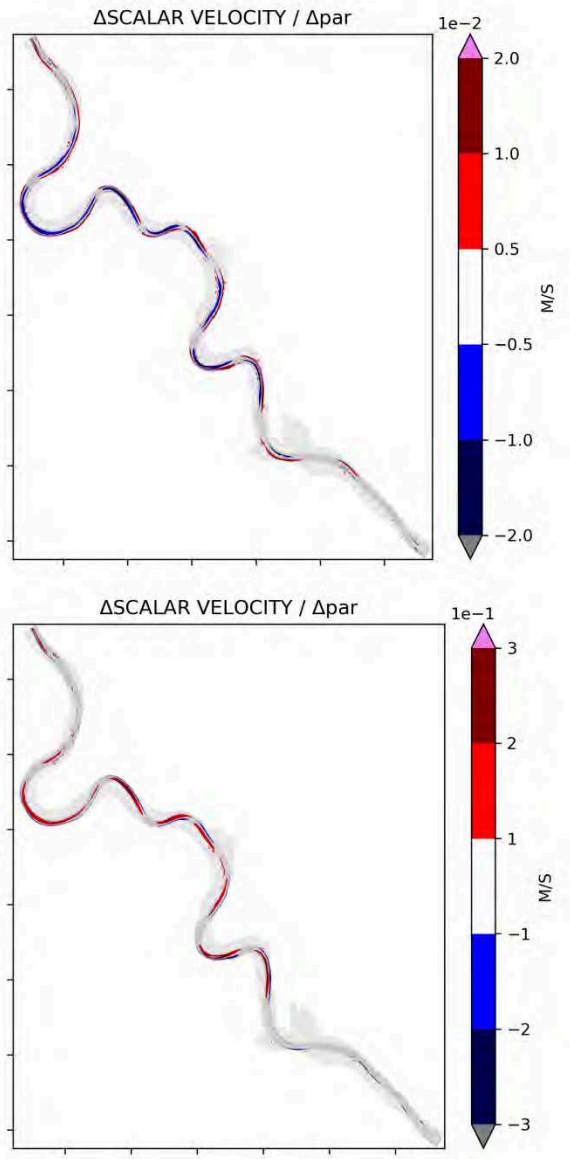

Figure 8. Sensitivity analysis of production A_s (top) and dissipation D_s (bottom) parameters w.r.t. current velocity.

V. DISCUSSION AND CONCLUSIONS

The differences in depth-averaged velocities and in water levels due to the incorporation of the secondary flow approach are generally small. Nevertheless the position of the maximum velocities in a cross-section is better reproduced by simulations including the secondary currents approach. As the approach induces additional friction, the water level is increased. The agreement with water level measurements could be improved by decreasing the roughness coefficient, decreasing the production coefficient (A_s) and/or increasing the dissipation coefficient (D_s).

A sensitivity analysis on the two coefficients showed that the default values are certainly within the range of application, in particular when model calibration is performed with the secondary flow approach already implemented. Since including the secondary flow approach affects the water levels, it is recommended for modellers to carry out a sensitivity analysis on these parameters and decide whether or not to include the secondary flow approach prior to model calibration.

The method was tested on a strongly-curved stretch of the Danube River. The method contains two empirical coefficients, which can be used as additional calibration parameters. Using the default values for these coefficients a good agreement was found between the measured and computed water levels and flow distribution.

The available method for secondary currents in TELEMAC-2D can be enabled for a more accurate representation of secondary flow effects in two-dimensional simulations. The default values of A_s and D_s (7.071 and 0.5 resp.) can yield improved results. However, due to expected changes in water level, adjustments in roughness should be considered.

ACKNOWLEDGEMENTS

We thank our colleagues Rebekka Kopmann and Frank W. Platzek for discussion and support.

REFERENCES

[1] K. Blanckaert and H.J. de Vriend, “Nonlinear modelling of mean flow redistribution in curved open channels,” Water Resour Res. 39(12):1375, 2003. doi:10.1029/2003WR002068,

[2] D. Wang and P. Tassi, “Secondary Flow Corrections into The Telemac-Mascaret Modelling System,” In O. Bertrand and C. Coulet (Eds.), Proceedings of the 21stTELEMAC-MASCARET User Conference, October 2014.

[3] F., Engelung, “Flow and bed topography in channel bends,” Journal of the Hydraulics Division, 1974;100(11):1631-1648.

[4] R. Bernard and M. Schneider, “Depth-averaged numerical modeling for curved channels,” Technical report, DTIC Document, 1992.

[5] J.W. Elder, “The Dispersion of Marked Fluid in Turbulent Shear Flow,” Journal of Fluid Mechanics 5, 544-560, 1959. DOI: 10.1017/S0022112059000374.

[6] J.-M. Hervouet, “Hydrodynamics of Free Surface Flows: Modelling With the Finite Element Method,” 2007.

[7] D. N. Moriasi, J. G. Arnold, M. W. Van Liew, R. L. Bingner, R. D. Harmel, T. L. Veith. “Model evaluation guidelines for systematic quantification of accuracy in watershed simulations”, American Society of Agricultural and Biological Engineers, 2007.

Definition of a restoration project on the river Loire

Matthieu de Linares and Pierre-Alain Rielland
ARTELIA Eau & Environnement
Echirolles, France
matthieu.delinares@arteliagroup.com

***Abstract*—This paper presents the different steps of a numerical study of the morphological evolution of a sand-bed river in France. Hydrologic and morphological calibration are detailed, as well as the modelling of the impact of proposed restoration operations. The limitations of the model and the way we have dealt with them are exposed.**

I. INTRODUCTION

In the framework of the large-scale restoration project of the Loire River (a sand-bed river in France) between Pont-de-Cé and Nantes (see [1]), ARTELIA is in charge of the restoration of the stretch of the Loire River between Oudon and Anetz. The objectives of the restoration operations are to raise the water level at low flows and re-equilibrate the sharing of discharge between the main and secondary channels (with emphasis on the sector of Neuve-Macrière Island). It involves in particular reworking (shortening and lowering) of the groynes and other man-made structures in the river bed.

In order to help define and optimize the restoration operations, a numerical model of hydraulics, sediment transport and bed evolution of the stretch of the river Loire studied was set-up and calibrated.

This paper describes the calibration process and shows how the model has been used to help optimizing the configuration of structures in the river bed. At the same time, limitations of the model are shared with the view of motivating modelers to improve the methodology of such numerical studies.

II. MODEL DESCRIPTION

ARTELIA Eau & Environnement has built and calibrated a fine scale hydraulic and sedimentary numerical model covering an 18 kilometres stretch of the river (see the extent and initial bathymetry in Fig. 1 below). Mesh size is about equal to 10 meters in the river channel. A close-up view of the mesh is displayed in Fig.2.

Hydraulics are computed with TELEMAC-3D. For all the computations presented here, TELEMAC 3D is run as "quasi 2D" using only two vertical planes, in order to reduce the computation time. It was checked that the results in terms of general hydraulics (water level profile) are identical when increasing the number of vertical planes. The initial choice of TELEMAC-3D instead of TELEMAC-2D came from the need to use a full 3D model when calibration data for it (i.e. detailed ADCP surveys of the 3D flow field) would be available. It turned out that such data could not be available during the project due to unusually weak hydrology of the river Loire.

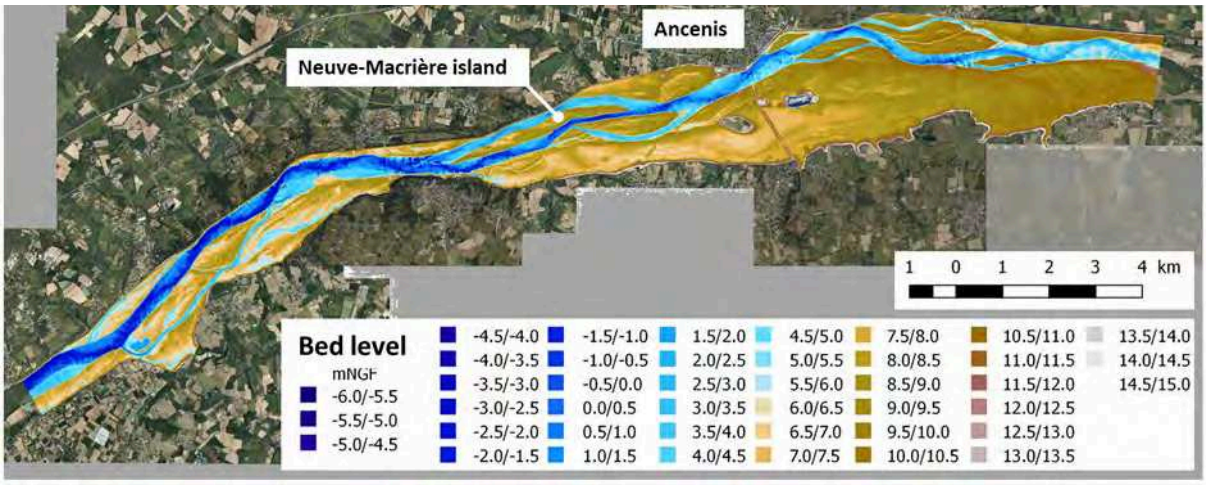

Fig. 1 - Bathymetry of the model.

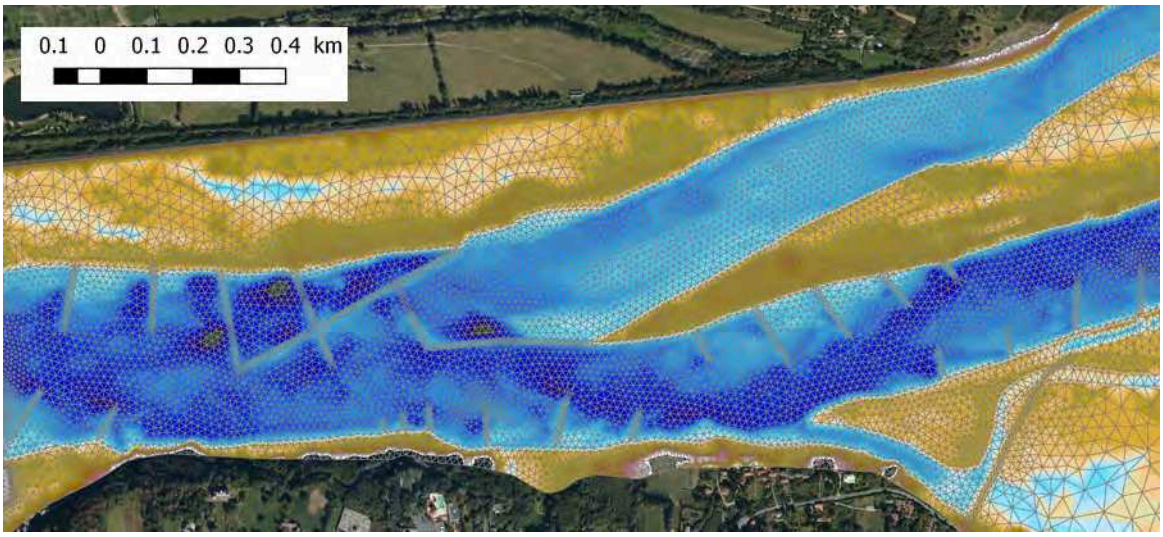

Fig. 2 - Mesh (partial view).

Sediment transport (bedload only) and bed evolution are computed with SISYPHE internally coupled with TELEMAC-3D.

III. COUPLED HYDRAULIC AND MORPHOLOGICAL CALIBRATION

A. Hydraulic calibration

Hydraulic calibration is performed based mainly on water surface profiles for low, medium and high flows. Different friction coefficient have been allocated to different zones: rip-rap structures, sandy bed in the main channel and the broad secondary channels, narrow secondary channels, floodplain. The roughness coefficient is considered constant with regards to the water stage on all zones except the sandy bed in the main river channel. The underlying assumption is that the dunes (the size of which increases with the water stage) are responsible for most of the friction of the sandy bed.

Despite the availability of a significant number of water levels surveys for different discharges, the determination of the friction parameters (variation between zones and variation with discharge) remains weak (i.e. the calibration remains non-univocal) for the three following reasons:

(i) Even if global, width-averaged friction is well determined, the relative friction between groynes and sand bed could not be determined because of the lack of available velocity profile surveys. Thus, the chosen repartition of Strickler coefficient between the two zones is somehow arbitrary. Two different repartitions have been used, which enable to assess the robustness of the morphological model in terms of impact to this uncertainty. The table below presents the two sets of values of the Strickler friction coefficient.

FRICTION COEFFICIENT

Zone	Set 1	Set 2
Rip-rap structures	8 $m^{1/3}/s$	15 $m^{1/3}/s$
Sandy bed	33 to 55 $m^{1/3}/s$	28 to 35 $m^{1/3}/s$
Secondary channels	25 $m^{1/3}/s$	25 $m^{1/3}/s$
Floodplain	18 $m^{1/3}/s$	18 $m^{1/3}/s$

(ii) The variation with water stages of the friction of the alluvial bed is based only on the incoming discharge, using an interpolation between the different water line surveys used for calibration. Bed roughness predictors exist that can link local sediment and hydraulic variables to dune dimensions and therefore roughness, and thus could, in theory, provide a more physically based spatial and temporal evolution of the friction coefficient. Such predictors were not tested in the framework of this study.

(iii) Water levels computations for low discharges are highly dependent on the bathymetry (while medium to high discharges are not very sensitive to the bathymetry). This is shown in Fig. 3, which shows water line results of the model for a low discharge considering two different model bathymetries.

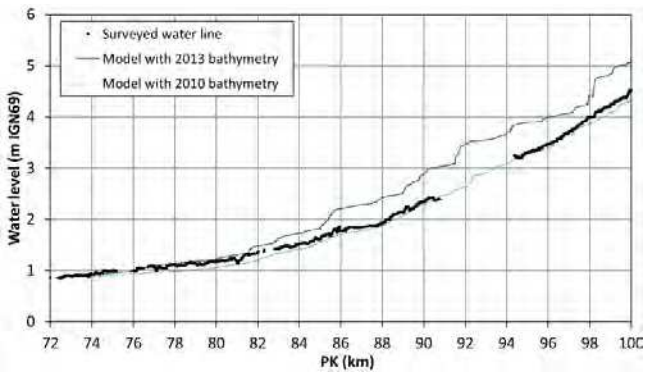

Fig. 3 - Surveyed and computed water lines for a discharge of 120 m^3/s.

The fact that water levels surveys are not concomitant with available bathymetric data can induce major discrepancies between computed and surveyed water levels. The methodology used to overcome this limitation consists in a coupled morphodynamic and hydraulic calibration. Indeed, as all water line surveys used for hydraulic calibration are within the time-frame of the morphodynamic calibration, the bathymetry computed during the morphodynamic model at the date of the water line survey is used for the hydraulic computation. The water line computed during the morphodynamic calibration cannot be directly used for hydraulic calibration because of the morphodynamic factor used for morphodynamic calibration, and because the effect of tide (significant for low flows at the downstream part of the model) is neglected for morphodynamic calibration.

B. Morphodynamic calibration

The transport model used in SISYPHE considers a single size-class (one millimetre sand) and is based on a transport formula that is an adaptation of the Meyer-Peter and Müller formula [2]. This formula (as well as bed slope effects and avalanching) was calibrated during a previous research work on another site of the Loire river, see [3]. Similar sediment and transport conditions are indeed found at both sites. A similar mesh size is also used because the very low, non-physical, value that is needed for the angle of repose of the sediment (parameter of avalanching process) is probably dependant on the mesh size.

In order to shorten computation durations, the "MORPHOLOGICAL FACTOR" keyword of SISYPHE is used. This factor is applied to the morphological evolutions, the hydrograph being "compressed" accordingly. Several morphological factors (up to 200) were tested on the calibration period, and the results compared with a reference computation with no time-acceleration (morphological factor of 1). A value of 100 was retained, which provides a good compromise in this case between accuracy and operational computation durations. It was possible to use a morphological factor here because it was checked that neglecting tide (by replacing the actual time-series of the water level gauge at the downstream end of the model by an averaged stage-discharge curve) has no significant morphological impact.

The morphological calibration then consisted of a simulation of the bed evolution between 2009 and 2013 and a comparison with the observed evolutions. The calibration results were satisfactory with both sets of friction coefficients, in particular in terms of localisation of areas of erosion and deposition (see Fig. 4 below for an example of results with set 2). It is notable that no changes to the sediment transport formulation (calibrated previously on another site, see [3]) was necessary.

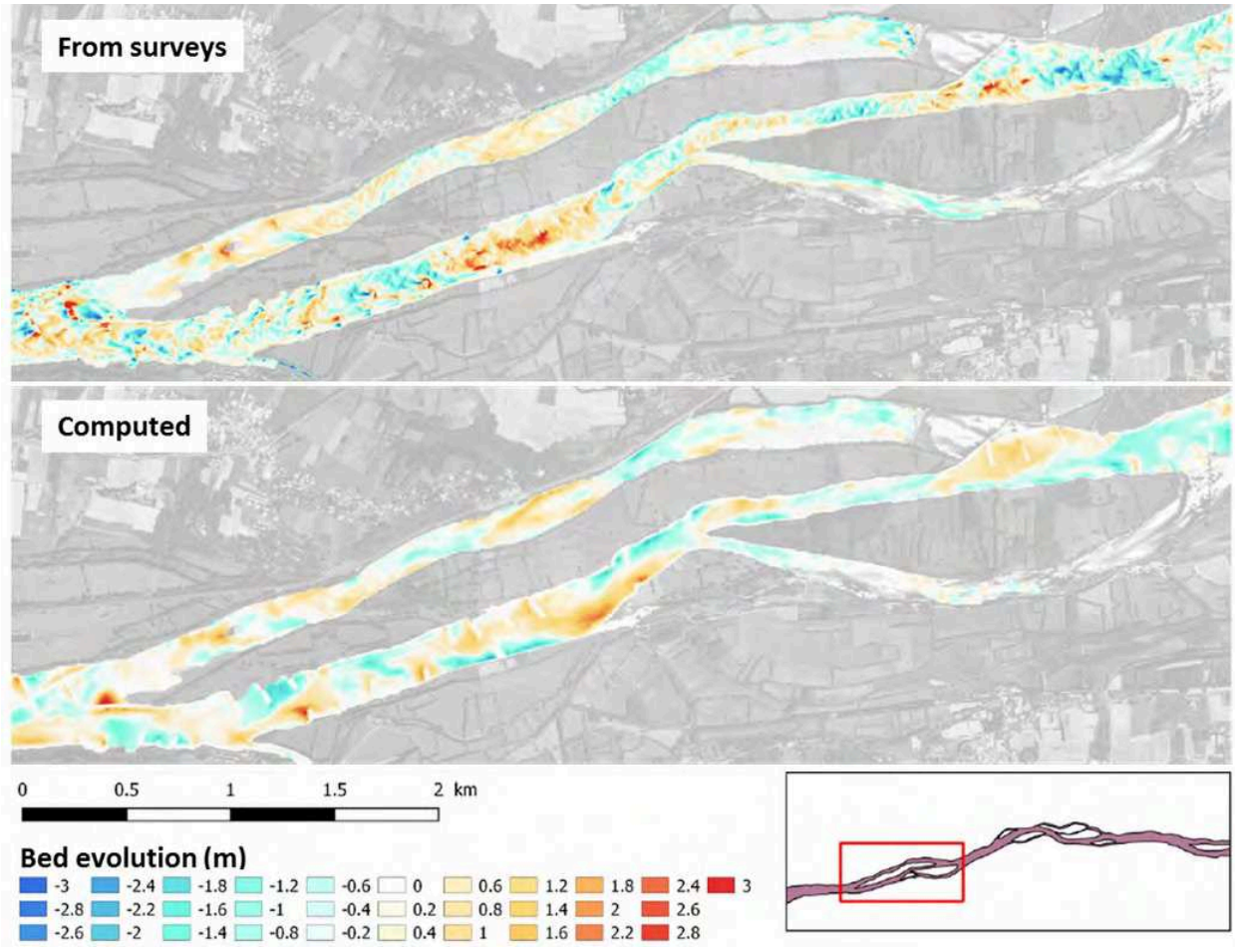

Fig. 4 - Comparison between surveyed and computed bed evolution for 2010-2013 – zoom on Neuve-Macrière island

The model validation was then made on the 2013-2017 period. For this period, results with set 2 were in general more accurate than those with set 1. Even with set 2 larger discrepancies appeared than for the 2009-2013 period. This is probably caused by the fact that floods were higher during the validation period than during the calibration period. It is probable than during high flood, sediment transport in suspension becomes significant and the bedload-only formulation used here becomes less accurate. More work would be needed here to test the impact of using a full solving of suspension transport (in addition to bedload) versus only a bedload-type formulation to compute morphological evolution in the Loire river (or in sand-bed rivers in general). More generally, it would be very beneficial for such studies to use other well documented test-cases to improve the robustness of transport formulations, not only for the computation of solid discharge, but also focusing on the lateral redistribution of sediment through slope effects or diffusion in suspension.

IV. LONG-TERM COMPUTATIONS

Future probable evolution in the case of no restoration (reference state) was then computed on a 50-years hydrologic scenario (based on past hydrology). Long-term results are very dependent on the chosen hypothesis for sediment loading at the upstream boundary of the numerical model. These results are thus not actual predictors of the future river morphology, but serve as a reference state in order to assess the impact of the proposed restoration operations.

V. IMPACT OF RESTORATION OPERATIONS

Restoration operations consist mainly in shortening and lowering the existing lateral groynes in the river bed. Groynes at the entrance and the exit of secondary branches, which in the present state completely block the flow for low stages, are also lowered or opened.

Long-term (50 years) computations were run with models implementing different versions of the restoration operations. The efficiency of these restoration operations was tested by comparison with results for the reference state for:

- Bed evolution (erosion or deposition on the main river channel and the secondary branches);
- Hydraulics indicators (water level stages, inundated areas, discharge in the secondary branches) for low discharge, mean discharge and flood discharge after 10, 20 and 50 computed years.

In the river main channel, the computed impact of groyne shortening and lowering was very positive since the new computed morphology consisted in a higher bed level. As a consequence a significant raising of water levels for low flows was computed (see Fig. 5 below for water lines results considering bed evolution computed by the final version of the restoration operation). Similar results were obtained for both sets of friction coefficients.

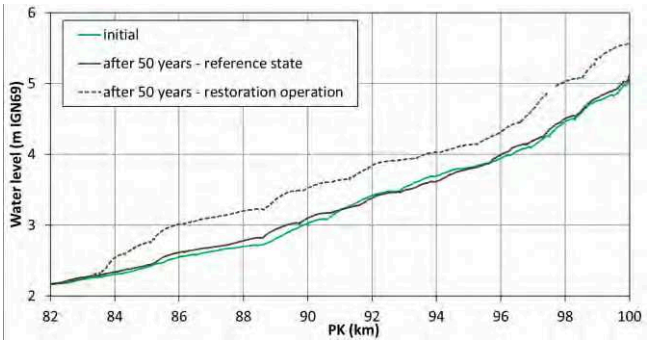

Fig. 5 - Impact on water lines of restoration operations - discharge of 207 m^3/s.

Concerning the configuration of the groynes at the entrance, exit, or inside of the secondary branches, no clear pattern emerged. Computed trends of evolution are indeed highly dependent on the secondary branch considered. Optimization of the structures around secondary branches was performed mostly for the entrance and the exit of the Neuve-Macrière secondary branch. Indeed, limiting further sediment deposition in this branch as well as improving its connectivity with the main channel was one of the main restoration objective. Computation results showed that for that purpose, an optimal configuration of the groyne field at the entrance consisted in maintaining groynes upstream of the entrance in order to limit entrance of sediment in this branch, while dismantling groynes at the entrance in order to improve connectivity at low water stages. This proposed new configuration is shown beside the actual configuration in Fig. 6 below. With this configuration, the computed morphology of the secondary branch of Neuve-Macrière Island after 50 years respects the two main objectives: a lower bed level and a better connectivity at low flow.

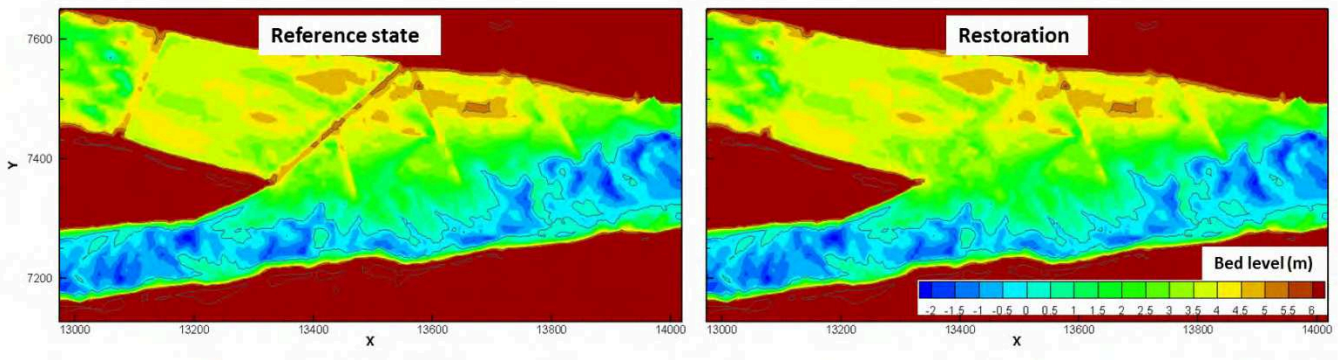

Fig. 6 - Proposed new configuration for the groynes at the entrance of Neuve-Macrière island

VI. CONCLUSION

The use of a numerical model in order to study long-term evolution of river morphology at a very fine scale is still not common practice in engineering. Nevertheless, stakeholders now regularly demand such studies.

The study presented in this paper enables to identify two paths for the improvement of the accuracy of such studies:

- using more measurements for internal calibration. If this is not possible, model operation should be run considering different alternatives for calibration parameters. For the study presented here, the stakeholder was very aware of the importance of measurements, and a rather large dataset was available (some surveys were even undertaken in parallel to the numerical study). Nevertheless comprehensive flow field data was lacking. Therefore, there was no unique solution for the parameters of the hydraulic calibration (equifinality). In order to limit the associated uncertainty on morphological results, the model was run with two different sets of parameters for friction coefficients. The model proved robust in our case as its main answers concerning the impact of restoration operations were similar using both sets.
- getting more feedback from real applications in order to improve formulations for sediment transport, and not only solid discharge itself (the prediction of which being not that problematic), but also bed slope effects and repartition between bedload and suspension.

ACKNOWLEDGEMENTS

This work was made possible thanks to the support of Région Pays de la Loire, Agence de l'Eau Loire-Bretagne, Fonds Européen de Développement Régional, and Voies Navigables de France.

REFERENCES

[1] SETEC-HYDRATEC - Rééquilibrage du lit de la Loire entre les Ponts-de-Cé et Nantes : phase 1, programme détaillé des travaux projetés - AELB / AGENCE DE L'EAU LOIRE BRETAGNE / VNF, 2015

[2] Meyer-Peter, E; Müller, R. (1948). Formulas for bed-load transport. Proceedings of the 2nd Meeting of the International Association for Hydraulic Structures Research. Stockholm, p39-64

[3] M. de Linares. « Modélisation numérique bidimensionnelle du transport solide et de la dynamique fluviale. Validation sur deux sites en Loire et sur l'Arc. » Université Joseph-Fourier -Grenoble I, 2007

Influence of numerical and physical parameters on the modelling of free bar morphodynamics

Florian Cordier[1,2], Pablo Tassi[1,2]
and Nicolas Claude[1]
EDF R&D LNHE[1] - LHSV[2]
6 Quai Watier, 78401 Chatou (France)
Corresponding author: florian.cordier@edf.fr

***Abstract*—Periodic bars are a common feature of rivers and are large sediment deposits alternating with deeper areas (pools) that arise from an instability phenomenon of the alluvial bed. A deep knowledge of bar processes is important for river engineers and river managers, because bars strongly alter the river bed topography and influence bank erosion, with consequences for navigation, water intakes and infrastructure. This work aims at setting-up a 2D morphodynamic model able to reproduce laboratory experiments of free bar formation with uniform sediment. To reach this goal, we investigate the impact of the numerical solution and physical parameters on the computed bar morphology and characteristics. Numerical results show that the domain discretization influences the propagation of the perturbation at the origin of free bar formation, where a finer computational mesh reduces the perturbation growth. Model convergence is attained with CFL values less or equal to 0.2. The use of two distinct morphodynamic boundary conditions shows that boundaries influence the computed bar dynamics. Slope effects due to deviation are necessary to trigger free bar formation, and their parameterization impacts their properties. The formulation for skin friction correction also strongly modify free bars morphology. Outcome of this study would help modellers to choose the correct set of numerical and physical parameters to model relevantly bars morphodynamics.**

I. Introduction

Rivers often present a wavy bed due to the presence of periodic bars, which are large sediment deposits alternating with deeper areas (pools) that arise from an instability phenomenon of the alluvial bed. A deep knowledge of bar processes is important for river engineers and river managers, because bars strongly alter the river bed topography and influence bank erosion, with consequences for navigation, water intakes and infrastructure.

Numerous studies [3], [7], [10], [18] have shown that the formation and the geometry of bars in straight or weakly curved channels are primarily governed by the width-to-depth ratio of the flow, also known as aspect ratio. At unstable conditions, starting from a flat bed, incipient bars tend to increase in size, eventually reaching a steady value of amplitude and wavelength [13] which scales with the water depth and the channel width, respectively. The commonly accepted definition for free bars is that they originate purely from morphodynamic instability, and migrate either in downstream or upstream direction, depending on river bar regime, with zero celerity at resonance conditions [34]. Free bar formation and propagation have been subject of extensive theoretical, experimental and numerical investigations in the past decades, with assuming uniform and later non-uniform grain size distributions [4], [28].

Nowadays, the increasing confidence given on the numerical modelling approach is explained by the continuous development of knowledge and computer technology, which allows to investigate physical problems with increasing the level of detail as well as the spatial extent and time scales [21]. As a result, numerical morphodynamic models are widely used for different purposes, from the basic morphodynamic research to dealing with complex river engineering problems [27]. However, numerical modelling of fluvial morphodynamics, which includes the processes bar formation and propagation, is far from being a solved issue and still involves many challenges [27].

Numerical and physical parameters can potentially control the computed free bar morphology and characteristics. The role of the computational domain discretization on the initiation of bed topographic perturbations and bar formation has been seldom explored. According to [26], the large-scale characteristics of the bar pattern in a self-forming braided river are independent of the computational mesh resolution, where a finer mesh better describes the bar topography. Morphodynamic models often implement equilibrium boundary condition for sediment supply [8], [24], but only few studies considered other boundary conditions such as sediment recirculation to study bar formation [19]. The influence of the bottom topographic perturbations set as initial conditions in numerical models on the initiation of free bars remains shortly understood [8]. The importance of accounting for gravity effects due to transverse bed slopes for computing bedload transport rates has been put in evidence in theoretical frameworks [7], [29]. Nevertheless, parameterization of the slope effects on numerical models not only increases numerical diffusion and may smooths results [28], but also remains generally a work of calibration, where the interval chosen for calibrating the empirical values is not necessarily justified [5], [22], [26]. For the same reasons, parameterization of the turbulence model could potentially play a role on the computed bar characteristics. Spatial roughness variations induced by the interactions between bed-forms of different origins and scale (i.e. grain roughness, ripples, dunes and bars) are often parameterized using a skin friction correction formulation [19]. The impact of using such formulation on free bar development deserves more attention.

The objective of this study is twofold. Firstly, this work aims at setting-up a numerical model able to reproduce accurately laboratory experiments of free bar formation and

propagation with uniform sediment [17]. Secondly, the authors investigate the impact of the numerical solution and physical parameters on the computed bar morphology and characteristics. The influence of the sediment boundary conditions, bed slope effects, skin friction correction and initial bed perturbation is studied and discussed. A convergence analysis is also performed to evaluate the impact of the space and time discretization on the numerical results.

A description of the mathematical model (hydrodynamics and morphodynamics) and of the numerical treatment of physical processes is provided in Section II, together with the study case from which numerical scenarios are derived. In Section III, attention is given on the numerical results. Outcome of this study presented in Section IV would help modellers to choose the correct set of numerical and physical parameters to set-up (physically and numerically) relevant morphodynamic models in the context of fluvial free bars morphodynamics.

II. Materials and methods

A. Mathematical and numerical model

The two-dimensional morphodynamic model used in this work presents two components: a hydrodynamic module (TELEMAC 2D) and a morphodynamic module (Sisyphe). The hydrodynamic module is based on the solution of the 2-D depth-averaged shallow-water equations (SWE) [23], [25], [32], [33], with a closure relationship for the turbulence based on a constant turbulent eddy viscosity ν_t [m^2/s], and the Nikuradse friction law to parameterize roughness effects. The morphodynamic module is based on the Exner equation [11], [14].

In this work, the sediment transport capacity q_{b0} [m^2/s] is determined with the formula of Meyer-Peter and Müller (MPM) [20]. The correction of bedload magnitude to account for the bed slope effects is modelled with the formula of [16], where the fractional transport rate q_{b0} is modified as a function of the bed slope degree with respect to the current direction with $q_b = q_{b0}\Big(1-\beta_1\partial_s z_b\Big) = q_{b0}\Big[1-\beta_1\big(\partial_x z_b\cos\delta+\partial_y z_b\sin\delta\big)\Big]$, where β_1 is an empirical coefficient accounting for the stream-wise bed slope effect, δ is the angle between the current and the x-axis direction, and s the coordinate along the current direction. The bedslope effect is similar to a diffusion term in the bed evolution equation [31] and may smooth the bed topography and prevent from numerical instabilities [2], [34]. The correction of bedload direction is given by the relation of [1] with $\tan\alpha = q_{b,n}/q_{b,s} = (\sin\delta - T\partial_y z_b)/(\cos\delta - T\partial_x z_b)$, where α is the angle between the sediment transport vector and x-axis direction which will deviate from the bed shear stress vector due to gravity effects, $q_{b,n}$ and $q_{b,s}$ correspond to the bedload magnitudes along the normal to the current direction and the stream-wise direction, respectively, and where $T = 1/(\beta_2\sqrt{\tau_b^*})$ [30], where τ_b^* is the Shields parameter and scales the gravity effects as a function of the grain diameter, and β_2 is an empirical coefficient used as a calibration parameter.

The total shear stress τ [Pa] is calculated from the depth averaged flow velocity field, where $\tau = 0.5\rho C_f(u^2+v^2)$ and C_f is equal to the sum of skin friction and bedform drag. In this study, the bed shear stress is determined as a function of the total shear stress with $\tau_b = \mu\tau$, where $\mu = C_f'/C_f$ is the friction factor and C_f' [-] is the equivalent Chézy coefficient only due to skin friction and is the only component acting on bedload [19]. C_f' is calculated assuming a flat bed by using the Nikuradse's formula, where the roughness height k_s' [m] is a function of the mean sediment diameter at the bed surface with $k_s' = \alpha_{ks}\times d_{s,m}$ with α_{ks} a calibration parameter.

The numerical solution of the SWE is based on the finite element method P_1, where the advective terms are computed with the method of the characteristics. The numerical solution of the sediment transport continuity equation is performed by a procedure that combines an implicit finite element scheme and an edge-based explicit upwind advection scheme. This procedure assures mass-conservation at machine accuracy, monotonicity of tracers, copes with dry zones and is easily applicable to domain decomposition [15].

B. Study case

The numerical models are meant to reproduce a laboratory experiment carried out at Delft Hydraulics (The Netherlands) [17]. Lanzoni's experiments were performed in a water and sediment-recirculating rectangular 55 m long, 1.5 m wide and 1 m deep straight flume with rigid vertical sidewalls, with an initially flat bed. The imposed downstream free surface was adjusted so that the water surface profile was parallel to the longitudinal bed slope. Exiting sediment was continuously weighted to estimate sediment transport and then recirculated upstream [17]. According to Lanzoni, sediment was mainly transported as bedload.

Among the multitude of experiments of bar formation carried out with uniform sediment, test P1505 is selected here because bars formed relatively rapidly in this run, and other numerical studies successfully reproduced bar formation under this given configuration [19]. This test was carried out with a constant flow discharge equal to $30\cdot10^{-3}$ m^3/s resulting in an average water depth equal to $\bar{h}$ =0.044 m, with an initial longitudinal bedslope equal to 0.00452. The width-to-depth ratio, denoted $\beta = B/\bar{h}$ [-] with B [m] the active width (i.e. at bankfull conditions), is equal to 34. The uniform sediment is composed of a mixture of well-sorted quartz sand with a geometric mean diameter of 0.48 mm, with $\rho_s = 2.65\cdot10^3$ kg/m^3. The averaged exiting discharge of sediment including pores was $2.63\cdot10^{-5}$ m^3/s.

C. Numerical model scenarios

We investigate here the impact of the numerical solution and physical parameters on the computed bar morphology and characteristics. The influence of the sediment boundary conditions, bed slope effects, skin friction correction and initial bed perturbation is studied and discussed considering uniform sediment. A convergence analysis is also performed to evaluate the impact of the space and time discretization on the numerical results.

The model computations are performed as follows: *i*) the hydrodynamic model is run without bedforms (*i.e.* considering a flat bed) to obtain the mean hydraulic variables measured during the laboratory experiments, which are then used later as initial conditions for *ii*) the sediment transport and morphodynamic model where both the numerical averaged

sediment transport and the bars characteristics are compared with experimental measurements.

D. Model parameters

The numerical model of reference from which other models are derived uses an unstructured computational mesh composed triangles with typical length of approximately 0.093 m. In this model, the computational time step is set equal to $\Delta t = 0.04$ s in order to keep a Courant number (=CFL) approximately equal to 0.2, $\nu_t = 10^{-6}$ m^2/s and $\rho = 1000$ kg/m^3. As originally pointed out by [8] and observed later by other researchers [19], [24], migrating bars could be observed in the numerical model only starting from approximately $x = 60$ m, which corresponds to the length of the laboratory flume. For this reason, the downstream boundary of this reference model has been extended to $x = 120$ m in order to observe the migration of fully developed bars in the system. No initial topographic perturbation is introduced in the reference model, i.e. the initial bed is flat. The boundary conditions of the hydrodynamic model correspond to an upstream constant flow discharge and a downstream constant free surface elevation, respectively. Sediment density and porosity are fixed to $\Delta_s = 1.65$ and $P_0 = 0.40$, respectively.

To carry out the sensitivity to the upstream morphodynamic boundary condition, two distinct formulations are imposed. The first boundary condition corresponds to the morphodynamic equilibrium (referred to -E), where the input solid discharge is determined from the bedload capacity formula such that the upstream topography remains constant overtime and the downstream boundary is let free. The second boundary condition corresponds to sediment recirculation (referred to -R), where the sediment exiting the flume is re-injected upstream at the next computational time-step. The sensitivity analysis to the temporal discretization is performed with using distinct computational time-steps $\Delta t \in [0.02 - 0.16]$ s, with considering both morphodynamic boundary conditions. The impact of domain discretization on computed bar formation and dynamics is investigated with the help of meshes composed of the same number of regular isosceles right triangles and irregular triangles. The reference coarsest mesh which is used (run P1505-E1/-R1) is composed of elements scaling 0.375 m. Three finer meshes are obtained by splitting the mesh of reference in 2 (run P1505-E2/-R2), 4 (run P1505-E3/-R3) and 8 (run P1505-E4/-R4). The low-resolution model (run P1505-E1/-R1) is run with a computational time step of $\Delta t = 0.16$ s, whilst the higher resolution models use a time-step equal to $\Delta t = 0.08$ s, $\Delta t = 0.04$ s and $\Delta t = 0.02$ s, respectively, in order to keep a Courant number around 0.2.

III. Numerical results

A. Influence of numerical parameters

1) Time discretization: Time-convergence analyses conducted under P1505 configuration show that the maximal CFL value for which the model remains stable is equal to 0.2. Above this value, the numerical model is unstable and compute physically irrelevant bed evolution. This result seems to be independent from the chosen morphodynamic boundary condition (i.e. equilibrium or recirculation, see Figure 1). The comparison between the numerical results computed with CFL=0.2 and CFL=0.1 shows that no major difference can be observed between both computed bed topographies. This suggests that using CFL values in this range do not affect the numerical solution which could have originated from diffusive effects. In this case, outcomes also suggest that model convergence is more related to the numerical scheme adopted for the solution, rather than a problem of numerical diffusion.

2) Spatial discretization: Outcomes from the mesh convergence analysis (Figure 2) show different trends depending on which morphodynamic boundary condition is used. When the mesh convergence analysis is carried out with the equilibrium boundary condition, free alternate bars always develop and migrate in the second part of the channel. Results show that bars generally form more downstream with decreasing mesh size, and suggests that perturbations at the origin of bar formation are reduced with finer computational meshes. When sediment recirculation is implemented, in the early stages of these runs, free alternate bars of similar characteristics can be observed from $x \approx 60$ m. During the late stages of these scenarios, the upstream stabilized bars produced by the coarse mesh trigger the formation of immediately downstream hybrid bars, which are originated from the growth and stabilization of free bars [9]. The alternate bar dynamics turns out completely different when finer meshes are used (i.e runs P1505-R3 and P1505-R4), where a continual formation and propagation of free bars is observed. In the last case, the upstream boundary condition does not generate a geometrical forcing high enough which could induce hybrid bar formation. Obviously, these upstream topographic perturbations are not observed when the equilibrium boundary is used, because by definition the bed topography has to remain constant overtime.

According to [26] the large-scale characteristics of the bar pattern in a self-forming braided river are independent of the computational mesh resolution, where a finer mesh better describes the bar topography rather than a coarser one. Results from the current analysis (Figure 2) partially support their conclusions, in the sense that convergence is not directly reached when sediment recirculation is considered (*i.e.* runs P1505-R1 and P1505-R2), where the formation of upstream topographic perturbations are larger enough -due to the large mesh size- to trigger the formation of upstream steady bars.

Comparison between the two scenarios using the irregular mesh (Run P1505-R3) and a regular mesh (Run P1505-R3b) shows that the irregular mesh enhances perturbation growth as free bars develop more upstream (Figure 3). Nevertheless, equilibrium bar characteristics remain unchanged, and the orientation of the mesh elements does not impact bar morphology.

The simulations were launched using the MPI library on Porthos cluster using 28 CPUs. Decreasing the computational time-step with keeping a constant CFL is showed to increase considerably the computational time, leading to cumbersome simulations when the time-step is equal to 0.02 s using both morphodynamic boundary conditions (Table I). Consequently, using $\Delta t = 0.04$ s is showed to be a good compromise between the quality of the numerical results and computational time efficiency.

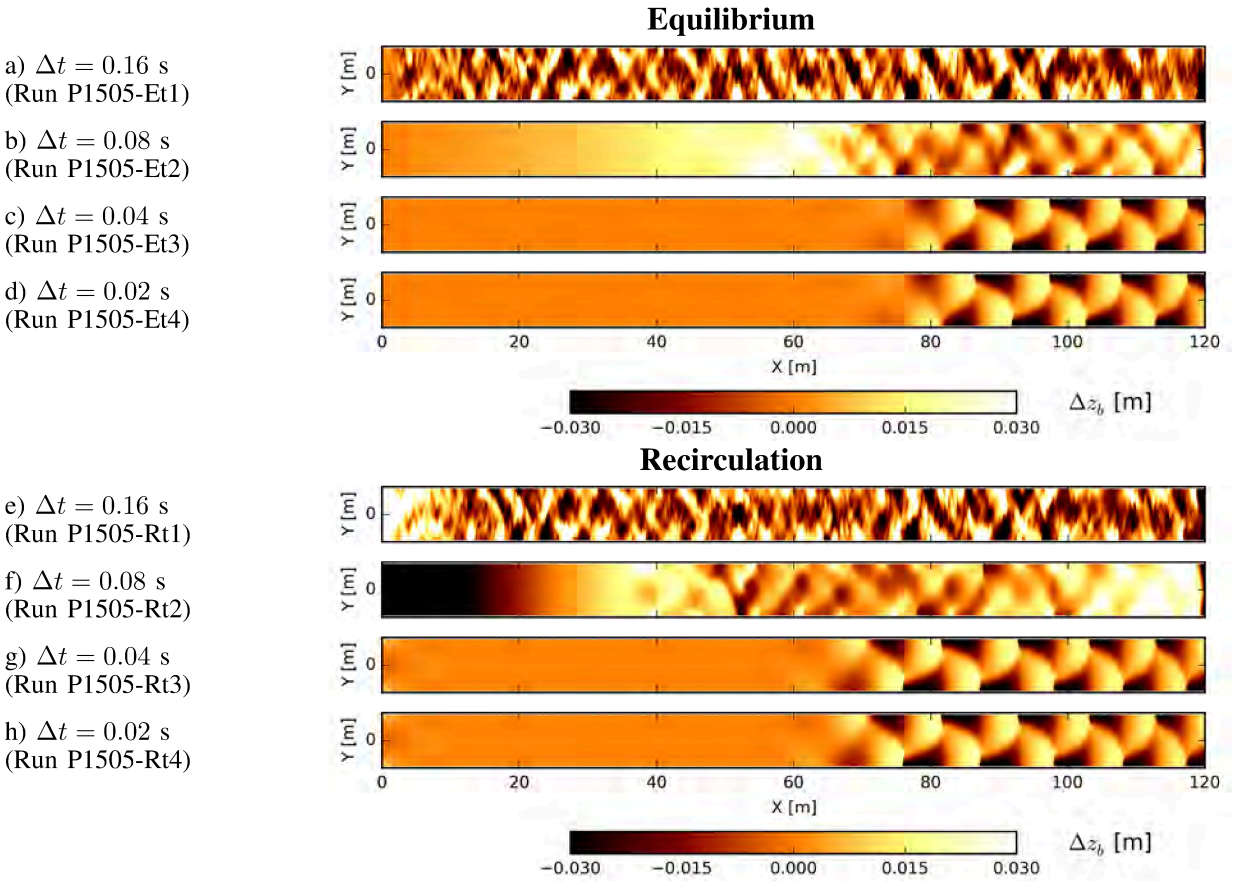

Fig. 1: Planform evolution of the bed at $t = 28$ h with using computational time-steps in the range of [0.02-0.16] s with the morphodynamic (a-d) equilibrium boundary and (e-h) sediment recirculation boundary.

Run	Δx [m]	Δt [t]	Run time [s]
P1505-E1	0.375	0.16	662
P1505-E2	0.1875	0.08	1911
P1505-E3	0.09375	0.04	8479
P1505-E4	0.046875	0.02	69215
P1505-R1	0.375	0.16	671
P1505-R2	0.1875	0.08	2011
P1505-R3	0.09375	0.04	8542
P1505-R4	0.046875	0.02	69520

TABLE I: Computational time obtained for the different scenarios assuming a constant CFL=0.2.

B. *Influence of physical parameters*

1) Sediment boundary condition: The comparison between numerical results obtained with the two different morphodynamic upstream boundary conditions measured over a period of 600.000 s shows that free bars are forming more upstream in the case of sediment recirculation (Figure 2c vs. g). The last observation suggests that the periodic condition of sediment recirculation enhances free bar dynamics with respect to the upstream equilibrium morphodynamic boundary condition. It is in agreement with the conclusions made by [19], as they observed the complete decay of bars after a given time, even if small topographic perturbations continue to grow in the current runs, giving rise to smaller amplitude bars (Figure 4). As a result, free bar dynamics is not completely stopped as the system remains under the unstable condition for bar formation, but morphodynamic evolutions are importantly reduced and in the case where the flume would be longer, bars would continue to grow before eventually reaching their equilibrium characteristics.

2) Bed slope effects: To quantify the influence of the bed slope effects on bar morphodynamics, a sensitivity analysis is carried out on the coefficients for the correction of bedload magnitude β_1 (=1.3 by default) and bedload deviation β_2 (=1.7 by default). Firstly, under the given configuration, numerical results show that bed slope effects affect very weakly the computed averaged sediment transport, where a difference between using $\beta_1 = 1.3$ and $\beta_1 = 2.5$ is less than 1%. While the formulation for bedload magnitude correction has no impact on bars properties because bar phase and dimensions are similar with various values of β_1 (Figure 5a), bedload deviation is showed to strongly impact bar morphodynamics (Figure 5b). In fact, increasing coefficients of deviation β_2 tend to increase bar amplitude by increasing the pool depth, resulting in a lateral constriction of the bedload transport over the lee side located at the opposite bank (Figure 5b and 6). Increase of β_2 is also followed by an earlier formation of bed perturbations and bars in the channel, that begins from around $x = 40$ m for $\beta_2 \geq 2$ (Figure 5). In terms of free bar

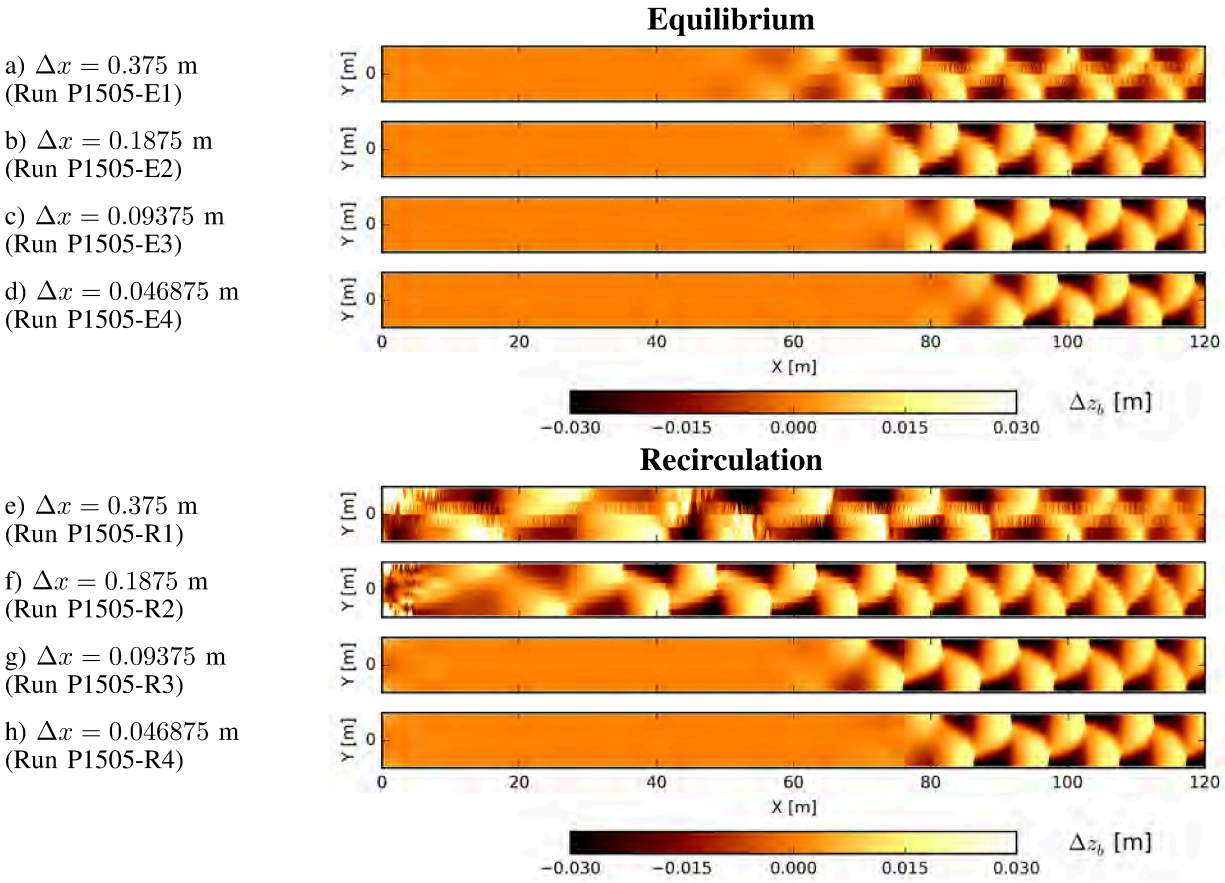

Fig. 2: Planform evolution of the bed at $t = 28$ h with using computational mesh sizes in the range of [0.046875-0.375] m with the morphodynamic (a-d) equilibrium boundary and (e-h) sediment recirculation boundary.

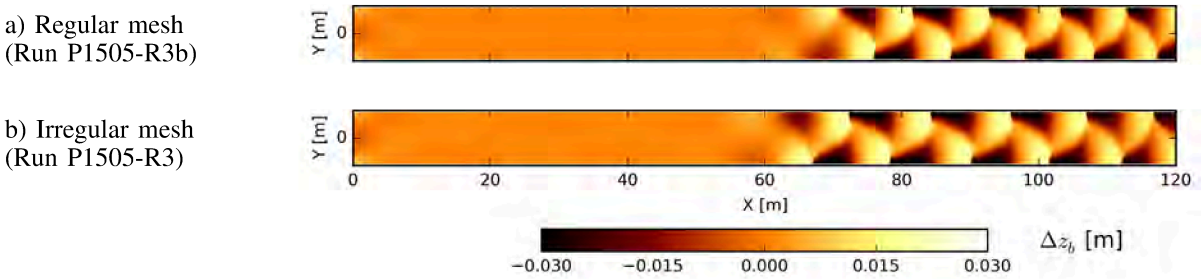

Fig. 3: Planform evolution of the riverbed at $t = 28$ h using a regular and an irregular computational mesh.

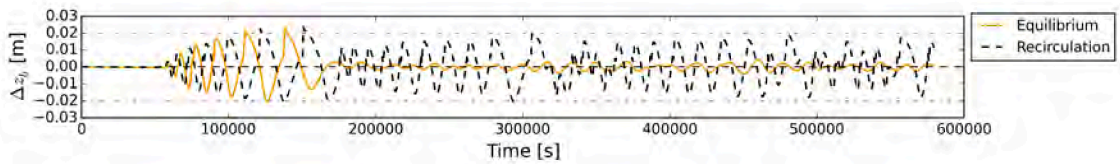

Fig. 4: Time-series of the bed evolution at (X=114 m;Y=0.375 m) with using the equilibrium and recirculation upstream morphodynamic boundary conditions.

morphology, the more β_2 increases, the more the longitudinal profile shows an irregular shape, with an abrupt transition between the bar top and the pool (*i.e.* lee side), which tends to form a terrace when $\beta_2 \geq 1.5$ (Figure 5b). When β_2 is decreased, bars display a smoother and more sinusoidal shape, resulting to a smaller bar amplitude. With $\beta_2 = 0.5$, bed perturbations are completely smoothed-out and bar formation is not observed.

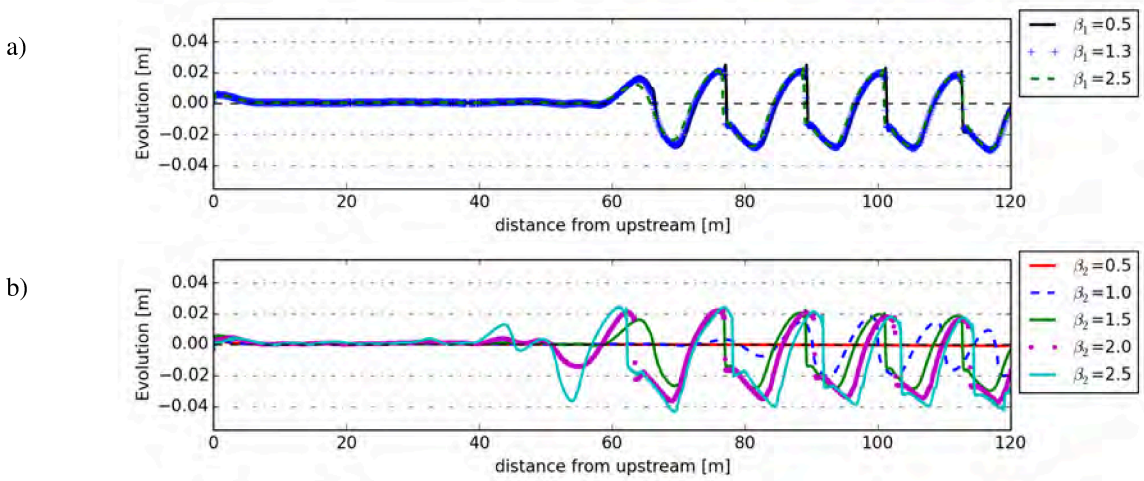

Fig. 5: Longitudinal profiles of bed evolution at 0.55 m from the left sidewall obtained with various coefficients for the correction of bedload a) magnitude β_1 and b) direction β_2.

Increasing β_2 immediately increases the lateral transport rate as illustrated on Figure 6, where the sediment is steered from the bar toward the pool. The highest magnitude of lateral transport rates is located close to the steepest bedslopes, *i.e.* on the transition between a bar top and a pool, and the lowest lateral transport rates are found in the *thalweg* and along the two sidewalls. Finally, increased β_2 increase the bar wavelength (Figure 5b and 6) and decrease the bar celerity, which is approximately 1.1 m/h with $\beta_2 = 2.5$ and 1.7 m/h with $\beta_2 = 1$.

Bars could not be obtained with the current model without accounting for bed slope effects, leading to an unrealistic bed evolution. This result is in agreement with the fact that slope effects are necessary to obtain bars numerically. The last outcomes also coincide with [12] who showed that including the effects of local high slopes in the numerical model can affect bar dynamics, and [22] who showed that slope effects control actively the bars topography, where the bed displays steeper cross-stream slopes when the slope effects are increased.

3) Skin friction correction: In this work, the authors propose to compare two types of models: a model assuming that the bed shear stress is equal to the total shear stress (i.e. $\mu = 1$); models that recompute the bed shear stress accounting for the bed surface roughness. Four numerical scenarios are used to assess the role of skin friction correction on computed equilibrium bar characteristics. The same approach is systematically used for each run, where a weighting coefficient which multiplies the transport rate computed with the bedload formula is calibrated in order to keep the averaged volumetric discharge close to the value measured in the laboratory [17]. This approach has been chosen to only evaluate the influence of the skin friction correction on computed bars properties, with excluding the impact on the averaged transport of sediment.

The skin friction correction is showed to impact significantly the sediment transport distribution over space and resulting bars morphology (Figure 7). Indeed, any variations of the coefficient α_{ks} modify the computed sediment transport rates and requires to calibrate the weighting coefficient of the bedload capacity formula α_b to compute relevant volumetric transport rates of sediment. Even if the same averaged sediment transport rate is computed for each scenario, the correction of skin friction impacts bar characteristics with damping the bar amplitude for increasing values of bed roughness (*i.e.* with increasing α_{ks}), showed in Figure 7. While the bar amplitude is decreased of 25% between experiments with $\mu = 0.5$ ($\alpha_{ks} = 3.7$) and $\mu = 0.75$ ($\alpha_{ks} = 10$), the bar wavelength is less affected with a small reduction of $\approx 5\%$, while the bar velocity is increased by $\approx 25\%$. In the case where the shear stress is equal to the total shear stress (*i.e.* $\mu = 1$), bar amplitudes are strongly decreased, and scale half the bar amplitude obtained with $\mu = 0.5$, which outlines that skin friction correction is a crucial physical parameter to compute free bar morphodynamics.

Results obtained using uniform sediment show that the parameterization of the friction correction plays an important role on the dimensions of bars (Figure 7). It suggests that, in presence of non-uniform sediment, this process should also have a strong influence on computed bars properties, because the planform spatialization of non-uniform sediment adds a degree of nonlinearity in the system with allowing for the variability of bed roughness and associated variability of α_{ks}.

4) Initial bed perturbation: Comparison between models without and with a uniformly distributed initial bed perturbation in the range [-5;5] mm shows that free bars formation is not necessarily due to the initial bed perturbation (Figure 8), but is rather due to the propagation of numerical disturbances [6]. Moreover, the formation of bed perturbations is clearly accelerated with introducing initial topographic perturbations (Figure 8). While bars are continually growing in amplitude and wavelength in the case where no initial topographic perturbation is used, the opposite phenomenon can be observed when using a randomly distributed initial perturbation. Finally, the initial random topographic perturbations used in this analysis seem not to affect significantly the long-term morphodynamics and equilibrium free bars characteristics.

IV. General Outcomes

In this work, a 2D morphodynamic model has been set-up and is able to reproduce laboratory experiments of free

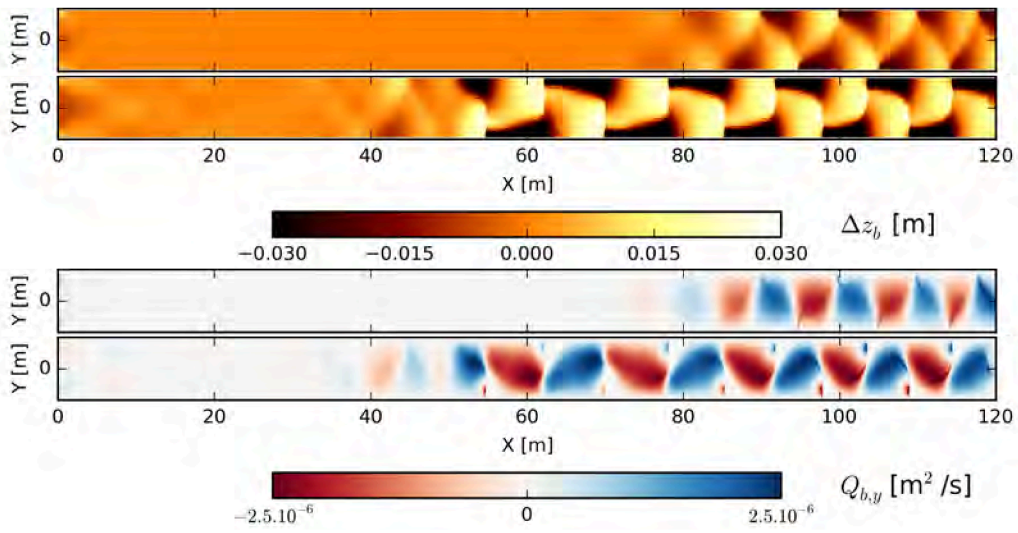

Fig. 6: Impact of the bedload deviation on planform bar morphology and cross-stream bedload transport rates at $t = 28$ h with $\beta_2 = 1$ and $\beta_2 = 2.5$.

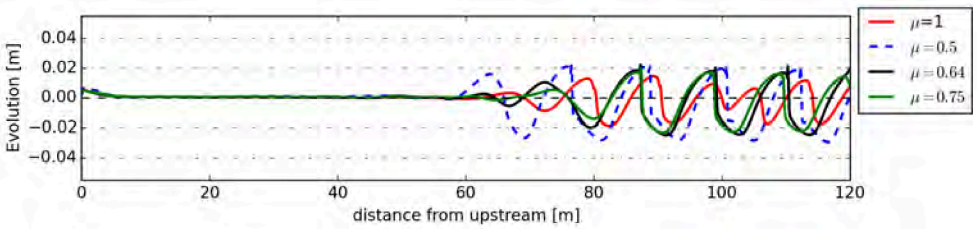

Fig. 7: Longitudinal profiles ($y = 0.55$ m) of the bed evolution plotted with different values of α_{ks} at $t = 28$ h.

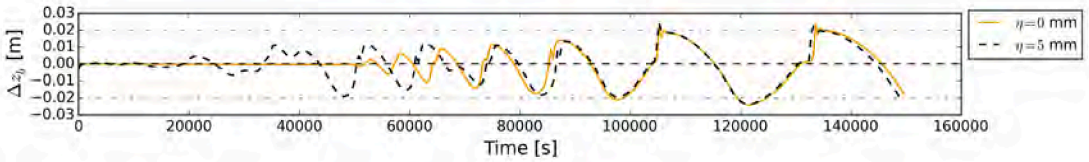

Fig. 8: Time-series of bed evolution at (X=102 m;Y=0.415 m) with using the equilibrium and recirculation upstream morphodynamic boundary conditions.

bar formation with uniform sediment. Before that, it has been necessary to investigate the impact of the numerical solution and physical parameters on the computed bar morphology and characteristics. Numerical results from this comprehensive numerical analysis firstly show that the domain discretization influences the propagation of the perturbation at the origin of free bar formation, where a finer computational mesh reduces the perturbation growth. This result particularly illustrates that the numerical truncation errors at the origin of these perturbations become more important when the computational mesh becomes coarser, and also explains why bars require a longer distance to form in comparison to the laboratory experiment. This analysis also shows that using approximately 15 to 20 cross stream computational nodes is enough to observe the bar features correctly, with a computational time which remains acceptable. Model convergence is attained with CFL values less or equal to 0.2. The use of two distinct morphodynamic boundary conditions shows that boundaries influence the computed bar dynamics. Sediment recirculation enhances free bar dynamics with respect to the equilibrium morphodynamic boundary condition. Numerical results are in agreement with the theory, which shows that gravity effects are necessary to trigger free bar formation, and also suggest that only the correction of bedload deviation determine whether bars should form or not. The formulation for skin friction correction is also showed to strongly modify free bars morphology, hence a careful parameterization is required to compute physically relevant bar dynamics. Outcome of this study can provide guidance to modellers for choosing the correct set of numerical and physical parameters to model relevantly free bars morphodynamics in straight or weakly-curved channels.

ACKNOWLEDGMENT

We would like to kindly acknowledge S. Lanzoni for sharing his experimental data. The authors gratefully acknowledge the support of Electricité de France (EDF).

VII. REFERENCES

[1] L. V. Bendegom, "Some considerations on river morphology and river improvement, de ingenieur vol. 59–4, pp. b1–11," *Dutch. English translation: Nat. Res. Council of Canada, Technical Translation*, vol. 1054, p. 1963, 1947.

[2] O. Cabrit, "Modélisation des flux pariétaux sur les tuyères des moteurs à propergol solide," Ph.D. dissertation, Montpellier 2, 2009.

[3] M. Colombini, G. Seminara, and M. Tubino, "Finite-amplitude alternate bars," *Journal of Fluid Mechanics*, vol. 181, pp. 213–232, 1987.

[4] F. Cordier, P. Tassi, N. Claude, A. Crosato, S. Rodrigues, and D. Pham Van Bang, "Influence of sediment size heterogeneity on free and hybrid alternate bar morphodynamics," *Water Resources Research*, vol. submitted, pp. 1–30, 2017.

[5] F. Cordier, P. Tassi, M. Jodeau, and B. Camenen, "Large-scale morphodynamics structures in the arc en maurienne river (france)," *River Flow 2016*, vol. 1, pp. n/a – n/a, 2016.

[6] A. Crosato, F. B. Desta, J. Cornelisse, F. Schuurman, and W. S. J. Uijttewaal, "Experimental and numerical findings on the long-term evolution of migrating alternate bars in alluvial channels," *Water Resources Research*, vol. 48, no. 6, pp. 1–14, 2012, w06524. [Online]. Available: http://dx.doi.org/10.1029/2011WR011320

[7] A. Crosato and E. Mosselman, "Simple physics-based predictor for the number of river bars and the transition between meandering and braiding," *Water Resources Research*, vol. 45, no. 3, pp. 1–12, 2009.

[8] A. Defina, "Numerical experiments on bar growth," *Water Resources Research*, vol. 39, no. 4, pp. 1–12, 2003.

[9] G. Duró, A. Crosato, and P. Tassi, "Numerical experiments to explore bar management by channel width variations," *E-proceedings of the 36-th IAHR World Congress*, vol. 1, pp. 1–4, 2015.

[10] F. Engelund, "Instability of erodible beds," *Journal of Fluid Mechanics*, vol. 42, no. 2, pp. 225–244, 1970.

[11] F. M. Exner, *Zur physik der dünen*. Hölder, 1920.

[12] S. Francalanci, L. Solari, and M. Toffolon, "Local high-slope effects on sediment transport and fluvial bed form dynamics," *Water Resources Research*, vol. 45, no. 5, 2009. [Online]. Available: https://agupubs.onlinelibrary.wiley.com/doi/abs/10.1029/2008WR007290

[13] Y. Fujita and Y. Muramoto, "Studies on the process of development of alternate bars," *Bulletin of the Disaster Prevention Research Institute*, vol. 35, pp. 1 – 33, 1985.

[14] M. H. García, "Sedimentation engineering," *Processes, Measurements, Modeling, and Practice. ASCE Manuals and Reports on Engineering Practice*, vol. 110, pp. 1–1132, 2008.

[15] J. Hervouet, E. Razafindrakoto, and C. Villaret, "Dealing with dry zones in free surface flows: a new class of advection schemes," in *Proceedings of the 34th World Congress of the International Association for Hydro-Environment Research and Engineering: 33rd Hydrology and Water Resources Symposium and 10th Conference on Hydraulics in Water Engineering*, A. Barton, Ed. Australia, 2011, pp. 4103–411.

[16] F. Koch and C. Flokstra, *Bed Level Computations for Curved Alluvial Channels: Prepared for the 19th IAHR Congress, New Delhi, India, February 1981*. Waterloopkundig Laboratorium, 1980.

[17] S. Lanzoni, "Experiments on bar formation in a straight flume 1. uniform sediment," *Water Resources Research*, vol. 36, no. 11, pp. 3337–3349, 2000.

[18] S. Lanzoni and M. Tubino, "Grain sorting and bar instability," *Journal of Fluid Mechanics*, vol. 393, pp. 149–174, 1999.

[19] A. Mendoza, J. D. Abad, E. J. Langendoen, D. Wang, P. Tassi, and K. E. K. Abderrezzak, "Effect of sediment transport boundary conditions on the numerical modeling of bed morphodynamics," *Journal of Hydraulic Engineering*, vol. 143, no. 4, p. , 2016.

[20] E. Meyer-Peter and R. Müller, "Formulas for bed-load transport," in *International Association for Hydraulic Structures Research*. IAHR, 1948.

[21] E. Mosselman, "Modelling sediment transport and morphodynamics of gravel-bed rivers," *Gravel-Bed Rivers: Processes, Tools, Environments*, vol. 1, pp. 101–115, 2012.

[22] P. A. Nelson, R. R. McDonald, J. M. Nelson, and W. E. Dietrich, "Coevolution of bed surface patchiness and channel morphology: 1. mechanisms of forced patch formation," *Journal of Geophysical Research: Earth Surface*, vol. 120, no. 9, pp. 1687–1707, 2015.

[23] I. Nezu, H. Nakagawa, and G. H. Jirka, "Turbulence in open-channel flows," *Journal of Hydraulic Engineering*, vol. 120, no. 10, pp. 1235–1237, 1994.

[24] H. Qian, Z. Cao, H. Liu, and G. Pender, "Numerical modelling of alternate bar formation, development and sediment sorting in straight channels," *Earth Surface Processes and Landforms*, vol. 607, pp. 613–622, 2016, eSP-15-0409.R2. [Online]. Available: http://dx.doi.org/10.1002/esp.3988

[25] D. Saint-Venant, *Comptes rendus hebdomadaires des séances de l'académie des sciences.* Gauthiers-Villars, July-December 1871, vol. 73, no. 1, ch. Hydrodynamique: Théorie du mouvement non permanent des eaux, avec application aux crues des rivières et à l'introduction des marées dans leur lit., pp. 147–154.

[26] F. Schuurman and M. Kleinhans, "Self-formed braid bars in a numerical model," in *AGU Fall Meeting Abstracts*, 2011.

[27] A. Siviglia and A. Crosato, "Numerical modelling of river morphodynamics: latest developments and remaining challenges," *Advances in Water Resources*, vol. 90, pp. 1–9, 2016.

[28] A. Siviglia, G. Stecca, D. Vanzo, G. Zolezzi, E. F. Toro, and M. Tubino, "Numerical modelling of two-dimensional morphodynamics with applications to river bars and bifurcations," *Advances in Water Resources*, vol. 52, pp. 243–260, 2013. [Online]. Available: http://www.sciencedirect.com/science/article/pii/S0309170812002928

[29] N. Struiksma and A. Crosato, *Analysis of a 2-D Bed Topography Model for Rivers*, W. O. Library, Ed. Wiley Online Library, 1989.

[30] A. Talmon, N. Struiksma, and M. Van Mierlo, "Laboratory measurements of the direction of sediment transport on transverse alluvial-bed slopes," *Journal of Hydraulic Research*, vol. 33, no. 4, pp. 495–517, 1995.

[31] C. Van der Meer, E. Mosselman, K. Sloff, B. Jagers, G. Zolezzi, and M. Tubino, *Numerical simulations of upstream and downstream overdeepening*, T. U. Press, Ed. RCEM 2011, Proceedings of the 7th IAHR Symposium of River, Coastal and Estuarine Morphodynamics, 2011.

[32] C. B. Vreugdenhil, *Numerical methods for shallow-water flow*. Springer Science & Business Media, 2013, vol. 13.

[33] T. Weiyan, *Shallow Water Hydrodynamics: Mathematical Theory and Numerical Solution for a Two-dimensional System of Shallow Water Equations*, ser. Elsevier oceanography series. Water & Power Press, 1992, no. vol. 55.

[34] G. Zolezzi and G. Seminara, "Downstream and upstream influence in river meandering. Part 1. General theory and application to overdeepening," *Journal of Fluid Mechanics*, vol. 438, pp. 183–211, 2001.

Sensitivity analysis to reflection and diffraction in ARTEMIS

Maria Amelia Araujo, Liam Fernand, John Bacon
Cefas, Pakefield Road, Lowestoft, Suffolk, NR33 0HT, UK
amelia.araujo@cefas.co.uk

Abstract - **A key element of simulating wave behaviour around man-made structures, e.g. piers or harbour walls is to understand the likely dominance of reflection or diffraction effects. Related to this is the selection of an appropriate reflection/absorption coefficient. There is little information in the literature regarding the values of reflection coefficients in piled structures and little published research work in the last decade specifically relating to the reflection/absorption coefficient. In this work, several sensitivity tests were conducted to better understand the behaviour of the ARTEMIS model and its response to different structures and the imposed reflection coefficient, to infer the most appropriate reflection coefficient to be used in piled structures. A theoretical arbitrary domain (200 m x 100 m) has been used to carry out a series of tests which consider various scenarios, including different types of structures: 1 wall (100m long); 2 walls (40m long and 20m spaced); 2 walls with a larger gap between them (30m long and 40m spaced); 3 walls (20m long and 20m spaced); 1 row of 21 piles (1m in diameter and 5m spaced); 1 row of 11 larger piles (2m in diameter and 10m spaced); 4 rows of 21 piles (1m in diameter and 5m spaced). For the wall simulations the chosen reflection coefficient was 0.85, and for the piles, reflection coefficients of 0.65, 0.95 and 1.0 have also been used. The transmission of wave energy was analysed for each case.**

Results from the various test cases show how a system dominated by reflection (walls) gradually becomes more dominated by diffraction (piles). Qualitatively, the piles show little reflection effects and patterns of energy distribution are relatively insensitive to the reflection coefficient. From a quantitative analysis and taking into account the few experimental observations available in literature, a reflection coefficient between 0.95 and 1.0 should be appropriate for piled structures where the pile spacing is about 5 times the diameter.

I. INTRODUCTION

A key task in simulating wave behaviour around man-made structures is determining the appropriate reflection/ absorption coefficients to apply. Walls reflect most wave energy whilst wave behaviour around piled piers is quite different, and an appropriate reflection/absorption coefficient is needed in the transition zone between the two effects. There is little information in the literature regarding values of reflection coefficients in piled structures and minimal published research work in the last decade specifically relating to the reflection/absorption coefficient. We aim to examine the sensitivity of the coefficient in the transition between reflection and diffraction.

The value used for the reflection coefficient is a critical parameter in ARTEMIS modelling, i.e. the ability of a solid boundary to reflect wave energy. This coefficient can be set in the model between a value of one (perfect reflector – no absorption of wave energy) and a value of zero where all energy is absorbed at the solid boundary [1]; each structure is considered as a boundary. Theoretically, the effect of using a reflection coefficient of 1 for a solid boundary (no absorption of energy) means that no attenuation of waves occurs as they pass through that boundary. A reflection coefficient near 0 has the opposite effect, and each contact of waves with the boundary absorbs energy such that after propagating through several solid boundaries almost all the wave energy was absorbed. In this work, several sensitivity tests were conducted to better understand the behaviour of the ARTEMIS model and its response to different types of structures and the imposed reflection coefficient. This helps addressing questions such as when does diffraction from a structure dominate over reflection.

Research carried out at the Field Research Facility (FRF) at the US Army Corp of Engineers, Duck, North Carolina, during the last decade, shows some of the difficulties in determining the correct values for reflection, or absorption, of wave energy by piled structures. The facility at Duck includes a shore-normal jetty which extends from the shoreline, for 561m into water with depth of ~6m. The jetty features two lines of support piles and the pile diameter is 0.85m. The FRF facility has hosted much coastal research during the last 20 years and provides comprehensive datasets of waves being attenuated by the jetty structure. [2] used FRF data to compare the performance of two wave models (CGWave and SWAN) under storm conditions. Both models are less complex than ARTEMIS, although as a phase resolving model CGWave is closest to ARTEMIS and bases mesh density on wavelength (minimum 10 nodes per wavelength), whereas SWAN, a spectral energy model, is closest in type to TOMAWAC and uses an orthogonal, 8m grid based on bathymetry. A feature of the FRF Jetty is a distinct bathymetric "low" under the structure and whilst design details are not known, would suggest significant local erosion (scour) has occurred due to turbulence generated by the piles emerging from the seabed. Due to the specific working of each model (CGWave includes a reflection/diffraction effect but SWAN does not), direct comparison of the mechanisms leading to wave attenuation was not possible. [2] concludes that the pier piles had little effect to block propagating waves and that the effects seen on the wave field were due to the bathymetric "trench" under the jetty. Work performed by [3] presents transmission coefficients for closely spaced lines of piles. Even when the

gap is 0.2 times the pile diameter, their results show a transmission coefficient (ratio of transmitted to incident wave height) of 80% or more. Flume tests carried out by [4] on a 4 x 4 array of piles with spacing 2 times the pile diameter gave transmission coefficients of 90-95%.

II. METHOD

In order to better understand the behaviour of the ARTEMIS model and address the issues of wave reflection compared to diffraction, a series of theoretical tests were conducted, which included response to reflection coefficient. The ARTEMIS model aims to simulate, reflection, diffraction, refraction and wave-wave interactions. A theoretical arbitrary domain (200m x 100m) has been used, with a flat bathymetry- eliminating refraction effects- (-5m in all the domain). Monodirectional random waves with a peak period of 6s, wave direction of 180° and incident wave height of 0.5m have been applied at the southern boundary; waves are able to freely leave the domain. Bed friction is constant across the domain, using the formulation of Putnam and Johnson. These conditions, using the intermediate depth wave formulation, correspond to a wavelength of 38m. The incident wave energy for these scenarios was 306.5J/m^2.

Various scenarios have been considered in the domain, including different structures: 1 wall (100m long); 2 walls (40m long and 20m spaced); 2 walls with a larger gap between them (30m long and 40m spaced); 3 walls (20m long and 20m spaced); 1 row of 21 piles (1m in diameter and 5m spaced); 1 row of 11 larger piles (2m in diameter and 10m spaced); 4 rows of 21 piles (1m in diameter and 5m spaced). A reflection coefficient of 0.85 was selected for the wall cases, although for the scenarios with the piles, the reflection coefficients of 0.65, 0.95 and 1.0 have also been considered (a sub set are shown here).

III. RESULTS

Fig. 1 presents the wave energy for a solid wall, using a reflection coefficient of 0.85. It shows how reflected waves interact with the oncoming waves travelling in different directions, combining their energy and forming interference patterns. This results in regions where increases occur in wave height where the waves combine, alternating with regions of decreased wave height where they cancel out (standing waves). At the end of the wall is a region of diffraction with increased energy at the edge.

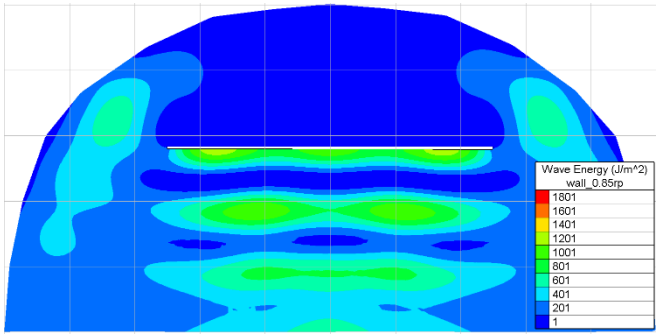

Figure 1. *Wave Energy: Solid wall case; reflection coefficient 0.85. Incident wave from South.*

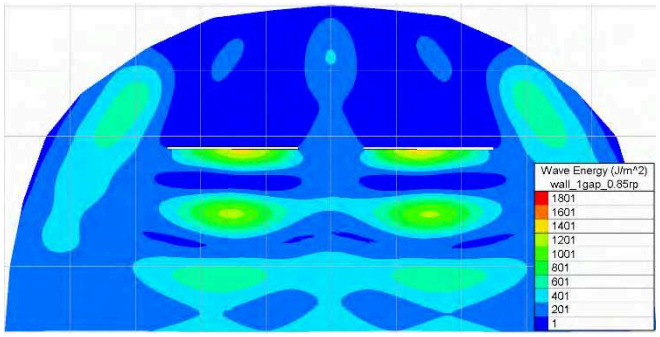

Figure 2. *Wave Energy: 2 Walls 40m long and 20m gap. Reflection coefficient 0.85.*

The wave energy for the scenario using 2 walls is represented in Fig. 2, where the standing waves are still evident in front of the walls, but to a reduced extent. There is some limited passage of energy through the gap between the walls. In Fig. 3, for the three wall simulation, a significant increase in wave energy is observed directly in front of the walls. Away from the walls, the maximum energy is aligned with the gaps. There is greater energy propagating behind the wall with diffracted waves interacting to produce zones of high energy. Fig. 4 shows the wave height and direction associated with the single wall; limited diffraction can be seen around the edges of the wall. In the three wall case (Fig. 5) diffraction is greater and leads to wave-wave interaction increasing wave height behind the walls. In all of these cases, the reflected waves have increased in energy in front of the structure.

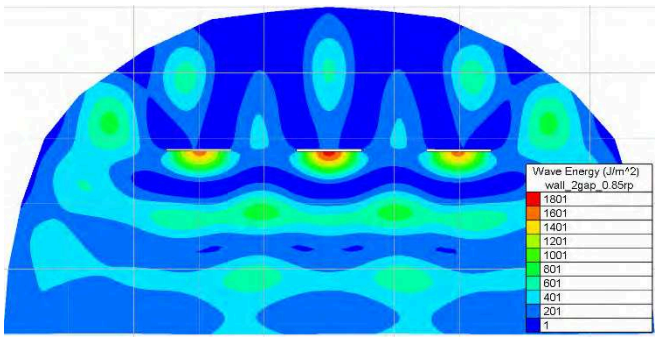

Figure 3. *Wave Energy: 3 Walls 20m long and 20m gap. Reflection coefficient 0.85.*

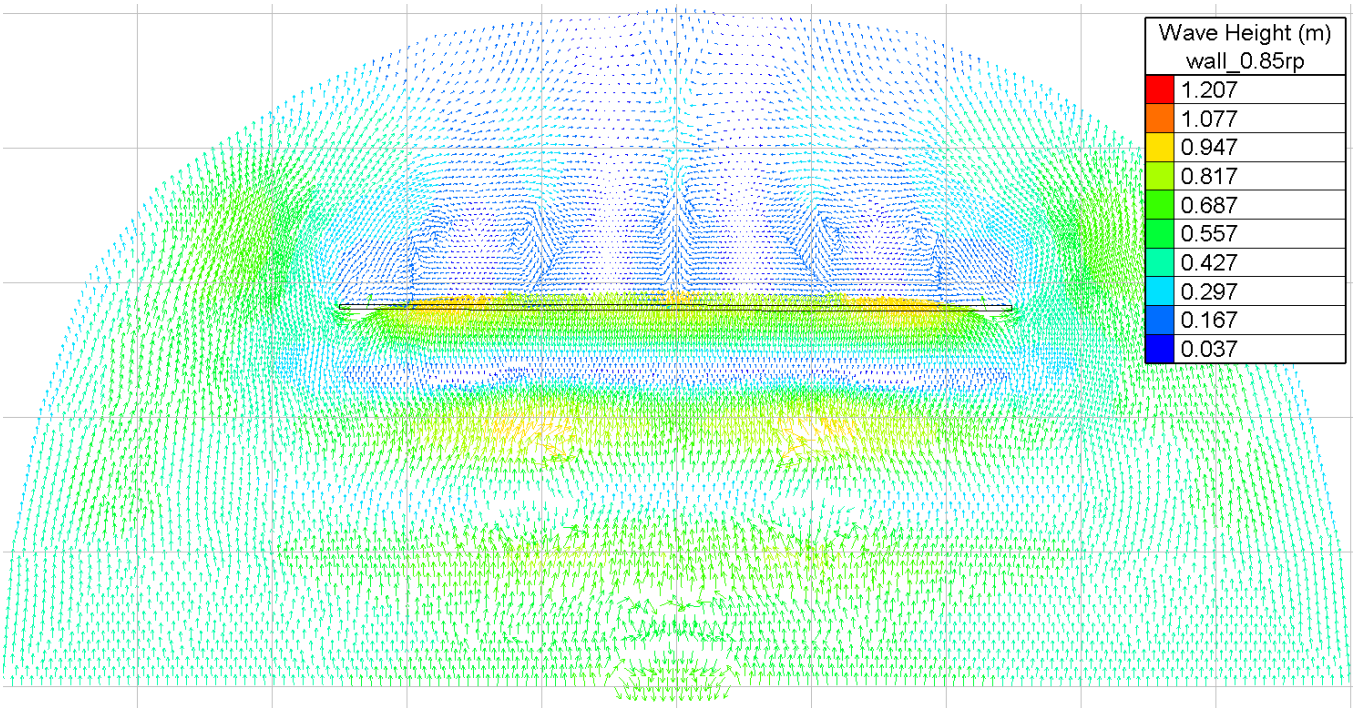

Figure 4. *Wave Height (colour scale) and direction arrows for single wall. Reflection coefficient 0.85.*

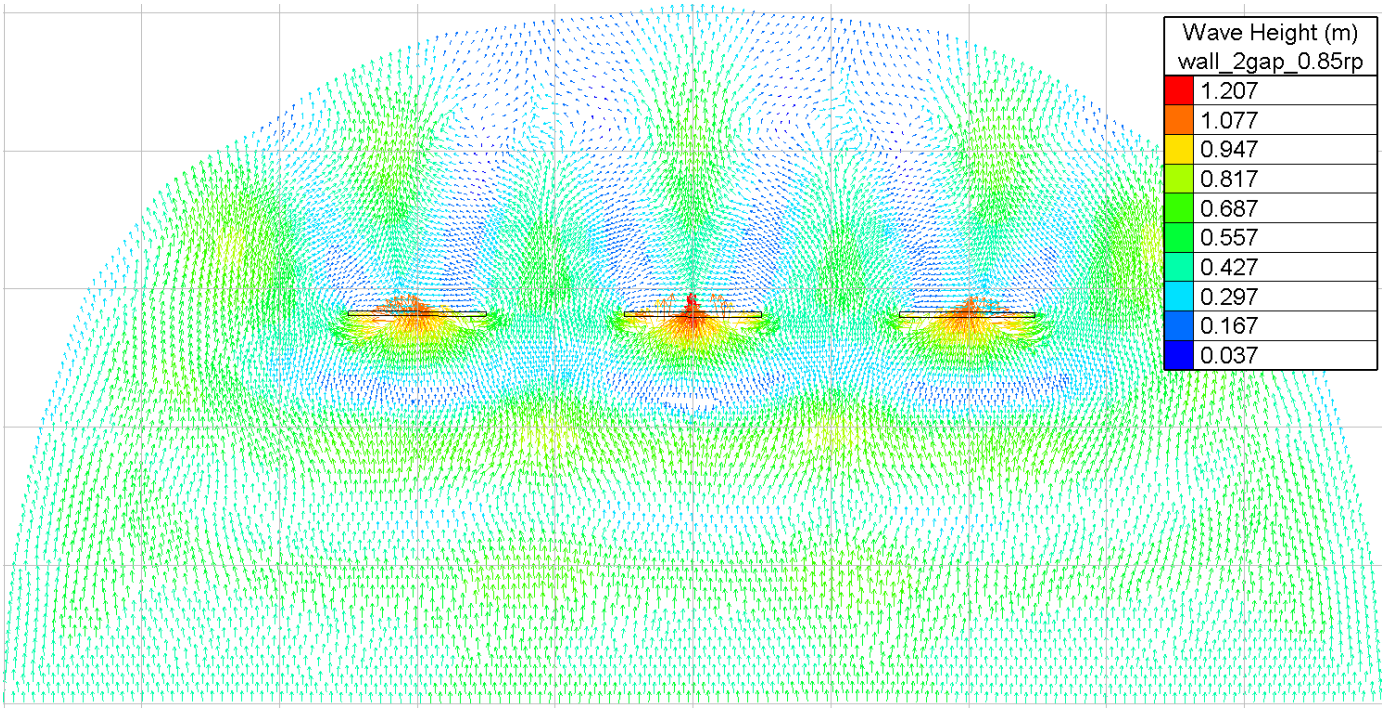

Figure 5. *Wave Height (colour scale) and direction arrows for three 20m walls spaced 20m. Reflection coefficient 0.85.*

Considering densely piled structures, Fig. 6 shows the effect of a single row of piles, while Fig. 7 presents the effect of the multiple layers of piles. The effects of reflection are almost unnoticeable; there is an increase in wave height behind the structure where diffracted waves interact with decreased wave height at the edge of the piles. There is little difference between the 1 row or 4 row simulations. In the transition from the walls (Fig. 5) to the piles configuration (Fig. 6), it is possible to see a substantially lower impact of the piles on the wave height either in front of the piles or behind them.

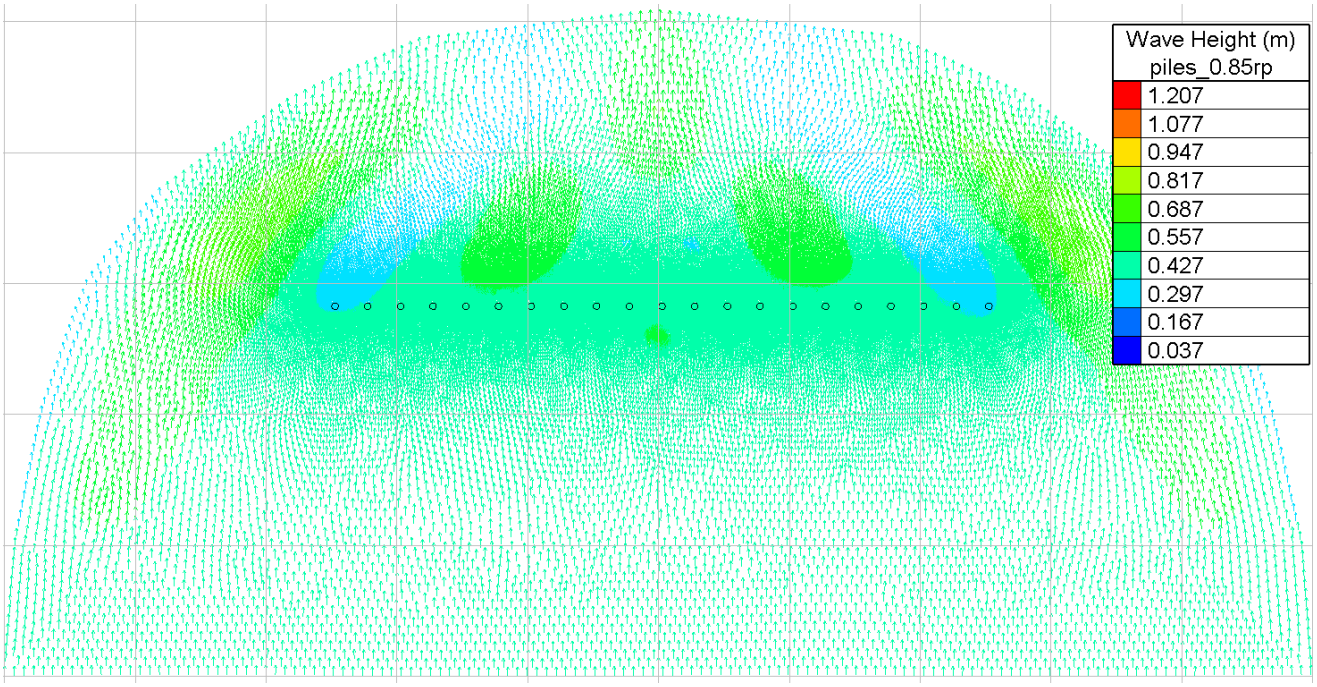

Figure 6. *Wave Height (colour scale) and direction arrows for a piled structure of 1 row of 1m diameter piles with 5m spaces. Reflection coefficient 0.85.*

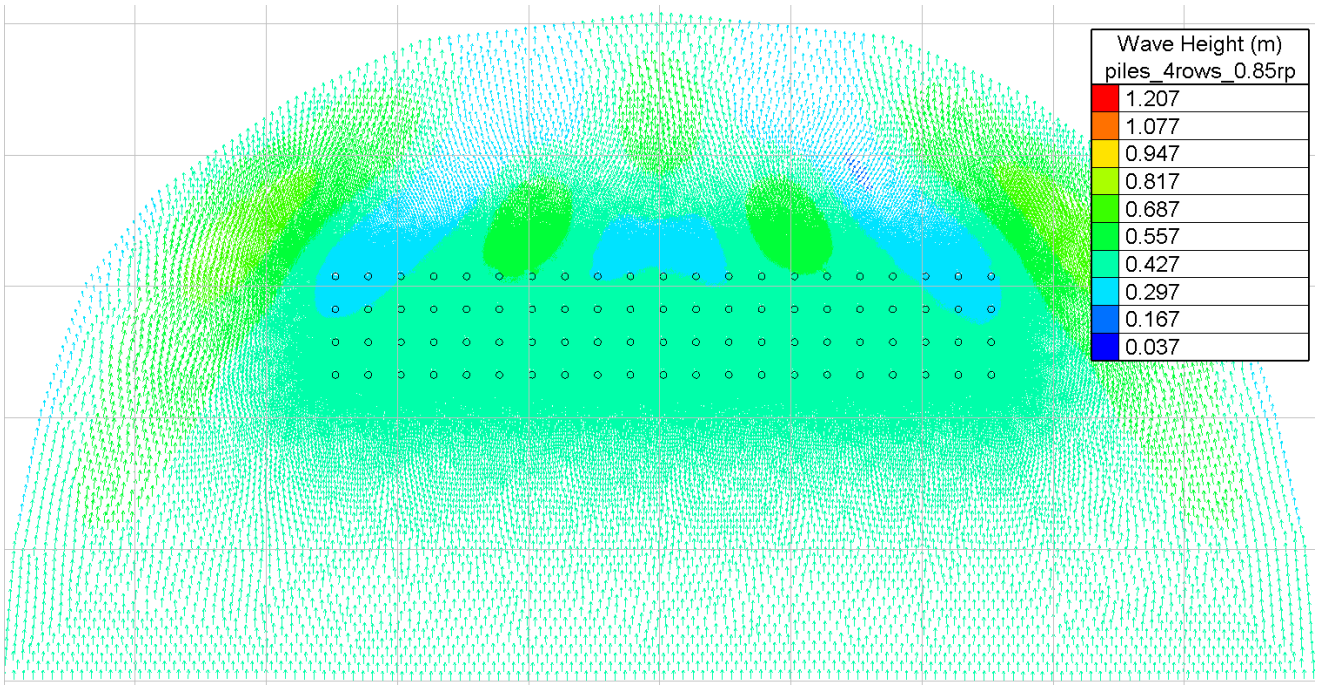

Figure 7. *Wave Height (colour scale) and direction arrows for densely piled structures of 4 rows 1m diameter piles with 5m spaces. Reflection coefficient 0.85.*

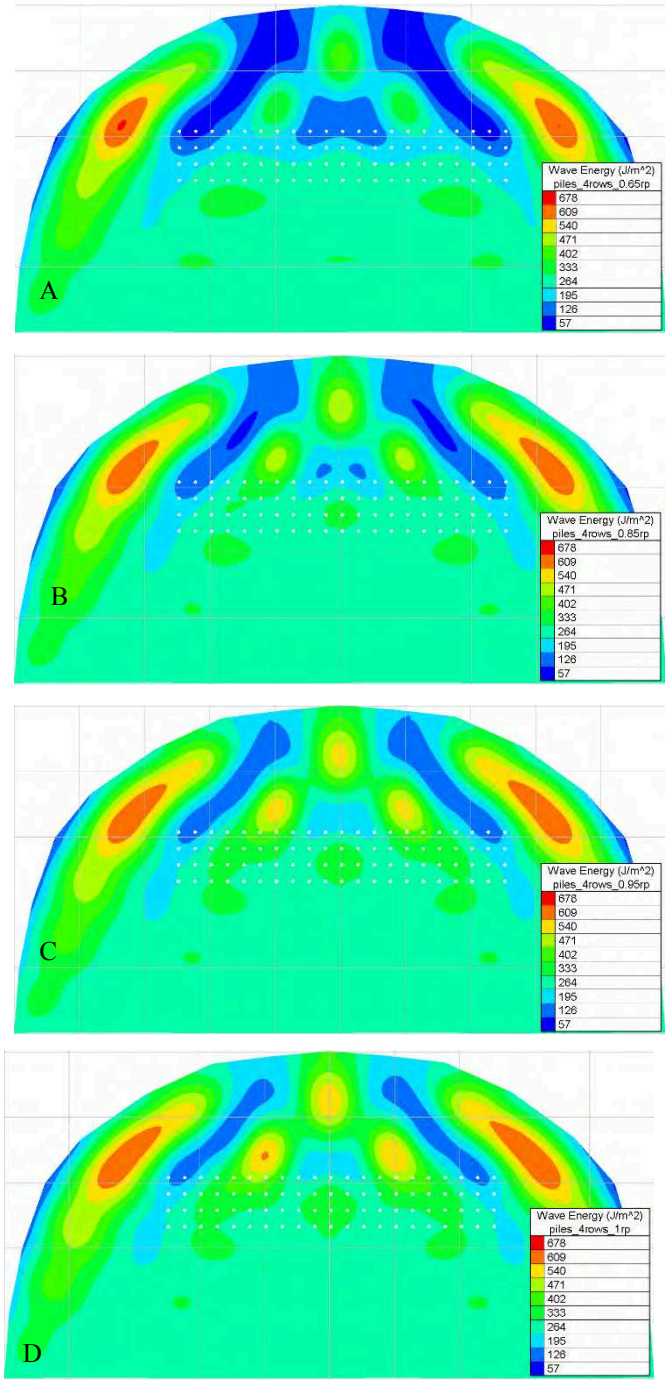

Figure 8. *Wave Energy from simulations on four rows of piles, for different reflection coefficients: A) 0.65, B) 0.85, C) 0.95, D) 1.0 (a perfect reflector).*

Fig. 8 presents the wave energy for the simulations using 4 rows of piles. The effect of changing the reflection coefficient, from 0.65 (A) to a perfect reflector (D), is shown in this figure. Evident is the relatively little difference between the scenarios, in qualitative terms, presenting similar patterns. Some of those external patterns might be related to boundary effects. Either side of the piles are zones of increased wave energy, and behind the piles (North) are zones of decreased energy. The exact amount of reduction does vary between each scenario (see the quantitative analysis in Table 1). At the scale presented, there is little difference between the scenarios in the wave energy in front of the piles.

With a reflection coefficient of 1.0 it is actually expected some evidence of waves reflected from the piles, leading to increases in wave energy on the incident side and a small reduction in wave energy transmitted.

Table 1 presents the maximum percentage decrease in wave energy behind the obstacle (considering the piles scenarios with 1 row and with 4 rows), for the various reflection coefficients investigated. Some of those percentages are referred to a small localized region. As expected, when increasing the reflection coefficient, the effect of the piles is less pronounced.

TABLE 1 PERCENTAGE DECREASE IN WAVE ENERGY BEHIND THE PILE ROWS FOR DIFFERENT REFLECTION COEFFICIENTS

Reflection coefficient	% decrease	
	piles_1row	piles_4rows
0.65	63.1	81.4
0.85	56.6	66.4
0.95	53.6	56.9
1	52.7	52.0

IV. SUMMARY

In this work, the response of Artemis model to structures with different geometry and by imposing a range of reflection coefficients has been investigated. The physical structures considered in the study were walls and piles, configured in different ways, and the reflection coefficients were 0.65, 0.85, 0.95 and 1.0. The simulations demonstrate the progression from a system dominated by reflection (i.e. walls) to that where diffraction is the dominant aspect (i.e. piles) and when reflection itself is of relatively low importance. As the solid structure becomes smaller, the effect of reflection become less significant and diffraction becomes the dominant effect. As a consequence, the wave transformation imposed by the structure takes place differently, resulting in piles having a smaller impact. Although a qualitative analysis shows small changes in the wave energy patterns, a quantitative assessment presents localized differences in the maximum percentage decrease in wave energy behind the piles, for the various reflection coefficients. Based on these numerical results and considering the few experimental observations available in literature, a reflection coefficient between 0.95 and 1.0 should be appropriate for piled structures with a pile spacing about 5 times the diameter, representing near perfect reflection. As a result, high transmission of wave energy will take place and the piles have little effect on the transmission of the waves through the structure.

ACKNOWLEDGEMENT

This work was funded by EDF through the BEEMS programme.

REFERENCES

[1] EDF, "The TELEMAC Modelling System - Theoretical Note and User manual - ARTEMIS software for Wave Agitation", version 6.2, 2012.

[2] K. Zubier, V. Panchang, and Z. Demerbilek, “Simulation of waves at Duck (North Carolina) using two numerical models”, Coastal Engineering Journal, Vol 45, No 3, pp 439-469, 2003.

[3] C. Truitt, and J. Herbich, “Transmission of random waves through pile breakwaters”, Coastal Engineering, Chapter 169, pp. 2303-2313, 1986.

[4] B. Van Weele, “Wave reflection and transmission for cylindrical pile arrays”, MS Thesis, May 1965, Reprint no 313. Fritz Laboratory Reports, Paper 183, 1965.

Two-dimensional modelling of flow conditions generated by piled piers and turbulence-based erosion risk assessment

Pierre-Louis Ligier
Hydropower and Dams Department
Sweco Energuide AB
Stockholm, Sweden
pierre-louis.ligier@sweco.se

***Abstract*—A hydraulic study has been performed in the Gavleån River in Sweden, to assess the impacts of an architectural project composed of piled piers to be built into the riverbed in the city centre of Gävle. The aim of the study was to assess the impacts in terms of high water levels, change in flow conditions and erosion risk. Hydraulic modelling was performed with a two-dimensional model, TELEMAC-2D. The article presents a description of the study area, of the architectural project and of the hydraulic model. A description of the methodology used to model the piers is given, with some of the piers having their deck being submerged during high flows, thus inducing an increased flow resistance. The impacts of the project are an increase of flow velocities in the centre of the river due to flow contraction between piers and quays and an increase of turbulence below the piers generated by the piles. The erosion risk has been assessed with a turbulence-based approach, in which the bottom shear stress is calculated from the turbulence parameters given by the k-ε turbulence model instead of from the local depth-averaged flow velocity and bed friction parameters.**

I. INTRODUCTION

A hydraulic study has been performed in the Gavleån River in Sweden, to assess the impacts of the "Å-rummet" architectural project composed of piled piers to be built into the riverbed in the city center of Gävle. The aim of the study was to assess the impacts in terms of high water levels, change in flow conditions and erosion risk. Firstly, the article gives a presentation of the study area and of the Å-rummet project. In a second part, the two-dimensional hydraulic model developed, using the software TELEMAC-2D, is detailed and the method used to account for flow resistance generated by the piers is described. The project impacts on water levels and flow velocities are then analyzed. Finally, the method used to perform the erosion risk assessment, which is based on turbulence parameters, is presented and results are discussed. The work presented in this article has been performed as part of a consulting assignment during approximatively 70 hours.

II. STUDY AREA AND PROJECT DESCRIPTION

The city of Gävle is located approximately 170 km north of Stockholm, Sweden, where the Gavleån River is released into the Baltic Sea, see Fig. 1. The last 2.5 km of the Gavleån River are located in the city centre of Gävle where the river

Figure 1: Geographical location of the city of Gävle, Sweden (red dot).

Figure 2: Overview of the city of Gävle and loation of the Å-rummet project in the Gavleån River.

banks are artificial and composed of quays and harbour piers. The city of Gävle has started a recreation project called "Å-rummet" which aims at making the centre of the city and the

promenade along the river more attractive by building piers within the riverbed. The location of the Å-rummet project within the city centre is depicted in Fig. 2. Artistic illustrations of the planned piers are presented in Fig. 3.

The Å-rummet project consists of building nine piers and two pedestrian bridges on a total length of about 500 m at the upstream part of the artificialized reach, see Fig. 4. The pedestrian bridges will not interfere with the river for any discharge and have therefore no significance regarding hydraulic impacts. The nine piers will be divided into three types with i) pier 1 composed of a concrete slabs founded on piles, ii) piers composed of steel structures founded on piles (pier 3, 6, 7, 8 and 9) and iii) suspended piers composed of steel structures without contact with the riverbed (pier 2, 4 and 5). The piers can be temporary submerged depending on river discharges and downstream sea levels. The three pier types are illustrated in Fig. 5. Pier 1 has a total length of approx. 190 m and a width of approx. 10 m. Its lower face has varying elevations, ranging from 0.2 to 1.0 m above mean sea level in the downstream direction. The other piers are much smaller with horizontal dimensions of approx. 5 x 10 m and their lower faces are located at different elevations, the lowest being 0.9 m above mean sea level.

The piles have a diameter of 0.3 m including an ice protection layer. The structure of the piers' lower face is composed of either concrete (pier 1, height 0.4 m) or steel beams (other piers, height 0.195 m) that will generate friction and turbulence when submerged. The expected impacts induced by the piers are additional head losses and increased turbulence generated by the piles and by the piers' lower face roughness leading to a redistribution of the velocities across the river.

Figure 3: Artistic illustration of the Å-rummet project. Pier 1 seen from downstream.

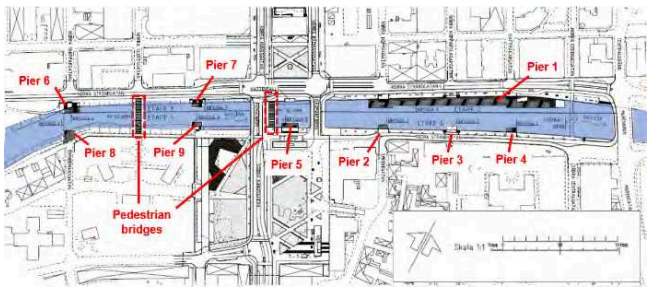

Figure 4: Overview of the Å-rummet project. Flow direction: left to right.

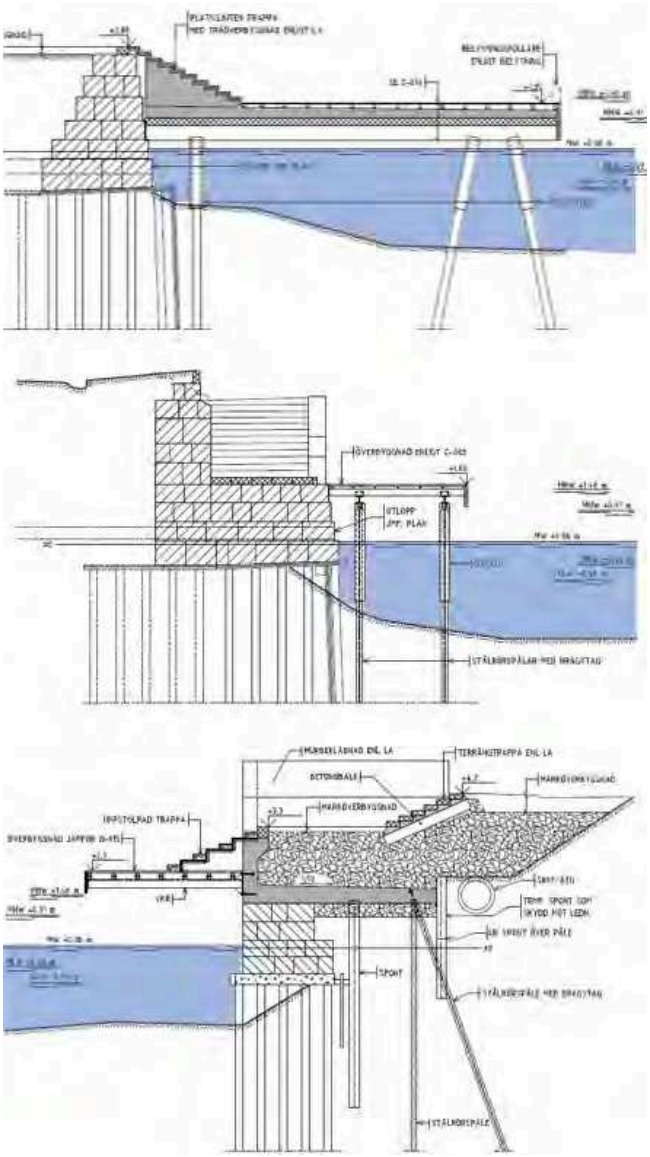

Figure 5: Three different pier types. Top: concrete slab founded on piles (pier 1). Middle: steel structures founded on piles (pier 3, 6, 7, 8 and 9). Bottom: suspended steel structures without contact with the riverbed (pier 2, 4 and 5).

III. PRESENTATION OF THE HYDRAULIC MODEL

A. Type of hydraulic model

The flow conditions in the estuary of Gavleån River can be complex due to the discharge of fresh water in a stratified water body (Baltic Sea). However, in this part of the Baltic Sea the salinity is low with values in the range of 6 g/l with a weak stratification. The water depths in Gavleån River are rather small (maximum 3 m along the Å-rummet project) which means that during flood events the flow conditions are likely to be close to two-dimensional.

The Å-rummet project adds complexity to the flow conditions especially when piers start to be submerged. However, the study presented in this article has been performed with a two-dimensional hydraulic model (TELEMAC-2D version 7.1). This assumption is reasonable

as i) not all the piers are submerged, ii) the area of the submerged piers is small (excepted for pier 1) and iii) the absence of calibration data and detailed riverbed material data prevented from using a three-dimensional model.

B. Mesh and bathymetry

The computational meshes covers approx. 2.5 km of Gavleån River from upstream of the Å-rummet project down to the river mouth in the harbour area (see Fig. 6). Two meshes were created, one for the current state geometry and one for the project geometry. Mesh size is approx. 1 m along the Å-rummet project and approx. 3 m downstream. The mesh has been refined around existing bridge piles with a mesh size of approx. 0.5 m and pier piles of the Å-rummet project has been discretized with a mesh size of approx. 0.1 m (see Fig. 7). It has been assumed that all piles a purely vertical. Current state and project meshes are composed of approx. 77,000 and 111,500 triangular elements, respectively.

A digital elevation model has been created using available echo sounding survey, bridge drawings and LIDAR data for land in the upstream bend (see Fig. 8). Water depths in Gavleån River related to mean sea level are comprised between 1.5 and 3 m along the Å-rummet project and progressively increase in the downstream direction to reach approx. 4 to 5 m below the railway and highway bridges and

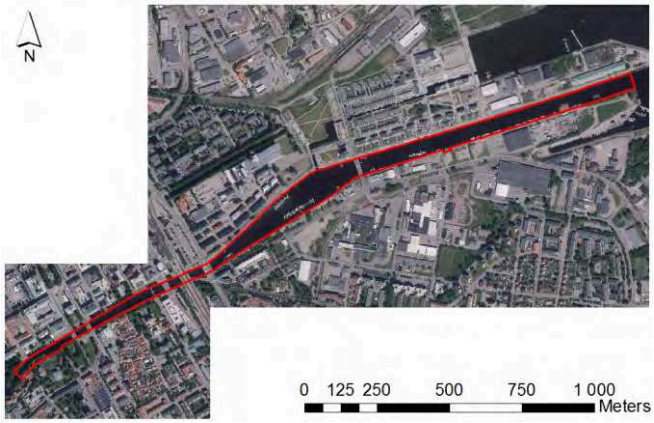

Figure 6: Model domain.

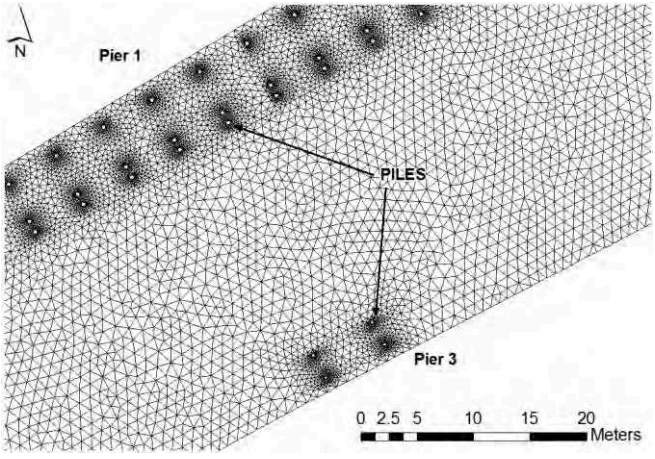

Figure 7: Detailed view of the mesh for the project geometry.

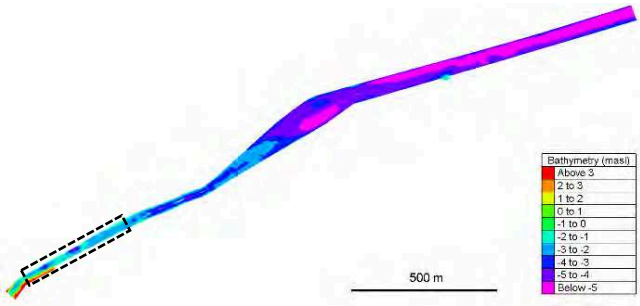

Figure 8: Digital elevation model. Project location is indicated by the dashed polygon.

approx. 4 to 6 m in the lower part of the reach just upstream the river mouth.

C. Numerical parameters

Bottom friction has been modelled using Strickler's friction law with a friction coefficient of 25 $m^{1/3}/s$ based on available information on river geometry and riverbed material and existing hydraulic studies in the same river reach. It is recalled that no calibration data was available meaning that the absolute results are somewhat uncertain but the relative differences on both water levels and flow velocities between the current state and project geometries can be assessed with a reasonable level of uncertainty. Simulations were performed with a time-step of 0.1 second until steady state conditions were reached. Turbulence was modelled with a k-ε turbulence model which offers the advantages of providing the local depth-averaged turbulent kinematic energy used in the erosion risk assessment as well as being a well-established model for river flow applications.

D. Modelling of flow resistance induced by the piers

The flow resistance induced by the piers is generated by the piles and by the submerged decks. The flow resistance generated by the piles is modelled directly by the hydraulic model as each pile is included in the model geometry. The submerged decks generate two types of flow resistance with i) additional friction generated by the irregular profile of the lower face (beams) and ii) flow contraction once the deck structure itself is submerged. Friction term is expressed as shear stress, see Eq. 1 [1].

$$\vec{\tau} = -\frac{1}{2} \cdot \rho \cdot C_f \cdot U \cdot \vec{U} \quad (1)$$

Where $\vec{\tau}$ is the shear stress vector (N/m^2), ρ the water density (kg/m^3), C_f the quadratic friction coefficient (-), U and $\vec{U}$ the depth-averaged velocity component and vector, respectively (m/s). The quadratic friction coefficient is dimensionless and can be expressed by different friction law such as Strickler and Nikuradse, see Eq. 2 and Eq. 3.

$$C_{f,St} = \frac{2 \cdot g}{St^2 \cdot h^{1/3}} \quad (2)$$

$$C_{f,ks} = 2 \cdot \left[\frac{\kappa}{ln\left(\frac{11 \cdot h}{k_s}\right)} \right]^2 \quad (3)$$

Where St is the Strickler friction coefficient (m$^{1/3}$/s), h the water depth (m), g the gravitational acceleration (9.81 m/s^2), κ the von Karman constant (0.4) and k_s the equivalent sand roughness coefficient (m).

Bottom friction is modelled using Eq. 2 as detailed in section III.C above. The additional friction induced by the submerged decks has been modelled with Eq. 3 in which the equivalent sand roughness is taken as the submerged height of each beam, based on local water level, see Eq. 4.

$$k_s = MIN\left(H_B; (WL - LF_B)\right) \quad (4)$$

Where H_B is the total beam height (0.4 m for pier 1, 0.195 m for other piers), WL the local water level (masl) and LF_B the elevation of the beam's lower face (masl). The LF_B parameter values have been assigned to mesh nodes using the PRIVATE VARIABLES procedure making it possible to compute the actual equivalent sand roughness coefficient at each computational node.

Friction terms have then been modelled with $C_f = C_{f,St}$ at nodes affected by bottom friction only and with $C_f = C_{f,St} + C_{f,ks}$ at nodes affected by both bottom and pier friction. Flow contraction effects have not been modelled. The absence of calibration data and detailed riverbed material survey prevented from using the Nikuradse friction law to model bottom friction. This approach would have been preferable in order to ensure that the total quadratic friction coefficient could be based on the same friction law. Nonetheless, the method used in this study can be considered as acceptable being given the uncertainties and simplifications at play (calibration data, material, 2D model) in relation to the study's scope.

E. Boundary conditions and simulated cases

Simulations have been performed for a combination of two design flows prescribed at the upstream boundary (Q_{50} = 168 m^3/s and Q_{100} = 210 m^3/s) and three sea levels prescribed at the downstream boundary (mean sea level +0.06 m, average of yearly highest sea levels +0.91 m and average of yearly lowest sea levels -0.49 m).

IV. PROJECT IMPACTS ON WATER LEVELS AND FLOW VELOCITIES

A. Water levels

The project impacts on water levels have been estimated by comparing longitudinal profiles extracted in the river axis for the two simulated geometries for each flow case. Such a comparison is presented in Fig. 9 for the 100-year flood combined with a mean sea level. Results show that for this particular flow case pier 1 is submerged on nearly all its length (approx. 180 m) with a maximal submergence of approx. 0.8 m at the upstream end. This generates head losses in the reach in which water levels increase between 0.09 m and 0.25 m upstream of pier 1. For this particular flow case, pier 6, 7 and 9 are also submerged while pier 3 and 5 have only a

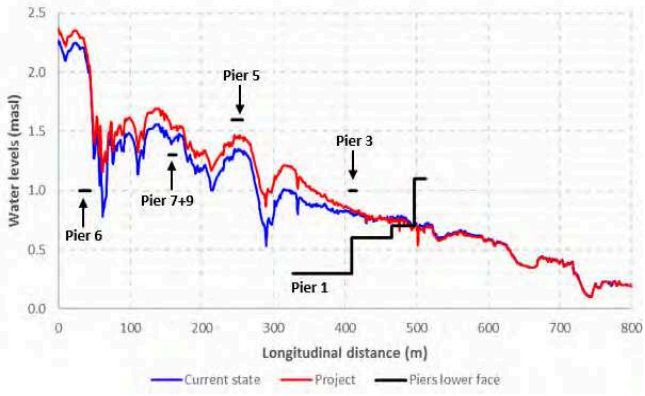

Figure 9: Water level evolutions. Longitudinal profile in river axis. 100-year flood with mean sea level.

0.15 m freeboard. Pier 2, 4 and 8 are located above elevation +3.0 m and are thereby not affecting flow conditions. Project impacts for other flow cases are varying within ± 0.05 m from the impacts presented above.

B. Flow velocities

As for water levels, impacts are presented for the 100-year flood combined with a mean sea level flow case. Analysis of flow velocities in current state shows that strong velocities occur at the upstream end of the Å-rummet project location, just downstream of pier 6 due to a cross section contraction at the end of the bend (approx. 5 m/s). Flow velocities along the project location are mainly varying between 2.0 and 3.5 m/s. Along pier 1 flow velocities are somewhat lower, especially in the downstream part, ranging from 1.0 to 2.5 m/s.

The velocity evolutions generated by the project are strongest in the reach along pier 1 and 3 with i) a decrease of velocities under pier 1 up to -1.5 m/s along the outer pile row exposed to flow, ii) a decrease of velocities up to -0.3 m/s in the wake of pier 3 and iii) an increase of flow velocities in the middle of the river up to 0.5 m/s due to the flow contraction generated by pier 1 and 3 (see Fig. 10). Detailed analysis of velocity changes along pier 1 reveals that the velocities are lowered mainly in the wake of the pile rows and in the upstream half of the pier where submergence is high (see Fig. 11). Upstream of pier 1 and 3 the flow velocities are less impacted. The most significant evolution is a flow contraction between pier 7 and 9 generating a velocity increase of approx. 0.2 m/s.

A simulation comparing flow velocities with and without the additional pier friction term has been run in order to analyse the influence of this additional friction term on the results. Comparison is presented in Fig. 12. It can be seen that the pier friction generates a decrease of flow velocities at and in the wake of pier 1, 6 and 7, leading to slightly different cross-sectional velocity profiles. The influence is strongest at pier 1 between the two pile rows where pier friction reduces the velocities by approx. -0.15 m/s (i.e. approx. 10%) while flow velocities in the centre of the river are approx. 0.05 m/s higher than the case without pier friction (flow contraction).

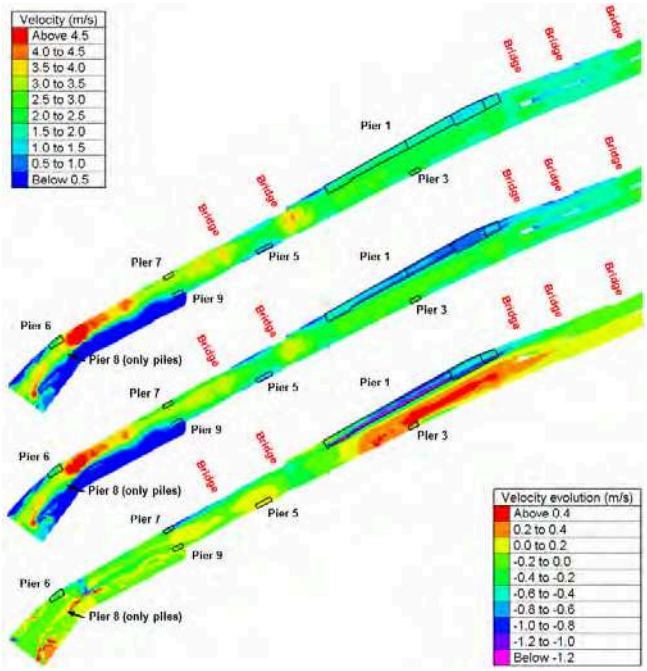

Figure 10: Project impacts on flow velocity. Top: velocities with current state geometry. Middle: velocities with project geometry. Bottom: Velocity evolutions. 100-year flood with mean sea level.

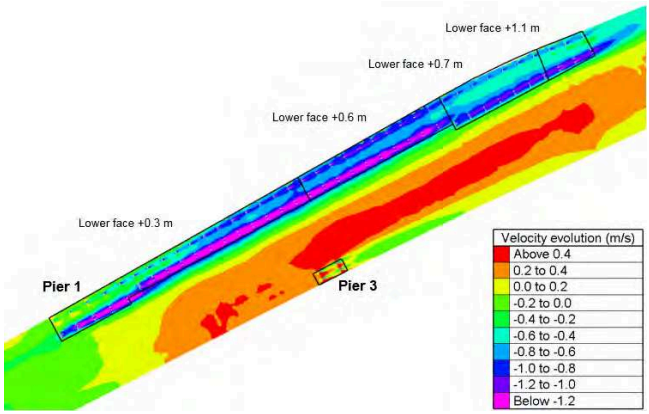

Figure 11: Detailed view of velocity evolutions along pier 1 and 3.

V. TURBULENCE-BASED EROSION RISK ASSESSMENT

A. Accounting for turbulence in erosion processes

Bed erosion occurs when the local bottom shear stress is greater than the material's critical shear stress. Local bottom shear stress is expressed by Eq. 5.

$$\tau = \rho \cdot u_*^2 \tag{5}$$

Where τ is the bottom shear stress (N/m^2), ρ the water density (kg/m^3) and u_* the friction velocity (m/s). The friction velocity is calculated from the flow velocity and the bed friction coefficient. This expression is valid for flow conditions in which turbulence is generated by bottom friction. However, for flow conditions in which turbulence is also generated by other factors than bottom friction, the expression above might underestimate the actual shear stresses. For example, analysis of turbulent structures in eddies shows that

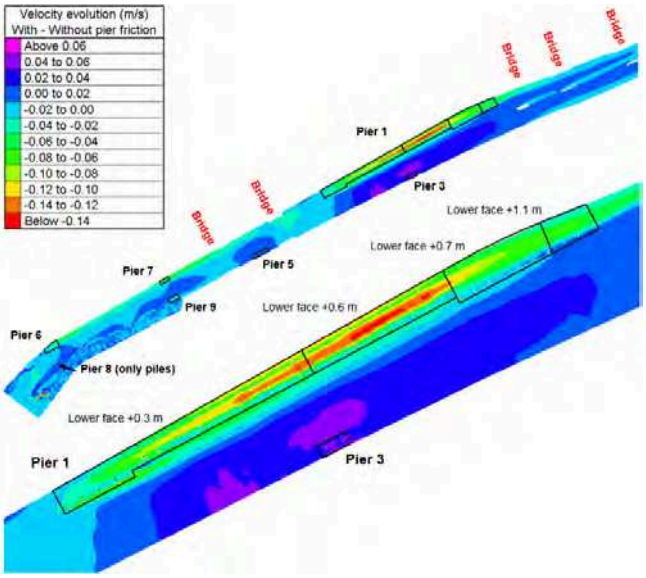

Figure 12: Velocity evolutions due to the impemented pier friction term. Top: global view. Bottom: detailed view along pier 1 and 3. Negative values indicate a decrease of velocities due to the additional pier friction term.

pressure can vary up to a factor 18 [2]. Hence it is proposed here to use a turbulence-based approach to assess the erosion risk along the Å-rummet project. This method is inspired from Hoffmans [2] and more generally from erosion protection design praxis [3].

A common way to analyse flow turbulence is to use the so-called relative turbulence intensity defined in Eq. 6.

$$r_0 = \frac{u\prime}{U} = \frac{\sqrt{k}}{U} \tag{6}$$

Where r_0 is the relative turbulence intensity (-), u' the root mean square of the turbulent velocity fluctuations (m/s), U the local depth-averaged flow velocity and k the local depth-averaged turbulent kinematic energy (m^2/s^2). Classical values for relative turbulence intensities are presented in Table 1 [2].

TABLE 1. RELATIVE TURBULENCE INTENSITY VALUES [2]

r_0	Turbulence level	Comments
0	No turbulence	Laminar flow
< 0.08	Small turbulence	-
0.08 – 0.15	Normal turbulence	Channel, river flow
0.15 – 0.20	High turbulence	Downstream of structures (bridges, piers, etc.)
0.20 – 0.30	Very high turbulence	Downstream hydraulic jumps, sharp bends, etc.
0.30 – 0.60	Extreme turbulence	-

The turbulent kinematic energy is linked to the friction velocity by the dimensionless turbulent energy as defined in Eq. 7.

$$k^+ = \frac{k}{u_*^2} \quad (7)$$

Where k^+ is the depth-averaged dimensionless turbulent energy (-). By rearranging Eq. 6 for k, Eq. 5 and 7 can be combined to express the shear stress as a function of the relative turbulence intensity and the dimensionless turbulent energy, see Eq. 8.

$$\tau = \frac{\rho(r_0 U)^2}{k^+} \quad (8)$$

This expression can then be used to express the Shields parameter as a function of turbulence parameters, see Eq. 9.

$$\theta = \frac{\tau}{\Delta \rho g d_{50}} = \frac{1}{k^+} \cdot \frac{(r_0 U)^2}{\Delta g d_{50}} \quad (9)$$

Where θ is the Shields parameter, Δ the relative density of bottom material (typically 1.65) and d_{50} the median diameter of the riverbed material (m). In this expression, the dimensionless turbulent energy k^+ should be defined as a constant in order to keep the influence of the turbulent term $k = (r_0 U)^2$, which can be considered being valid for uniform flows. This is a weakness of this method since we introduce an uncertainty in how k^+ should be defined. In the depth-averaged k-ε model, k^+ can be assessed by Eq. 10 assuming equilibrium conditions between the turbulent energy produced by bottom friction and its dissipation rate [1].

$$k^+ = C_{2\epsilon} \cdot \frac{P_{kv}^2}{u_*^2 \cdot P_{\epsilon v}} = \left(3.6 \cdot \sqrt{C_\mu} \cdot C_f^{1/4}\right)^{-1} \quad (10)$$

Where $C_{2\epsilon}$ and C_μ are constants of the k-ε model (1.92 and 0.09 respectively) while P_{kv} and $P_{\epsilon v}$ are production terms along the vertical (see [1] for more details). k^+ values estimated by Eq. 10 are typically ranging between 2.2 and 3.5 for classical friction coefficients and flow characteristics (water depth) expected in river flow. k^+ values computed from TELEMAC-2D results using Eq. 7 in the vicinity of pier 1 and 3 in the middle of the river, that is avoiding the influence from the piers, are approximatively 2.9. This value has been chosen to assess the erosion risk.

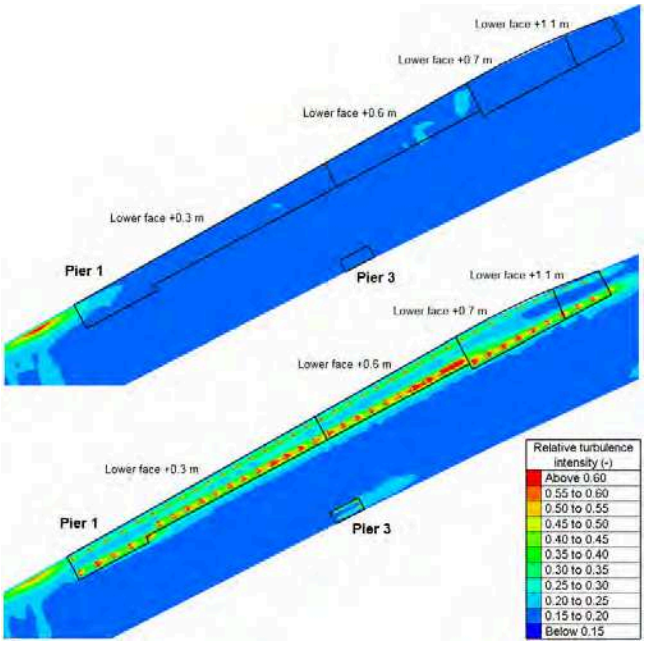

Figure 13: Relative turbulence intensities in the vicinity of pier 1 and 2. Top: current state geometry. Bottom: project geometry. 100-year flood with mean sea level.

B. Results

The relative turbulence intensities computed in the current state geometry for the 100-year flood are comprised between 0.15 and 0.20 along the planned piers which corresponds to a high turbulence level, see Fig. 13. This result is reasonable being given the flow velocities in this region (2.0 to 3.5 m/s) and the Strickler coefficient used. For the project geometry, the relative turbulence intensities increase below and in the wake of the piles. The strongest influence is observed for pier 1 where the average turbulence level is increased up to approx. 0.4 with maximum values in the wake of the outer piles, the most exposed to the current, exceeding 0.6. The turbulence level in the centre of the river is not significantly impacted.

The relative turbulence intensities were used to compute

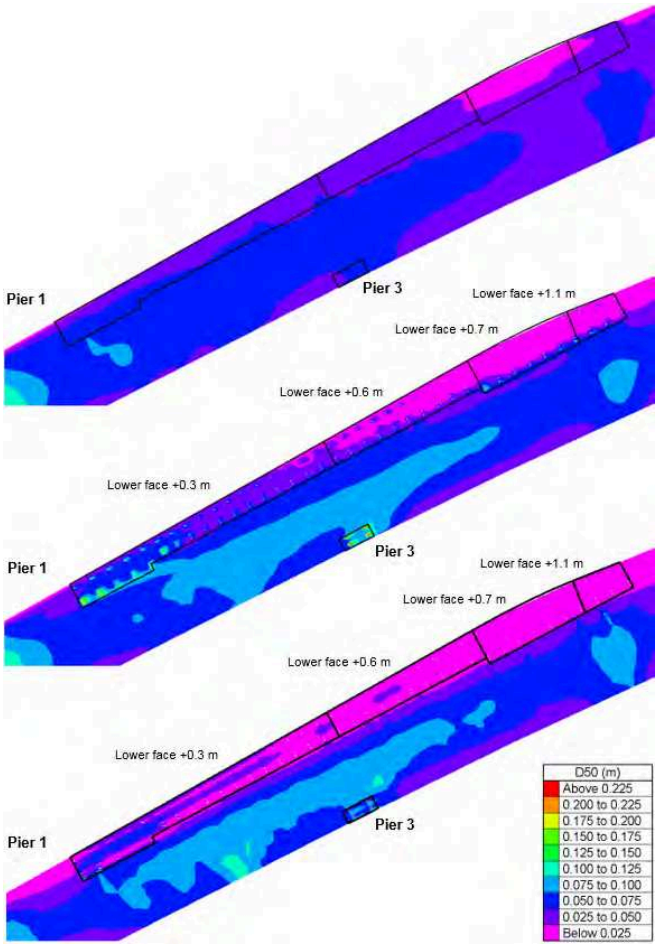

Figure 14: Critical particle size d_{50} in the vicinity of pier 1 and 3. Top: current state geometry (turbulence-based). Middle: project geometry (turbulence-based). Bottom: project geometry (classical approach). 100-year flood with mean sea level.

the critical particle size below which erosion occurs. Eq. 9 was used, rearranging for d_{50} and using the chosen dimensionless turbulent energy k^+ = 2.9. The particle Reynolds number being large (Re_* > 1000), the critical Shields parameter was chosen as θ_c = 0.06. For comparison purposes, the critical particle size has also been computed using the classical approach based on friction velocity. The obtained critical particle size is presented on Fig. 14. As expected, results show that the upstream piles of pier 1 are subject to a high erosion risk due to both high flow velocities and turbulence level. If results show that the erosion risk is high in the vicinity of the piles, it is interesting to note that the critical particle size is actually smaller in the downstream part of pier 1 compared to the current state. This is due to the fact that flow velocities are decreasing in this area compared with current state. The critical particle size also increases in the centre of the river due to the contraction effect between pier 1 and 3. It is worth noting that the classical approach clearly shows a correlation between flow velocities and erosion risk with a much lower critical particle size below and in the wake of piles than results obtained with the turbulence-based approach.

Unfortunately, no detailed information on the actual riverbed material was available for this study. Hence, this analysis has been performed mainly in order to highlight how the erosion risk is affected by the Å-rummet project. It is important to note that further analysis is required prior to using this methodology for erosion protection design, especially regarding how to define the depth-averaged dimensionless turbulent energy k^+.

VI. Conclusion

This article presents the methodology and results of a hydraulic study performed in the Gavleån River in Gävle, Sweden, in which an architectural project with piled piers within the riverbed is planned. The results showed that piers (especially pier 1), which can be submerged during high flows, induce negative impacts on water levels. However, the increase in water levels is not generating a significant aggravation of the flooding risk. Piers also induce a new cross-sectional distribution of the flow velocities with lower velocities under and in the wake of piers and higher velocities in the center of the river due to flow contraction. Flow conditions under the piers are very turbulent which has a negative impact on erosion risk.

References

[1] J-M. Hervouet, Hydrodynamics of free surface flows, John Wiley & Sons, Ltd, 2007.

[2] G. Hoffmans, The Influence of turbulence on soil erosion, Eburon Delft, 2012.

[3] CIRIA, CUR, CETMEF, The Rock Manual. The use of rock in hydraulic engineering (2nd edition), C683, CIRIA, London, 2007

Implementation of a wind-farm specific operational wave forecasting tool in the North-Sea: methods and forcing sensitivity

C.P.C Beraud[1], J.C. Bacon[1,2], S. Dorling[2], R. Jones[3]
[1]Centre for Environment, Fisheries and Aquaculture Science, Pakefield Road, Lowestoft, UK
[2]School of Environmental Sciences, University of East Anglia, Norwich, UK.
[3]Weatherquest Ltd, University of East Anglia, Norwich, UK
claire.beraud@cefas.co.uk

***Abstract*— The development of marine renewable energy generation from offshore wind turbines has been exponential during the last two decades, along with the need for operational forecasting tools to maintain safe working practise for construction and offshore maintenance teams and for planning maintenance to support improved efficiency in energy production. The principal requirement of an operational wave-modelling tool is to provide forecast wave parameters, in near-real-time, over a discrete windfarm operational area. A balance between model computational time and refinement in the mesh and wave discretisation must be reached.**

The present study presents a 0.5°×0.6° bespoke operational wave model to predict wave conditions over the Greater Gabbard Offshore Wind Farm in the southern North Sea using the finite element Telemac/Tomawac models. To fully capture the tidal effect on the waves, an offline coupling was made between the Tomawac and Telemac hydrodynamic modules. The Tomawac model was calibrated against observations at West Gabbard 2 WaveNet Waverider buoy and model forcing includes wave forcing at the boundaries and wind forcing over the domain. Multiple sources of forcing have been used to calibrate and refine the model to achieve the best performance, assessed by analysis of error statistics in wave parameter prediction. Model computational time was also considered to determine the most suitable forcing combinations for an operational application. The most efficient set up has been implemented on a commercial cloud based HPC cluster, and uses a scheduler to routinely download the model forcing data and initiate the computation. The full operational system will, ultimately, be used by offshore wind farm maintenance providers. The results of the various forcing combinations highlight the importance of accurate and high frequency wind forcing data and the role of the relatively coarse global wave model inputs as boundaries suitable to generate a very effective high resolution operational forecast system.

I. INTRODUCTION

Operational wave modelling to produce near-real time wave parameter forecasts is at present limited to meso-scale, regular gridded datasets, produced mainly by the governmental meteorological services of the coast-bounding countries. Forecasts mostly provide wave-only solutions and do not provide results which include the enhancement of the tide acting on the waves. As a result, significant changes to shape and height of waves, as a function of phases of the tide cycle, are not captured well and the tidal currents are ignored. The accuracy and low resolution of current wave forecasts has several significant cost implications for developers and contractors during both the construction and operational phases of Offshore Wind Farms (OSWF). Ship to platform personnel transfers are prohibited when significant wave heights exceed critical thresholds (which themselves are a function of vessel size) and imprecision in the predicted wave field or the timing of when conditions may change results in costly, abortive ship movements or the loss of operational working time. Currently the largest operation and maintenance cost incurred by OSWF operators is 'waiting for weather' [1]. However, these losses are insignificant when compared with the loss in generating capacity and revenue due to delayed repairs to commissioned turbines and offshore installations.

To improve the information stream informing the OSWF management process, an operational wave forecast is required at precisely the cycle times when go/no-go decisions are made. Greater accuracy in the forecast data is achieved by:

i. Including the phase of the tide by coupling the wave and tide hydrodynamic models to include wave-current interactions.
ii. Providing high spatial resolution and forecast data in precise locations of interest to the client
iii. Providing the forecast data stream at the optimum time in the decision process.

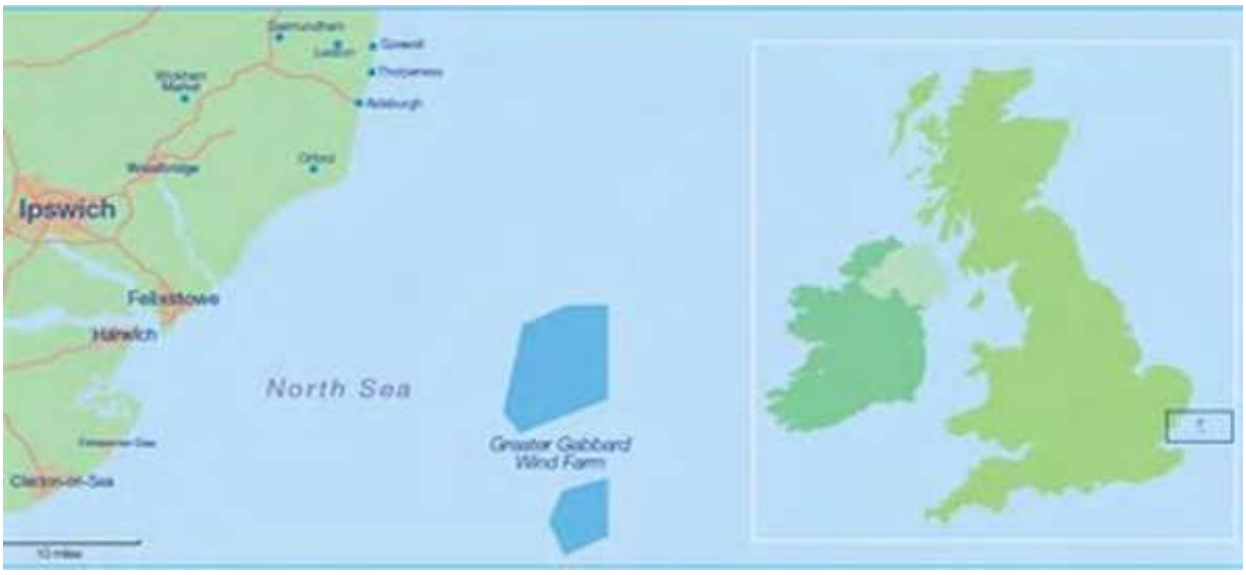

Figure 1: Map of the Greater Gabbard windfarm site in the southern North Sea

The highest resolution of operational wave forecasts available at present is ~4 kilometres, which for general marine information systems may be adequate. However, in the regions of the sandbanks and complex bathymetric features over which the wind-turbines are located, wave models which do not include the effect of tides are less accurate.

The model domain and boundary inputs were specifically designed for the Greater Gabbard site (Figure 1) and the variable resolution of the TELEMAC finite element model enables precise focussing of computational effort to key areas of construction or maintenance operation.

The aim of the project was to initiate and validate an operational wave model for the North Sea Greater Gabbard Wind Farm, producing 48 hour forecasts of significant wave height and peak period including meteorological forcing and wave-tide interactions in shallow water. By increasing spatial resolution over the complex shallow bathymetry and including wave-tide interaction, we aimed to exceed the accuracy of the current state-of-the-art model, operated by the UK Meteorological Office (Wavewatch III, WW3), to predict periods when safe significant wave height working thresholds are exceeded. We achieved this by creating a coupled finite element wave/current model using the TOMAWAC wave and TELEMAC2D tidal current modules of the TELEMAC suite.

II. PROJECT OBJECTIVES

Several objectives were addressed by the project:

- Improve the accuracy of wave forecasts at times when thresholds for wave-height, for the safe transfer of personnel at sea, are approached.
- Provide the data at times coincident with the go/no-go decision path in the operational planning process.
- Design the model domain to provide tailored results which match the complete range physical conditions encountered at the site.
- Enable run-times and results processing to be completed within a pre-defined period, for operational application
- Develop a scalable system with applicability to other domains.

III. MODEL SET-UP

A. Site location and model domain

The Greater Gabbard turbine site is situated in the southern North Sea over an area of shallow and complex bathymetry and relatively close to one of the North Sea's amphidromic points. The site was commissioned in August 2013 and now generates up to 500MW from the 140 turbines. The location of the turbine site is shown in Figure 1.

An identical horizontal mesh was used for the TELEMAC2D and TOMAWAC simulations and was designed specifically to work efficiently over the Greater Gabbard wind farm; the boundaries of the model are close to the site border and include locations of the Wavenet Waverider buoy. BODC (British Oceanographic Data Centre) wave and current data sites over the model domain area used to calibrate and validate both models (Figure 2). The mesh has less than 4000 nodes and the bathymetry was derived from UK Hydrographic Office survey data.

The wind over the model domain is fairly consistent, with really small spatial variation. Predicted waves from the WW3 global model are mainly bi-directional, with the predominant directions from the South-West and from the North. This bi-directionality is in agreement with the direction of the largest fetch-lengths.

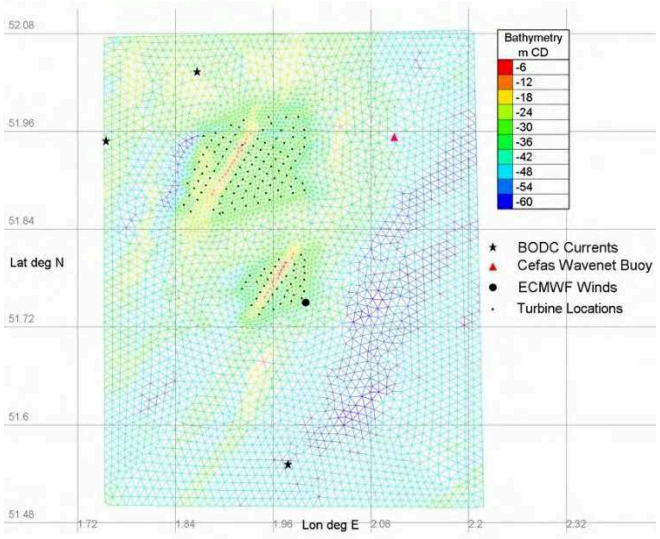

Figure 2: TELEMAC mesh with bathymetry. The small black points locate each wind turbine, large black points the location of ECMWF ERA-Interim forcing data, and black stars the measurement data used over the calibration and validation process. The resolution is refined over the sand banks, where the wind farm is located.

B. Tidal model

TELEMAC2D was used to generate the tidal currents over the Gabbard site area, crucial for capturing the true nature of the wave field. The hydrodynamics are forced along the open boundaries using 11 tidal constituents (M2, S2, N2, K2, K1, O1, P1, Q1, M4, MS4 and MN4) from the OSU TPXO European Shelf 1/30° regional local model.

To transfer the tidal information between the later TPXO large scale model and the Gabbard site, TELEMAC2D options were tested to calibrate the tidal range and tidal velocities.

Wind forcing was first derived from the ECMWF ERA-Interim re-analysis which gives wind data at six hourly intervals with a spatial resolution of 0.125˚. A time-series of wind was then extracted at the domain central point, giving a suitable representativeness of the wind over the small domain due to its small spatial variability. The Met Office's EURO4 model winds are more refined with an hourly interval and a special resolution of 0.04˚. The tidal model was run independently for a 72 hour duration and the results provide tidal velocities to enhance the computation made for significant wave height.

The 22-day-long dataset available from the BODC tidal model results portal (measurement b0010031 measured in November 1978) were used for the validation of the tidal time series (Figure 3). Data were from the Proudman Oceanographic Laboratories, Coastal Ocean Modelling System (POLCOMS), from which model derived outputs have been widely adopted as a resource for tidal currents in many operational marine data systems in the UK. As the mean water level measured at the BODC site with a pressure sensor varied over the survey, we could not use it for the calibration of the tidal water level; however, the simulated tidal period was perfectly in phase with the observations (Figure 3).

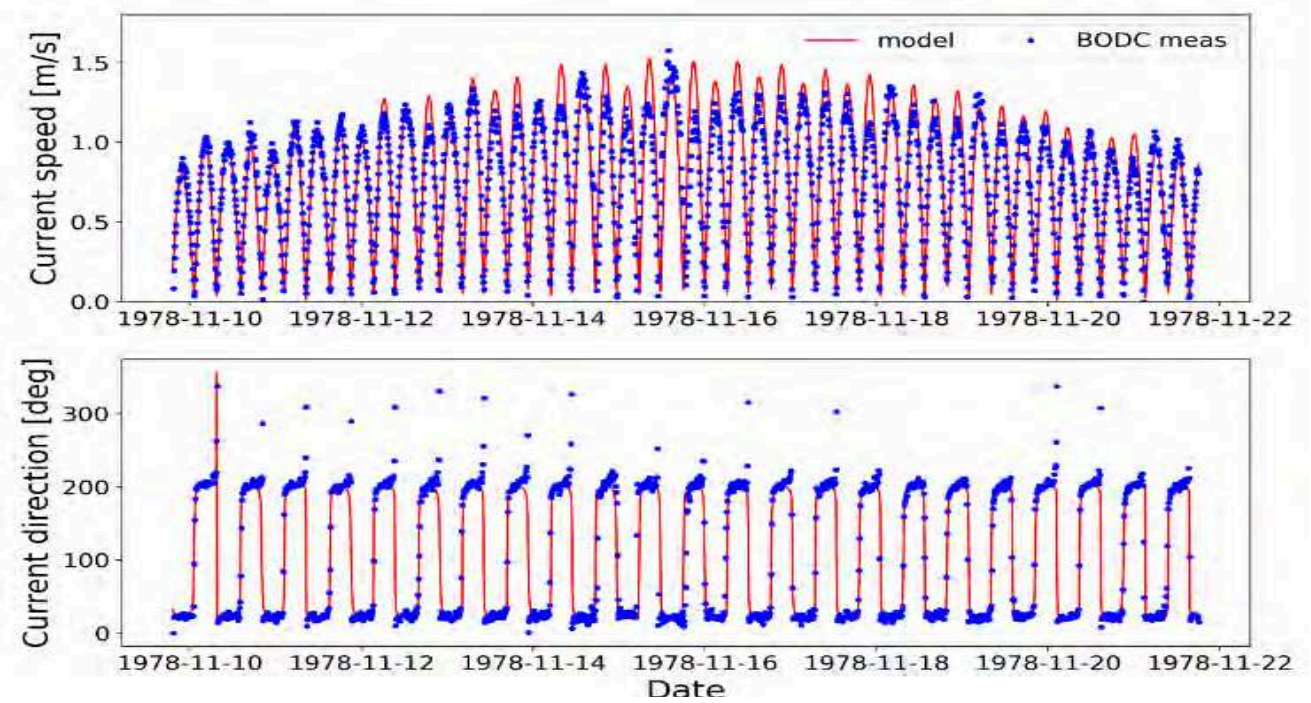

Figure 3: Comparison of current speed (top) and direction (bottom) between BODC measurements (blue dots) and TELEMAC2D prediction (red line)

TABLE 1: TIME PERIODS OVER WHICH THE WAVE CALIBRATION HAS BEEN PERFORMED

Name	What	Time period	Forcing	Location of calibration
A	Predominantly Northerly wind and wave	1 October 2016 until 15 October 2016	From North (lat 52, lon 2.0)	South WW3 location, against WW3 results

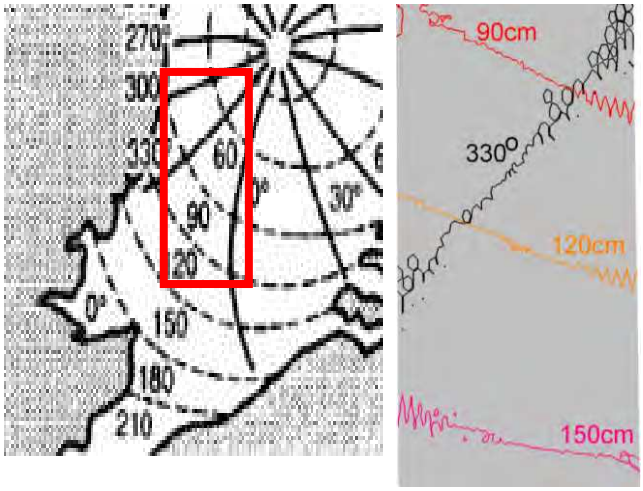

a) b)

Figure 4: Comparison of Amplitude and Phase of the tidal component M2 in [2] (a) and in the present model (b). The red rectangle in a) delimits the model domain.

The BODC tidal velocities have been compared with the predictions (Figure 3). The predicted current speed was slightly under-estimated over spring current (strong current) and the average absolute error between TELEMAC2D predicted tidal current and BODC measured data over 22 days is less than 12cm/s, giving a relative error of 16% in the current speed. On average the predicted current direction was off by 11 degrees compared to measurement.

A harmonic analysis of a 30-day duration tidal run was undertaken and the principal tidal component M2 has been extracted (Figure 4). Slight rotation of the predicted M2 co-tide and an amplitude under-prediction with [2] model outputs was detected, but the ranges of amplitude and phase are similar (Figure 4).

As those discrepancies could not be improved by amending both the tidal range and velocity options and the internal physical parameters (bottom friction and water viscosity) in TELEMAC2D and as model tuning for tides can be a very time-consuming operation, the present tidal model was considered validated.

C. *Wave model*

TOMAWAC is the phase-averaging energy density spectral wave model which enables local enhancement of the resolution adjacent to the Wind Turbine Locations, whilst widening nodal density at the bounds of the turbine site. Whilst the UK Waters wave model has relatively coarse resolution our model resolution is increased over the sand-banks and complex bathymetry over which the wind farm was constructed. The model is coupled externally to the TELEMAC2D tidal currents and provides results which include alteration of the surface wave field by the tide which is advecting the waves as they propagate. The wave input data (boundary and initial conditions) are derived from the WWIII model and taken from the nearest points to either the north or southern boundary, depending upon the prevailing conditions indicated in the regional model. This information is read prior to running the initialisation scripts for the model run. Given the

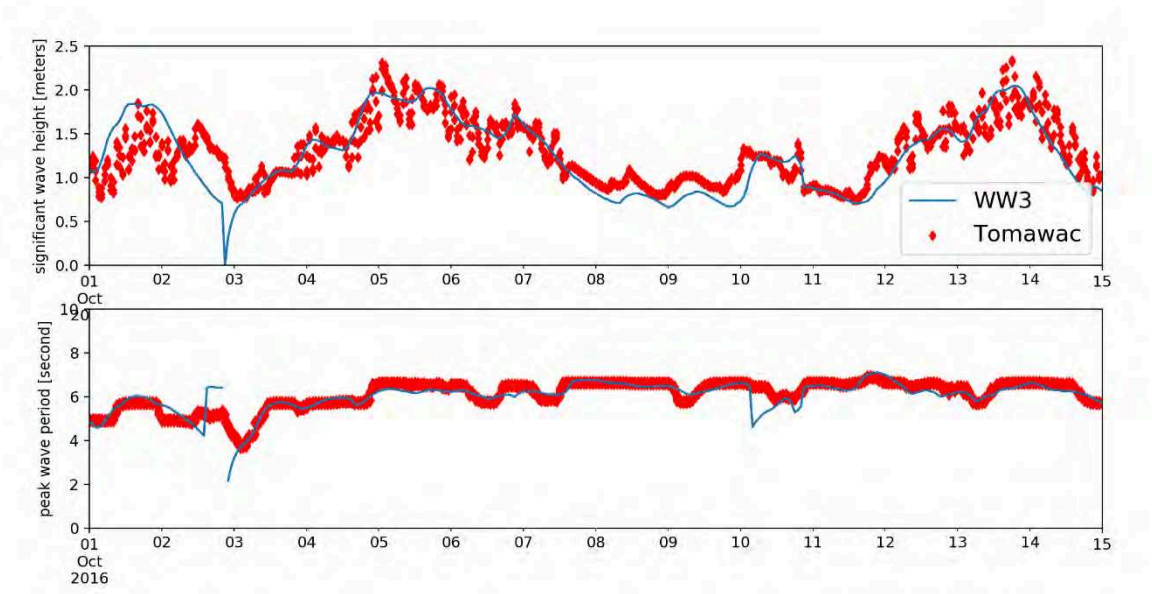

Figure 5: Comparison of significant wave height (top) and peak wave period (bottom) of WW3 model (blue line) and TOMAWAC (red dots)

scarcity of wave forcing, we did not implement a space varying boundary wave forcing.

The physical wave-only processes affecting wave generation and transformation have been calibrated against the validated and widely used WW3 model prediction. A time-period over which the wind was predominantly coming from the North were selected as indicated in TABLE 1. The wave time-series over this period included waves close to the 1.2m-wave-height threshold (Siemens Energy, SSE), above which the transfer to turbine is not recommended for some vessel sizes.

For the TOMAWAC calibration we chose the best performing parameters in simulation A to reproduce the WW3 prediction near the southern boundary using a northerly forcing. As neither TOMAWAC nor WW3 models include tidal effects, both models could be directly compared, and wave-only processes were calibrated.

Over the calibration process, the best wind generation was found using the formulation from [3], that has been used in the cycle 3 release of WAM model [4]. White capping dissipation was best reproduced with the formulation from [5], triad interactions with LTA model and non-linear transfer between frequencies with the DIA method. Bottom friction dissipation was reproduced with [6] and wave growth was limited following the formulation of [7] using the mean of wind sea frequencies. Triad interactions were best reproduced with the LTA model. The Jonswap spectrum was used, completely appropriate for the North sea wave, and the boundary angular distribution following the model from [8] was selected.

The TOMAWAC predicted wave height and peak period (Figure 5) follow the WW3 wave history. Due to missing data in the wave forcing, we cannot rely on the Tomawac prediction over the ~three first days. Some instabilities appear for strong winds, and further development will be needed to adapt the time-step to the wind magnitude.

IV. COUPLING TIDE AND WAVES

D. Coupling method

The initial aim of the project was to provide a direct internal coupling between the tide and wave models such that a precise evaluation of the wave-current interaction would be gained. To meet the requirements for completing the model run in an operational timescale, running in parallel mode was anticipated. However parallel operation has not been used as this would have required an update of the subroutines reading the forcing at the boundary. In Figure 6 the increase of the wave height of up to 0.5m can be seen around the 19th of September when strong (spring) tidal currents occur. The option “strong current” has been tested, but did not result in different wave heights.

TABLE 2:PERIOD OVER WHICH THE COUPLED TIDE-WAVE VALIDATION HAS BEEN PERFORMED

Name	What	Time period	Forcing	Location of validation
Sept	Wave and wind coming from both directions Wind from ecmwf ERA-Interim	September 1st-30th 2016	From both North and South, depending on the wind direction.	At the West Gabbard 2 Site, against measurement from WaveNet

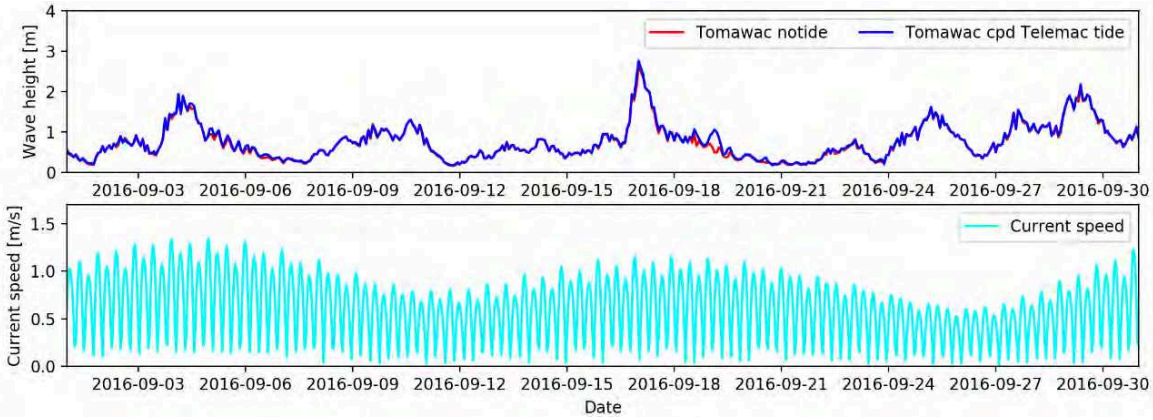

Figure 6: Predicted wave height at West Gabbard site for the uncoupled model (red) and the offline coupled TOMAWAC-TELEMAC2D (blue). The bottom figure shows the strength of the tidal current.

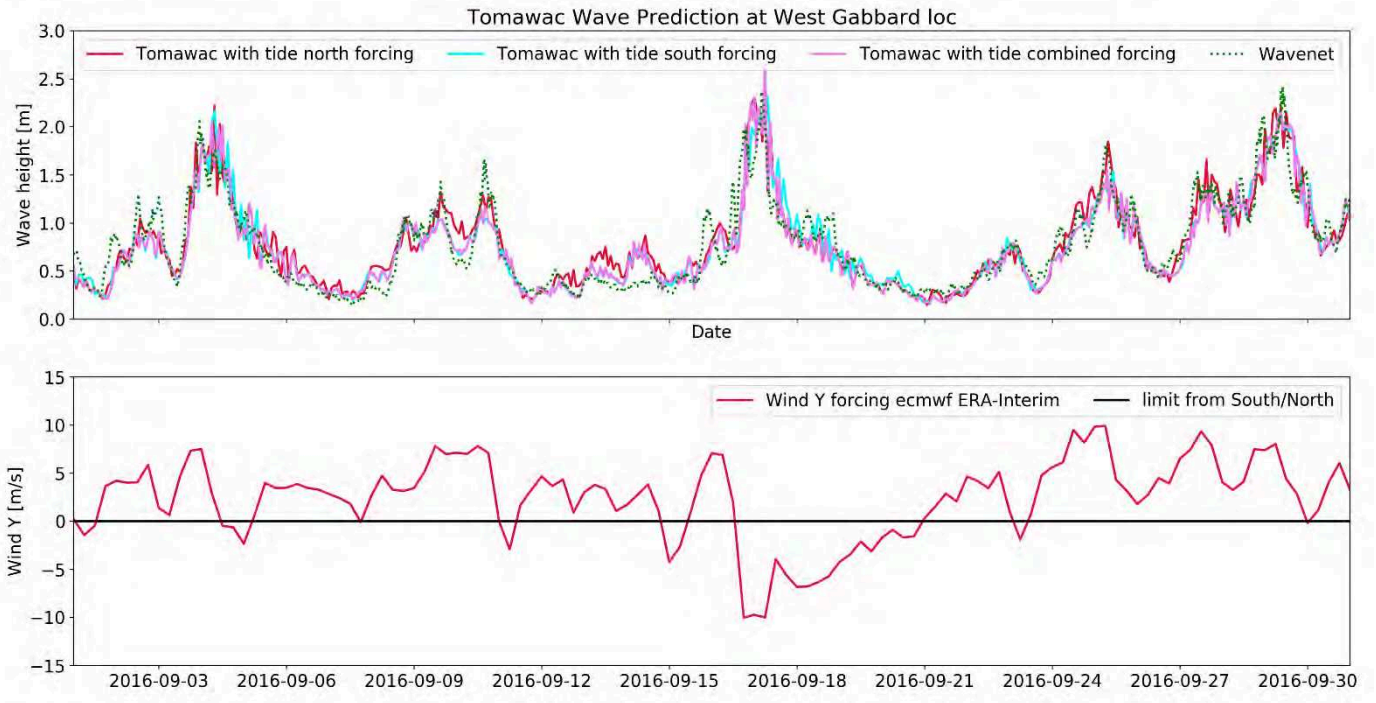

Figure 7: Comparison of the coupled TELEMAC2D-TOMAWAC offline coupled model with wave prediction against Wavenet observations, for three different wave forcings.

E. Validation of the coupling and sensitivity to forcing condition

The final calibrated wave-processes-related parameters from the first step calibration (A in table 1) have been used in the simulation "Sept" (Table 2) and the wave forcing has been improved by linking the wave forcing (from Northern or Southern WW3 prediction) with the direction the wind is coming from.

The sensitivity to the boundary wave forcing in the offline coupled TELEMAC2D-TOMAWAC model has been assessed for three simple cases: i) with wave forcing from WW3 North, ii) with wave forcing from WW3 South, and iii) selecting the wave forcing in accordance with the wind direction, i.e. selecting the Northern waves with a wind from the North, and conversely from the South (Figure 8).

The model is improved overall, when the selection of the wave is a function of the wind direction. For example in Figure 8, really good agreement is found for the period 2016-09-11 to 2016-09-14, with the combined forcing as the wind input has been dynamically switched to the Southern forcing data. However, over the period 2016-09-24 until 2016-09-25, EURO4 data indicate a strong wind coming from the North-east, which was not captured in ecmwf ERA-Interm and the combined forcing did not switch to the Northern wave forcing, resulting in an under-prediction of the wave height. We assume that the ecmwf wind temporal-resolution is not high enough resolution, and did not pick-up all the changes in direction. The recent adoption of the EURO4 winds provided to us very recently improves this sensitivity, but results will not be presented in this paper.

To inter-compare the performance of the different forcing configurations, the statistical measures of the error in the prediction with respect to the Wavenet measured data are shown in Table 3 with the maximum error indicated in red and the smallest in green. The "Absolute difference" error (or residual) measures the deviation to the observation. The "Root Mean Square Error" (RMSE) measures this deviation too but is more sensitive to outliers. The "standard deviation" (std) of the error represents how much the prediction varies from the observation. The bias indicates if the model over- or under-predict (respectively associated with a positive and negative

TABLE 3: STATISTICAL MEASURES OF THE ERROR IN THE PREDICTION OF WAVE HEIGHT

Statistical error in wave height prediction	Absolute difference [m]	RMSE [m]	Std	Bias
TOMAWAC with WW3 South forcing	1.310E-01	1.778E-01	1.778E-01	-0.203E-02
TOMAWAC with WW3 North forcing	1.546E-01	1.932E-01	1.887E-01	4.129E-02
TOMAWAC with both WW3 South and North forcing	1.324E-01	1.777E-01	1.776E-01	-0.493E-02
WW3 South prediction	2.270E-01	2.753E-01	2.584E-01	-9.505E-02
WW3 North prediction	1.567E-01	1.949E-01	1.767E-01	3.240E-02

bias). Predictions from the WW3 South model gridpoint are the least accurate and under-predict wave heights (Table 3). The most accurate predictions are found when TOMAWAC is forced with WW3 South model prediction and the model slightly under-predicts wave heights. When TOMAWAC is forced by both the North and South WW3 predictions, it minimises the largest errors (small RMSE and std in Table 3).

V. TUNING FOR OPERATIONAL DELIVERY

As TOMAWAC would not run in MPI mode when forced by a time varying wind and wave input using a fortran user subroutine, the design of the mesh over a small, discrete area became paramount. The models run in scalar mode on the University of East Anglia (UEA) High Performance Computing (HPC) system and computational efficiency is sufficiently good to run the system as an operational service (twice daily), using the most efficient configuration for a future cloud based system.

VI. RESULTS

The developed Gabbard model greatly improves the wave height prediction compared to the currently used WW3 global model (0.5˚ resolution): the effect of the tide is included and the bathymetry is well reproduced over the domain. The prediction is improved both i) in space with the refined mesh over the wind farm and ii) in accuracy, as RMSE of the predicted wave height is less than 0.18m.

The model can be run as a forecasting tool, and does not require large computing requirements.

The best model forcing consisted of boundary waves forced with the WW3 North conditions, or both WW3 North and South conditions. However, poor time-resolution in free-access wind data leads to the largest remaining uncertainties in wave height prediction, as some rapid change in direction is not always captured in the model. This needs to be improved further in the future development of the model by using other sources of wind data (for example: EURO4 model winds).

ACKNOWLEDGEMENT

This work was carried out on the High-Performance Computing Cluster supported by the Research and Specialist Computing Support service at the University of East Anglia. We also want to thank WeatherQuest for supporting us with wind data and the University of East Anglia for support through its Development Fund.

REFERENCES

[1] Asgarpour, M., 2016. Assembly, transportation, installation and commissioning of offshore wind farms, Offshore Wind Farms: Technologies, Design and Operation. Elsevier Ltd. https://doi.org/10.1016/B978-0-08-100779-2.00017-9

[2] Dyke, P., 2007. Modeling Coastal and Offshore Processes, Imperial College Press/World Scientific Press.

[3] Snyder, R.L., Dobson, F.W., Elliott, J.A., Long, R.B., 1981. Array measurements of atmospheric pressure fluctuations above surface.

[4] WAMDI Group, T., 1988. The WAM model - A third generation ocean wave prediction model. J. Phys. Oceanogr. https://doi.org/10.1175/1520-0485(1988)018<1775:TWMTGO>2.0.CO;2.

[5] Komen, G.J., Hasselmann, K., Hasselmann, K., 1984. On the Existence of a Fully Developed Wind-Sea Spectrum. J. Phys. Oceanogr. https://doi.org/10.1175/1520-0485(1984)014<1271:OTEOAF>2.0.CO;2

[6] Bouws, E. and G.J.K., 1983. On the Balance Between Growth and Dissipation in an Extreme Depth-Limited Wind-Sea in the Southern North Sea. J. Phys. Ocean. 13, 1653–1658.

[7] Hasselmann, K. Herbach H., J.P., 1996. Change of wam model integration scheme. Personal communication - 12/06/96.

[8] Mitsuyasu, H., Tasai, F., Suhara, T., Mizuno, S., Ohkusu, M., Honda, T., Rikiishi, K., 1975. Observations of the Directional Spectrum of Ocean WavesUsing a Cloverleaf Buoy. J. Phys. Oceanogr. https://doi.org/10.1175/1520-0485(1975)005<0750:OOTDSO>2.0.CO;2.

Neumann (water level gradient) boundaries in TELEMAC 2D and their application to wave-current interaction

WA Breugem[1], E Fonias[1,2], L Wang[1,2], A Bolle[1], G Kolokythas[2], B De Maerschalck[2]
[1]International Marine and Dredging Consultants, Antwerp, Belgium
[2]Flanders Hydraulics Research, Antwerp, Belgium
abr@imdc.be

***Abstract*— In this paper, an implementation of the Neumann boundary conditions is presented in TELEMAC 2D. In this paper, the term "Neumann boundaries" are used to refer to water level gradient boundary conditions. The application of these boundary conditions is shown in idealized test cases, in which a schematic representation of a coastal area is simulated. Examples are presented for cases with tidal flow, a wave-driven current (in which TELEMAC-2D is coupled to TOMAWAC), as well as for a combination of wave-driven currents and tidal flow.**

I. INTRODUCTION

In the coastal zone, the flow patterns are determined by both tides and waves, leading to a complex interaction. In order to simulate these flow patterns well, Roelvink and Walstra [1] showed that it is advantageous to use the so-called Neumann boundary conditions for the lateral model boundaries. In these Neumann boundaries, the water level gradients are prescribed, rather than water levels or velocities, such that the flow can develop freely at the lateral boundaries and in this way, the flow parallel to the coast is not disturbed by the lateral boundaries. In the present paper the terminology of the paper of Roelvink and Walstra [1] is followed, and therefore the water level gradient boundary condition will be referred to as Neumann boundary condition.

In TELEMAC 2D, the main open boundary types are water level boundaries and velocity boundaries. Prescribing water level boundaries for the lateral boundary may lead to instabilities. Velocity boundaries can in principle be used. However, it can be difficult to know the velocities at the boundary in advance, because they are sensitive to the water depth at each location of the boundary. Further, in case of wave-current interaction, the velocity at the lateral boundary may be difficult to know as it also depends on the wave conditions. Therefore, it is advantageous to prescribe water level gradients (i.e. Neumann boundaries), because these are more easy to know in advance, they are almost constant over the boundary (and depend little on the water depth) and can incorporate the effect of wave conditions.

Therefore, an implementation of the Neumann boundary conditions is presented in this paper for TELEMAC 2D. The application of these boundary conditions is shown in idealized test cases, in which a schematic representation of a coastal area is simulated. Examples are presented for cases with tidal flow, a wave-driven current (in which TELEMAC-2D is coupled to TOMAWAC), as well as for combinations of wave-driven currents and tides

II. NEUMANN BOUNDARY CONDITION

A. Strategy

In order to use Neumann boundary conditions, the following strategy is used:

1. Water level gradient conditions are prescribed perpendicular to the boundary.
2. The water level gradients are converted to velocities normal at the boundaries.
3. In case the calculated velocities describe inflow, these velocities are applied at the boundary. Otherwise, an outflow boundary condition is used.

B. Derivation of the velocity perpendicular to the boundary

In order to derive the Neumann boundary condition, the depth averaged momentum equations are first written in a coordinate system aligned with the boundary (ζ,ξ), with ζ the direction perpendicular to the boundary (positive outward) and ξ the direction parallel to the boundary. Perpendicular to the boundary this gives:

$$\frac{\partial u_\zeta}{\partial t} + u_\zeta \frac{\partial u_\zeta}{\partial \zeta} + u_\xi \frac{\partial u_\xi}{\partial \zeta} = -g \frac{\partial \eta}{\partial \zeta} - \frac{c_f |u|}{H} u_\zeta + F_\zeta^{ext} + D \qquad (1)$$

Here, u_ζ and u_ξ are the velocity components, perpendicular and parallel to the boundary, |u| is the velocity magnitude, g is the acceleration due to gravity, η is the water level elevation, H the water depth, c_f a friction coefficient, $F_\zeta^{ext_t}$ the external forces (Coriolis force, atmospheric pressure gradient, waves and wind), and D is the diffusion term. Neglecting the advection and diffusion terms as the boundary and noting that the water level gradient is prescribed, the equation reduces to and ordinary differential equation:

$$\frac{du_\zeta}{dt} = -g \left(\frac{\partial \eta}{\partial \zeta}\right)^{ext} - \frac{c_f |u|}{H} u_\zeta + F_\zeta^{ext} \qquad (2)$$

This equation is discretised with the semi-implicit theta scheme giving:

$$\frac{u_{n+1}-u_n}{\Delta t} = -g\left(\frac{\partial \eta}{\partial \zeta}\right)^{ext} - \frac{c_f|u|}{H}(\theta u_{n+1} + (1-\theta)u_n) + F_\zeta^{ext} \quad (3)$$

, leading to:

$$u_{n+1} = \frac{1+(1-\theta)\frac{c_f|u|}{H}\Delta T}{1+\theta\frac{c_f|u|}{H}\Delta T}u_n + \frac{\Delta T}{\left(1+\theta\frac{c_f|u|}{H}\Delta T\right)}\left(F_\zeta^{ext} - g\left(\frac{\partial \eta}{\partial \zeta}\right)^{ext}\right) \quad (4)$$

In order to obtain a more stable behaviour during drying and flooding at the boundary (such may occur at a beach), the second term on the right hand side of (4) is multiplied with a drying flooding factor α, which is defined as:

$$\alpha = \max(\min\left(\frac{H}{H_{min}}, 1\right), 0) \quad (5)$$

, with H_{min} a threshold water depth, currently set to 0.5 m.

C. Velocity parallel to the boundary

A similar equation as (4) can be derived for the velocities parallel to the boundary. However, the water level gradient parallel to the boundary is not prescribed. Test were performed using this equation by estimating the water level gradient from the existing free surface gradient. However, these tests showed that the model became unstable. Hence the flow parallel to the boundary is set to zero.

D. Implementation

The Neumann Boundary condition implementation consists of three parts:

- Routines to read the prescribed Neumann boundaries (`dedx.f` as well as changes in `bord.f`).
- A new subroutine (`neumann.f`), in which the velocities at the lateral boundary are calculated, which is called in `propag.f`, reusing the forces and bed friction terms that have already been calculated in this routine.
- A new subroutine `corr_outflow.f` called by `propag.f`, which is used in order to determine whether the flow at the boundary consist of inflow or outflow. In case of outflow the internal arrays LIMPRO and MASK are changed from a Dirichlet value to a Neumann value.

Parallelization was taken into account in the implementation and all the test cases described in this paper were performed in parallel.

III. USER MANUAL

In order to use the Neumann boundary conditions the user should set the following steps:

- Specify the boundary conditions for the Neumann boundaries as boundaries with prescribed velocity and free water level (5 6 6) in the CONLIM (`.cli`) file. Note that the implementation assumes smooth changes in the direction of the segments of the Neumann boundary. It is strongly recommended to apply only straight boundaries for the cross shore boundaries. Hence this should be taken into account when generating the mesh of the test case.
- Set the keyword OPTION FOR LIQUID BOUNDARIES = 3 for the Neumann boundaries.
- Specify time series of the water level gradients for each Neumann boundary in the liquid boundary file, using the code DEDX followed by the number of the boundary. As an alternative, it is possible to program the routine `dedx.f` in order to provide the water level gradients. When doing so, care must be taken to the sign of the gradients, which is positive outward from the boundary. This means that typically, both cross shore boundaries will have a different sign.
- Additionally, it is needed to specify a water level on the offshore boundary. For typical tidal applications, this boundary need to change in space and time. In the applications, this is performed using some additional routines, which allow the specification of space and time varying water levels and velocities at the boundary using an ASCII input file. However, the authors consider that it is highly needed that space and time varying boundary conditions are standardized within TELEMAC

IV. APPLICATION OF NEUMANN BOUNDARIES IN A SCHEMATIC COASTAL MODEL

A. Model setup

The domain for the application of the Neumann boundary condition implementation is an idealized bathymetry of the Belgian coast west of Zeebrugge port (Figure 1).

Figure 1: Numerical domain of the present application, part of the Belgian coast.

The bathymetry of the numerical domain considered has a constant slope of 1:50 from the coastline towards the offshore for a length of 1.1 km and the rest of the offshore

bathymetry is flat at -17.33 m. The vertical levels reference is Mean Sea Level (MSL). A detail of the bathymetry formation is given by section A-A at Figure 2.

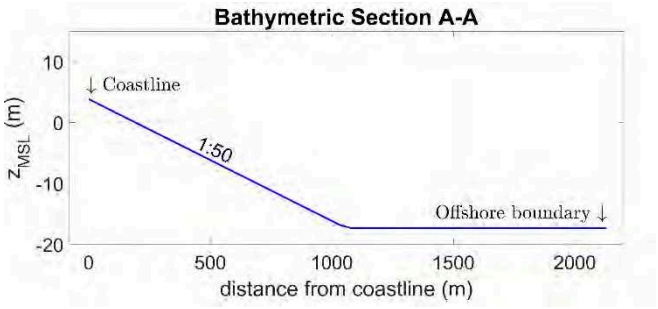

Figure 2: Bathymetric Section A-A for the schematized coastal model

The numerical domain (see Figure 3) is discretized using a channel type mesh in the nearshore region with elements of 60 m long along the coastline and 20 m wide in the other direction. This has been chosen since the flow patterns are not expected to demonstrate variations in the longshore direction. In the rest of the domain (offshore) a triangular mesh is used with minimum element size equal to 60 m and expansion ratio of 7%.

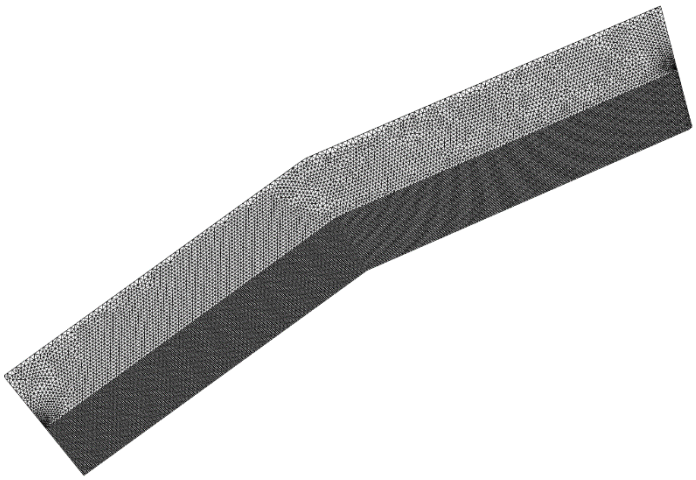

Figure 3: Computational mesh for the schematized coastal model

Concerning the boundary conditions of the numerical domain, two separate boundary conditions (.conlim) files are considered, one for TELEMAC 2D and one for TOMAWAC. In both the .conlim files the coastline side is considered as a solid boundary. For TELEMAC 2D the offshore boundary is an open boundary with prescribed water levels, whereas the lateral boundaries are open boundaries with prescribed UV velocities through which the Neumann boundaries will be imposed. For TOMAWAC, the side boundaries and offshore boundaries are considered as open boundaries with prescribed wave heights, wave periods and wave directions, which are then internally converted to a JONSWAP spectrum.

B. Model settings

Within the aforementioned numerical configuration, flows consisting of tide and/or wave action have been simulated.

The tidal flow is introduced by means of a sinusoidal free surface elevation in time and space using the expression:

$$\eta = \eta_o \, sin\left[2\pi\left(\frac{t}{T} - \frac{x}{L}\right)\right] \quad (6)$$

, where η_o=2 m is the tidal amplitude, T=12 hr is the tidal period and the tidal wavelength is $L = T\sqrt{gH_{max}} = 43\,200s \cdot \sqrt{9.81\,m/s^2 \cdot 17.33m} = 563\,241m$. The above free surface expression is applied along the offshore boundary of the numerical domain and the length x is equal to 0 on the east corner of the offshore domain and it increases along the offshore up to the maximum value of 13092 m on the west corner of the offshore domain. Those temporally variable values on the offshore nodes of the domain are included within the FORMATTED DATA FILE 1 required to assign the offshore boundary conditions in TELEMAC 2D. For the implementation of Neumann boundary conditions a LIQUID BOUNDARIES FILE is required to assign the free surface spatial gradient $\partial\eta/\partial x$ according to:

$$\frac{\partial\eta}{\partial x} = -2\pi\frac{\eta_0}{L}\cos\left[2\pi\left(\frac{t}{T} - \frac{x}{L}\right)\right]\hat{n} \quad (7)$$

, where $\hat{n}$ is the unit normal vector to the boundary, pointing outside of the numerical domain. This means that for the eastern boundary the value $\partial\eta/\partial x$ is assigned, whereas for the western boundary the value $-\partial\eta/\partial x$ is assigned. Finally, the OPTION FOR LIQUID BOUNDARIES has to be assigned with one value for each of the open boundaries. For the implementation of Neumann boundary conditions the value 3 must be assigned to the corresponding boundaries. For the numerical solution of TELEMAC 2D a constant time step of 10 s is considered.

For TOMAWAC boundary conditions, a constant wave attack from North is considered with a significant wave height H_s=2.0 m and a peak period T_p=6.32 s. TOMAWAC will be coupled with the TELEMAC 2D and a time step of 10 min is considered for the computation of the source terms and the advection time step is equal to 1 min in TOMAWAC. Non-linear interactions between frequencies, white capping dissipation, depth induced breaking dissipation (NUMBER OF BREAKING TIME STEPS = 20) and triad interactions have also been considered along with stationary wind conditions from north with a velocity equal to 12.24 m/s.

TELEMAC 2D is used independently for the simulation of tidal flow, or coupled with TOMAWAC either for wave-driven currents or a combination of tidal flow and wave-

driven currents. The total simulation time for each case was one week.

C. *Results tidal flow*

The simulation results for the tidal flow with TELEMAC 2D are presented in Figure 4. This figure shows contour plots of the velocity magnitude along with velocity vector fields throughout the last simulated tidal cycle every 1.5 hr. The velocity vectors are interpolated on a coastline conforming grid for clearer view. It can be observed that throughout the tidal cycle, the lateral boundaries using the newly implemented Neumann boundary conditions allow the tidal velocities to exit and/or enter the numerical domain smoothly. In addition, the formation of the boundary layer along the coastline and its temporal variation throughout the tidal cycle can be observed. At the snapshot at HW+1.5 hr the separation of the nearshore flow from the offshore flow can be observed as well, which is presumably because the change tin the flow velocity occurs later close to the coast, because of its lower water depth. This application indicates that the implementation of the Neumann boundary conditions works smoothly for simulating tidal flow.
In Figure 5, the results are shown for the same simulation, where prescribed water levels are used at the lateral boundary conditions, rather than Neumann boundaries. It is clear that the results from this simulation show rather distorted and unphysical velocity profiles at the lateral boundaries.

D. *Results for wave driven currents*

In this section, the results of online coupling of TELEMAC 2D with TOMAWAC considering only wave action as described above, will be presented. The only difference with the above considerations is that the timeseries for Neumann conditions used here in the LIQUID BOUNDARIES FILE is equal to 0. The occurring velocity vectors and velocity magnitude contour plot are shown in Figure 6. The formation of the longshore current can clearly be observed. However, certain velocity disturbances are evident along the lateral boundaries. They are probably due to the applied wave boundary conditions in TOMAWAC. In TELEMAC 2D and TOMAWAC, the model domain must be the same, which means that the Neumann boundaries in TELEMAC 2D are calculated from the prescribed boundaries in TOMAWAC, rather than a calculated wave field. Hence, the changes in the wave field along the boundary (due to shoaling refraction and breaking) are not taken into account. This means that the velocity calculated at the boundary is not corresponding to the velocities in the inner domain, leading to disturbances. There may be another effect caused by neglecting the momentum balance perpendicular to the shore line. Nevertheless, the instabilities at the boundary are not affecting the current and the final solution in the inner part of the numerical domain.

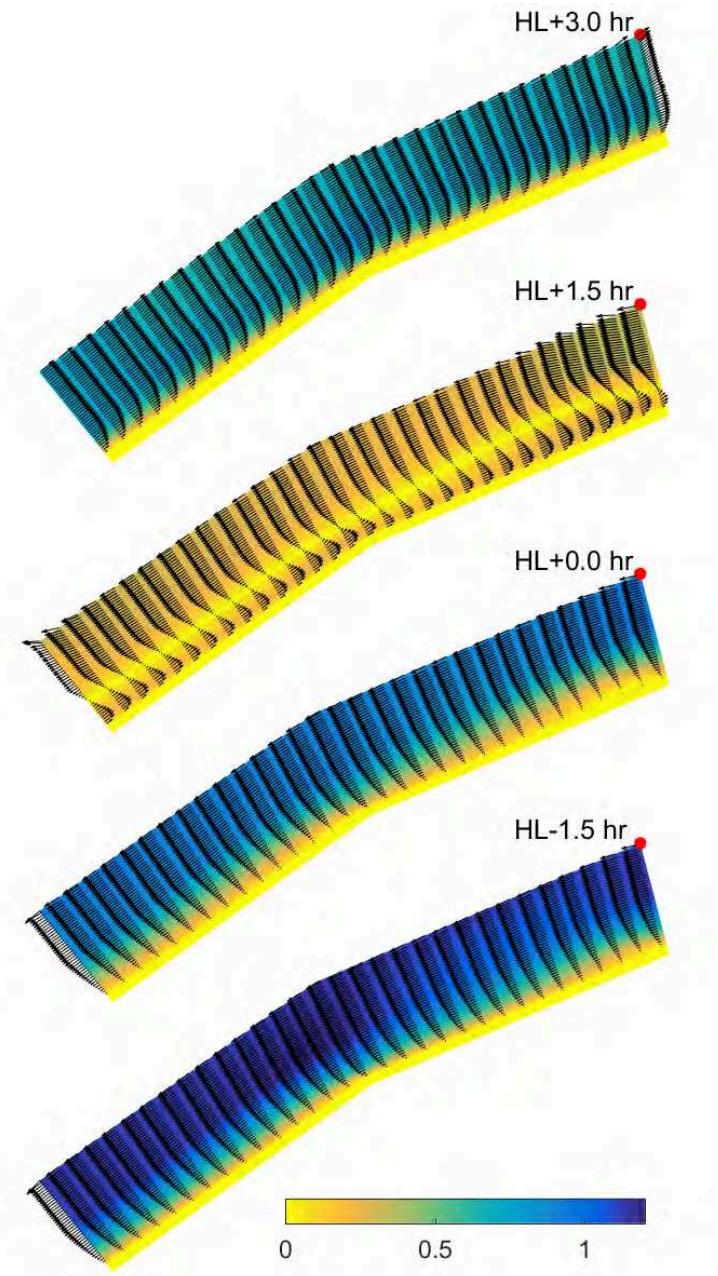

Figure 4: Contour plots of velocity magnitude(m/s) and velocity vector fields for tidal flow every 1.5 hours for half the tidal cycle for a simulation with Neumann (water level gradient) boundary conditions at the lateral boundaries.

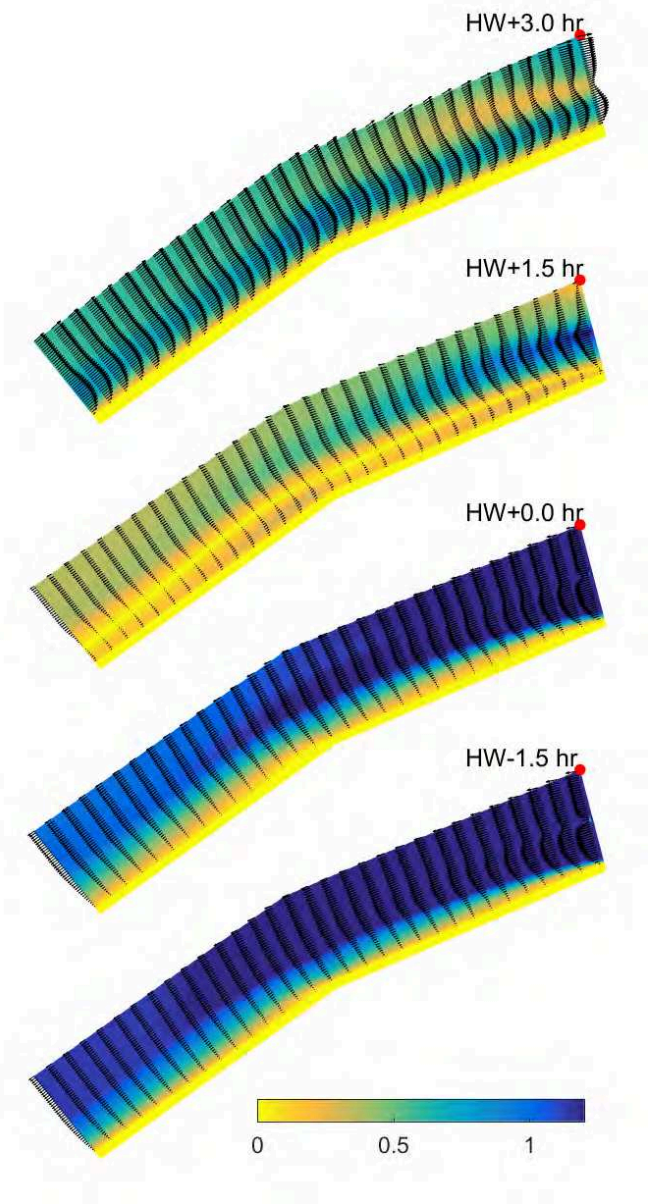

Figure 5: Contour plots of velocity magnitude(m/s) and velocity vector fields for tidal flow every 1.5 hours for half the tidal cycle for a case with water level boundary conditions at the lateral boundaries.

A. Results for combined tides and wave driven currents

In the last simulated case, TELEMAC 2D and TOMAWAC are coupled to simulate the combined action of the tide and waves on this idealised coastal area. The values of the Neumann boundary conditions in this test case are determined using (7), and the results are demonstrated in Figure 7. The longshore wave-driven current is evident throughout the whole tidal cycle, whereas a tidal flow pattern can be observed offshore. The flow separation is also observed here at 1.5 hr after high water, but the separation region is pushed more to the nearshore and the flow velocity magnitude in the nearshore zone is clearly reduced in comparison with the tidal case. Finally, slight disturbances in the flow field are observed at the lateral boundaries in the velocity profiles. This is again due to the fact that the wave field from the boundary in TOMAWAC is applied to calculate the velocity at the Neumann boundaries in TELEMAC 2D. However, even in this case, those disturbances do not seem to have a strong effect inner part of the computational domain.

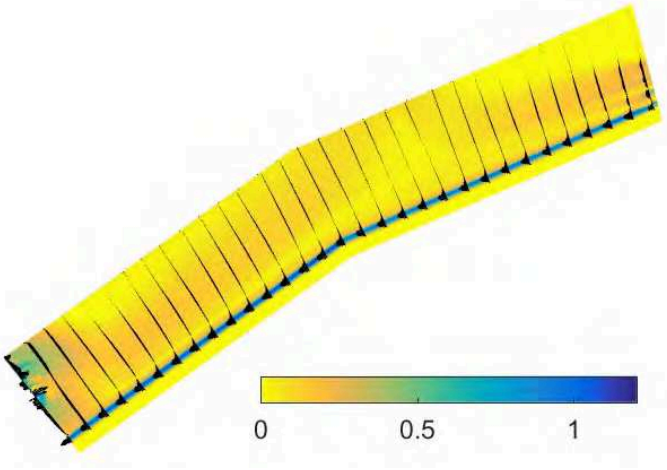

Figure 6: Contour plots of velocity magnitude(m/s) and velocity vector fields for wave driven currents.

V. FUTURE DEVELOPMENTS

The Neumann boundary conditions are shown to work well in tidal conditions and to show promising results in test cases where waves and currents are combined. The main deficiency in the latter test cases is because at the boundary, the wave field coming from TOMAWAC consist of a boundary condition, rather than a calculated wave field, leading to an overestimation of the wave field and hence inflow conditions that are too strong. There are two way to solve this:

- Implement Neumann boundaries conditions in TOMAWAC as well. However, Neumann boundaries for TOMAWAC have to be implemented in a rather different way than the ones presented in this paper. A possibility might be to use the mirror image of the characteristic curves at the location of the boundary for each spectral energy bin. However such a method seems rather cumbersome to implement.
- Change the coupling between TELEMAC and TOMAWAC, such that both models can use different meshes, with a larger domain for TOMAWAC than for TELEMAC. In a two-way coupled simulation, the information that is send from TOMAWAC to TELEMAC then needs to be determined by some sort of extrapolation.

It is considered that the latter approach offers many additional advantages (such as a large speed up by using

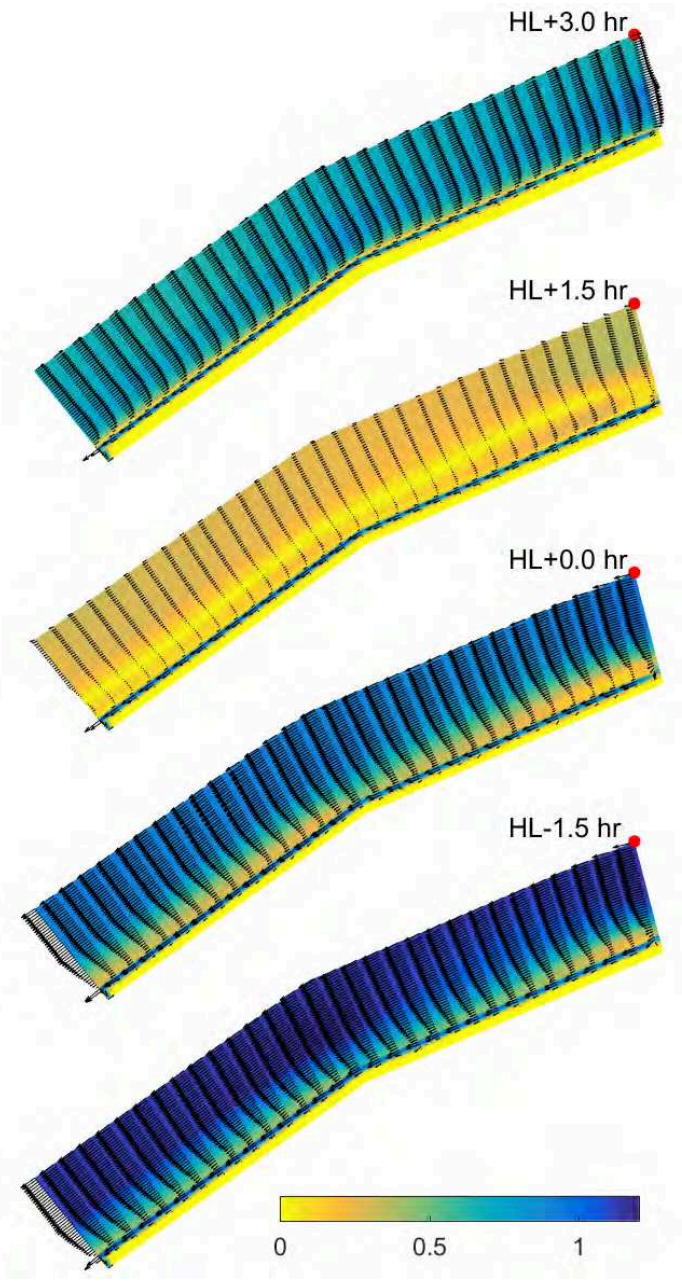

Figure 7: Contour plots of velocity magnitude (m/s) and velocity vector fields for combined tidal flow and wave driven currents every 1.5 hour for half a tidal cycle.

coarser resolutions in TOMAWAC or by cutting off parts of bays of rivers with limited wave activities in TOMAWAC). Therefore, works is currently being performed in order to implement such a flexible coupling.
Additionally, it is considered to implement a modification to the OSU/TPXO routines, such that the water level gradients can directly be obtained from the tidal database.
Finally, it is considered to perform more testing with respect to the calculation of the velocities parallel to the boundary, as it is considered a substantial disadvantage that the flow needs to perpendicular to the boundary in the present implementation.
Because it is necessary to have space and time varying water levels at the offshore boundaries, it is highly recommended to standardize the different implantations that currently exist within the TELEMAC community, such that one standard file format can be used to prescribe space and time varying boundary conditions without any additional programming.

VI. Conclusion

In this paper, the implementation of water level gradient boundary conditions for TELEMAC 2D is presented. This implementation is tested in three different test cases: a tidal flow, a wave-driven longshore current and a combination of both. The implementation is shown to give good results at the boundary for all these three test cases, although some additional work is still needed in order to improve the coupling between TELEMAC and TOMAWAC, in order to improve the results.

References

[1] J.A Roelvink and D.-J. Walstra, “Keeping it simple by using complex models,” Advances in Hydroscience and Engineering ,6 pp. 1-11, 2004

Modelling the fate and transport of faecal bacteria from sewage overflows: The Dart Estuary case study

Luz García[1], John Bacon[1] Carlos Campos[2]
[1]Centre for Environment, Fisheries & Aquaculture Science, Pakefield Road, Lowestoft, NR33 0HT, UK
[2]Centre for Environment, Fisheries & Aquaculture Science, The Nothe, Barrack Road, Weymouth, DT4 8UB, UK
luz.garcia@cefas.co.uk

***Abstract*—In this paper, we present results of a Telemac 3D application developed to investigate the fate and transport of *Escherichia coli* from sewer overflows (SOs) in the Dart Estuary, an important area for fisheries and water-based recreation activities on the south west coast of England. Model simulations were produced to investigate the effects of river discharges and tidal conditions. The results showed that the largest area of *E. coli* contamination in the estuary occurred during neap tides and low river discharges, due to longer persistence of contamination from SOs. This model can be used to investigate the effects of climate change and human population growth on water quality or active management of microbiological contaminants in bivalve shellfisheries.**

I. Introduction

The Dart Estuary is located in Devon, on the south west of England. It is a macrotidal estuary with range of up to 5.2m during spring tides, and up to 1.8m during neap tides. The tidal flow is ebb dominant and the upper tidal limit of the estuary occurs at Totnes, which is approximately 17 km upstream of the estuary mouth at Dartmouth.

The Dart Estuary is a regionally important center for yachting and boating. Bivalve shellfish, principally Pacific oysters (*Crassostrea gigas*) and mussels (*Mytilus* spp.*),* have been harvested for human consumption on the Dart for centuries.

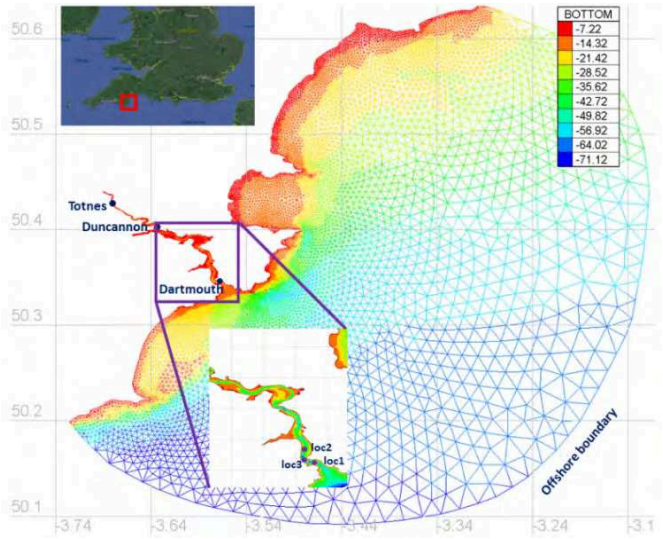

Figure 1: Model domain together with the location of the tidal gauges used for the validation of the water levels and the locations used for the validation of the tidal currents

In recent years, concerns have been raised about the impact of sewage discharges on water quality, wildlife and the amenity value of the area. Despite substantial investment made by the water company to reduce point-source pollution in this catchment, the designated shellfish water has never complied with the Guideline (G) microbiological standard of the Shellfish Waters Directive (repealed by the Water Framework Directive in 2013 and transposed to the national legislation through The Shellfish Water Protected Areas Directions (SWPAD) 2016) [9]. Following rainfall events, bivalve molluscs on the Dart are known to rapidly accumulate peak levels of *E. coli* and maintain these levels for several days [10]. The Cefas sanitary survey reports periodic downgrades in the microbiological classification of bivalve mollusc production areas (BMPAs) suggesting chronic sewage pollution impacts (Cefas, 2010). To achieve the G standard by 2027, the Environment Agency has recommended further pollution remediation work to deliver an average of 10 spills per annum for SOs in the Dart catchment (Environment Agency, 2015). In this context, this modelling study is very timely and can help water resource managers to identify appropriate measures to reduce sewage pollution in this estuary. The focus of this study is bacteria *E. coli* which is the indicator of faecal contamination prescribed by the relevant European legislation. It is important to acknowledge that, in addition to sewage discharges, the Dart Estuary BMPAs are impacted by diffuse sources of *E. coli*, from agricultural and urban land. It is estimated that agricultural sources contribute >40% of the total *E. coli* loading to the estuary [9]. Nevertheless, our interest here lies on the effect of the intermittent sources or, in other words, on the Sewage Overflows (SOs) as these are associated with higher health risk from exposure to enteric pathogens via contaminated water and bivalves. Approximately 70% of waste water in England and Wales is collected via combined sewers, collecting and discharging both foul sewage and surface water runoff. When the amount of sewage and surface water flowing into a combined sewer exceeds the hydraulic capacity of the collection system, the excess flow in the sewage network is discharged in untreated form into the environment via SOs. In this context, the main aim of this paper was to evaluate, by means of numerical modelling tools, the impact of spills from individual identified SOs in the Dart Estuary on the BMPAs under different conditions of river runoff and tidal regime.

II. HYDRODYNAMIC MODEL

A. Model set-up

A three-dimensional hydrodynamic model of the Dart Estuary was built using Telemac 3D (v7p2r2). The model domain extends approximately between 3.114ºW-3.726ºW and 50.08ºN-50.64ºN, and comprises the estuary and the adjacent coastal and offshore waters to allow for a better propagation of the boundary conditions and to investigate the variability of the river plume (see Fig.1). The domain was discretized by means of an unstructured grid with 12054 nodes and 22429 elements in the horizontal and 10 equally spaced layers in the vertical. The refinement in the grid varied spatially, with higher resolution inshore and coarser offshore (13-3843 m is the resolution range). The model bathymetry was mostly obtained from the Department for Environment, Food & Rural Affairs' UK Sea Map 2010, although minor manual modifications had to be done in the upper estuary to be able to properly reproduce the tidal propagation. The boundary conditions for the velocities and surface elevations at the offshore open boundary were obtained from the OSU TPXO European Shelf 1/30º regional model (11 tidal constituents: M2, S2, N2, K2, K1, O1, P1, Q1, M4, MS4 and MN4). Temperature and salinity were kept constant in space and time along the boundary (12.2ºC and 35.1, respectively). The input of fresh water of the Dart river was accounted for in the model by imposing a time series of river runoff obtained from the Austins Bridge station. The river temperature and salinity were prescribed at a constant value of 12.2ºC and 1.0, respectively. It must be noted that, since the temperature inputs are constant and equal along time, and since no atmospheric forcing is considered in this simulation, the temperature will remain constant along time. However, salinity variations seem to dominate the density distribution, being the contribution of temperature negligible [5], therefore this approximation will not affect the modelled circulation in the estuary.

For this study we considered the non-hydrostatic version of the Navier-Stokes equations. The κ-ε turbulence model was selected for the horizontal and vertical dimensions. Flooding and drying was included in the calculations due to the presence of tidal flats. Advection schemes that ensure conservative and monotonic behavior were selected for tracers. The Nikuradse law for bottom friction was considered, with a constant value of roughness length k_x=0.05 applied to the whole computational domain. The time step for the numerical resolution of the model was 1s.

The model was run for a two-month period, starting the 1st of December 2015, aiming at capturing periods of high and low river discharge during different tidal phases. The first days of the simulations were considered the spin-up period and hence, discarded from the analysis.

B. Model validation

The water levels were validated against observations at three tidal gauges (Totnes, Duncannon and Dartmouth, https://www.valeport.co.uk/InsideValeport/DartNetTides). In Fig. 2 the model results are shown for the Dartmouth gauge in comparison with the observations and the predictions from the UK Hydrographic Office (UKHO). The model reproduces well the observations both for spring and neap tide, showing a reasonable fitting in terms of amplitude and phase.

Owing to the lack of direct measurements of current velocities, the model was validated with velocity values found in the literature. According to [8] the characteristic flow velocities on the flood tide are 0.6m/s during spring tide at the mouth and 0.3m/s during neap tide. Tidal velocities at three different locations in the mouth of the estuary were extracted (Fig. 1) and very similar values to those reported in the literature during the flood phase of the tide were found (Fig. 2).

Salinity data available for the upper part of the Dart Estuary show that, as expected, the variability in the salinity range increases as we approach the estuary mouth. However, these data correspond to a period of very low river discharge during March 2003, and therefore could not be directly compared with the model results. The simulation period comprises low and high river discharge periods, in which the response of the model shows a similar behavior to the observations.

In any case, our model shows a similar behavior and, since the simulations last long enough to consider high and low river discharge periods, the response in the salinity levels can be seen. For the purposes of the model salinity validation, Fig.3 depicts the

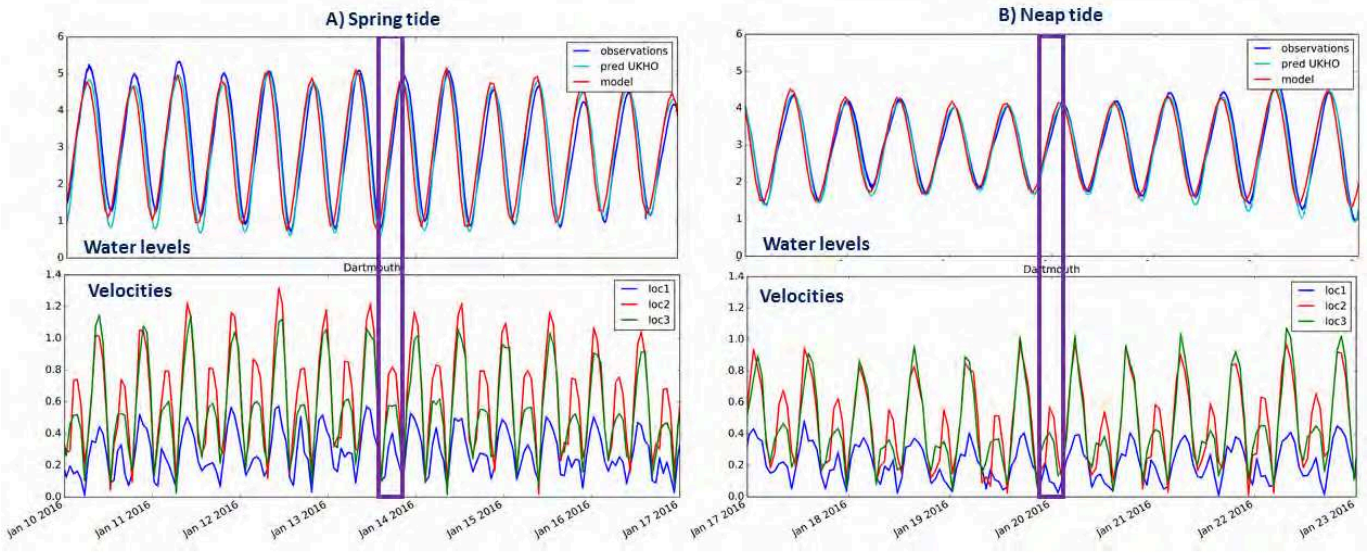

Figure 2: Validation of the water levels at Dartmouth (top panel) and current velocities (bottom panel) at locations 1, 2 and 3 (see Figure 1)

daily averaged salinity at the estuary mouth (C) at the surface and bottom layers, together with the tidal regime (A) and the river discharge (B). According to the literature, the Dart Estuary is partially mixed and experiences a complete stratification/destratification cycle with the neap/spring transition ([8]). In Fig. 3 we show that the model reproduces an increase in the stratification during neap tide. However, this stratification is modulated by the river discharge. In this sense, the stratification is stronger if the river discharge is higher (compare periods 1 and 2, both corresponding to neap tide conditions). The stratification can be strong in spring tide too if the river discharge is high enough. This is the case of the period highlighted as 3, that is characterized by stronger stratification than the previous neap tide (around 20th January).

III. Modelling Faecal Bacteria Released Through Sewage Overflows

A. Characterization of SOs in the Dart Estuary

As mentioned in the Introduction, SOs are intermittent discharges that spill untreated sewage at different points of the shoreline, with variable duration and volume. In the UK, the Environment Agency (EA) applies a set of standards to the determination of consent applications for discharges that impact on shellfish waters. For shellfish waters impacted by multiple SOs, the EA recommends aggregating spills by frequency and volume so that the combined impact of the aggregated spills does not exceed 10 spills per annum or 3% of the time on average. However, sometimes spills occur beyond the regulations.

Fig. 4 shows SOs spill data for the period 1st of April 2006 to 31st of March 2016 into the Dart Estuary. The colour scale shows in blue spills of less than 12h, in green spills between 12-24h, in yellow those lasting between 24-72h and in red spills of more than 72h. From Fig. 4 it is clear that six SOs (Totnes STW-SO, Stoke Gabriel SPS-PSCOEO, Mill Creek SPS-PSCOEO, Kiln Road SPS-PSCOEO, Ferry Boat SPST-PSCOEO and Dittisham STW-SO) have been more active than the others, specially from 2012 on, showing multiple long-lasting periods of spills and a certain degree of overlapping among the different SOs. In this study, we focused on the six SOs above, being the average duration of the spills compiled in Table 1.

Table 1. Average duration of SOs spills

SO	*Average duration*	*Number of data*
Totnes STW-SO	71.62	144
Stoke Gabriel SPS-PSCOEO	58.57	50
Mill Creek SPS-PSCOEO	9.51	143
Kiln Road SPS-PSCOEO	19.64	123
Ferry Boat SPST-PSCOEO	29.98	185
Dittisham STW-SO	27.92	195

Not much information is available on the SOs runoff. Indeed, among the selected ones, only data for Ferry Boat and Mill Creek were available, with flow rates of 23 and 17 m^3/day, respectively. Therefore, we decided to consider a baseline runoff for all the SOs of 20m^3/day. A test was done to evaluate the impact of higher discharges (200m^3/day).

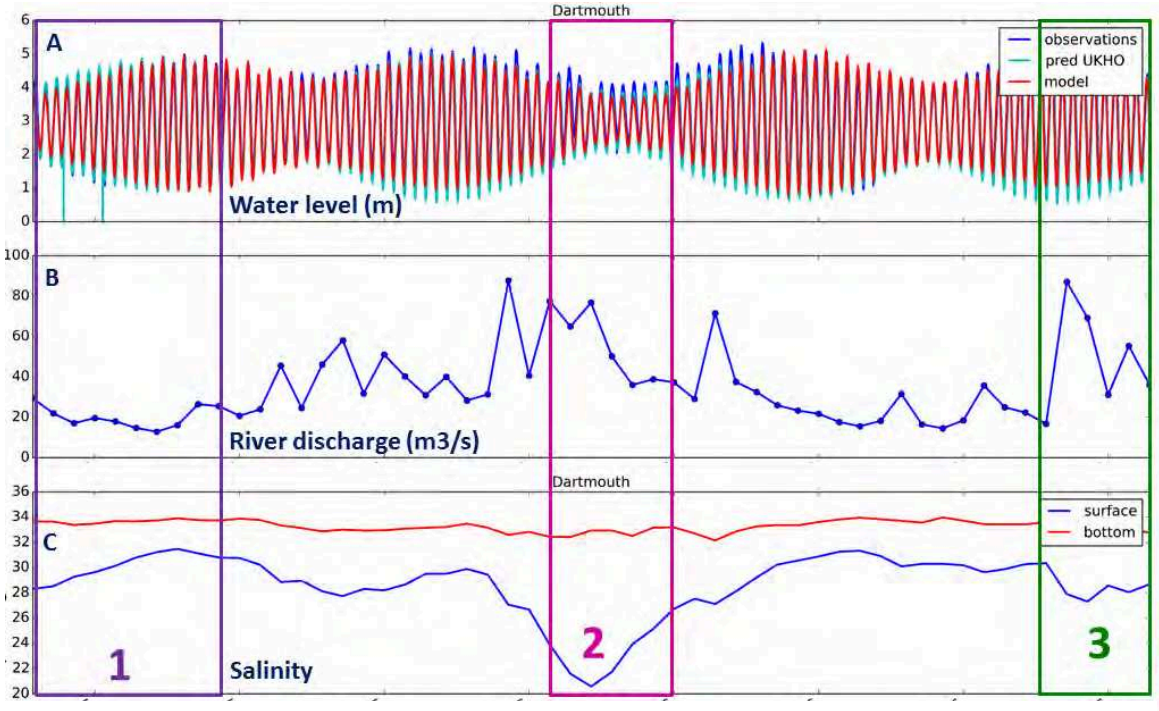

Figure 3: A) Observed and predicted water levels at Dartmouth, B) River discharge in m^3/s and C) Daily averaged surface (blue line) and bottom salinity (red line). The periods marked by 1, 2 and 3 are explained in the text.

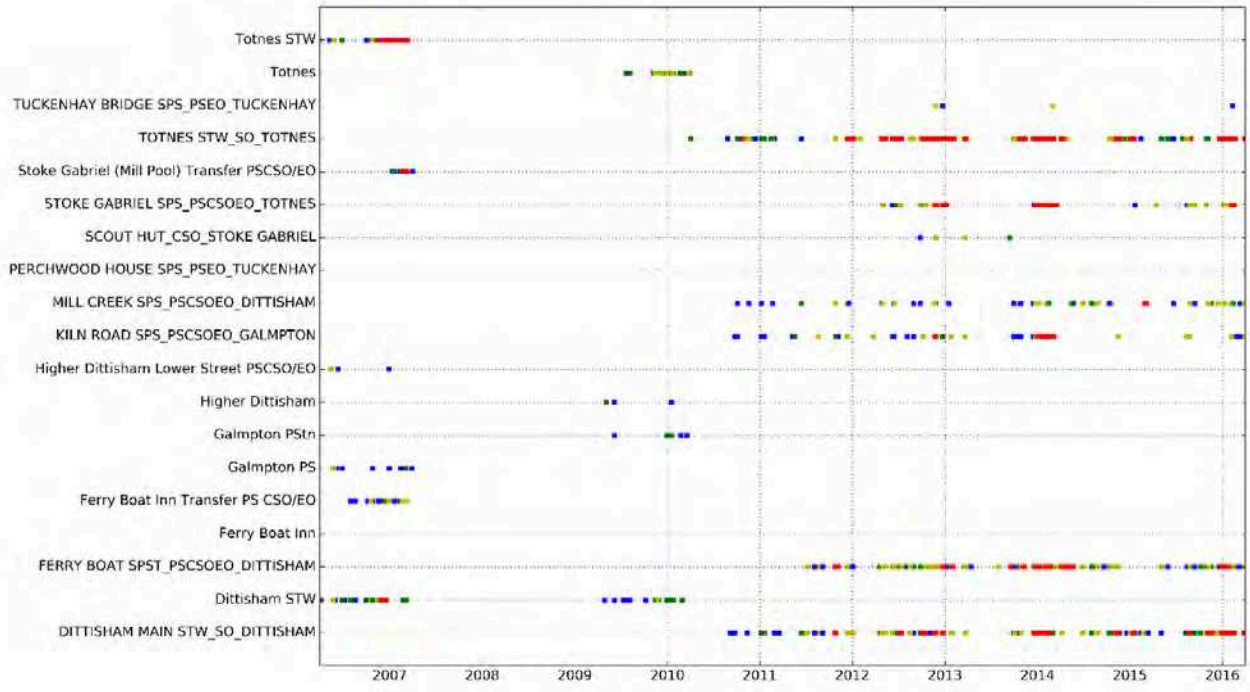

Figure 4: Spills of several sewage overflows in the Dart Estuary. Blue colours correspond to spills of less than 12h, green between 12-24h, yellow between 24-72h and red > 72h

Monitoring of concentrations of *E. coli* in effluents from SOs is not required under the EA discharge consenting policy. However, [4] published reference concentrations for different treatment levels and individual types of sewage-related effluents under different flow conditions. In this sense, Totnes STW-SO and Dittisham STW-SO were assigned a concentration of $8x10^5$cfu/100ml, corresponding to stored settled sewage, whereas for the rest of the SOs we used $2.5x10^6$cfu/100ml, which was Kay's characterization for storm sewage overflows.

B. *Modelling E. coli transport and decay*

In Telemac, the transport and decay of *E. coli* (EC) is modelled through (1)

$$\frac{\partial EC}{\partial t} + \vec{u}.\nabla(EC) = div\left(\vec{K}.\nabla(EC)\right) - k_d EC, \qquad (1)$$

with the left-hand side representing the advection of the faecal coliform, the first term on the right-hand side showing the diffusion and, finally, the last term representing the exponential decay. It is known that k_d for E. coli is a function of temperature, salinity and irradiation (see, for instance, [1] and [3]). However, for this study we have started by only considering a temperature dependence given by

$$k_d = k_{20}\theta^{(T-20)}, \qquad (2)$$

with $k_{20} = 0.036h^{-1}$, $\theta = 1.07$ and T the temperature [6]. Notice that since the temperature is kept constant in the model, the decay rate will be constant as well.

C. *Modelling scenarios*

To evaluate the effect of the river discharge and the tidal phase on the dispersal of *E. coli* in the estuary, four scenarios were considered:

- Scenario 1: Neap tide and high river discharge. The simulation starts the 4[th] of January 2016 and lasts for 5 days.

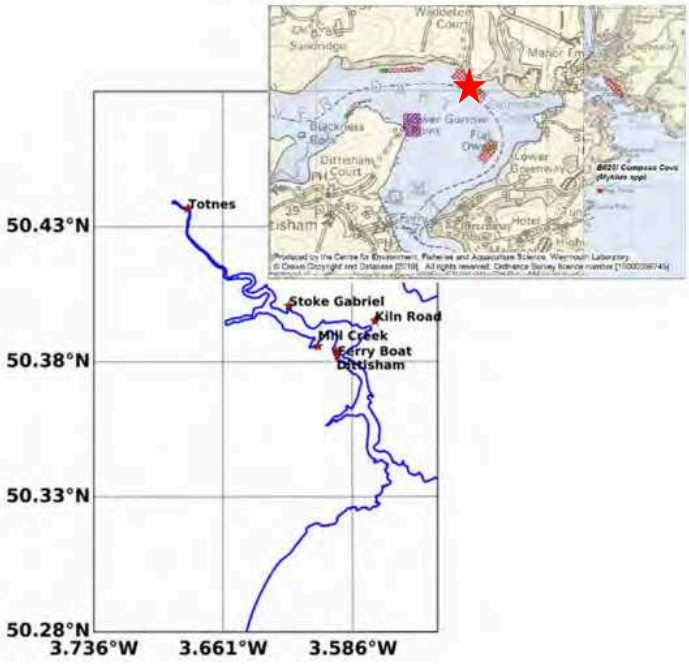

Figure 5: Location of the sewage overflows considered in this study and map showing the location of the BMPAs in the Dart Estuary (extracted from [2])

- Scenario 2: Neap tide conditions and low river discharge. The simulation starts the 19th of January and lasts for 5 days. This scenario was repeated for a spill discharge of 200m^3/day.
- Scenario 3: Spring tide and low river discharge. The simulation starts the 26th of January and lasts for 5 days.
- Scenario 4: Spring tide and high river discharge. The simulation starts the 13th of January and lasts for 5 days.

The different periods and conditions, although not explicitly indicated, can be seen in Fig. 3. The considered SOs, their duration and discharge are shown in Section III.A.

The location of the six considered SOs together with the BMPAs in the Dart Estuary is shown in Fig. 5.

IV. RESULTS

The concentration of *E. coli* one day after the beginning of the spill in the neighbourhood of the BMPAs of the Dart Estuary for the four studied scenarios is shown in Figure 6. The red colour in the map represents *E. coli* levels of > 10cfu/100ml (estimated mean concentration equivalent to G standard of the SWPAD). According to the model results, the area of exceedance is larger for scenario 2 (see Figure 6 B), followed by scenario 1 (Figure 6, A) at this time, with the BMPAs located in the areas of exceedance. This result is reasonable considering that retention of the spill increases at neap tide and low river discharge, whereas flushing increases in spring tide. The time series shown under each map represents the evolution of the concentration of the BMPA highlighted with a red star in Fig. 5. Higher concentrations are obtained for scenario 2 (Figure 6, B), although the maximum value is observed for scenario 1.

Table 2 compiles the averaged and maximum concentration of *E. coli* along the simulation period in the considered BMPA, together with the number of hours for which the concentration exceeds the standard of 10cfus/100ml. It is clear that scenarios 1 and 2 represent the worst-case scenarios of contamination, with scenario 2 showing a longer exposure to high concentrations (24h). The results for the test case considering higher discharges (200m^3/day) are also included in Table 2. In this case the

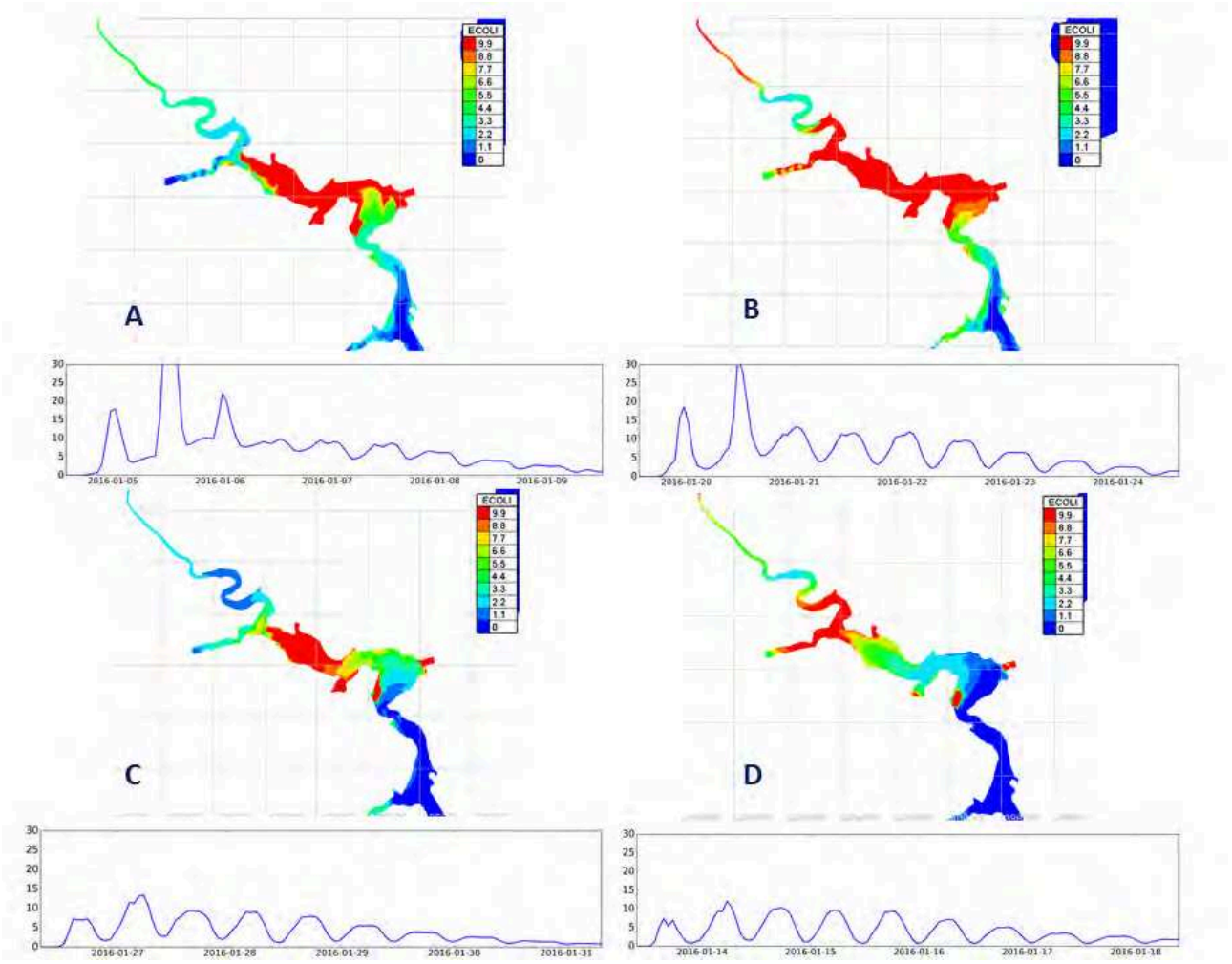

Figure 6: Model results corresponding to one day after the beginning of the spill. A) Scenario1, B) Scenario 2, C) Scenario 3 and D) Scenario 4. The time series below each plot represent the evolution of the concentration of E. coli at the BMPA indicated with a red star in Fig. 5.

averaged concentrations greatly exceed the G standard (56.08cfu/100ml), being this standard exceeded for most of the simulation time (4.45 days).

TABLE 2. AVERAGED AND MAXIMUM CONCENTRATION OF E. COLI FOR THE DIFFERENT SCENARIOS. NUMBER OF HOURS FOR WHICH THE CONCENTRATION EXCEEDS 10CFUS/100ML

Scenarios	Average concentration	Maximum concentration	Hours conc.>10cfus/100ml
Scenario 1	7.2	58.1	16
Scenario 2	6.1	31.33	24
Scenario 2-HD	56.08	313.8	107
Scenario 3	3.99	13.5	5
Scenario 4	3.99	12.0	4

V. SUMMARY AND CONCLUSIONS

In this paper, we have shown the first stages of the implementation of a hydrodynamic model of the Dart Estuary that is able to reproduce the water levels and current velocities along the estuary, as well as the stratification/destratification periods promoted by the tides and the variability of the river discharge. In this sense, we have a model that is suitable to investigate the fate and transport of faecal bacteria released through sewage overflows. The characterization of sewage overflows in terms of frequency of discharge and run-off is complex, therefore we have used the available data to define a constant run-off and an average spill duration applied to four simple scenarios from which we concluded that the worst conditions (higher exposure to *E. coli* in the BMPAs) in terms of tides and river discharge occur at neap tide when the river discharge is low.

Although beyond the scope of this initial study, further studies analysing the correlations between rainfall and the spill occurrence, frequency and duration would provide additional information to inform the identification of appropriate pollution remediation measures through the WFD Programmes of Measures process and/or support initiatives to proactively manage microbiological risks in BMPAs. Thus, this model constitutes a useful predictive tool available to better characterise episodes of poor water quality following intermittent discharges. A similar study, although based on statistical models, has been recently published (see [7]). This model could also be used to study the effects of climate change and population growth on the microbiological quality of the waters and shellfish.

ACKNOWLEDGEMENT

This study was funded by Cefas Seedcorn Project 'Impact and evaluation of combined sewer overflow discharges in shellfish waters' (DP407).

REFERENCES

[1] R.A Blaustein, Y. Pachepsky, R.L. Hill, D.R. Shelton and G. Whelan. Escherichia coli survival in waters: Temperature dependence. Water research, 47, 2013, pp. 569-578

[2] Cefas, 2010. Sanitary survey of the Dart Estuary (Devon). Cefas report of behalf of the Food Standards Agency, to demonstrate compliance with the requirements for classification of bivalve mollusc production areas in England and Wales under regulation (EC) No. 854/2004

[3] G.Gao, R.A. Falconer, B. Lin. Modelling the fate and transport of faecal bacteria in estuarine and coastal waters. Marine Pollution Bulletin 100, 2015, pp. 162-168.

[4] Kay D, Crowther J, Stapleton CM, Wyer MD and others (2008) Faecal indicator organism concentrations and catchment export coefficients in the UK. Water Res 42: 2649−2661

[5] Priestley, A.D., 1998. The Dart Observatory: an estuarine monitoring system. International Ocean System Design 2, 5-9

[6] Selvakumar, a., m. Borst, and s. D. Struck. Microorganisms die-off rates in urban stormwater runoff 2007. Presented at 2007 TMDL Conference, Bellevue, WA, June 24 - 27, 2007.

[7] W. Schmidt, H.L. Evers-King, C. Campos, D.B. Jones, P.I. Miller, K. Davidson and J.D. Shutler. A generic approach for the development of short-term predictions of Escherichia coli and biotoxins in shellfish. Aquaculture Environment interactions, vol. 10, 2018, pp. 173-185

[8] R.H. Thain, A.D. Priestley and M.A. Davidson. The formation of a tidal intrusion front at the mouth of a macrotidal, partially mixed estuary: a field study of the Dart Estuary, UK. Estuarine, Coastal and Shelf Science, 61, 2004, pp. 161-172

[9] Environment Agency, 2015. Shellfish water action plan. Issued Sep 2015.

[10] C.J. Campos, S. Kershaw, R.J. Lee, O.C. Morgan and K. Hargin. Rainfall and river flows are predictors for beta-glucuronidase positive Escherichia coli accumulation in mussels and Pacific Oysters from the Dart Estuary (England). Journal of Water Health, 2011, 9(2). Pp. 368-381

Development of a Three-Dimensional Hydrodynamic Model of Port Vila, Vanuatu, for Water Quality Assessment

David Haverson
Centre for Environment, Fisheries & Aquaculture Science
Lowestoft, UK
david.haverson@cefas.co.uk

***Abstract*— To help assess the dispersion of pollution in Port Vila, Vanuatu, a 3D baroclinic model was developed using TELEMAC-3D. Scenarios were tested to investigate the vulnerability of the system and identify control measures. Model results show those undertaking recreation activities in the bay are vulnerable to exposure to high concentrations due to a buoyant plume forming along the waterfront. Fatumara Bay contains ecologically important sea grasses which are particularly vulnerable as the model shows high concentrations quickly build up. The purpose of the model is to provide a tool for investigating the potential problems and solutions for water quality within Port Vila. The control measures tested with the model were shown to be effective, but there are no substitutes for a fully functioning sewage treatment system.**

I. Introduction

Vanuatu is a Pacific Island nation in the South Pacific Ocean and is an archipelago made up of over 80 islands. Port Vila is the capital of Vanuatu on the island of Efate and is of interest as part of a wider water quality programme in the region for the Commonwealth Marine Economies (CME) Programme. Water quality issues have become increasingly more important as population, tourism and coastal infrastructure grow and expand. Accurate water quality data enables national decision makers and local stakeholders to plan how to use and manage the bay's natural resources for sustainable marine economic development for a range of purposes, such as diving and other tourism activities or the identification of areas suitable for aquaculture sites. This ensures multi-use activity whilst protecting the marine environment into the future.

In Vanuatu, only 46 % of the population have piped drinking water. 47 % of all private households use a pit latrine, while 21 % use a flush toilet. Access to flushable toilets is 65 % in urban areas and only 6 % in rural ones. Nutrient data collected around Port Villa show a gradient of change related to the proximity of site to the Port Villa coast line and the influence of the storm-water drains. Interpolation analysis of the water quality data clearly shows the hot spots for Port Villa close to shore and clustered around the main storm water drains, identifying that urban runoff is a serious issue for the surrounding coastal area. Outputs of previous 2D modelling showed that the movement of the pollutants is influenced by the location of drains, and identified the priority actions around the storm-water drains that could be taken to reduce the pollution inputs into the bay.

As part of the water quality assessment of the CME programme, the aim of the hydrodynamic modelling project has been to improve upon the existing 2D hydrodynamic modelling and converting it to a 3D model. This is to provide a more accurate assessment of pollutant dispersion and test potential control mechanisms.

II. Hydrodynamic Model

A. Model Description

A 3D hydrodynamic model has been developed using the hydrodynamic software TELEMAC-3D (v7p2r2). The model domain, as shown in Figure 1 has been built using an unstructured triangular mesh and the spatial coverage has been expanded upon the existing 2D model domain. The domain now extends between 165.967 °E – 170.587 °E and 15.559 °S – 19.802 °S. The 2D mesh was discretised with 53,872 nodes

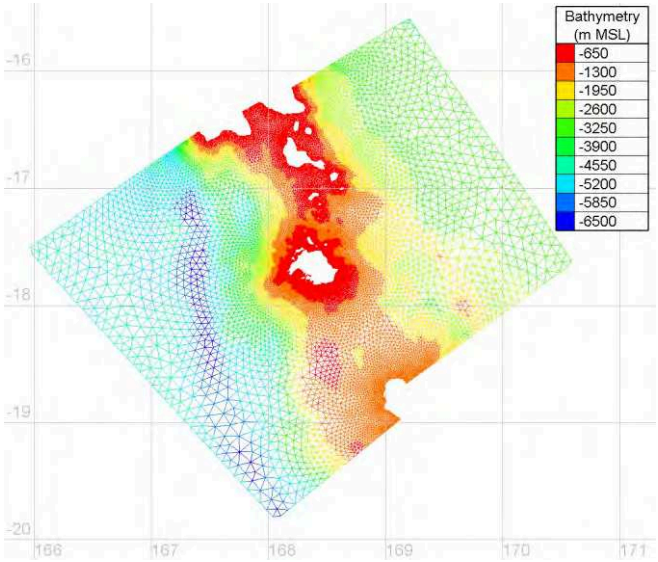

Figure 1: 3D model domain.

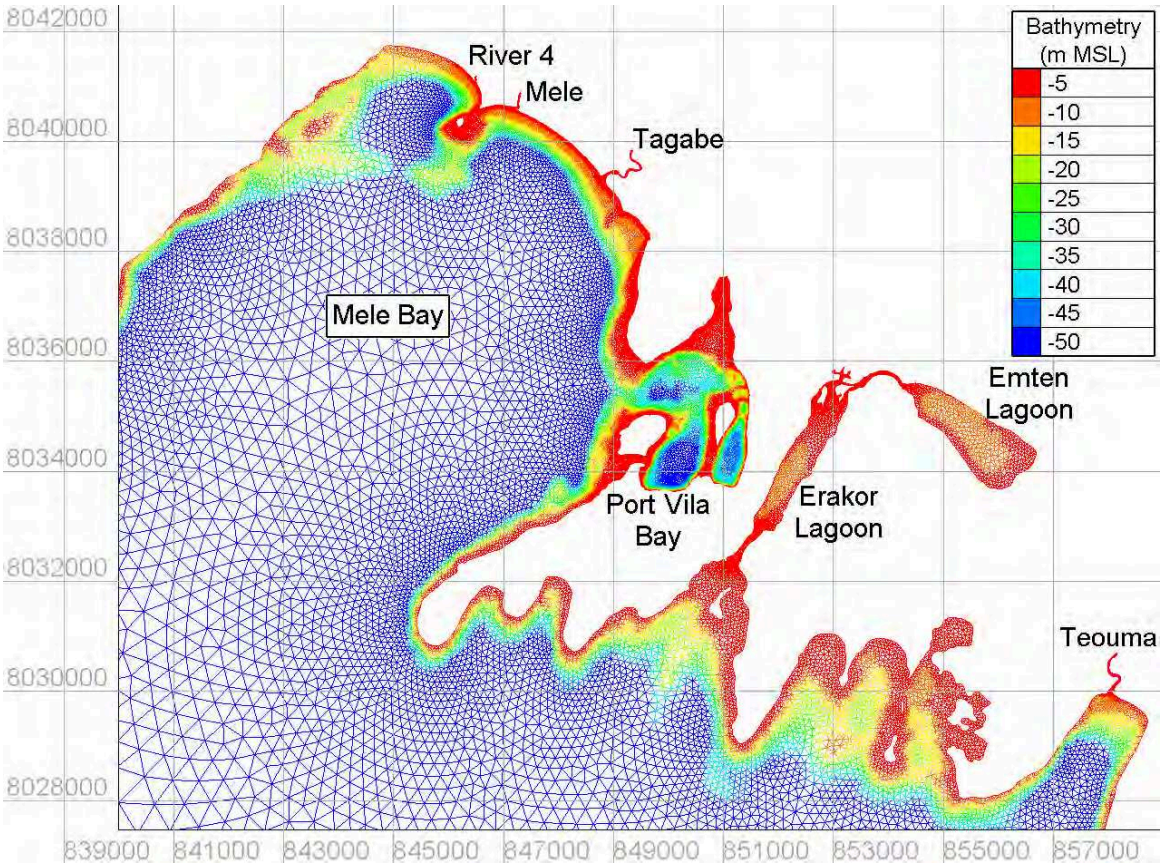

Figure 2: 3D model domain, zoomed into Port Vila.

and 102,160 elements. The 2D mesh has a resolution of approximately 8 km along the open boundaries. In Mele Bay, the resolution is refined to approximately 50 m and again refined further to approximately 20 m in Port Vila Bay. Furthermore, a new addition to the model domain was the inclusion of the Erakor and Emten lagoons, the Teouma River into Teouma Bay and the Tagabe, the Mele and an unnamed fourth river into Mele Bay, which are all shown in Figure 2.

Bathymetry for the model was provided by several sources. The bathymetry surrounding Efate island up to approximately 25 km from shore was provided by EOMAP at a resolution of 50 m [1]. Beyond this, the remainder of the model domain was sourced from GEBCO with a resolution of 1.5 km [2]. From the shoreline to depths less than 25 m have been sourced from optical clear satellite derived bathymetry, provided by EOMAP, with a spatial resolution of 10 m. Within Port Vila Bay bathymetry was provided by the UK Hydrographic Office at a resolution of 5 m. The vertical datum of the bathymetry in the model domain is with respect to Mean Sea Level (MSL).

The models vertical plane distribution was split into 10 layers with a sigma transformation with given proportions (MESH TRANSFORMATION = 2). The proportions, as a percentage of depth, are: 1, 2, 10, 20, 50, 80, 90, 95, 98 and 100. The layers were distributed to provide a more accurate representation of currents and pollution dispersion near the sea surface.

The hydrodynamics are forced along the open maritime boundaries using 11 tidal constituents (M2, S2, N2, K2, K1, O1, P1, Q1, M4, MS4 and MN4) from the OSU TPXO Pacific Ocean 1/12° regional model [3]. The TPXO harmonics are used to drive the prescribed elevations with free velocities. However, due to steep bathymetric gradients on the open boundary, this can lead to numerical instability. To overcome this, the bathymetry has been smoothed so there are no lateral bathymetric gradients on the boundary. All bathymetry below the 1000 m depth contour has been smoothed to 1000 m. Due to the large distance between the open boundary and the area of interest and the depths included in the model domain, the bathymetry smoothing is not considered to have greatly affected the velocities in the near vicinity around Efate Island.

As the tidal range in Port Vila is small, 1.64 m, and the main source of pollution into Port Vila bay is introduced at the sea surface, the dispersion of pollution is likely to be heavily influenced by wind driven surface currents. Therefore, wind forcing has been included in the model in addition to tidal forcing. A yearly record of hourly winds for Port Vila has been sourced from the Australian Bureau of Meteorology for 2016 [4]. The data shows that the mean wind speed is 1.29 m/s with a peak of 8.4 m/s. The predominant wind direction is from the South-West.

B. Modelling Temperature and Salinity

To investigate the water quality in Port Vila Bay, the pollution in the model was represented by a passive tracer.

Specifically, the pollution was represented by the level of Dissolved Inorganic Nitrogen (DIN). The main sources of DIN, investigated with this model, are introduced through the sewage and storm water system. The associated salinity of the sources is treated as freshwater which is considerably different from the salinity of Port Vila Bay (i.e. sea water). As such, the effects of salinity have been included in the model.

During the field measurement campaign in December 2017, temperature and salinity profiles were collected in Port Vila Bay using a handheld CTD. Figure 3 and Figure 4 show two temperature and salinity profiles from within Port Vila Bay. The first was collected by the cruise ship dock (168.303 °E, 17.735 °S), one of the deepest points in the bay, and the second by the mouth of Port Vila Bay north east off Ifira Island (168.311 °E, 17.755 °S). As the main area of interest is within Port Vila Bay and that the salinity profiles show little stratification, a constant salinity has been applied to the whole model domain, both vertically and horizontally.

In addition to the sewage and storm water system, fresh water is introduced into the model at the source of the four rivers, whose location is shown in Figure 2. During the field measurement campaign in December 2017, the flow rate was measured at the Teouma, the Tagabe, the Mele and an unnamed fourth river into Mele Bay. The river flow was measured using the SonTek FlowTracker2 (FT2) handheld Acoustic Doppler Velocimeter (ADV). For each river, the velocity was measured at three points across the river along with the cross-sectional area of the river, to compute a flow rate. The observations are summarised in TABLE 1. In addition, the pH, salinity, dissolved oxygen and temperature were also measured, but not presented.

Since the storm drains are open to the environment, the difference between source temperature and background is very small. As such, the temperature of the source terms is considered to be that of the ambient air. The difference between the air temperature and the water temperature, as recorded by the Australian Bureau of Meteorology, is on average 1.6 °C. Furthermore, the temperature profiles shown in Figure 3 and Figure 4, show little stratification. As such, the temperature tracer has not been included in the model.

TABLE 1. OBSERVED RIVER FLOWS.

River	Depth	Velocity Sample			Area	Flow rate
		1	*2*	*3*		
	m	m/s	m/s	m/s	m^2	m^3/s
Teouma	0.80	0.67	0.71	0.69	6.29	4.46
Tagabe	0.85	0.82	0.92	0.91	4.68	4.29
Mele	0.52	0.61	0.65	0.62	1.30	0.84
Unknown	0.63	0.56	0.53	0.58	1.58	0.91

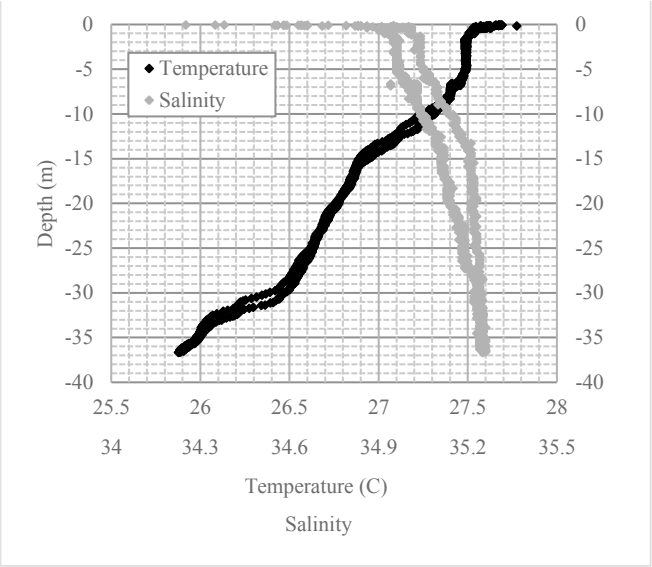

Figure 3. Temperature and salinity profile at cruise ship port.

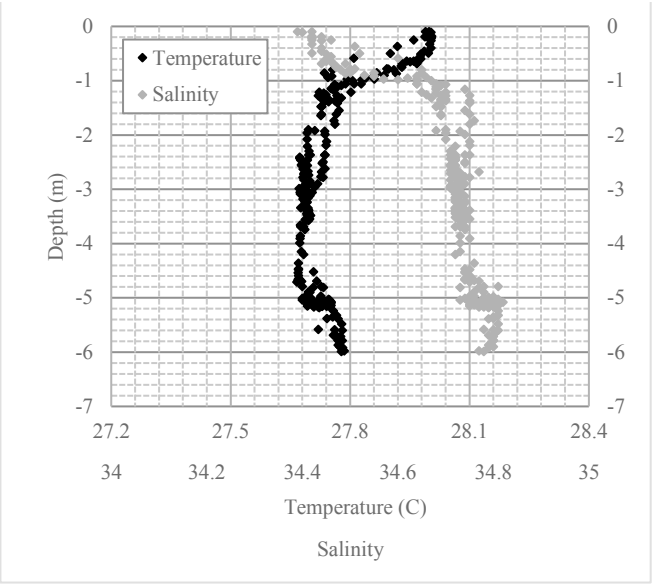

Figure 4. Temperature and salinity profile at Ifira Island.

III. MODEL VALIDATION

To assess the model performance, the tidal elevations were validated against data obtained from the tide gauge in Port Vila (168.308 °E, 17.755 °S), as provided by the Australian Bureau of Meteorology. After a spin up period of 10 days, the model was run for 30 days to cover a full spring-neap cycle. The model showed good agreement to observed tidal elevations. Figure 5 shows the comparison of observed and model elevation. The solid black line denotes a $y=x$ relationship, with the dashed black line representing a linear regression of best fit of the data. TABLE 2 summarises the validation statistics of the Port Vila tide gauge comparison.

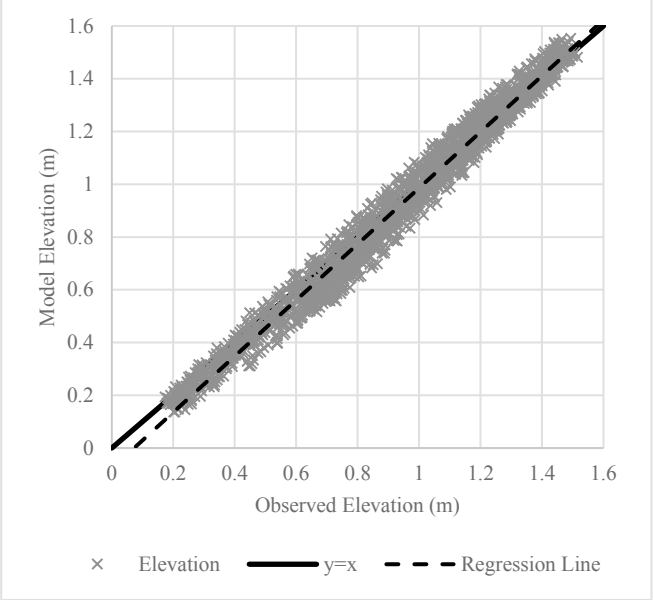

Figure 5: Comparison of observed and modelled free surface elevation at Port Vila tide gauge. The black line represents a $y=x$ relationship with the dashed line representing a regression line of best fit.

TABLE 2. VALIDATION STATISTICS OF PORT VILA TIDE GAUGE.

Tide Gauge	R^2	RMSE (m)	Scatter Index (%)
Port Vila	0.979	0.051	5.450

IV. WATER QUALITY ASSESSMENT

A. Sewage Outfalls

Along the newly developed waterfront in Port Vila, sewage outfalls can be seen within the sea wall at the height of the sea surface. A number of these are in immediate proximity to public access points into the water for recreation activities, such as swimming. A total of 17 outfalls have been identified and included in the model whose location into Port Vila Bay and Fatumara Bay have been obtained from the PVUDP Civil Design Sketches of the Port Vila Urban Development Project on behalf of the Port Vila Ministry of Infrastructure and Public Utilities. The outfalls source positions are located one node in from the solid boundary and are shown in Figure 6. It is known that there are outfalls into the Erakor and Emten lagoons. However, due to the uncertainty in their location, no outfalls into the lagoons were included.

Presently, there are no known monitored flow rates at the outfall locations and observations could not be obtained during the field measurement campaign. Although, significant surface runoff during a rainfall event was witnessed. In the absence of measurements, comparable regional values were obtained from the Solomon Islands. The Solomon Water 5 Year Action Plan: 2017 to 2022 details the design capacity of the sewage system at Honiara [5]. The report provides three values:

- Average Dry Weather Flow rate – 25.9 l/s
- Peak Dry Weather Flow rate – 93.3 l/s
- Peak Wet Weather Flow rate – 178.8 l/s

These values provide the basis for the subsequent scenarios tested by the model. Whilst flow rates are likely to vary throughout the day, for simplicity the model assumed a constant flow rate.

B. DIN Concentrations

As the samples collected during the December 2017 field campaign could not be analysed in time for the modelling, samples collected during August 2016 were used for the parameterization of DIN. Combined with the river flow measurements, a horizontal tracer diffusion coefficient of 0.1 m^2/s was found to give a good representation. Based on DIN measurements, the background concentration for DIN was 5 mg/l, which was applied uniformly to the whole model domain. For the rivers, a concentration of 40 mg/l was applied to the Tagabe River, 200 mg/l for the Mele River and 200 mg/l for River 4. As no measurements were taken for the Teouma River or in the surrounding area, the background concentration for DIN was applied, negating any contribution. However, a fresh water input was still applied as this would influence the local hydrodynamics.

From the May and August 2016 DIN observations, only two samples match the location of outfall positions. The two concentrations were 11 mg/l and 4451 mg/l. The range is indicative of treated waste compared to untreated waste. During the December 2017 field trip, it was discovered 4 of the 5 sewage treatment plants in Port Vila were not functioning. As this will adversely affect water quality and is a worst case extreme, all the subsequent modelling will assume values representing non-functioning sewage treatment plants. Initially, a conservative estimated concentration of 200 mg/l was applied uniformly to every outfall, but was found to underestimate values observed within Port Vila Bay. As such, a concentration of 500 mg/l was applied and results showed improvements.

C. Model Scenarios

To investigate how water quality evolves throughout Port Vila Bay under various conditions, four different scenarios were considered for testing with the model. The first two scenarios consider the influence of the flow rate. For Scenario 1, a constant average dry flow rate of 25.9 l/s with a concentration of 500 mg/l was applied uniformly to all 17 outfalls. For Scenario 2, a constant peak dry flow rate of 93.3 l/s with a concentration of 500 mg/l was applied uniformly to all 17 outfalls.

Many of the sewer outfalls along the Port Vila Bay seafront are next to public access points to the water at the sea surface. To improve public health, Scenario 3 tests the impact of moving the outfall positions further offshore and releasing just above the seabed. The sources along the waterfront have been moved approximately 100 m offshore, as shown in Figure 10. As Fatumara Bay is very shallow, 3 outfalls were moved further offshore at the shelf edge of Fatumara Bay at approximately 20 m depth. The remaining outfalls in Fatumara Bay have been left at their original location as they are not near any public access points but have been set to release at the

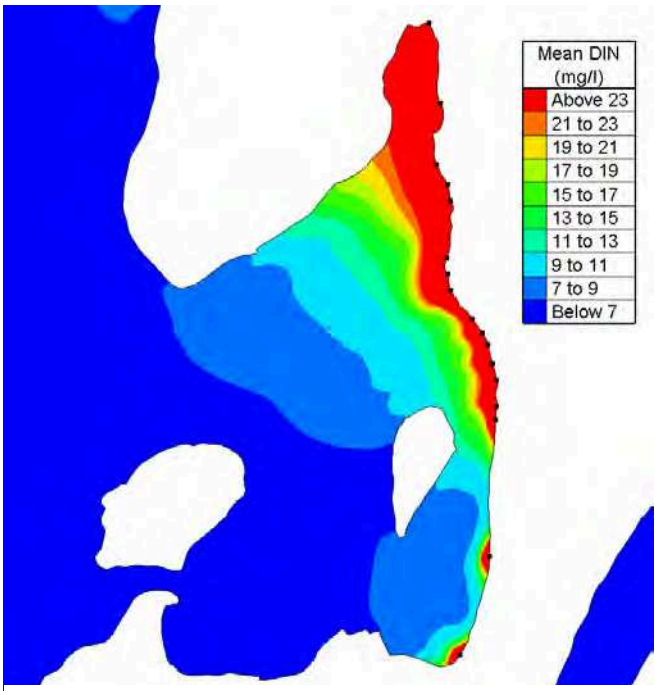

Figure 6: Mean concentrations of DIN at the sea surface for Scenario 1. The black dots represent the outfall positions.

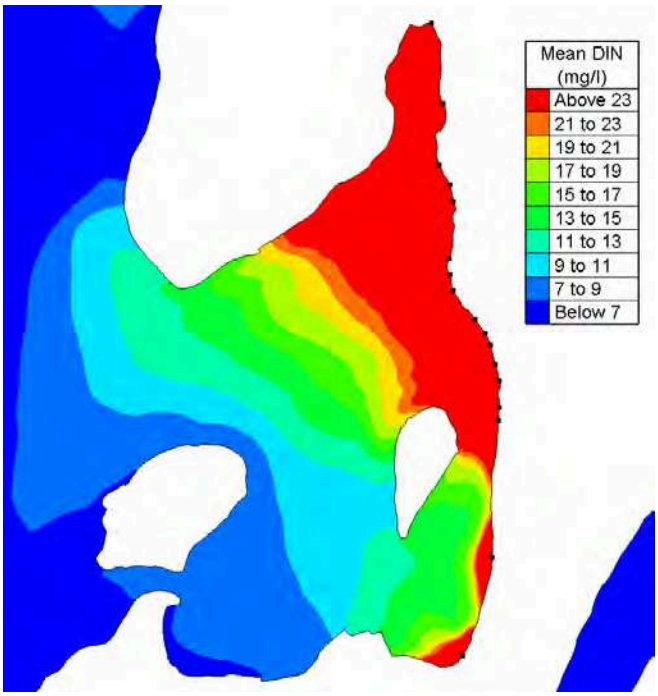

Figure 7: Mean concentrations of DIN at the sea surface for Scenario 2. The black dots represent the outfall positions.

seabed instead of the sea surface. For comparison with Scenario 1, the flow rates are set to 25.9 l/s, and the concentrations set to 500 mg/l.

The final scenario considers reducing the impact on Fatumara Bay as it contains ecologically important sea grasses. As depths are very shallow and the tidal exchange between Fatumara and Port Vila Bay is very small, high concentrations can build up quickly. In order to reduce concentrations, Scenario 4 uses only 12 of the 17 outfalls, with the five outfalls within Fatumara Bay closed off. The remaining 12 outfalls are positioned as in Scenario 3 with the same flow rate, concentration and seabed release.

V. Results

A. Scenario 1

Whilst the base case for validation was run for 30 days, the tracer studies were limited to 12 days. This encompassed the spring tides, representing the largest tidal range and fastest flows, meaning the dispersion of DIN would travel its furthest. Figure 6 shows the mean concentration of DIN at the sea surface, excluding the first 24 hours. The first 24 hours are excluded as the concentration of DIN starts uniformly at the background value and would bias the mean value. The black dots represent the position of the 17 outfalls.

The results agree with the trend seen in the observations in that the high concentrations are found in front of the Port Vila waterfront. The model also shows that concentrations within Fatumara Bay are even higher, with the mean concentration exceeding 30 mg/l, over 5 times the background value. The concentrations quickly start to build up within Fatumara Bay and after only four days the tracer distribution starts to resemble the mean values at the sea surface. Outside of

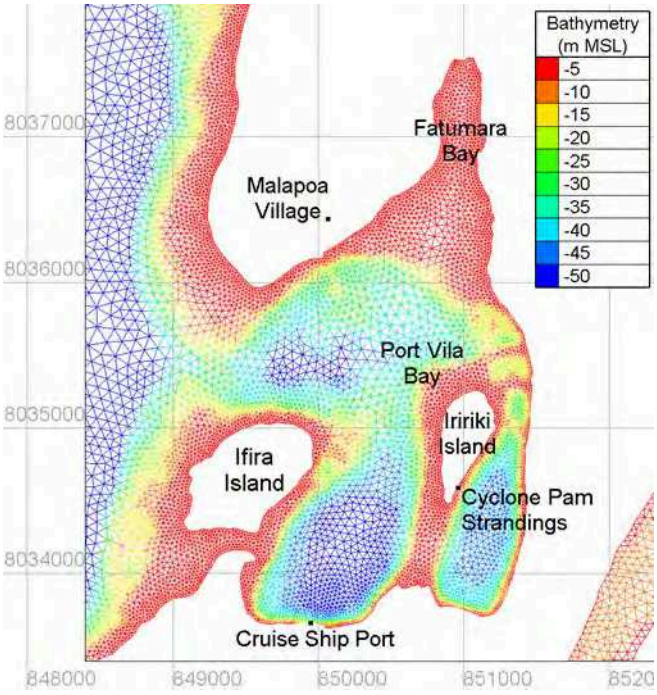

Figure 8: Bathymetry and key locations in Port Vila Bay.

Fatumara Bay, elevated concentrations permeate into the wider Port Vila Bay. However, the highest concentrations are limited to the immediate vicinity of the outfall positions and tend to hug the coastline, forming a narrow band of high concentration along the Port Vila waterfront. Whilst the model does show DIN from the outfalls leave Port Vila Bay, it quickly diffuses once into Mele Bay, as the bathymetry rapidly drops from approximately 45 m to over 300 m. The southern

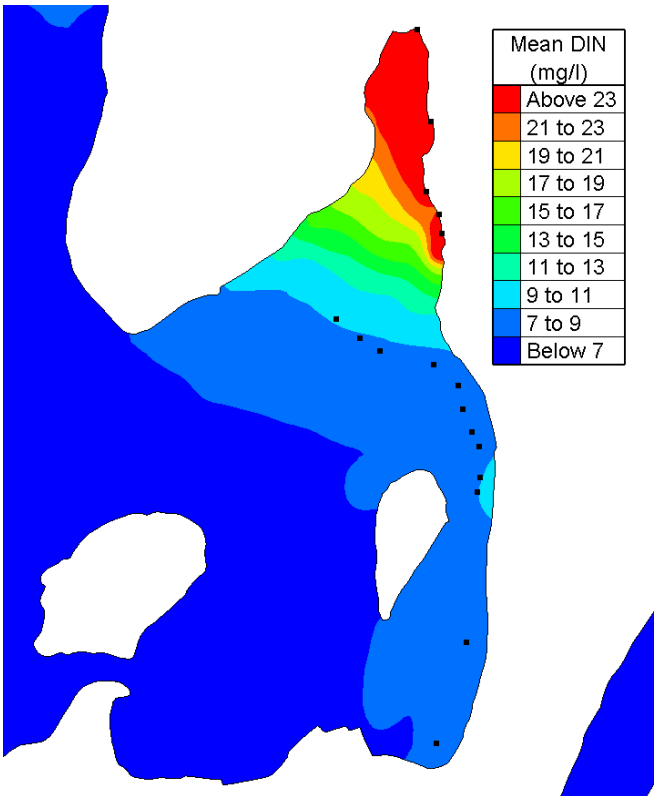

Figure 10: Mean concentrations of DIN at the sea surface for Scenario 3. The black dots represent the outfall positions.

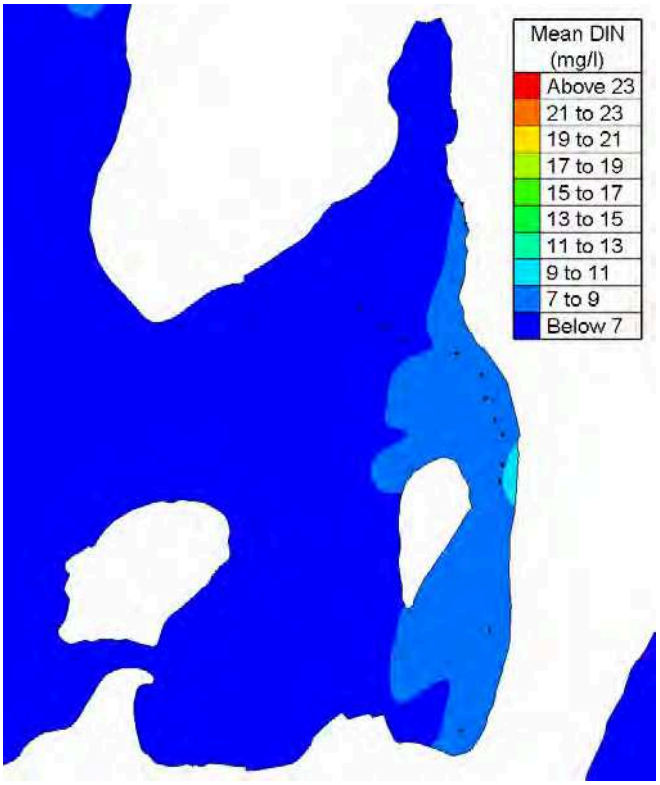

Figure 9: Mean concentrations of DIN at the sea surface for Scenario 4. The black dots represent the outfall positions.

half of Port Vila Bay can be split into two halves by Iririki Island and a bar that extends from its southern tip to the port harbour. Either side of this bar, the bathymetry drops into two deep craters, approximately 40 m deep. The result is the bar effectively acts as a barrier containing the higher concentrations within the eastern half.

B. Scenario 2

The results of Scenario 2 show a similar spatial distribution of DIN throughout Port Vila Bay as seen in Scenario 1. Unsurprisingly, the result of higher flow rate is a higher concentration of DIN throughout the Bay, as shown in Figure 7. Concentrations within Fatumara Bay now exceed 50 mg/l, over 10 times the background concentration. Within the wider bay, the DIN plume extends further west than Scenario 1 and the narrow band of high concentrations along the Port Vila waterfront extends almost 4 times further. Whilst higher concentrations reach into Mele Bay, they also dissipate quickly.

C. Scenario 3

Scenario 3 investigates the impact of moving the outfalls further offshore and releasing from the seabed. Figure 10 shows the mean concentration of DIN at the sea surface, with the new outfall positions shown as black dots.

The result is a dramatic reduction in the concentration of DIN at the sea surface, particularly in front of the Port Vila waterfront. Whilst the concentrations are still high at the seabed, by the time the concentrations have diffused through the water column to the sea surface, the values are significantly lower. Approximately 100 m off the Port Vila waterfront, the concentrations are reduced by 20 mg/l. This value rises to an excess of 100 mg/l reduction within the first 25 m off the waterfront where the public access points to water are located. Whilst there is a reduction in the mean concentrations within Fatumara Bay, the concentrations at the sea surface are still in excess of 25 mg/l.

D. Scenario 4

Scenario 4 investigates the impact of not allowing the outfalls to release in to Fatumara Bay using the same outfall positions as used in Scenario 3. Figure 9 shows the mean concentration of DIN at the sea surface. For comparison, the location of the outfall positions within Fatumara Bay are included in the figures, but the top five outfalls release no tracers.

The result of Scenario 4 shows the same response, as in Scenario 3, a dramatic reduction in the concentration of DIN at the sea surface. The difference between Scenario 3 and 4 clearly shows that the main contribution to the high concentrations within Fatumara Bay are from the outfalls not included and not the outfalls along the Port Vila waterfront. Whilst there is a small plume from the waterfront outfalls, the high concentrations attributed to these outfalls remains within close proximity to the waterfront.

VI. Discussion

One of the main problems with assessing the performance of the model is that it is significantly difficult to give an accurate quantitative assessment due to the number of

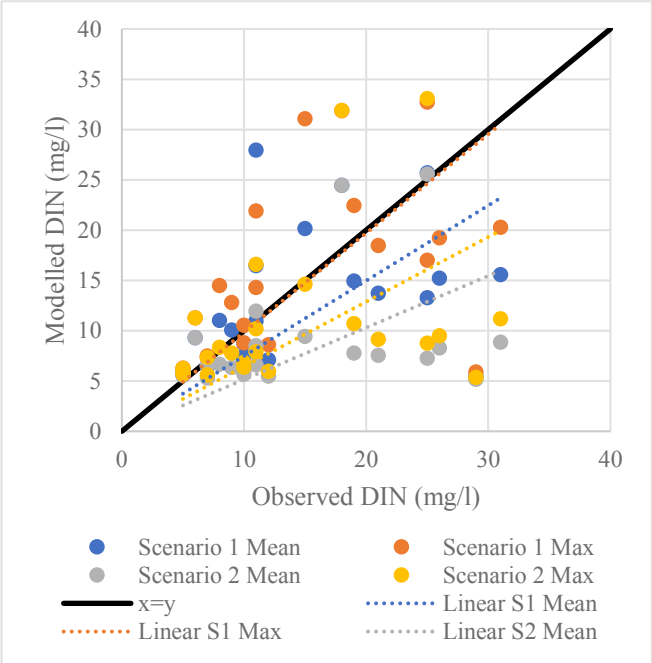

Figure 11: Comparison of the August 2016 observations and the mean and maximum concentrations of Scenario 1 and 2.

uncertainties with the model, notably the outfall flow rates and concentrations. One of the model assumptions is a constant flow rate and concentrations uniformly applied to every outfall. Realistically, these are likely to vary with time. Figure 11 shows the comparison between the observed concentrations in August 2016 and the mean and maximum concentrations of Scenario 1 and 2.

The lower flow rates of Scenario 1, overall, provide a closer representation of the observed concentrations. However, the model both under-predicts and over-predicts concentrations. Overall the model does qualitatively perform well, agreeing with the trends in the observations and representing many key features, such as the high concentrations in front of the Port Vila waterfront and the higher concentrations in the eastern half of the southern Port Vila Bay. One trend the observations show is that the concentrations in the eastern half of the southern Port Vila Bay are higher than the western half. The model shows this but under-predicts the concentrations in the eastern half. Whilst one solution would be to alter the outfall source conditions, the potential cause of the discrepancy is the lack of other sources. For example, there are no sources from the Port Harbour nor Iririki Island. The outfall for the Iririki Island resort is believed to be located to the south-east of the Island but could not be confirmed. The addition of this source, even with a constant flow rate and concentration is likely to improve the results. There are a number of other potential sources not included in the model that might change results, such as leeching from the stranded vessels from Cyclone Pam, the cruise ship port, the boat cleaning/repair site to the west of the cruise ship port, outfalls from the population of Ifira Island and outfalls from the population of Malapoa Village on the western shore of Fatumara Bay. These locations are shown in Figure 8 The likely consequence of including these additional sources is to raise the levels of DIN even higher within the bay.

Despite these uncertainties, the model does provide a good representation of the characteristics of the bay and can be readily applied to a number of different scenarios or assimilate any additional observation data. The purpose of the model is to provide a tool for investigating the potential problems and solutions for water quality within Port Vila, to which it has successfully demonstrated.

Presently, the outfalls along the Port Vila waterfront release at the sea surface. This is a potential hazard to those using the public access points for recreational activities, such as sea swimming, because of the buoyancy of the outfall plume. As a result, anyone entering the water must travel through the outfall plume. Figure 12 shows how the concentration of DIN develops in the vertical profile over the model run for a point approximately 175 m in front of outfall position number 13 from Scenario 1.

The results show that the concentration of DIN only disperses into the top layers, with the highest concentrations staying within the top two layers. Layer 7 represented a depth of 80 % of the water column. At this location, the depth was 15 m, meaning the plume was extending 3 m deep. Scenario 3 and 4 was effective at reducing the concentration of DIN along the waterfront by moving the outfalls further offshore into deeper water. By releasing from the seabed, the plume disperses both laterally and vertically. As there is significantly more water above the release point, the plume has a larger quantity of water to dilute and the concentration at the sea surface is dramatically reduced. However, this is also why Scenario 3 is not as effective at reducing the concentrations within Fatumara Bay as the bay is only a few meters deep. The plume permeates through the entire water column. The only solution to dramatically reduce the concentrations is to not release within Fatumara Bay, as shown in Scenario 4.

To provide a comparison between the four scenarios and to visualize the effectiveness of the proposed control measures, a horizontal profile of the concentration of DIN has been taken at the sea surface extending from within Port Vila Bay to the top of Fatumara Bay. Figure 13 shows the horizontal profile of the mean DIN concentrations at the sea

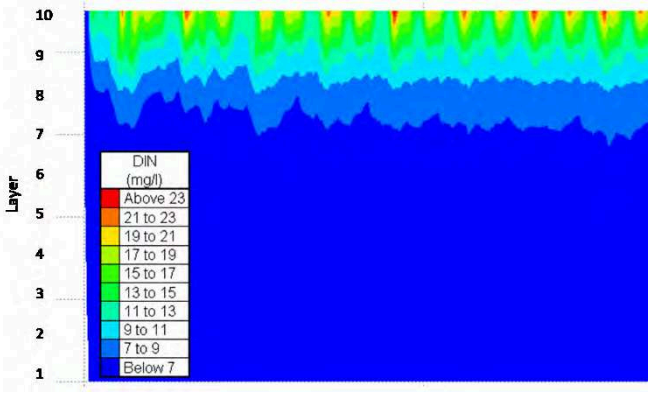

Figure 12: Vertical profile of DIN concentration in Scenario 1, approximately 175 m in front of outfall No.13.

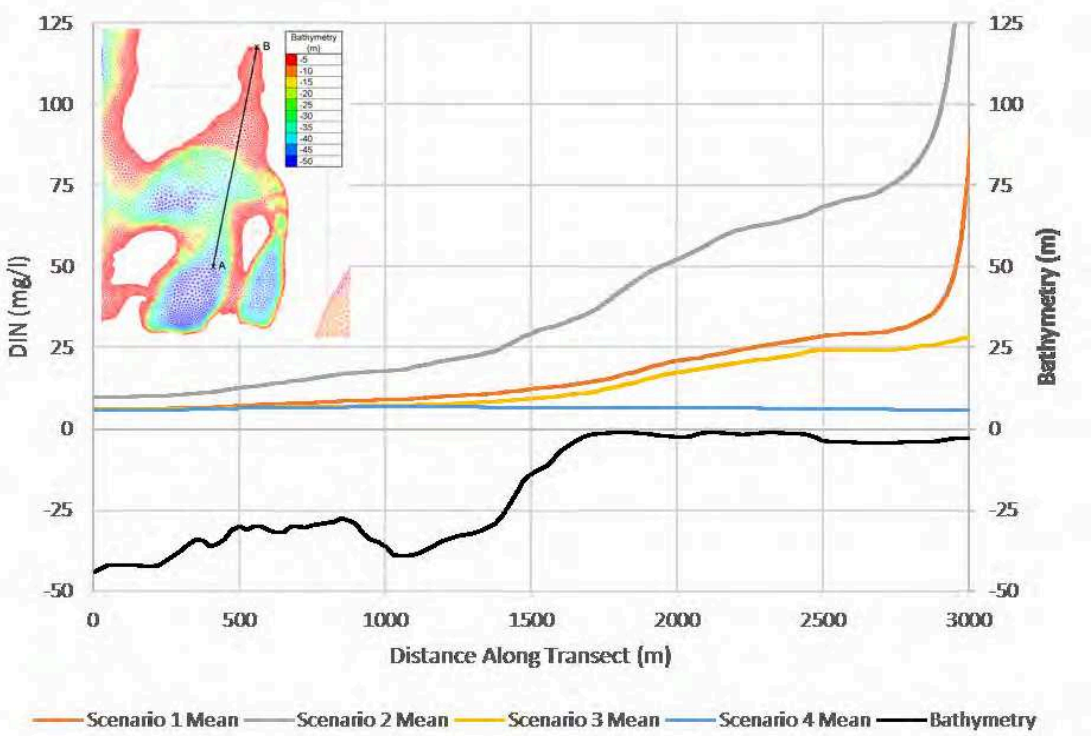

Figure 13: Horizontal profile of the mean DIN at the sea surface for all four scenarios.

surface for all four scenarios. In addition, the black line shows the depth contour along the transect.

By increasing the flow rate, in Scenario 2, to over three times that in Scenario 1, the concentration of DIN is almost doubled. Furthermore, it can be clearly seen that the concentrations dramatically increase as the depth of water reduces into Fatumara Bay. Again, the figure reiterates the only way to radically reduce concentrations in Fatumara Bay is to not release within the Bay. The 3 m depth contour along the shelf edge of Fatumara Bay would provide a natural delineation in which to mark a no release zone.

VII. SUMMARY

A 3D barotropic model of Port Vila, on the island of Efate, has been developed as part of the wider water quality monitoring programme in Vanuatu. Integrated analysis of the water quality data identified the coastal hot spots for Port Vila, and showed that urban run-off is a serious issue in the coastal area. The purpose of the model was to provide a more accurate representation of pollutant dispersion in Port Vila Bay, over the existing 2D model.

Those undertaking recreation activities in the bay, such as swimming, are vulnerable to exposure to high concentrations. The model shows that outfalls form a buoyant plume along the Port Vila waterfront. Moving the outfall positions approximately 100 m offshore and releasing at the seabed was shown to be effective at reducing concentrations. Fatumara Bay contains ecologically important sea grasses which are particularly vulnerable. The model shows high concentrations quickly build up due to the shallow depths and small tidal exchange between Fatumara and Port Vila Bay. Whilst the outfalls along the waterfront do contribute to the build-up, the outfalls in the bay are the main problem. The most effective way to limit concentrations is to allow no outfalls to release into Fatumara Bay. The 3 m depth contour along the shelf edge of Fatumara Bay would provide a natural delineation in which to mark a no release zone.

The purpose of the model is to provide a tool for investigating the potential problems and solutions for water quality within Port Vila. The control measures tested with the model were shown to be effective, but there are no substitutes for a fully functioning sewage treatment system. The model is readily adaptable to test alternative solutions.

ACKNOWLEDGEMENT

This work was carried out on the High-Performance Computing Cluster supported by the Research and Specialist Computing Support service at the University of East Anglia.

REFERENCES

[1] Earth Observation and Environmental Services, [Online], Available: www.eomap.com

[2] IOC, IHO and BODC, 2003, Centenary Edition of the GEBCO Digital Atlas, published on CD-ROM on behalf of the Intergovernmental Oceanographic Commission and the International Hydrographic Organization as part of the General Bathymetric Chart of the Oceans; British Oceanographic Data Centre, Liverpool.

[3] Egbert, G.D. and Erofeeva, S.Y., 2002. Efficient inverse modeling of barotropic ocean tides. Journal of Atmospheric and Oceanic Technology, 19(2), pp.183-204.

[4] Australian Bureau of Meteorology, Hourly Sea Level and Meteorology Data for 2016, [Online], Available: www.bom.gov.au/pacific/vanuatu/index.shtml

[5] Solomon Water, 2017, 5 Year Action Plan 2017-2022. Honiara: Solomon Water.

ARTEMIS developments at HR Wallingford

Noémie Durand, Sébastien Bourban, Nigel Tozer
Coasts & Oceans Department, HR Wallingford, Wallingford, United Kingdom
N.Durand@hrwallingford.com

***Abstract*— The ARTEMIS model (Agitation and Refraction with TElemac on a MIld Slope) from the TELEMAC suite of solvers solves the elliptic mild slope equation using finite element techniques. Its main field of application is wave disturbance studies inside harbours or small bays, often driven by a regional model. ARTEMIS is a well-established model, used in consultancy studies for over 20years.**

ARTEMIS was originally developed by the Laboratoire National d'Hydraulique et d'Environnement (LNHE of EDF-R&D). In recent years, with the transfer of the model to open source, development efforts have been open to entities other than LNHE. This paper presents developments of the ARTEMIS model, at HR Wallingford, available or soon to be available in future releases of the TELEMAC system.

I. SPECIFYING BOUNDARY NODE PROPERTIES

This feature was introduced on the opentelemac cue system (http://cue.opentelemac.org/) as Feature #391: `LECLIM` to replace coding in `BORH`.

A. What's new?

Boundary conditions in the TELEMAC modelling system are specified via a table of variables known as the CONLIM or .cli file. The CONLIM file holds as many lines as there are boundary nodes in the finite element mesh, with each line defining the boundary node properties, characterised by 13 variables (refer table below).

TABLE 1: BOUNDARY NODE PROPERTIES IN THE TELEMAC SYSTEM.

Data column	Parameter name	Parameter description
1	LIHBOR	Code for Depth
2	LIUBOR	Code for U (velocity or flow)
3	LIVBOR	Code for V (velocity or flow)
4	HBOR	Prescribed value for Depth
5	UBOR	Prescribed value for U (velocity or flow)
6	VBOR	Prescribed value for V (velocity or flow)
7	CHBORD	Friction coefficient
…	…	…
12	NBOR	Global node number in mesh
13	K	Sequential boundary node number
14	BndName	Optional: # Name of the boundary

Historically in ARTEMIS, while the boundary node type LIHBOR is routinely defined in the CONLIM file (e.g. solid, open, incident), other boundary node properties have been coded in subroutine `BORH`. This is where the incident wave height HB, angle of incident wave attack TETAP, reflection coefficient RP etc. are informed, typically using a do loop on boundary node numbers. This process can be prone to coding errors and feature #391 is meant as a user friendly, simpler alternative.

In this new approach, the user can document all the boundary node properties directly in the CONLIM file: HB in column 4 (in place of HBOR), TETAP in column 5 (in place of UBOR), ALFAP in column 6 (in place of VBOR) and RP in column 7 (in place of CHBORD). The values are then read in automatically by the `LECLIM` subroutine and available for future use, without invoking subroutine `BORH`.

This meant minor changes to the following subroutines:

- `ARTEMIS`,
- `CONDIH`,
- `DECLARATIONS_ARTEMIS`,
- `LECLIM`, and
- `POINT_ARTEMIS`

to allow the CONLIM values to be read in and used. These changes were committed to the repository and are available since release v7p3.

It is noted that the use of the CONLIM file in this way is not compulsory, but is an added functionality. FORTRAN files developed with the `BORH` subroutine will still work and give the same results.

B. Validation

The test cases developed for ARTEMIS and available from the repository have all been migrated to using an edited CONLIM file rather than coding in `BORH`, but for test cases *flam* and *kochin*. Test case *creocean* has both functionalities (while art_creocean.cas works with a CONLIM file, art_creocean_2.cas works with subroutine `BORH`).

It was verified that the results of simulations run with a CONLIM file were identical to those of simulations run with subroutine `BORH`.

C. How is it triggered?

By default the boundary node properties are read in from the CONLIM file.

HB values are read from the 4th column.

TETAP values are read from the 5th column.

ALFAP values are read from the 6th column.

RP values are read from the 7th column.

An example is shown below.

1 LIHBOR	2 LIUBOR	3 LIVBOR	4 HB	5 TETAP	6 ALFAP	7 RP
1	5	5	1.4142135	0.00	0.000	0.000
2	5	5	0.000	90.00	0.000	1.000
2	5	5	0.000	90.00	0.000	1.000

Figure 1: Example CONLIM file (excerpt from test case stive85).

The values read from the CONLIM file can be updated at a later stage through the subroutine BORH. This is usually the case when the user does not document all the boundary node properties in the CONLIM file (historical approach).

It is noted that, since release v6p2, the use of the LECLIM subroutine has been uniformed across all modules of the TELEMAC system. In LECLIM are performed, in particular, some general consistency checks geared towards the flow modules. The implication is that the TETAP and ALFAP values are reset to 0 when the corresponding codes LIUBOR and LIVBOR are other than KENT (5) or KENTU (6).

It is, therefore, essential to give LIUBOR and LIVBOR (2nd and 3rd columns) values of either 5 or 6 (see Figure 1) such that the values of TETAP and ALFAP (5th and 6th columns) are taken into account correctly.

For simple applications, the CONLIM file can be defined directly in software such as Blue Kenue. For more complex applications, or even to facilitate change of boundary node properties, the user may benefit from an external CONLIM file generator (e.g. using QGIS). Such a tool has not been developed at HR Wallingford to date.

II. PRESCRIBING THE PHASE AT THE INCIDENT BOUNDARY

This feature was introduced on http://cue.opentelemac.org/ as Feature #392: PHBOR to compute phasing automatically, starting with the angle of wave impact.

A. *What's new?*

Prior to release v6p2, the phase of the incident boundary was computed internally, without user intervention. This has changed with release v6p2, from which point the user was expected to document the phase ALFAP for incident boundary node in particular in subroutine BORH. This has sometimes been perceived as a hindrance, and feature #392 is meant to revert to a more user friendly approach.

One of the reasons for the change in release v6p2 was compliance with parallel computations.

Subroutine PHBOR was modified in this development to host the automatic phase calculation as it did prior to release v6p2, with a few changes:

- Allowance is made for parallel computations,
- The first step is the identification of the "node of attack": the incident boundary node first hit by waves from the specified direction (Figure 2),
- The phase of all other incident boundary nodes is then iteratively computed from that node to the next.

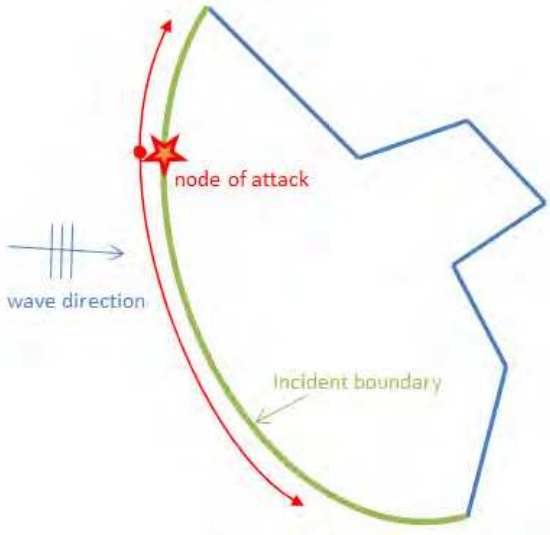

Figure 2: Definition of "node of attack" for phase computation.

These changes were committed to the repository and are available since release v7p3.

B. *Validation*

The test cases developed for ARTEMIS and available from the repository have all been repeated and validated with the modifications.

C. *How is it triggered?*

Nothing is required from the user to activate the automatic phase calculation. The phase for the incident boundary non longer needs specifying in subroutine BORH, unless specifically required for particular applications.

III. GENERATING FREE SURFACE ANIMATIONS

This feature was introduced on http://cue.opentelemac.org/ as Feature #185: Generate the files necessary to produce an animation of the free surface.

A. *What's new?*

The ability to animate the free surface elevation over the model domain, as predicted by ARTEMIS, is thought to be useful in helping to explain and illustrate the physical processes of wave transformation and disturbance, in particular to a non-scientific audience.

An example is shown below in Figure 3.

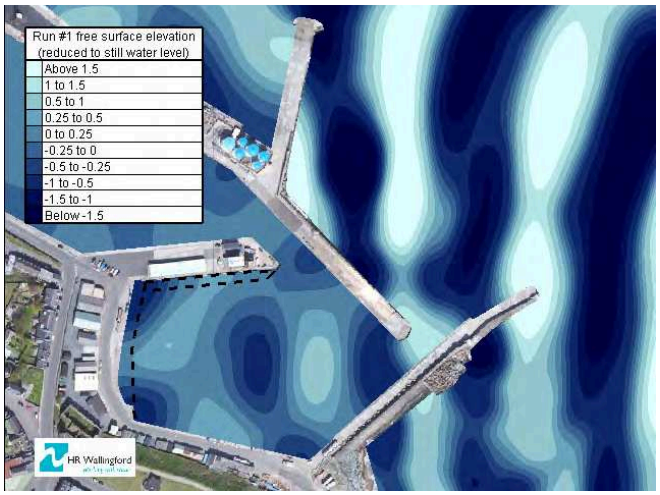

Figure 3: Example of an animation.

Standard output from random wave runs in ARTEMIS does not allow animations to be generated, which can currently only be achieved by running each component separately and outputting the amplitude and phase for each single component run.

New keywords were added that allow a more automatic approach, and generate an amplitude/phase file covering the model area for an ARTEMIS multi-component run. A post-processing tool was developed that will run, if requested, after the ARTEMIS simulation is complete. This will compute the free surface elevation at every point in the model area from the phase and amplitude predicted for each period/direction component run in ARTEMIS and for a user-specified range of times and time increment. A free surface elevation file in SELAFIN format is generated from these.

This post-processing development meant minor changes to the following subroutines and python scripts:

- `ARTEMIS`,
- `DECLARATIONS_ARTEMIS`,
- `LECDON_ARTEMIS`,
- `POINT_ARTEMIS`, and
- runcode.py,

as well as the introduction of subroutine `BIEF_ANIMP`.

These changes were committed to the repository and are available since release v7p3.

B. *Validation*

Two test cases out of those developed for ARTEMIS and available from the repository have been converted to produce time histories of free surface elevation. These are *bj78* and *creocean*.

Time histories were generated at a number of locations throughout the model areas and Fast Fourier Transform of the resulting time histories were performed to estimate the associated significant wave height (Hs) and mean wave period (Tm02). These were successfully compared against the wave height parameters predicted by ARTEMIS directly to within less than 0.5%.

C. *How is it triggered?*

New keywords were introduced in the ARTEMIS steering file that output the amplitude and phase for each run component and covering the model area:

- `FREE SURFACE ANIMATION` (yes/no)
- `AMPLITUDE AND PHASE FILE'`

A post-processing tool was added to the artemis.py script that will generate a time-varying free surface file, for a user-specified range of times and time increment, should the following keywords be documented. It is noteworthy that the size of the resulting file will quickly become prohibitive so careful consideration should be given to these values.

- `FREE SURFACE FILE`
- `FIRST TIME IN THE FREE SURFACE FILE`
- `TIME STEP`
- `NUMBER OF TIME STEPS`

IV. NESTING ARTEMIS IN A REGIONAL MODEL

This feature was introduced on http://cue.opentelemac.org/ as Feature #205: TOMAWAC / ARTEMIS coupling.

A. *What's new?*

Current practice in the application of the ARTEMIS model consists in specifying representative uniform conditions along the ARTEMIS model boundary. If a regional model is used to inform these conditions (functionality available since release v7p0), a single representative point is used for sharing the information between the regional (e.g. TOMAWAC) and the ARTEMIS models, such that variations along the ARTEMIS model boundary are not allowed.

It is recommended that the incident model boundary sit in reasonably constant water depth. However, there are circumstances when this is not practical and when, as a consequence, allowing variations along the incident model boundary may be beneficial. This is the case, for example when the modelling includes a navigation channel, which modifies the refraction wave patterns.

The nesting approach developed at HR Wallingford aims at reducing loss of information between the regional spectral wave model and the local wave disturbance model, with a more accurate representation of boundary conditions. This allows in particular spatial variations.

The approach can be summarised in the following simple steps:

- The spatial output from the regional (e.g. TOMAWAC) model is used to inform the spatial variations in significant wave height along the ARTEMIS incident boundary.

- The spectral output from the regional model (more than one point allowed) is used to determine the NDALE directional components independently at each of the incident boundary nodes.
- The spectral output is also used, at a user-designated location along the ARTEMIS incident boundary, to select the NPALE period components that will be run in the model.

A number of existing subroutines were amended to allow the new nesting functionality. These are:

- ARTEMIS,
- DEALL_ARTEMIS,
- DECLARATIONS_ARTEMIS,
- INTERFACE_ARTEMIS,
- LECDON_ARTEMIS,
- POINT_ARTEMIS,
- SPD,
- SPE, and
- TWCALE.

Some subroutines were also added, in keeping with the TELEMAC coding standards and use of the HERMES module to access SELAFIN files. These are:

- ALLSPEC,
- FASP_SP,
- GET_DATA_TIMESTEP,
- GET_TOMSPEC_DIMENSIONS,
- GET_TOMSPEC_VALUES,
- GET_TOMSPEC_VALUE1,
- GET_TOMSPEC_VALUE2,
- LISSAGE,
- STIRLING,
- STWC1,
- STWC2,
- TWCALE2,
- TWCCLOSEST,
- XY_TOMAWAC.

It is proposed to make these developments available to the TELEMAC community but more testing is required before then. The following is an initial example that illustrates how the spatially varying information is passed from the regional model to the ARTEMIS model.

B. Validation

An old ARTEMIS test case: *beach* was reinstated to validate the developments. In this test case, the TOMAWAC model is run on a uniformly sloping beach. The ARTEMIS model is nested before the top of the beach, in varying water depths (and wave field). Waves approach from the South-West and so, in ARTEMIS, the westernmost and southernmost boundaries are defined as incident, while the easternmost and northernmost boundaries are defined as open. AUTOMATIC TETAP CALCULATION is turned on in these tests.

Figures 4 to 6 show the results of the TOMAWAC (background) and ARTEMIS simulations under different configurations:

- Figure 4: currently available nesting approach, using a single representative point to share information between the regional and ARTEMIS models;

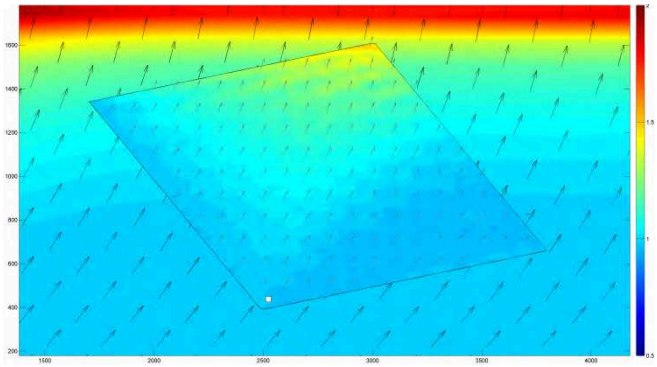

Figure 4: *beach* test case
background: global model wave field (Hs and direction);
foreground: ARTEMIS wave field with current nesting approach;
white square: nominated spectrum.

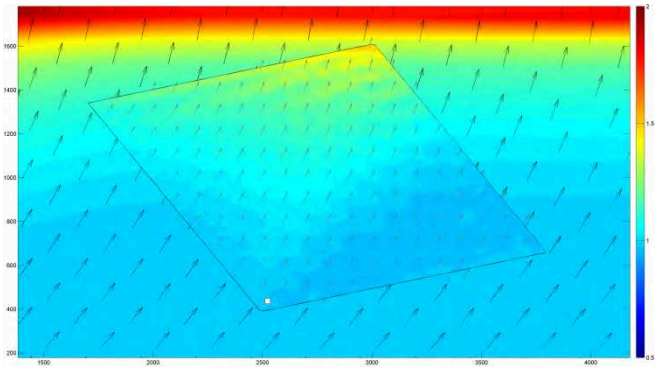

Figure 5: *beach* test case
background: global model wave field (Hs and direction);
foreground: ARTEMIS wave field with new nesting approach;
white square: nominated spectrum.

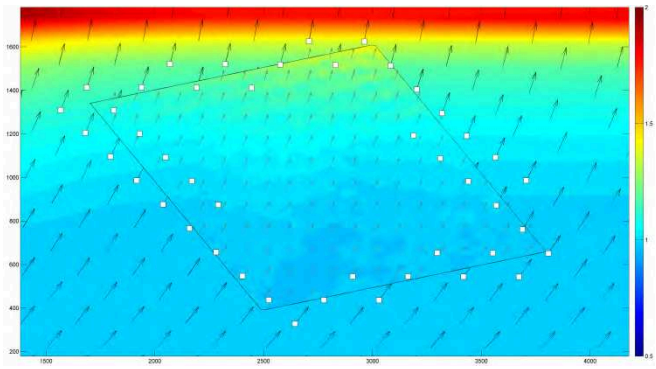

Figure 6: *beach* test case
background: global model wave field (Hs and direction);
foreground: ARTEMIS wave field with new nesting approach;
white square: 45 input spectra.

- Figure 5: new nesting approach, using the same single representative point. Notice how the wave heights at the westernmost boundary of the ARTEMIS model are a better match to the wave heights predicted by TOMAWAC. This is due to the use of the TOMAWAC spatial output to inform the spatial variations in significant wave height along the ARTEMIS incident boundary;
- Figure 6: new nesting approach, making use of more spectral data points from TOMAWAC to improve the representation of the incident boundary. Notice how the wave directions at the westernmost boundary of the ARTEMIS model are now a better match to the wave directions predicted by TOMAWAC.

C. How is it triggered?

New keywords are introduced or modified in the ARTEMIS steering file that trigger the proposed nesting approach:

- `COUPLING WITH TOMAWAC OUTER MODEL`
- `TOMAWAC OUTER SPECTRAL FILE`
- `TOMAWAC OUTER RESULT FILE`
- `COORDINATES OF THE REFERENCE F SPECTRUM`

It is noted that the currently available nesting method (using a single representative spectrum) is preserved as `COUPLING WITH TOMAWAC OUTER MODEL = 1`. `COUPLING WITH TOMAWAC OUTER MODEL = 2` activates the new nesting approach. `COUPLING WITH TOMAWAC OUTER MODEL = 0` is the default, meaning no nesting is required.

The `TOMAWAC OUTER SPECTRAL FILE` is the .spe file from a TOMAWAC run. This is a time-varying file and the user is required to specify `INSTANT FOR READING TOMAWAC SPECTRUM`, time from which the ARTEMIS boundary conditions need developing.

The `TOMAWAC OUTER RESULT FILE` is the spatial file of integrated parameters from a TOMAWAC run. This is also a time-varying file and the time specified in `INSTANT FOR READING TOMAWAC SPECTRUM` will be used to extract boundary conditions. However, currently, and for efficiency purposes, the development relies on the boundary conditions interpolated from the regional model being specified in a binary file (`BINARY DATA FILE 1`) created by convertToBND.py in the python script folder.

convertToBND.py [input1: ARTcliFile] [input2: ARTgeoFile] [input3: TOMslfFile] [output: ARTbndFile]

The `TOMAWAC OUTER RESULT FILE` is currently only directly used to access the coordinates of the spectral data points in the `TOMAWAC OUTER SPECTRAL FILE`. A process more transparent to the user may be considered in time.

The `COORDINATES OF THE REFERENCE F SPECTRUM` are required if using `COUPLING WITH TOMAWAC OUTER MODEL = 2`. This will select the closest data point, within those present in the `TOMAWAC OUTER SPECTRAL FILE`, from which to compute the frequency spectrum. This spectrum is taken to be representative of the incident boundary conditions and is the basis for the discretisation into NPALE period components in the ARTEMIS run.

This development is subject to further testing before it can be shared with the community, and as such is not part of the general ARTEMIS release at the moment.

CONCLUSIONS

This paper presents developments of the ARTEMIS model, at HR Wallingford. Some of these developments are already available to the TELEMAC community since release v7p3. Others (namely nesting ARTEMIS in regional models) are still ongoing and subject to further testing before they become available in future releases of the TELEMAC system.

Comments and suggestions on the developments presented in this paper are welcome.

Modelling morphological changes over time scales of decades to centuries: a review

Michiel Knaapen[1]
[1] HR Wallingford, Howbery Park, Wallingford, OX10 9BA, United Kingdom
m.knaapen@hrwallingford.com

Abstract: Predicting morphological changes to coasts estuaries and rivers has always been one of the core aims of sediment transport modelling. Impact of human activity can last for decades to centuries. With computer power increasing exponentially, extrapolation of short term calculations or simplified models are now being replaced with long-term simulations of detailed area models. SISYPHE is shown to handle these simulations with varying success. From a number of theoretical and practical applications, issues arising from the long-term simulations are discussed:

- *Numerical instabilities*. Sub-mesh distribution of sediment leads to accretion in places where there is no sediment transport. Although this is now stopped for dry nodes, it can still lead to upslope transport creating ridges that are too high and channels too deep or accumulation onto a non-erodible edge. A downslope transport term can correct this, if it is not proportional to the calculated transport rate. Alternatively, an analysis of the sub mesh transport gradients might provide a better solution for the distribution of accreting material over the nodes.
- *Missing cross-shore processes*. Coastal modelling is known to be difficult. The interaction between waves, currents and sediments, leading to inherent 3D processes, with an onshore mass flux through asymmetric waves and wave rollers and an offshore undertow near the bed. This process is as difficult to solve in 3D as it is in 2D. In 3D, the spectral wave models give a poor approximation of the onshore mass flux and the distribution of the wave forces across the vertical are not understood well. In 2D, the onshore mass flux and offshore undertow can only be approximated with long known formulae. On top of that, there simply is a missing knowledge regarding the process that leads to the gradual built-up of beaches after a storm. Still, the results with SISYPHE models compares well with the results of 1-line modelling. Moreover, it brings the benefit of the additional insight in the small-scale effects.
- *Representative wave conditions.* For a long time, long-term morphological predictions relied on a representation of the wave conditions that are representative for the wave climate at the site of interest. However, when comparing results from models using time varying waves with models applying a representative wave condition; this does show up significant errors due to the wave breaking. The runs using a representative wave have the breaking waves in a single location, whereas the breaking zone for the time varying waves varies over time. Whereas the errors in the sediment transport rates are small, these small errors result is large difference in the erosion deposition pattern.
- Morphological speed-up. Several approaches have been proposed to speed up calculations by multiplying the bed changes. The maximum achievable speed-up with this approach depends on the complexity of the models, with about 20 possible for low energy situations, but approximately10 the maximum for high energy situations such as a coastline.

Key words: Longterm morphology; sediment transport.

Coupling TELEMAC-3D with the General Ocean Turbulence Model (GOTM)

Thijs Lanckriet, Alexander Breugem, Boudewijn Decrop
International Marine and Dredging Consultants nv
Antwerp, Belgium
thijs.lanckriet@imdc.be

***Abstract*— The General Ocean Turbulence Model (GOTM), a 1DV water column model for coastal, oceanic and limnic waters, was coupled to TELEMAC-3D, expanding the model capabilities for the description of vertical mixing processes. The coupled TELEMAC-3D GOTM model was applied to four cases: the lock exchange test case, the stratification test case, a case of large-scale ocean circulation, and a case of salinity-driven stratification in an estuary mouth. The lock exchange test case shows that the TELEMAC-3D GOTM model with $k-\epsilon$ closure delivers comparable results to the TELEMAC-3D mixing length model for a simple geometry, and that the increase in computation time due to the GOTM coupling is very limited The large-scale ocean circulation case shows that TELEMAC-3D with the K-Profile Parametrization (KPP) in GOTM makes it possible to simulate large-scale ocean circulation, including surface boundary layer dynamics under the influence of radiative and atmospheric forcing. The estuarine circulation test case shows that in more complex environments, TELEMAC-3D with GOTM *k-ϵ* closure better captures the physics of salinity density stratification than the simple mixing length model, and this has a significant effect on the macroscale circulation in the estuary mouth.**

I. INTRODUCTION

As TELEMAC-3D is applied to ever larger and deeper domains including (coastal) oceans, the need also grows for flexible, case-specific descriptions of vertical turbulent mixing processes. As an alternative to implementing additional turbulence modules in the existing TELEMAC-3D code, TELEMAC-3D was coupled to the 1DV General Ocean Turbulence Model (GOTM) [1].

II. GOTM DESCRIPTION

GOTM (www.gotm.net) is an open-source community model for hydrodynamics and turbulent mixing processes in coasts, oceans and lakes, and can be run in standalone mode or coupled to a 3D circulation model. The philosophy behind GOTM is to make different turbulence models available in a uniform, reusable code, creating a user-friendly environment for the application of turbulence models in oceanic studies, as well as a tool for the further development of turbulence schemes. In standalone mode, GOTM solves the one-dimensional vertical (1DV) transport equations of momentum, salt and heat, as well as the turbulent mixing processes of these variables. At the heart of GOTM is a library of several turbulence closure models for the parametrization of vertical turbulent fluxes of momentum, heat and tracers, including energy models, two-equation models such as the $k-\epsilon$ closure scheme, $k-\omega$ closure, the Mellor-Yamada closure scheme, Algebraic Stress Models, and the K-profile parameterisation. The implementation of the $k-\epsilon$ closure scheme and $k-\omega$ closure in GOTM is based on a generic length scale equation [2]. GOTM has been coupled to several ocean circulation models including GETM [3], MIT-gcm [4], FVCOM [5], SLIM-3D [6], and now TELEMAC-3D (in a branch version), making it possible to generically employ all GOTM turbulence formulations in the 3D circulation model. A limited biogeochemical water column model (GOTM-bio), was also available in GOTM until version 4.0, and is now superseded by the separate Framework of Aquatic Biogeochemical Models (FABM), which can be coupled to GOTM.

III. COUPLING IMPLEMENTATION

A. General

The coupling with TELEMAC-3D is implemented as a two-way online coupling. In the newly added module *GOTM_coupling.F*, the GOTM main turbulence subroutines (*turbulence.f* or *kpp.f*) are called, with all relevant parameters such as velocity, density, diffusivity, turbulent kinetic energy and dissipation passed from and returned to the main TELEMAC-3D code. In GOTM, a staggered vertical grid is used, with velocities and scalars defined at the cell centres (C-points) and the diffusivities and viscosities at the edges (W-points). In TELEMAC-3D, all variables are defined at the nodes. In order to convert the variables from the TELEMAC edges to the GOTM cell centres, a simple averaging was used:

$$U_j = 0.5(U_{j+1/2} + U_{j-1/2}), \tag{1}$$

with U_j a GOTM variable at the cell centre and $U_{j+1/2}$ a TELEMAC variable at the edge above the cell centre. GOTM also requires the buoyancy frequency N and shear frequency S as inputs:

$$N^2 = -\frac{g}{\rho}\frac{\partial \rho}{\partial z} \tag{2}$$

$$S^2 = \left(\frac{\partial U}{\partial z}\right)^2 + \left(\frac{\partial V}{\partial z}\right)^2, \tag{3}$$

with U and V the velocities in x and y directions, ρ the potential density, and g the acceleration due to gravity. The gradients at the edges are obtained from the TELEMAC variables at the layers above and below:

$$\left|\frac{\partial U}{\partial z}\right|_{j+1/2} = \frac{U_{j+\frac{3}{2}} - U_{j-\frac{1}{2}}}{z_{j+3/2} - z_{j-1/2}} \quad (4)$$

At the free surface and the bottom, the velocity gradient at the edge below or above is used.

GOTM uses the potential density in order to define the stratification. Because of the importance of an accurate definition of the density and density gradients, the 25-term equation of state of [7] was also implemented in the code.

Since GOTM is a one-dimensional model, the horizontal advection and horizontal diffusion of the turbulent kinetic energy k as well as the turbulence dissipation ε are neglected in the present implementation of the coupling. It is relatively straightforward to add these terms using a fractional step method. However, for applications in rivers, estuaries, coastal seas and oceans, typically the vertical variation is much larger than the horizontal one, and hence horizontal processes can typically be neglected. By neglecting the horizontal advection and diffusion of k and ε, a substantial amount of calculation time is saved. The same approximation is also used in other coastal ocean models such as DELFT3D and COHERENS.

In the GOTM K-Profile Parametrization (KPP [8]), vertical mixing of scalars (temperature and salinity) is defined using two terms, a local process, and a non-local process:

$$\overline{w'c'} = K_c \frac{\partial c}{\partial z} + \gamma, \quad (5)$$

with $\overline{w'c'}$ the turbulent vertical scalar flux, K_c the vertical diffusivity and γ the non-local flux. The non-local flux is typically used to parameterize convective mixing in situations with an unstable stratification. The non-local term was included by specifying a vertical velocity term containing γ in the call to *cvdf3d.f* in which the advection and diffusion of scalars is calculated.

GOTM-specific model settings are specified in a separate namelist file, similar to a standalone GOTM simulation. The TELEMAC-3D – GOTM coupling is freely available in the cookiecuttershark branch of the TELEMAC SVN repository, which is based on Telemac V7P2.

B. Installation instructions GOTM- TELEMAC

In order to install the coupled TELEMAC GOTM model, the following steps need to be done:

- Download and compile GOTM and (if necessary) FABM using the specifications found on www.gotm.net. It is important that the same compiler is used as for compiling TELEMAC. Because GOTM uses some modern additions to FORTRAN such as object orientation, a recent FORTRAN compiler is required (we use gfortran 4.9.4). During compiling, it is recommended to change the variables stderr and stdout in the file cppdefs.h to 6 such that the log messages of GOTM are written to the TELEMAC log files. Further, it may be needed to set some preprocessor flags in order to specify the required settings of the GOTM KPP model.
- In the $SYSTELCFG configuration file, specify the preprocessor flag –DGOTM and add the include and library paths to GOTM (-lturbulence and -lutil).
- Compile TELEMAC as usual using the compileTELEMAC.py scripts.

C. Usage instructions for GOTM-TELEMAC

In order to use GOTM with TELEMAC-3D, two keywords need to be specified:

- The keyword VERTICAL TURBULENCE MODEL needs to be set to:

  5: Standard GOTM

  6: GOTM KPP model
- The keyword GOTM FILE needs to be set to the file name of the namelist file used by GOTM. In this file, all settings of the turbulence model can be specified, as in a standalone GOTM simulation. Details of the specific meaning of the variables in this file can be found in the GOTM manual.

Note that there are some specific requirements when using the GOTM KPP model, related to the surface fluxes and short-wave radiation. In this case, TELEMAC-3D must be coupled to WAQTEL as well. Further the new 25-term equation of state of [7] is obligatory, using the keyword DENSITY LAW = 5. These settings are checked by the code on the first call of the GOTM subroutine. For the standard GOTM model, it is required to use the Nikuradse friction law by setting LAW OF BOTTOM FRICTION = 5. Turbulence quantities such as k and ε calculated by GOTM can be exported by specifying them in the keyword VARIABLES FOR 3D GRAPHIC PRINTOUT. The surface and bottom boundary layer as computed by the GOTM KPP model can be exported as 2D graphic output variables BLTOP and BLBOT, respectively. The variables BLTOP and BLBOT are calculated directly by GOTM and are new to this coupled version.

IV. APPLICATIONS

A. Lock exchange test case

The lock exchange test case, one of the standard test cases for TELEMAC-3D, is a simple internal dam break problem, in which a horizontal jump in salinity at $t = 0$ s induces a baroclinic wave. The V7P2 version of the test case was used. To generate sufficient current velocities and turbulence levels, the salinity difference was set to 10 PSU for this test simulation. Fig. displays the predicted salinity field in the lock exchange test case using TELEMAC-3D with the mixing length turbulence model (with the mixing length parametrization of Nezu and Nakagawa) using the Munk-Anderson stability function (top), the native $k-\epsilon$

model (middle) and with the $k-\epsilon$ closure using an algebraic second order turbulence model to compute the scalar diffusivities in GOTM (bottom). Results using the mixing length model and the GOTM $k-\epsilon$ model are highly similar, although a closer inspection of the calculated diffusivities shows higher mixing with the mixing length model. The TELEMAC-3D with native $k-\epsilon$ model displays instabilities, as was also evidenced by the exceedance of iterations in the simulation log file, i.e. the simulation did not converge. Computation times on a single processor were 11 s for the mixing length model, and 12 s for the GOTM $k-\epsilon$ simulation, indicating that the GOTM coupling step occurs at little additional computational cost, even though a rather advanced turbulence scheme is used.

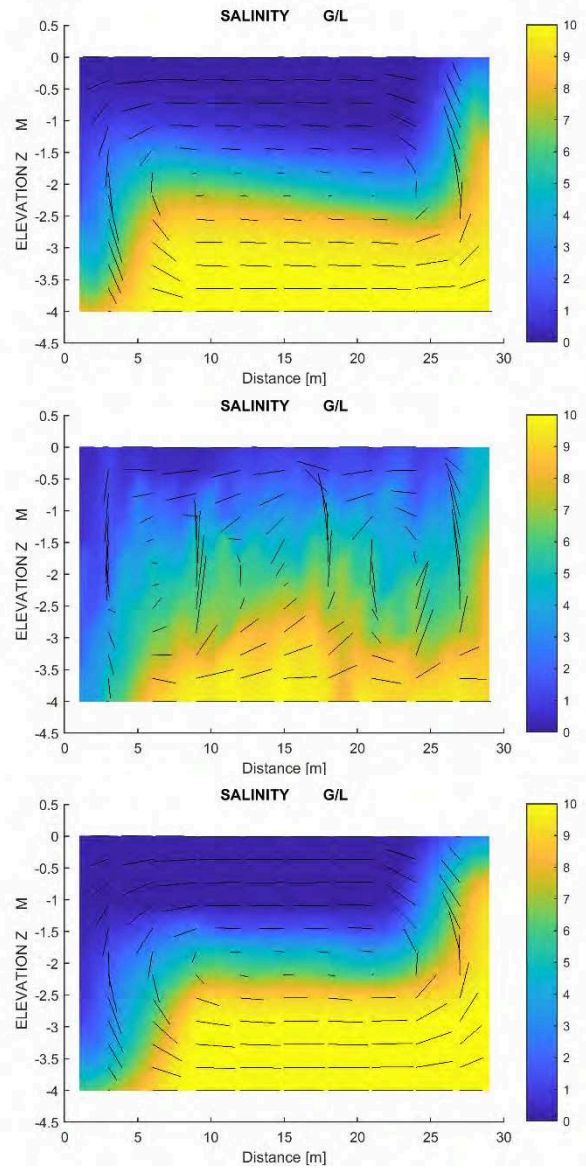

Fig. *1*: Salinity field after 100 s for lock exchange benchmark test. Top: TELEMAC-3D mixing length model. Middle: TELEMAC-3D $k-\epsilon$ model. Bottom: TELEMAC-3D + GOTM $k-\epsilon$ model.

B. Stratification test case

The stratification test is one of the standard test cases for TELEMAC-3D. It simulates the development of a velocity profile from the upstream boundary in a stratified flow. The test case was run using the standard setting (except that the friction law was set to Nikuradse) with the TELEMAC-3D $k-\epsilon$ model and for TELEMAC-3D with the GOTM $k-\epsilon$ model. The test took 3min29s for the TELEMAC-3D $k-\epsilon$ model, and 1min59s for the TELEMAC-3D with the GOTM $k-\epsilon$ model. The velocity and salinity fields are shown in fig. 2 and 3. The differences in the salinity field are extremely limited. Both models show the stratification clearly. There are some slight differences in the velocity field between both models, which can be attributed to the differences in turbulence settings that are used and the fact that the TELEMAC3D – GOTM implementation neglects the horizontal advection of k and ε, which may have some influence in the zone where the velocity profile develops.

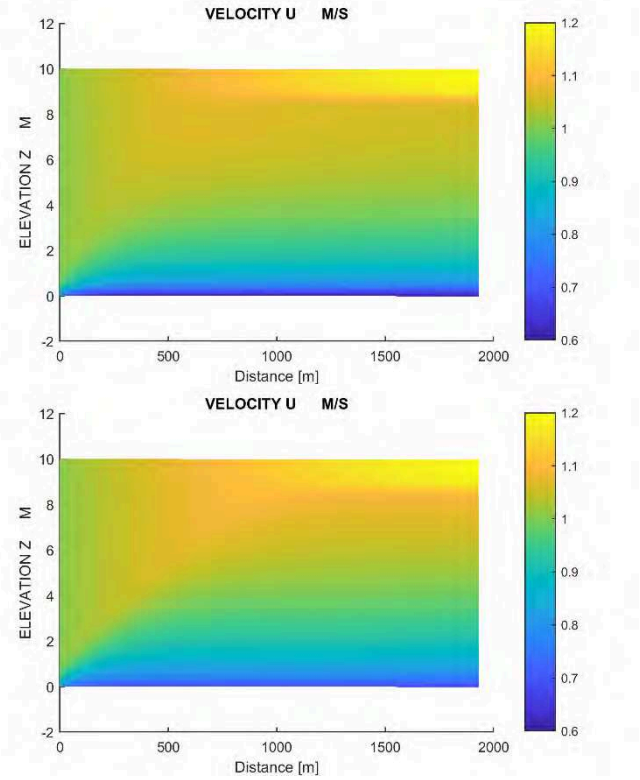

Fig. *2*: Velocity field in the final situation for the stratification benchmark test. Top: TELEMAC-3D $k-\epsilon$ model. Bottom: TELEMAC-3D + GOTM $k-\epsilon$ model.

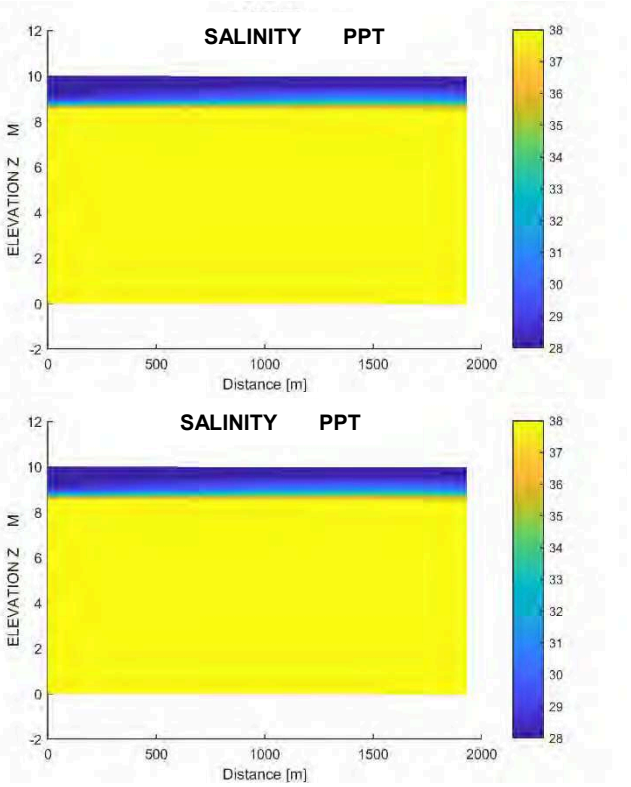

Fig. *3*: Salinity field in the final situation for the stratification benchmark test. Top: TELEMAC-3D $k-\epsilon$ model. Bottom: TELEMAC-3D + GOTM $k-\epsilon$ model.

C. Large-scale ocean modelling with K-Profile Parametrization

In the deep ocean, two distinct mixing regimes can usually be distinguished: mixing in the surface and bottom boundary layers under the influence of radiative and atmospheric surface forcing and bottom shear stress, and mixing in the ocean interior due to internal waves and shear instability [8]. The K-Profile Parametrization (KPP) model of Large *et al.* [8] is a frequently used parametrization for oceanic mixing that determines the boundary layer depth based on a bulk Richardson number, and provides expressions for diffusivity and non-local transport in both the boundary layers and in the ocean interior. It is frequently used in large-scale ocean simulations such as the operational HYCOM model (www.hycom.org).

A test simulation of large-scale open-ocean modelling was performed with the TELEMAC-3D/GOTM coupling with KPP on 32 parallel processors. In the open ocean, surface boundary layer thickness is at first order determined by wind shear, temperature- and salinity-driven density stratification, and surface heat fluxes (sensible and latent heat flux and short- and long-wave radiation). Fig. displays an instantaneous vertical profile of temperature, salinity and vertical eddy viscosity in the surface boundary layer calculated using TELEMAC-3D coupled with GOTM and WAQTEL, using data from HYCOM as forcing [9]. The boundary layer depth extends to approximately 50 m, the limit of stratification. The eddy viscosity in the surface boundary layer scales with the boundary layer depth h, a depth-dependent turbulent velocity scale w_x and a prescribed polynomial shape function $G(\sigma)$ (see [8] for further information):

$$\nu_z = h w_x G(\sigma). \quad (6)$$

Fig 4 displays a time series of surface boundary layer thickness, wind speed and short-wave radiative forcing over a one-month period. The surface boundary layer thickness displays a strong diurnal cycle with boundary layer thickness of 40-80 m during night time (convective) and high-wind conditions, down to 0-2 m during the daytime due to stabilization by short-wave radiation in the upper water column. Three notable events occurred in the one-month time series, indicated as A, B and C:

A: Strongly reduced day-time stabilization during cloudy conditions (reduced short-wave radiation); large boundary layer persists throughout the day.

B: Increase in maximum boundary layer depth due to increased wind speed.

C: Limited night-time boundary layer formation during low wind speed.

The use of the KPP model in GOTM makes it possible to simulate the impact of these meteorological events on the surface boundary layer within TELEMAC-3D.

D. Salinity-driven stratification in an estuary

Salinity-induced density stratification has a strong impact on turbulence and general estuarine circulation in many estuaries. Fig. displays vertical profiles of salinity c, horizontal velocity u, turbulent kinetic energy k and diffusivity of salt $\nu_{z,Sal}$ and momentum ν_z at an estuary mouth at three instances in time: during flood flow (top), flow reversal (high water slack, middle) and during ebb flow (bottom). A simulation was performed with the TELEMAC-3D vertical mixing length model using the mixing length parametrization of Nezu and Nakagawa (red curves), the TELEMAC-3D + GOTM $k-\epsilon$ vertical turbulence closure with an algebraic second order closure for the scalar mixing fluxes (blue curves), and the TELEMAC-3D internal vertical $k-\epsilon$ model. The latter simulation displayed instabilities and is therefore not shown in Fig. . Unfortunately, no measurements were available that could be used to compare the results of the different simulations.

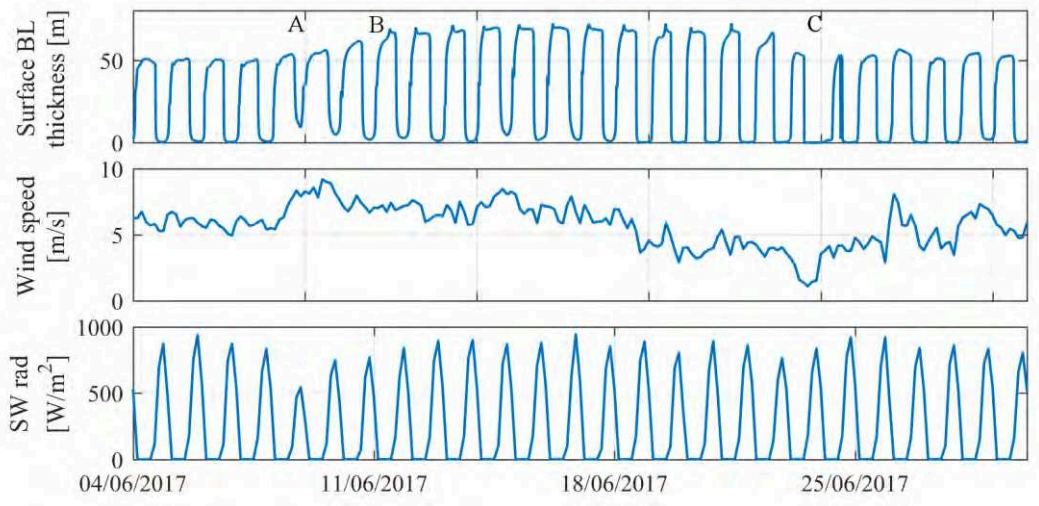

Fig. 4: Surface boundary layer, wind speed and short-wave radiative forcing in the open-ocean test case for the coupled TELEMAC-3D-GOTM model with the KPP turbulence model.

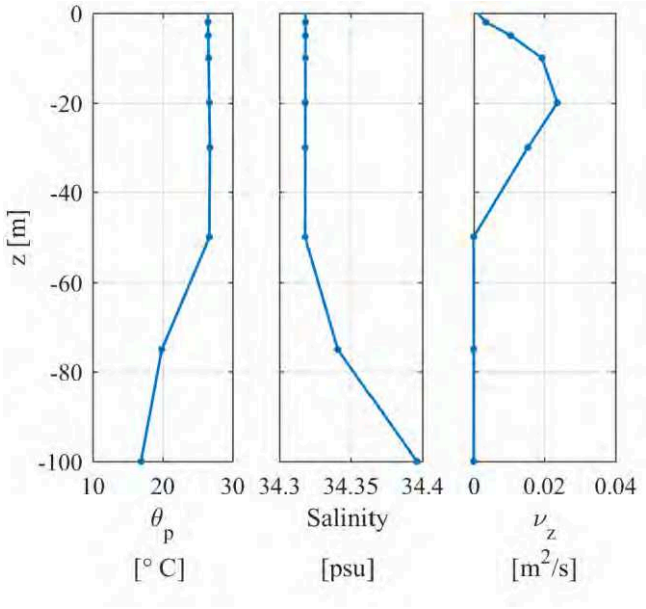

Fig. 5: Temperature (θ_p), salinity and vertical eddy viscosity (ν_z) in the surface boundary layer.

During flood flow (Fig. , top), velocities reach 1 m/s and the turbulent kinetic energy k reaches up to 0.013 m^2/s^2. Mixing in the $k-\epsilon$ model is mostly confined to the bottom half of the water column; in contrast, the mixing length model also predicts momentum mixing in the top half of the water column. Around flow reversal (Fig. , middle), turbulence levels are an order of magnitude lower than during flood (k less than $4 \cdot 10^{-3}$ m^2/s^2). More importantly, the turbulence and the vertical mixing are confined to the bottom 2 m of the water column. As a result, significant velocity differences occur between the upper half of the water column (ebb-directed velocities of up to 0.28 m/s) and the center of the water column (flood-directed velocities of up to 0.06 m/s). The mixing length model again predicts more mixing in the upper water column, which results in much smaller vertical variation in the flow velocity. During ebb flow (Fig. , bottom), the vertical viscosity profile is again markedly different in the GOTM $k-\epsilon$ model than in the mixing length model, which predicts a parabolic viscosity profile at this instance. The differences in mixing lead to a larger length of the salt tongue when GOTM is used than when the mixing length model is used (Fig.).

In conclusion of this test case, the TELEMAC3D GOTM $k-\epsilon$ better captures the physics of shear, salinity stratification, and turbulent mixing than the mixing length model, and this has a significant impact on the predicted macroscale estuarine circulation.

V. CONCLUSIONS

TELEMAC-3D was coupled to the 1DV General Ocean Turbulence Model (GOTM), enabling the use of various parametrizations and closure schemes for vertical mixing. The functioning of the coupled TELEMAC-3D GOTM model was illustrated with four different usage cases.

The lock exchange test case demonstrates that the GOTM model delivers results that are comparable to a simple mixing length model for the simple geometry of an internal dam-break, and that the GOTM coupling comes at very low additional computational cost. The same was shown in the stratification test case.

The open-ocean case illustrates the use of the non-local K-Profile Parametrization in combination with TELEMAC-3D, making it possible to simulate large-scale ocean circulation with a dynamic surface boundary layer under the influence of wind shear, radiative fluxes and convection.

The estuary model demonstrates that TELEMAC-3D coupled with the GOTM $k-\epsilon$ closure is capable of realistically simulating the complex interactions between salinity-induced density stratification and vertical turbulent mixing, rendering estuarine circulation patterns that are qualitatively different from simulations with a more rudimentary mixing-length model.

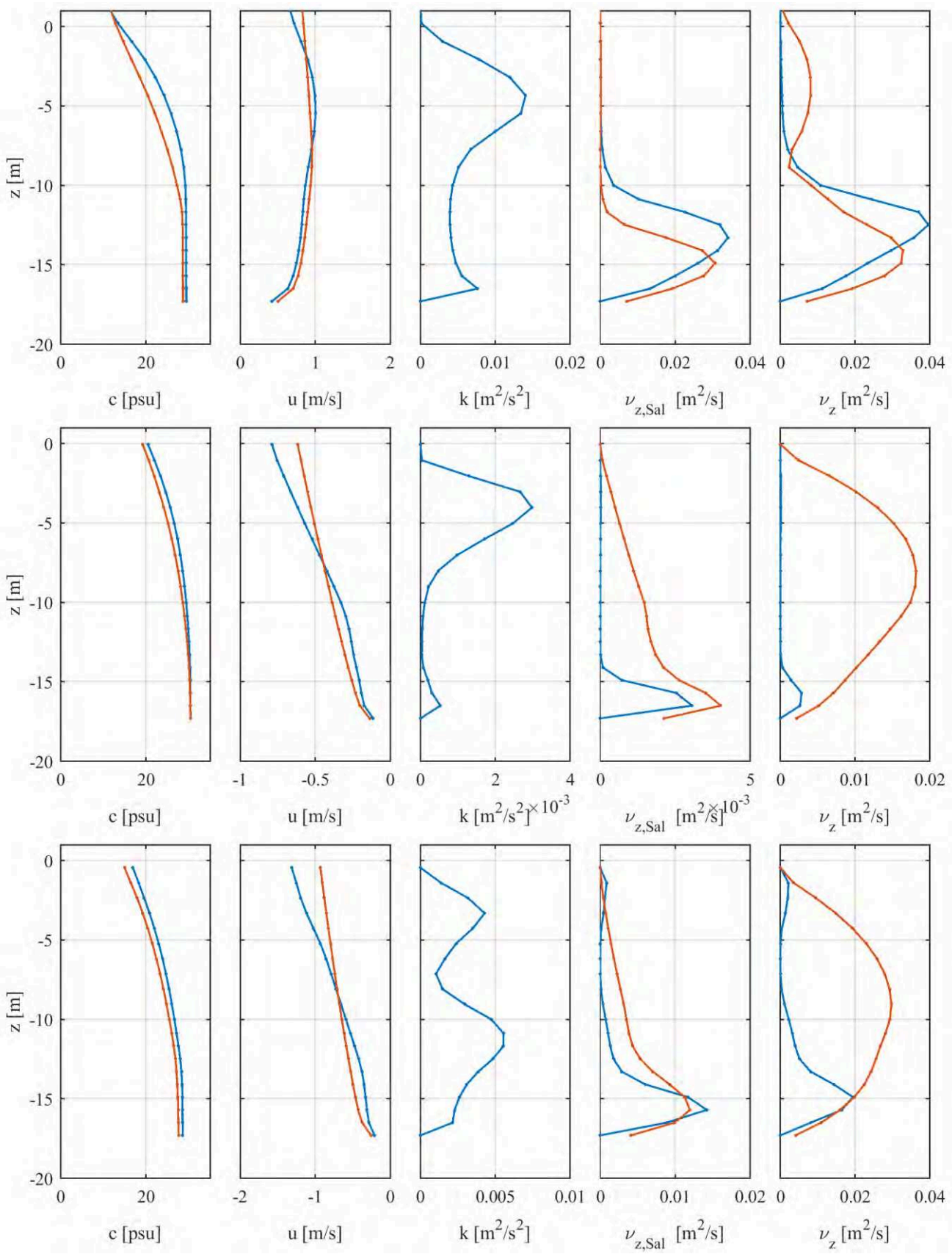

Fig. 6: Vertical profiles of salinity c, horizontal velocity u, turbulent kinetic energy k, salt vertical diffusivity $\nu_{z,Sal}$ and vertical viscosity ν_z during flood (top), high water slack (middle) and ebb flow (bottom). Red: TELEMAC-3D with vertical mixing length model. Blue: TELEMAC-3D with GOTM $k-\epsilon$ turbulence closure.

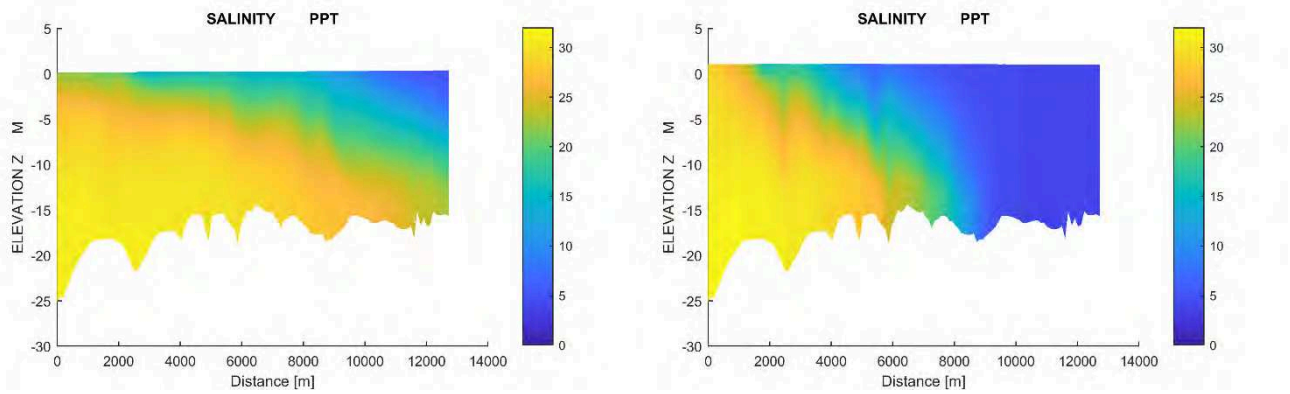

Fig. 7: 2DV profiles of salinity along the estuary thalweg. Right: TELEMAC-3D with vertical mixing length model. Left: TELEMAC-3D with GOTM $k-\epsilon$ turbulence closure.

REFERENCES

[1] H. Burchard, K. Bolding, and M. Ruiz-Villarreal, 'GOTM, a general ocean turbulence model. Theory, implementation and test cases', Technical Report EUR 18745. European Commission, Jan. 1999.

[2] L. Umlauf and H. Burchard, 'A generic length-scale equation for geophysical turbulence models', *Journal of Marine Research*, vol. 61, no. 2, pp. 235–265, 2003.

[3] H. Burchard, K. Bolding, and L. Umlauf, 'General Estuarine Transport Model', 2011.

[4] L. I. Enstad, K. Rygg, P. M. Haugan, and G. Alendal, 'Dissolution of a CO2 lake, modeled by using an advanced vertical turbulence mixing scheme', *International Journal of Greenhouse Gas Control*, vol. 2, no. 4, pp. 511–519, Oct. 2008.

[5] R. Tian and C. Chen, 'Influence of model geometrical fitting and turbulence parameterization on phytoplankton simulation in the Gulf of Maine', *Deep Sea Research Part II: Topical Studies in Oceanography*, vol. 53, no. 23, pp. 2808–2832, Nov. 2006.

[6] T. Kärnä, V. Legat, E. Deleersnijder, and H. Burchard, 'Coupling of a discontinuous Galerkin finite element marine model with a finite difference turbulence closure model', *Ocean Modelling*, vol. 47, pp. 55–64, Jan. 2012.

[7] D. R. Jackett, T. J. McDougall, R. Feistel, D. G. Wright, and S. M. Griffies, 'Algorithms for Density, Potential Temperature, Conservative Temperature, and the Freezing Temperature of Seawater', *J. Atmos. Oceanic Technol.*, vol. 23, no. 12, pp. 1709–1728, Dec. 2006.

[8] W. G. Large, J. C. McWilliams, and S. C. Doney, 'Oceanic vertical mixing: A review and a model with a nonlocal boundary layer parameterization', *Reviews of Geophysics*, vol. 32, no. 4, pp. 363–403, 1994.

[9] E. P. Chassignet *et al.*, 'The HYCOM (HYbrid Coordinate Ocean Model) data assimilative system', *Journal of Marine Systems*, vol. 65, no. 1–4, pp. 60–83, Mar. 2007.

Improving TELEMAC system pre-processing and IO stages

Judicaël Grasset[1,2],Yoann Audouin[1], Jacques Fontaine[1], Charles Moulinec[2], David R. Emerson[2]
[1]EDF R&D, LNHE, Chatou, 78400, France
[2]STFC Daresbury Laboratory, Sci-Tech Daresbury, Warrington, WA4 4AD, United Kingdom

Abstract— **Improvements in the pre-processing (partel serial) and IO stages are presented to facilitate running the suite of software on high-end machines. Firstly we present how the memory consumption of partel serial has been decreased and secondly, how partel serial can now generate only a set of files for all the MPI processes instead of one for each MPI process. Finally a work in progress dealing with the reduction of result files generated by a run of TELEMAC is presented.**

I. INTRODUCTION

In order to prepare TELEMAC-MASCARET for very large simulations, we present here some improvements in the serial version of partel to facilitate running the suite of software on high-end machines:

- We have drastically reduced the peak memory consumption of the serial pre-processor partel, as the current version of partel uses a huge amount of memory to pre-process meshes, which makes it impossible to use it for large meshes (several 10s or 100s million elements) even with access to fat memory nodes. However, there exists a parallel version of partel in the TELEMAC distribution, to circumvent this memory issue. It is split into a first serial stage where METIS is used as a default partitioner and where the mesh nodes/elements are allocated to their respective subdomain; and a second stage, which is parallel, where the rest of the pre-processing is carried out. Note that for very large meshes, the first stage still requires a lot of memory, whereas the second stage requires the same number of processors as the number of subdomains to be used, which makes the whole process tedious.

- We have reduced the number of files generated by partel serial; the current version of partel generates a set of files for each MPI process. This is an issue when using a large number of MPI processes as the high-end machine operating systems have a hard limit on the number of files a single user can open.

- We have worked to reduce the number of files generated by the solvers themselves. The issue is very similar to the one highlighted in the second item, where the input files are generated by partel, although the solution is different. This is still work in progress.

How these improvements have been made is explained in the following sections.

II. THE HIGH END MACHINE

All the benchmarks presented here have been carried out using the UK National Facility ARCHER [3].

The ARCHER supercomputer is made of 4,544 compute nodes. Each of these compute nodes has two twelve cores Intel Ivy Bridge E5-2697v2 and 64 GiB of memory. These are the nodes used to carry out all the benchmarks presented in this article.

ARCHER has also 376 high memory nodes with 128 GiB of memory, but these nodes have not been used for the present benchmarks.

III. IMPROVING PARTEL

A. Reduce peak memory consumption

partel is the pre-processing tool used by the TELEMAC-MASCARET hydrodynamic suite of software. It is used to pre-process a mesh in order to distribute the simulation load accross the MPI processes.

A major problem with partel is that it requires a lot of memory if a mesh has more than 6 million elements. In order to understand the root of the problem, we have used the heap profiler called massif [7] from the Valgrind profiling suite. This tool can provide the exact line of the program where a faulty allocation occurs.

massif shows that the memory intensive arrays are CUT_P, KNOGL, GELEGL. After looking at the contents of these arrays, it appears that they are mostly used to store zeros, e.g. in some cases the arrays have a non-zero density of less than 0.01%!

In order to reduce the peak memory consumption, we need to save only the non-zero values while still being able to know at which position the zero values should be. To achieve this, a better data structure than the existing one is needed. Using a hash table seems to be the right solution. It provides a quick insert and lookup (O(1) on average) as well as a low memory footprint, because it uses a default value of zero (if a lookup fails, it means that the index is not in the table and then the default value, e.g. zero, is returned). As hash tables do not exist in the Fortran standard library, a custom one had to be implemented.

The hash table (see Appendix) can *insert*, *modify*, *lookup* but cannot *delete* because the original code does not remove

any element from the arrays. This functionality is thus not implemented. The *modify* function is simply done by a call to the *insert* function. It looks for the value and modifies it. The hash table grows by doubling its size (default size is 2^{20} at the creation of the hash table).

The arrays are in two dimensions, which means that the key for the hash table is a pair of integers. These two integers are paired together into a single one by using the Elegant pairing algorithm of Matthew Szudzik [1]. Then this integer is hashed with a modified version of a hash function taken from the Google FarmHash library [2].

The internal structure of the hash table is made of an array of structures which contains a pair of integers and an indicator to know if the element is used or not. The collisions – a collision happens when two different keys are hashed to the same value, and so they should be placed in the same cell of the hash table – are solved via linear probing, which means that if the cell is already taken, we put the value in the next free one. If this mechanism becomes too slow for some reasons in the future, we could reduce the maximum number of collisions by using a better algorithm or combining it with another method, as for instance, the robin hood hashing method [4].

The effect of using the hash table instead of the original big arrays can be seen in Fig. 1. The benchmark uses the *geo_malpasset-small.slf* mesh from the TELEMAC2D examples and METIS [5] is used for partitioning. The original mesh is globally refined several times using STBTEL (see Table 1), the new meshes are then partitioned using both versions of partel serial. The objective is for each partition to contain about 10k elements, which is a good estimation of the smallest number of elements to be used per subdomain for TELEMAC2D to still show good scalability on fast high-end machines. The two compared versions are the last stable version at the time of this work (V7P3R1) and the trunk revision 11,882 with the last patch for the hash table [6].

As the original partel requires too much memory we do not have enough measurements from the stable version to carry out the full comparison. However, we have added an estimation of the minimal memory required, which is obtained by summing up the memory needed by the three biggest arrays (CUT_P, GELEGL, KNOLG), as p*(2n+e)*i ; where p is the number of partitions, n is the number of grid nodes, e is the number of elements and i is the size of an integer (4 bytes in the code). Using this estimation we can perform the comparison and see that the peak memory consumption has been drastically reduced.

TABLE 1. MESH CHARACTERISTICS AFTER REFINING WITH STBTEL

Case #	1	2	3	4	5	6
No. elements	104K	416K	1.66M	6.65M	26.6M	106M
No. points	53K	210K	836K	3.33M	13.3M	53M

Case 4, see Table 1, does not require more than the maximum memory available on the compute node (about 33GiB vs 64GiB), but the simulation still crashes because one of the arrays (GELEGL) exceeds the maximum memory per allocation prescribed by the cluster administrator. For Cases 5 and 6, even if we assume that there is no maximum memory per allocation imposed, the original partel would still crash because the compute node does not have hundreds of GiBs of memory available. With the hash table version, the memory consumption is much less intensive and it is possible to partition a one hundred million element mesh without any issue. Note that the main source of peak memory consumption is now due to the use of the METIS library.

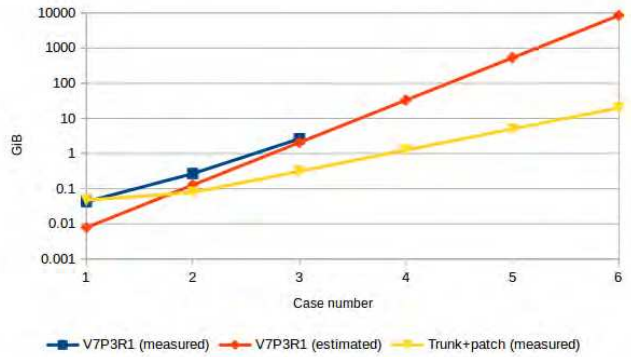

Figure 1. *Peak memory consumption of 2 different versions of partel for different size of meshes. (y-axis in logarithmic scale)*

We can also see on Fig. 1 that the estimation is below the measurements for the first two cases but is on par for the third case. This can be explained for the small cases by the memory consumption mostly coming from METIS and many small allocations. However, when the number of elements increases the memory consumption becomes dominated by the three aforementioned arrays.

During this optimisation stage, some useless iterations in some loops have been removed and the number of readings from the disk have also been reduced. These two modifications are completely independent from the hash table. However, Table 2 shows that they improve the execution time.

TABLE 2. COMPARISON OF THE EXECUTION TIME FOR BOTH VERSIONS OF PARTEL (IN SECONDS)

Case #.	1	2	3
V7P3R1	0.395	3.49	48.1
Trunk+patch	0.34	1.415	7.73

To replicate this experiment on your own cluster, you would need to download TELEMAC from the trunk and set it to the revision 11,882. You would also need to download the patch that contains the last version of the hash table and

the benchmarks script from [6]. Other details on how to apply the patch are available in the repository.

B. Reduce the number of files created

In the current version of the suite, each MPI process must have its own set of input files. These files are generated by partel from the original input files given by the user (mesh, boundary conditions and potential extra files to account for some more physics). For instance, the geometry file is divided into p files (one per MPI process). This division is repeated for every input file, which leads to at least X*p files where X is the number of original input files.

For example, for the TOMAWAC case called *opposing_current*, which requires 4 input files (WACGEO, WACCLI, WACPAR, WACCOB), if it is run using 250 MPI processes, 1,000 input files will be created by the pre-processing tool partel. This high number of files can be a real issue on a cluster, as the cluster administrator usually limits the number of files per user. With the high number of files generated by partel, it can be a source of problem. Furthermore, operating systems have a limit on the number of files opened at the same time, and some users have noticed this limit which causes TELEMAC to crash.

The patch described in this section intends to reduce the number of input files to 2*X for TELEMAC2D, TELEMAC3D, TOMAWAC and SISYPHE, by making it independent from the number of MPI processes used.

To reduce the number of files generated by the pre-processing stage, there are mainly two solutions. The first one consists of removing the pre-processing tool and carry out the partitioning at the beginning of the simulations, so that every MPI process would access some parts of the original geometry file using MPI-IO. This solution would require to modify a lot of files in the codebase and add some complexity because of MPI-IO.

The second solution is to concatenate the partitioned geometry files into a single file. Instead of writing each partition in its own file, all of them are appended in a single file, as if they were in a queue. This is easy to do because partel is sequential and creates the partition in an ordered manner, from 1 to p. So when partel has finished to write the partition X in the file we know that we can safely append the (X+1)th in the same file. This is the solution we chose to implement.

1. *SERAFIN geometry files*

All the geometry mesh files created by partel are concatenated into a single file named XXXGEO-CONCAT (XXX stands for T3D/T2D/WAC/SIS). Neither information nor padding is added between the meshes. If you know at which byte the mesh begins and ends it is possible to read it as a normal serafin mesh. This information is stored in a second file called XXXGEO-INDEX. This index file contains the pairs of offsets on which the mesh begins and ends. The offsets are encoded in 64 bits integers and should be in big-endian (default for the TELEMAC system). The offsets are ordered from the mesh part 0 to p-1.

As an example, if the MPI process number 10 needs to read its mesh subdomain from the concatenated mesh file, it should retrieve the offsets which are in the position (10-1)*8*2+1 (two integers of 8 bytes on which we add one because the first position in the file is one, not zero). When these offsets are retrieved the *open_mesh_srf* subroutine uses the first one to set *pos_title* which corresponds to the beginning of the mesh. The other one is used to compute the number of timesteps.

2. *MED geometry files*

The MED file format allows the user to store several meshes into the same file, so we neither need to concatenate nor need the index file. In order to add a mesh into a file, we simply concatenate the original name of the mesh with the rank of the MPI process that uses it and then add it to the file with the normal MED function.

However, there are still some edge cases: TELEMAC uses what is called *parameters* in the MED file format to store some information which might be different for each mesh part, but MED only allows one set of *parameters* per file. Therefore, in order to store the *parameters* NPTIR for each mesh, its name has been concatenated with the rank of the MPI process. It would have been better to create one set of *parameters* per mesh part, but it is not possible.

3. *Boundary files (CLI) and PAR files*

These two files are ASCII files and for this reason very easy to concatenate. The boundary file uses the same kind of index file as the concatenate SERAFIN geometry file. The main difference is that the index is encoded as a 32 bits integer, but as it represents a line number and not a byte count, this should be sufficient. The main reason to do so is because it is then used in the HERMES module to perform a comparison against another 32 bits integer.

4. *Index files*

The index files for the GEO and CLI files are only a list of integers in 32 or 64 bits. They are binary files as they are not meant to be used by the end user. But if someone would like to take a look at it, it is easy do so by using the od command. For instance, to read the index of a concatenate SERAFIN file: *od --endian=big -t d8 T2DGEO-INDEX*

5. *Steering configuration files*

A new boolean keyword has been introduced "CONCATENATE PARTEL OUTPUT" to the dictionaries of the various modules in order to be used in the steering files. If concatenation is asked for, but there is only one process, no concatenation is performed. By default the concatenation is not activated.

6. *partel itself*

partel serial has been modified to ask the user whether it should create concatenated files or not. This has been done by adding another question to *homere_partel.f*. The python script *runcode.py* has also been modified to take the new keyword into account. It takes the value written in the steering file. If it is not present the default value is NO. This value is then added to the input file used by partel.

Some modifications have also been made in order to manage the PARAL and WEIRS files which are in read only mode. Previously all these files were copied and renamed, one for each MPI process, even if the process was only reading it. This has been changed, and the files are not copied anymore in such cases.

C. Intermediate conclusion

These modifications work fine and are about to be commited to the main repository. The added code only impacts some parts of the TELEMAC suite. The major changes are within the function *bief_open_files*. However, the complexity of the subroutine has not increased. The code was slightly refactored and might be even simpler than in previous versions. This new functionality is almost transparent for the user, the only change residing in adding a new keyword in the steering file if needed.

IV. Replacing the Fortran IO by MPI-IO to output the results

In the current version each MPI process outputs its result in its own file. This means that for p processes, p result files are generated. At the end of the computation the post-processing tool gretel is called to merge all the result files into a single one. As for the input, generating one file per process is a bad idea, it can quickly fill up the allowed quota given by a cluster administrator.

This section describes the proposed solution to reduce the number of result files to only one by making all the MPI processes write directly their results at the correct place in a unique result file. This implementation is available in the rainbowfish branch of the TELEMAC repository.

A. Explanation of the implementation

So far, the implementation only exists for the SERAFIN mesh files, so most of the modifications are made inside the *utils_serafin.f* file of the HERMES module. This file contains all the subroutines to read and write SERAFIN files. All of them use pure Fortran IOs. Writing the results is carried out sequentially, e.g. primarily some metadata are written at the beginning of the files and then, during the simulation, the result of each timestep is added at the end of the files. gretel is used to read all these results, reordering them and writing them into a single result file when the simulations are complete. By using MPI-IO it would be possible to write the results into a single file directly at the right offset while performing the simulations, hence removing the need for a post-processing tool.

As can be seen in the algorithm Algo 1, using MPI-IO is more complex than just changing Fortran IO for its MPI-IO counterpart, particulary if good performance is expected.

B. Performance considerations

Most high-end clusters use a parallel filesystem. For ARCHER it is Lustre. In order to get good performance on Lustre, frequently reading and writing operations should be avoided. In the original TELEMAC distribution, each process writes all the data to be dumped on the disk sequentially in a single file (the file index is the #processor minus one). As this step is sequential, only a few writings are required. But to get rid of the post-processing tool gretel another method is needed.

Furthermore, striping should be considered to reach good performance on Lustre, when using large files. On Lustre, each file can be divided transparently into several chunks. This is called striping. Each of these chunks can be modified in parallel. It is usually advised to stripe big files that are modified by several MPI process in order to achieve good performance (see [3]). Unfortunately, we did not have the chance to test different stripings, as it was corrupting the results produced by our implementation.

C. The algorithm step by step

In this section the algorithm Algo. 1 is explained. However its description is presented in a different order to the one it is actually executed in the code, as a way to more simply explain why the main operations are performed.

- Create a subcommunicator
- Create an MPI derived datatype for the whole file
- Write the header
- Repeat for each "graphic printout" until end of computation
  - Gather results
  - Order results
  - Write results

ALGO. 1. STEP TO WRITE THE RESULTS WITH THE MPI-IO VERSION

1. Write results

Switching from Fortran IO to MPI-IO is not as easy as just replacing writing statements with *mpi_file_write*. By using *mpi_file_write* each MPI process writes independently from the others resulting in a lot of small outputs. To increase performance a collective writing is required, as for instance *mpi_file_write_all*. With this collective call all the writing processes synchronise and write at the same time. It the end the MPI runtime should be able to merge all the writes into a single one, or at least reduce the total number of writing operations.

Another optimisation is to overlap the writing by the simulations themselves. This can be done by using the nonblocking function *mpi_file_iwrite_all*. The only problem is that this function has been only added to the MPI 3.1 standard (2015), and is not supported by older MPI libraries.

2. Create an MPI derived datatype for the whole file

With the Fortran IO version (current distribution), each MPI process is writing parts of the final result in its own file sequentially. The new MPI-IO version is implemented to get rid of the post-processing tool gretel. This means that all the writers need to know where to write the data in the final file, and so each MPI process reorders its result. But this generates a non-contiguous array of data to dump to the disk. And this cannot be done in a single write by default.

The MPI standard provides a way to write efficiently data with this pattern. The solution is to create a model of the

whole file by using a MPI derived datatype. Each MPI process creates a type that represents the exact location of the part of the file it wants to modify. Then this type is used in the collective call of the *mpi_file_set_view* subroutine. With this new "view" of the file, each MPI process can write its result in a single write as if it was writing contiguous data. Since every process is doing a single write, they can do it with a collective write. This collective write should be optimised by the MPI runtime to obtain maximum efficiency.

3. Create a subcommunicator

A collective writing operation is needed to have good performance. But even with the collective writing routine, outputting the solutions can be still relatively slow when all the processes try to write at the same time. Profiling the code has shown that the more MPI processes try to write, the slower it will be. Profiling reports also identified as the cause the numerous small writing operations. This means that even with the collective routine, the MPI runtime is not able to merge the writing requests. To help it in this task, the number of writers has been reduced.

For each compute node one process is selected as the writer of the corresponding nod, usually the first one. All these writers are connected via a new communicator. When the program needs to write a result, all the non-writers of the compute node send their contribution to the writer. Afterwards all the writers start writing via a collective call using the new communicator, which is not the world communicator any longer. With this new way of writing the MPI runtime is now able to merge most of the small writes into bigger ones, which significantly improves the performance.

4. Gather the results

Since only one process per compute node writes the result, all the non-writers need to send their data to this one. This is done by a MPI communication before every writing. Even if it adds some complexity to the code, it is greatly beneficial because otherwise the collective call could not be used.

This step is performed by some gather functions, and is not very costly because the data do not move from a compute node to another one, hence all the operations use the memory of the same compute node.

5. Order the results

The MPI-IO version of the code needs to order the results. This step requires to be done before every writing operation and is actually carried out after every gathering step. Since there exists no sort function in the Fortran standard library, we have implemented a basic one (quicksort [8]), that might become a bottleneck in case of simulations using very large meshes, but this has not be observed yet in all the tests carried out in this work.

6. Other considerations

The SERAFIN files need to be written in big-endian format. The MPI standard provides a way to specify the endianess of the data to be written as an option in the *mpi_file_set_view*, native, internal or external32.

The external32 option provides a way to write in big-endian even when the processor is little-endian (most of the current existing processors), but it seems to be pourly implemented or not at all implemented in most MPI libraries. So we had to write a small set of functions to perform the conversion before writing the results.

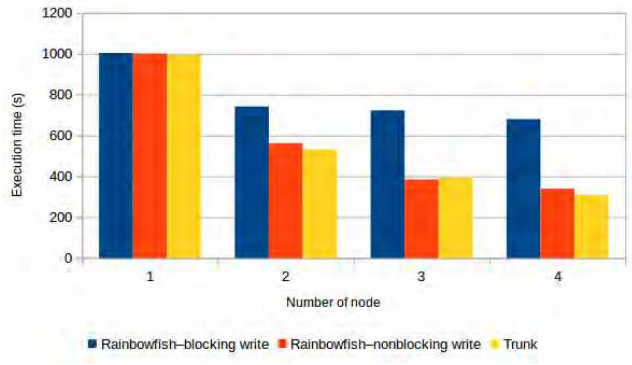

Figure 2. *Execution time comparison of the malpasset fine case with different writing methods and different numbers of compute nodes*

D. Performance comparison

The benchmarks have been carried out on ARCHER. Very different timings were obtained for a given simulation, and they showed a strong dependence on the load of the whole machine. In the worst case scenario a twofold increase in execution time could even be observed.

The performance comparison has been carried out in a way that all the measurements are recorded as closely to each other as possible. In order to do so, the number of executions was reduced, and the trust on the timings obtained was increased.

The test case used in the comparison is malpasset from the examples folder, with the case file *t2d_malpasset-fine.cas*. The mesh file has been refined twice via the script named *converter.py* to get a new mesh of 1,664,000 elements. The trunk code revision is 11,883 and the rainbowfish branch has been updated to that revision.

Figure 2 shows the comparison between two versions of MPI-IO, and Fortran IO from the trunk. In the rainbowfish blocking-write (BW) version, the program waits for the writings to be completed before continuing the computation. In contrast, the rainbowfish non-blocking write (NBW) version tries to overlap writings and computations.

Using a single compute node all the versions show the same performance. But when going for a second compute node, the BW version is outperformed by the NBW one. The NBW version and the trunk show similar performance for all tested numbers of compute nodes. Small differences may occur and result from the interference of the other users/processes running on ARCHER at the same time as the tests.

E. Intermediate conclusion

The MPI-IO implementation works fine and shows good performance for the SERAFIN file format. However, it adds a lot of new and complicated code lines to the HERMES module. It should also be noted that if the results produced by this new implementation are correct with the default options of the Lustre filesystem, they become wrong when changing the striping. It has not been possible so far, to identify where the problem comes from, whether it is because of our implementation, the Lustre filesystem or the MPI library.

Because of this issue the branch has not been merged, but this feature is at the moment available in the branch rainbowfish.

V. CONCLUDING REMARKS

In this paper an efficient way of reducing peak memory consumption in the pre-processing tool partel serial has been presented. This new implementation is aimed to be the default one for the next TELEMAC release.

Furthermore, a way to reduce the number of files generated by partel by concatenating them has been presented. This method works fine and should be pushed to the trunk in the coming weeks.

Finally, a method to reduce the number of result files generated by a run of TELEMAC by using MPI-IO has been presented. This method is still a work in progress and requires a lot of complex modifications to the codebase. Since the method used for partel has been proved successfully, more work should be devoted to investigate if this method could be used for the result files too instead of the here presented method using MPI-IO.

Appendix: Brief description of how a hash table works

In an array, every array index is mapped to an entry of the array. For instance, index 10 maps to cell 10 of the array. This data structure gives access to the cell in O(1). A downside is that if the index 10^6 has to be accessed but the previous one has not, it is still required to allocate an array of at least 10^6 elements. This is what happens in the original version of partel, the index being taken from a big set of indeces even if only a few of them are actually used.

A hash table is an array which indices are not necessary consecutive integers. More precisely a hash table is made of a standard array and a hash function.

The hash function is used to transform the non-consecutive indices given by the user to a smaller set of consecutive integers that map on the internal array of the hash table. An example of a very simple (but bad!) hash function would be h(k) = k mod n with k the index given by the user and n the size of the internal array. This function reduces the input integer enough to make it always fit in the table. The problem is that it outputs a lot of the same number for different inputs, which is called collision.

Even when using a good hash function, there will always be some collisions. There exist several techniques to manage these collisions. The one used in the newly developed version of partel is called linear probing. If two different inputs are mapped to the same cell of the table, we try to put the second one in the very next cell of the array; if this cell is already taken then we try the next one and so on until an empty cell can be found. The more we move further away from the original cell the more it takes time to write and read values in the table.

REFERENCES

[1] *Matthew Szudzik, Elegant Pairing, 2006,* *http://szudzik.com/ElegantPairing.pdf*

[2] https://github.com/google/farmhash

[3] http://www.archer.ac.uk/documentation/best-practice-guide/io.php

[4] Celis, P., Larson, P. A., & Munro, J. I. (1985, October). Robin hood hashing. In *Foundations of Computer Science, 1985., 26th Annual Symposium on* (pp. 281-288). IEEE.

[5] http://glaros.dtc.umn.edu/gkhome/metis/metis/overview

[6] https://doi.org/10.5281/zenodo.1323750

[7] http://valgrind.org/docs/manual/ms-manual.html

[8] Introduction to algorithms, second edition, Thomas H. Cormen, Charles E. Leiserson, Ronald L. Rivest, Clifford Stein, MIT Press, 2001

Uncertainty Propagation in Telemac 2D Dam Failures Modelling and Downstream Hazard Potential Assessment

Layla Assila[1], Matthieu Secher[1], Thomas Viard[1], Benoit Blancher[1], Cédric Goeury[2]
[1]Centre d'Ingénierie Hydraulique (CIH), EDF, Le Bourget du Lac, France
[2]LNHE – R&D, EDF, Chatou, France
matthieu.secher@edf.fr
layassila@gmail.com

***Abstract*— this work addresses uncertainty propagation in TELEMAC 2D models with respect to two major types of risks in river hydrodynamics: flood hazard and dam failures. The studied case is a TELEMAC 2D model that extends over approximately 14.4 km² with a river length of 41 km including 3 major tributaries to the main river and 3 dams. The implementation of the uncertainty propagation approach would not have been feasible and accomplished without the open source platform SALOME-HYDRO and the TELAPY module (PYTHON API) of the TELEMAC-MASCARET SYSTEM. The first step consisted of quantifying uncertain parameters for the acquired hydraulic model and defining adequate probability distributions based on expert judgment and previous specific studies that have been provided by EDF. A sensitivity analysis based on Morris screening method was then carried out to reduce the number of uncertain factors. Uncertainty propagation algorithms such as Monte Carlo and Polynomial Chaos expansion were used to estimate the maximum water depths and velocities, as well as their statistical moments such as the mean and variance and the Sobol indices of the considered parameters. The use of parallelism proved to be necessary to optimize the computation time. The final results are then used to assess the flood casualties and the flood damages. This second estimation is based on the FLOODRISK plugin of QGIS.**

I. INTRODUCTION

Numerical river hydraulics is based on the discretization of partial differential equations (Saint-Venant or Navier-Stokes) which include simplifying assumptions, input data such as rating curves, bathymetry, hydrographs, and parameters including uncertainties that may influence the results. In the current configuration, most parameters are calibrated a posteriori to ensure a good accuracy and representation of the flow dynamics. However, if the calibration could not be carried out due to lack of data, then the validation of the results is based on expert judgment and is subject to high uncertainties. Thus, uncertainty quantification can prove to be a valuable decision making tool since it can determine confidence intervals and whether model outputs will comply with the regulatory requirements (e.g. design requirements) given the random variation in inputs.

In this thesis, the uncertainty propagation methodology presented in Fig.1 is followed [1]. Three main steps are identified:

- Step A consists in defining the model, the statistical quantity of interest and the corresponding criteria (e.g. criteria on failure probability). The model description is similar to a classical deterministic approach as it defines the inputs and outputs of the model.
- Step B consists in quantifying sources of uncertainties on model input parameters which will be described by adequate probability distributions. The result of this step is a random vector of all uncertain variables which is represented by the joint probability distribution of all marginal distributions and a copula that describes the dependence between the variables.
- Step C consists in propagating uncertainties on the input through the model. In most cases, a sensitivity analysis (step C′) is required to assess the influence and the importance of input parameters with respect to the randomness of the output.

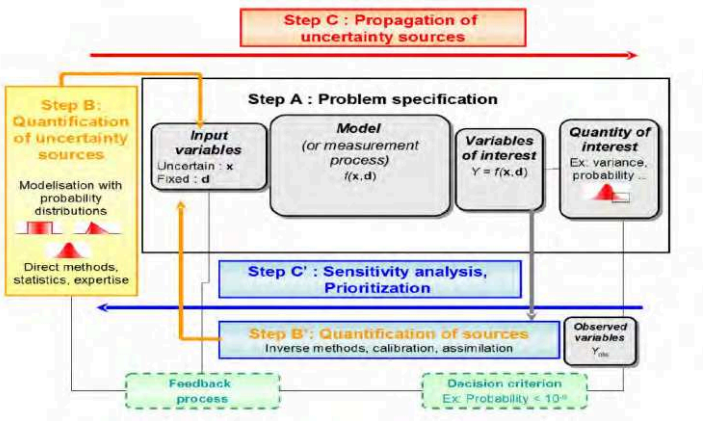

Figure 1 General framework for uncertainty propagation studies [2]

One objective of this work is to apply the previously defined steps; adopted by EDF R&D [2], on a TELEMAC 2D hydraulic model that includes dam failures scenarios through the conception of user-friendly PYTHON scripts. The main methods tested in this work are the classical algorithm of Monte Carlo using different sampling techniques such as Quasi-Monte Carlo with low discrepancy sequences, the Morris screening method for sensitivity analysis and the Polynomial Chaos Expansion to build surrogate models.

The model used to test this method of uncertainty propagation is part of an incremental damage study in which submersion waves are simulated for a reference no dam break scenario and an adverse dam break scenario, increments are calculated by comparing the results of both scenarios and flood damages are assessed.

II. METHODOLOGY

A. Hydraulic TELEMAC 2D model

The geographical location of the modeled river is confidential. The river is delimited by a city downstream which represent a major vulnerability to flood risk in case of dam breaks. The model extends over approximately 14.4 km^2 with a river length of 41 km and it includes 3 major tributaries to the main river. The mesh contains approximately 185 000 nodes. The DEM of the model is given in Fig.2.

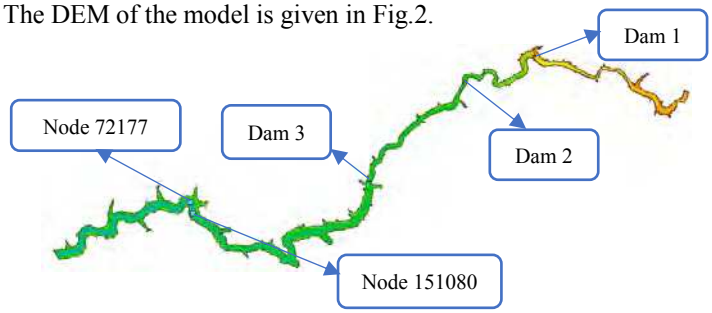

Figure 2 Bathymetry of the 2D model

The simulated discharge correspond to a return period of 5000 years and it deterministic value is estimated by the Schadex method [3]. A factor 10 is considered by assumption for the return period of the tributaries discharges; i.e. the discharges considered for the tributaries are associated with a return period of 500 years.

The dams are modeled by prescribing rating curves on the upstream boundaries and prescribing discharges on the downstream boundaries. A dam failure correspond to the event of exceeding a dam stability threshold defined based on expert judgment. The rating curves are switched once the break occurs via TELAPY PYTHON script and user FORTRAN file. The solution of Ritter is considered to represent the rating curve associated with the break [4]. The model also includes 7 bridges which are modelled as drag forces in the FORTRAN subroutine *Dragfo*. The bridges are considered unstable if the water level upstream of the bridge is higher than the bridge deck level.

In terms of computation time, one run of the model takes approximately 1h10min on 56 processors. This was found to be the optimal number of processors for the studied model.

For this study, the variables of interest are the maximal free surface elevation and the maximal water level (for the flood damages quantification). The statistical quantities of interest are the statistical moments; mainly the mean and the variance, as well as sensitivity measures such as Sobol indices.

B. Quantification of uncertain parameters

The quantification of uncertain parameters is carried out based on the categories of the model input data:

- Flow discharges: they correspond to the peak flood discharges at the main river and the 3 tributaries. For this model and based on expert judgment, only the discharges of the main river and one of the tributaries are considered uncertain. Their probability distribution is the truncated normal distribution with a mean equal to the deterministic peak flood discharge estimated with the Schadex method. Variances of approximately 5% and 25% of the means were respectively taken for the main river and the tributary.
- Strickler coefficients: the hydraulic model is divided into 5 areas with different Strickler coefficients. All these coefficients are considered uncertain following a uniform distribution. Since the model was not calibrated, the bounds for these distributions were estimated based on literature values [5] and are given in Table 1.

Table 1 Probability distribution for Strickler coefficients

Uncertain variable	Probability distribution	Bounds
Strickler for urban zones	Uniform	[10,15]
Strickler for forests	Uniform	[5,12]
Strickler for agricultural zones	Uniform	[15,25]
Strickler for meadows	Uniform	[20,30]
Strickler for the riverbed	Uniform	[28,32]

- Dam failure thresholds: the occurrence of a dam break is defined as the event of the hydraulic head upstream of the dam exceeding a specific stability threshold. The latter is considered uncertain following a truncated normal distribution. The parameters of the probability distributions of dam failure thresholds for the 3 dams included in the model were defined relying on expert judgment and previous EDF studies. The values of these thresholds are confidential.
- Drag coefficients for bridges: based on expert judgment, one of the seven bridges is considered stable since the vulnerabilities are located upstream of the bridge. The other six bridges which are modelled as drag forces, are unstable if the water level exceeds the bridge deck level. The drag coefficients are then considered uncertain since they are empirically estimated based on the shape

and material of the bridge. They follow a uniform distribution.

- Dams rating curves coefficients: the equations used to assess the rating curves include several empirical coefficients that are uncertain and that follow uniform distributions.
- Ritter coefficient: the dam break is described by the dam break solution of Ritter with a deterministic value of 0.209 for coefficient of Ritter. It follows a truncated normal distribution with the value 0.3 (spillway overflow coefficient used in the deterministic case to represent dam breaks) as maximal bound.

The quantification step resulted in 27 uncertain parameters that are assumed to be independent.

C. Sensitivity analysis and uncertainty propagation

Given the large number of quantified uncertain parameters, the Morris screening method is tested in order to reduce the problem dimensionality. This method was first introduced in [6] with the aim of identifying the subset of non-influent parameters in a model using a small number of model evaluations (output samples). The input factors are usually classified according to their effects: negligible, linear and uncorrelated, non-linear and correlated. It is based on moving the factors of a sample one at a time (OAT) by a step Δ in the input physical space. The elementary effects are quantified using (1). The absolute mean and standard deviation of these elementary effects are taken as sensitivity measures.

$$EE_i = \frac{Model(x_1, \dots, x_i + \Delta, \dots, x_p) - Model(x_1, \dots, x_p)}{\Delta} \quad (1)$$

where $x_1, \dots, x_p$ are the uncertain factors of the model, and EE_i is the elementary effect of parameter x_i.

Sobol indices from a polynomial chaos expansion (PCE) of approximately 7200 Monte Carlo simulations are computed to compare with the results of the Morris screening method. The PCE is implemented based on a Least Angle Regression Strategy (LARS) using a corrected Leave-One-Out error [7]. The LARS uses a Least Square Regression truncation method of the polynomial decomposition.

The classical algorithm of Monte Carlo is implemented to propagate uncertainties. Convergence of Monte Carlo and Quasi Monte Carlo are studied [8]. The aim is the computation of statistical moments such as the mean and the variance of the maximal water depth and maximal velocity which will be used to assess the flood damages.

D. Dam break scenarios

The scenarios considered in this study are:

- Break scenario: total and instantaneous dam breaks triggered by the break of the 1[st] upstream dam.
- Reference scenario: no dam breaks

E. Implementation using the APIs and the Clusters

The sensitivity analysis and uncertainty propagation methods were implemented using the C++/PYTHON library OPENTURNS [9] designed for the treatment of uncertainties. It coupling with the hydraulic model (i.e. TELEMAC 2D) is facilitated by the use of the TELAPY module [10] which allows to set and run TELEMAC instances via PYTHON.

Since a large number of simulations are going to be executed, the optimization of the computation time using the available EDF clusters is deemed necessary to accomplish this study. If the TELEMAC model only is parallelized, a minimal time of approximately 48 days 14 hours is required for 1000 simulations. However, if the 1000 simulations are also parallelized according to Fig.3, then a minimal time of approximately 23h20min is sufficient for all the simulations.

Figure 3 Parallelization scheme on Clusters

III. RESULTS

A. Morris screening method results

For the Morris screening method, several numbers of trajectories were tested as shown in Table 2.

Table 2 Cases ran for the Morris screening method

Number of trajectories	Number of simulations	Minimal Calculation Time on Cluster
20	560	~20 hours
40	1 120	~38 hours
60	1 680	~60 hours
100	2 800	~4 *days*

The results for the Morris screening method were not coherent with the expert judgment. In fact, the dam break thresholds and the upstream discharge that were expected to have the major influence on the results based on expert judgment were found to have minimal to zero influence. This is due to the constant delta that is chosen for all parameters even though their values and their types differ significantly. A possible solution to this problem would be to perform an iso-probabilistic transformation on the set of input parameters before generating the samples. Thus, to reduce the set of uncertain parameters, we finally used expert judgment.

B. Uncertainty propagation and sensitivity analysis

1. Convergence

Given the incoherent results of the Morris method, the Monte Carlo algorithm is performed using random sampling

method and Quasi Monte Carlo sampling method based on low discrepancy Sobol sequences.

First, the convergence of the dispersion coefficient (σ/μ) and the mean of Monte Carlo is graphically analysed. The mean is bounded by its 95% confidence interval. The dispersion coefficient and the mean of the maximal surface elevation estimated at node 151080 (node displayed in Fig. 2) and shown in Fig. 4 and Fig.5 suggests that the convergence of Monte Carlo is obtained at approximately 7000 simulations. Quasi Monte Carlo converges more rapidly at approximately 3500 simulations.

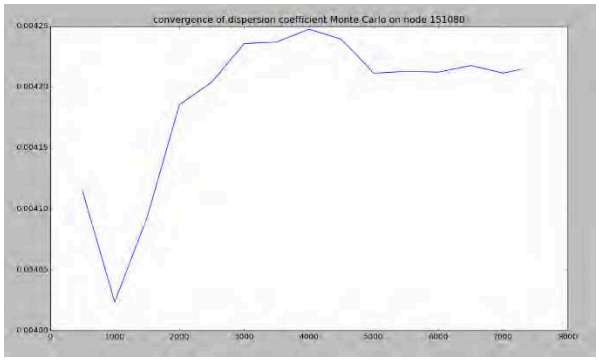

Figure 4 Convergence of the dispersion coefficient of Monte Carlo

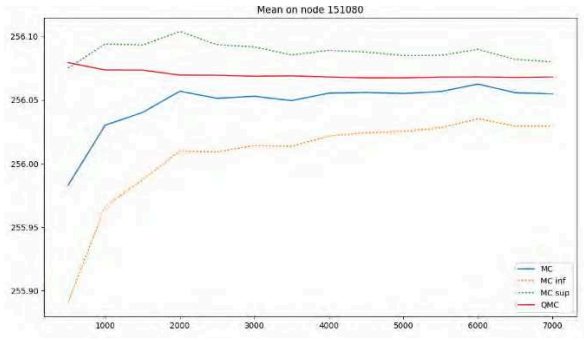

Figure 5 Convergence of the mean of the surface elevation for Monte Carlo and Quasi-Monte Carlo sequence

Second, a convergence study based on a criteria set on the coefficients of variation of the mean and the variance of the Monte Carlo samples is performed. The criteria were defined a priori (based on the precision deemed acceptable for the model at hand) and are given in (2) and (3).

$$Criterion\ 1:\ CV_{mean} \leq 0.00005 \quad (2)$$

$$Criterion\ 2:\ CV_{variance} \leq 0.01 \quad (3)$$

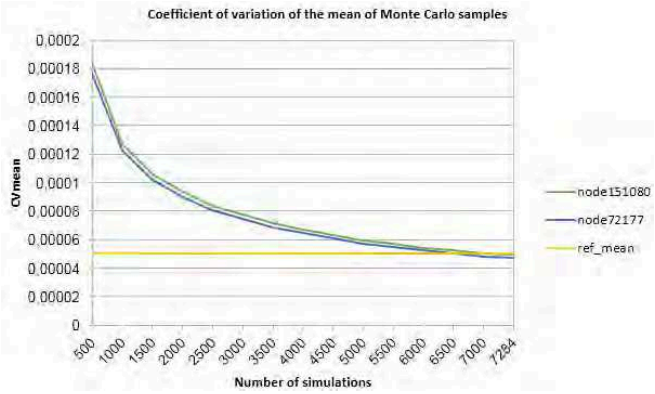

Figure 6 Convergence of the coefficient of variation of the Monte Carlo samples variance using criterion 1

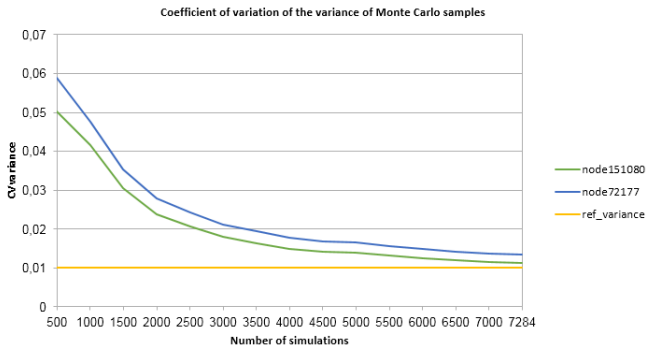

Figure 7 Convergence of the coefficient of variation of the Monte Carlo samples variance using criterion 2

The results displayed in Fig. 6 and Fig. 7 and estimated on 2 nodes: node 151080 and node 72177 located on the downstream agricultural floodplain (Fig.2), confirm that the convergence of Monte Carlo is obtained for approximately 7000 simulations.

2. Polynomial Chaos Expansion based on LARS

This method is tested here since it allows the computation of Sobol indices with smaller samples than Monte Carlo or Saltelli algorithm [14]. The theoretical number of simulations required to construct a surrogate model of degree 4 is given by:

$$N_{th} = \binom{p+d}{d} = \frac{(p+d)!}{p!\,d!} = 31465\ simulations \quad (4)$$

This number implies a computation time of approximately 47 days on the Eole cluster.

Although the available number of Monte Carlo simulations (~7200) is inferior to the theoretical number required for a PCE (4), this method was still tested with this sample. A cross-validation was then performed on the constructed surrogate model using a validation Monte Carlo sample of size 1000.

First, all 7200 simulations were used to construct surrogate models of different degrees in order to find the optimum precision. The reference values are the mean and variance of the 7200.

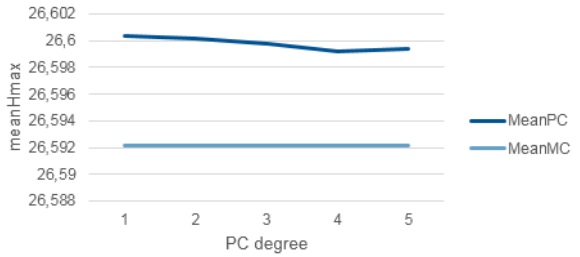

Figure 8 Estimated mean of the surface elevation on node 151080 for PCE using 7200 Monte Carlo simulations

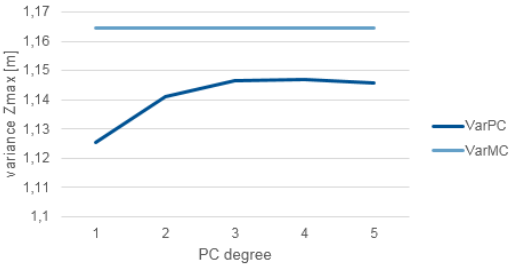

Figure 9 Estimated variance of the surface elevation on node 151080 for PCE using 7200 Monte Carlo simulations

The differences between the means and the variances are approximately 7.10^{-3} and 8.10^{-3} respectively (as shown in Fig.8 and Fig.9). These errors are acceptable and the degree 4 is thus retained for an accuracy study based on the approximation accuracy coefficient Q_2 computed using (5).

$$Q_2 = 1 - \varepsilon_{LOO} \quad (5)$$

Where ε_{LOO} is the Leave-One-Out error. This error is a special case of K-fold error estimate where the number of folds is chosen equal to the cardinality N of the experimental design X. Let's denote $\widehat{M}$ the surrogate model of the real model M, $\widehat{M}^{-i}$ the surrogate model built from the experimental design $X\backslash\{x^i\}$ with the i-th sample x^i being set aside, and $cov(Y)$ the empirical covariance of the response sample Y. The Leave-One-Out error can be calculated using (6).

$$\varepsilon_{LOO} = \frac{\frac{1}{N}\sum_{i=1}^{N} M(\mathrm{x^i}) - \widehat{M}^{-i}(x^i)}{cov(Y)} \quad (6)$$

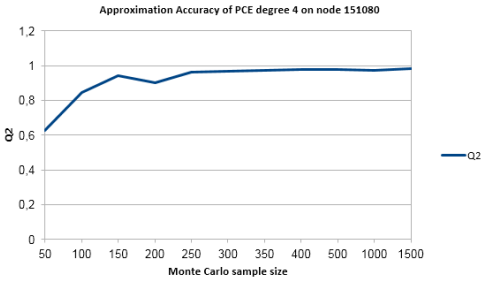

Figure 10 Approximation accuracy coefficient of a degree 4 PCE using different sizes for the Monte Carlo sample

Fig.10 indicates that an approximation accuracy coefficient of approximately 0.97 estimated on node 151080 is obtained for a sample size ≥400.

A cross validation is performed for the PCE surrogate model of degree 4 constructed with 400 Monte Carlo simulations using 1000 samples. Fig.11 indicates that the surrogate model gives a good approximation even if the sample size is less than the required theoretical number of simulations calculated in (4).

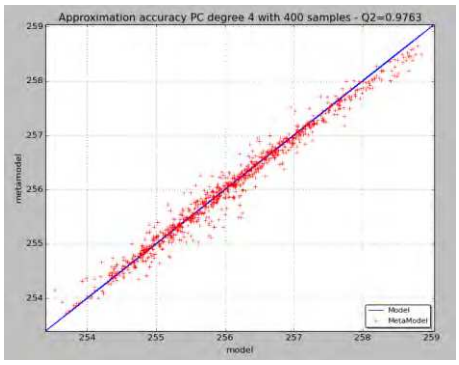

Figure 11 Cross validation of the degree 4 PCE using 1000 Monte Carlo samples for validation

3. Sobol' indices using PCE surrogate models

The surrogate models that have been built using polynomial chaos expansion can also be used to perform a sensitivity analysis by computing Sobol indices. In fact, first order Sobol indices have been calculated using a PC model of degree 4 built with all 7200 Monte Carlo samples. In Fig.12, the conveyance coefficients of dam j are denoted $QZ_{ji},\ i = 1, \ldots, n_j$, where n_j is the number of conveyance coefficients of dam j. The drag coefficients of bridges are denoted $drag$, the Strickler coefficients are denoted $CF_i,\ i = 1,\ldots,5$ and the surface elevation dam failure thresholds are denoted $Break_i,\ i = 1,2,3$. $Qmain$ and $Qtrib$ refer respectively to the discharges of the main river and the tributary. The results shown in Fig.12 are more coherent with the expert judgment than those of the Morris method. The Strickler coefficient of forest areas stands out as the most influential parameter. This could be explained by the location of the node used for the computation of these indices (node 151080) or by the fact that the surrogate model still needs to be refined.

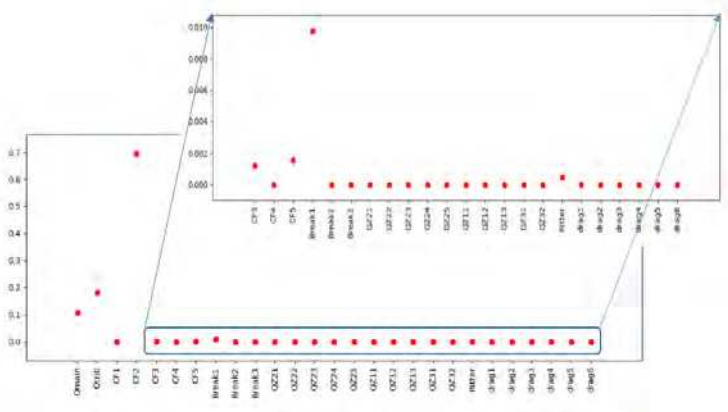

Figure 12 First order Sobol' indices estimated from a degree 4 PCE

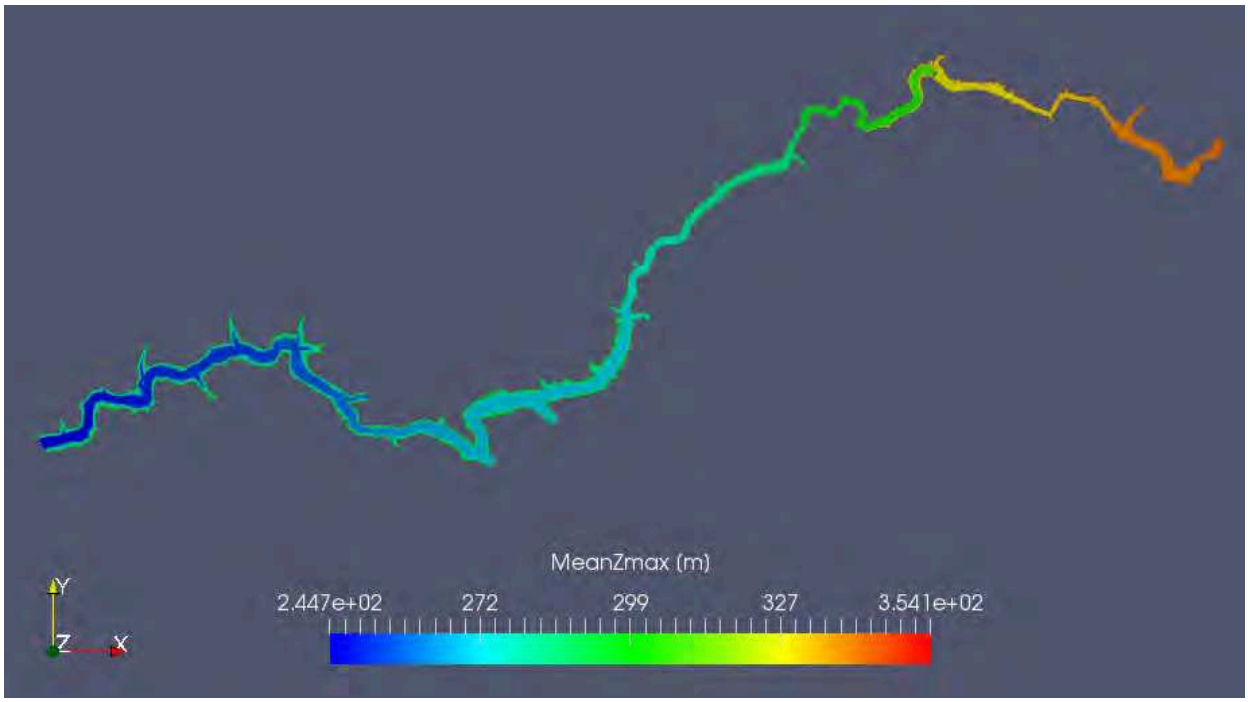

Figure 13 Integration of the mean of surface elevation to the MED result file

4. Post-treatment and damages assessment

Statistical moments such as the mean and the variance of the maximal water depth of the Monte Carlo output sample have been computed. For visualization purposes, these moments are integrated in a result MED file using HERMES APIs, MEDCOUPLING and MEDLOADER [11]. An example of the addition of the mean of the maximal surface elevation from 7200 Monte Carlo simulations to the results file is given in Fig.13.

Downstream flood damages were quantified using 2 methods:

- Ramsbottom or Flood risk to People method [12]: used to quantify casualties based on a danger factor.
- FLOODRISK plugin of QGIS [13]: used to evaluate economic damages based on depth-damage curves.

Figure 14 Vulnerabilities map at the downstream area for total instantaneous dam failures scenario

The FLOODRISK plugin was used to quantify the damages downstream of the last dam using 7200 simulations. The resulting vulnerability map is given in Fig.14.

The vulnerabilities are mainly concentrated downstream of the last dam.

IV. PERSPECTIVES AND LIMITATIONS

The results presented here remain indicatory of the prospects uncertainty propagation and sensitivity analysis methods can provide. In fact, a 2nd scenario describing total and consecutive dam breaks (any dam can be the first to fail) is considered and its results still need to be post-treated. Monte Carlo was not exploited yet to calculate Sobol indices since it requires a larger number of simulations [14]. Other nodes, for which the same methods can be applied, located along the streamline or the floodplain can be taken into account. Hence, maps of Sobol indices can be created. Another perspective is the quantification of casualties using the Ramsbottom method, as well as automating the FLOODRISK method without using the QGIS interface.

As for the limitations of the study, the convergence criteria were defined for the specific model at hand. Hence, one should modify and adapt these criteria based on expert judgment and regulatory requirements.

All the methods and the steps of this study were carried out using PYTHON scripts. However, this methodology can be partially implemented using the SALOME-HYDRO platform except for the user FORTRAN and the TELAPY scripts that handle specific aspects of the hydraulic simulation (i.e. dam breaks here). SALOME-HYDRO only lacks the launching parallelization which should be soon available.

V. CONCLUSIONS

The implementation of the uncertainty propagation approach would not have been feasible and accomplished without the open source platform SALOME-HYDRO, OPENTURNS and the

TELAPY module (PYTHON API) of the TELEMAC-MASCARET SYSTEM. The main difficulty - which is generally common to probabilistic models that treat uncertainty propagation - remains the optimization of computation time with respect to the number of simulations considered and the run-time of the TELEMAC case; whether it is in parallel or sequential mode.

The main objectives of this study; which were the application of the uncertainty propagation methods on a hydraulic model at an engineering scale and the conception of user-friendly PYTHON scripts that makes such parametric studies within the reach of any TELEMAC user, were accomplished. From an engineering point of view, the quantification of sources of uncertainties and their representation with suitable probability distributions is the step that takes the longest time to complete since it mostly relies on expert judgment.

ACKNOWLEDGEMENT

We would like to express our gratitude to Yoann Audouin for his availability and his help regarding the use of TELAPY and parallelism. A special thank you is due to Jérôme Condette for providing GIS data and methods for the quantification of flood damages, as well as Emmanuel Paquet for providing a database of different hydrographs for the considered river.

REFERENCES

[1] B. Sudret, "Uncertainty propagation and sensitivity analysis in mechanical models. Contributions to structural reliability and stochastic spectral methods," Rapport d'Habilitation à Diriger des Recherches, 2007

[2] C. Goeury, T. David, R. Ata, S. Boyaval, Y. Audouin, N. Goutal, A.-L. Popelin, M. Couplet, M. Baudin, "Uncertainty quantification on a real case with Telemac-2D," Telemac-Mascaret user conference proceedings, pp 44-51, 2015

[3] E. Paquet, M. Lang, J.C Carré. Schadex method for extreme flood estimation: overview, applications and perspectives. 24th ICOLD Congress, Jun 2012, Kyoto, Japan. 29 p., 2012. <hal-00861194>

[4] O. Castro-Orgaz, H. Chanson, "Ritter's dry-bed dam-break flow: positive & negative wave dynamics," DOI 10.1007/s10652-017-9512-5.

[5] G. Degoutte, "Chapitre 1: aide-mémoire d'hydraulique à surface libre," cours en ligne d'AgroParisTech, https://tice.agroparistech.fr/coursenligne/courses/COURSDHYDRAULIQUEDYN/document/Texte%20de%20cours/degoutte1.pdf?cidReq=COURSDHYDRAULIQUEDYN

[6] M.D. Morris, "Factorial sampling plans for preliminary computational experiments," journal of Technometrics, vol. 33, pp. 161-174, 1991.

[7] G. Blatman, B. Sudret, "Adaptive sparse polynomial chaos expansion based on least angle regression," Journal of Computational Physics 230 (2011) 2345–2367.

[8] R.E. Caflisch, "Monte carlo and quasi-monte carlo methods," Cambridge University Press, 1998.

[9] M. Baudin, A. Dutfoy, B. Iooss, A.L. Popelin, "OpenTURNS: An industrial software for uncertainty quantification in simulation, " Handbook of uncertainty quantification (pp.2001-2038), 2015

[10] C. Goeury, Y. Audouin, F. Zaoui, "TelApy User Manual", V7P3 Telemac-Mascaret documentation

[11] MEDCoupling and MEDLoader API Documentation, Salome platform version 8.4.0

[12] HR Wallingford, Flood Hazard Research Centre, Middlesex University, Risk & Policy Analysts Ltd., "The Flood Risks to People Methodology: PHASE 2 FD2321/TR1," Department for Environment, Food and Rural Affairs, Pb no. 11545, March 2006

[13] L. Mancusi, R. Albano, A. Sole, "FloodRisk: a QGIS plugin for flood consequences estimation," Geomatics Workbooks n° 12 – FOSS4G Europe Como 2015

[14] A. Saltelli, M. Ratto, T. Andres, F. Campolongo, J. Cariboni, D. Gatelli, M. Saisana, S. Tarantola, "Global sensitivity analysis: the primer," John Wiley & Sons Ltd, 2008

Finding Good Solutions to Telemac Optimization Problems with a Metaheuristic

C. Goeury[1], F. Zaoui[1], Y. Audouin[1], P. Prodanovic[2], J. Fontaine[1], P. Tassi[1], R. Ata[1]
[1] EDF R&D – National Laboratory for Hydraulics and Environment (LNHE), 6 quai Watier, 78401 Chatou, France
[2] Riggs Engineering Ltd., 1240 Commissioners Road West, London, Ontario, N6K 1C7, Canada
cedric.goeury@edf.fr

Abstract— **Derivative-free optimization methods are typically considered for the minimization/maximization of functions for which the corresponding derivatives neither are available for use nor can be directly approximated by numerical techniques. Problem of this type are common in engineering optimization where the value of the cost function is often computed by simulation and may be subject to statistical noise or other form of inaccuracy. In fact, expensive function evaluations would prevent approximation of derivatives, and, even when computed, noise would make such approximations less reliable. Thus, the objective of this work is to implement an efficient heuristic-designed procedure in order to find optimal solution when using TELEMAC-2D to assess a hydrodynamic performance. Two examples are given dealing with a shape optimization and a model calibration. In both cases the underlying optimization problems are solved by coupling a population-based metaheuristic to the numerical model with the help of TelApy [1]. For the shape optimization problem, some design variables define the geometrical configuration of the structure whose optimal configuration is not known a priori. The shape optimization problem consists of finding an optimum position of the slots of a typical fish passage. The second application case focuses on calibration problem. In fact, calibrating a hydrodynamic model (here the Gironde estuary site) is typically an engaged and difficult process due to the complexity of the flows and their interaction. In this paper, both friction and tidal are highlighted. Theoretically, Particle Swarm Optimization algorithm does not ensure to find optimal solutions but in practice it performs very well. Moreover it does not rely on gradient computations as it does not assume the problem to be differentiable. Finally its convergence is fast enough in comparison with other algorithms even when coupled with TELEMAC-2D.**

I. INTRODUCTION

Optimization is an area of critical importance in engineering and applied sciences. When designing products, materials, factories, production processes, manufacturing or service systems, and financial products, engineers strive for the best possible solutions, the most economical use of limited resources, and the greatest efficiency. Although the problem of minimizing or maximizing a differentiable function is a frequently met problem, the golden age of optimization has been enabled by developments in the three main areas: computing capability, data, and methods. The optimization former can be very different according to the form of the cost function to be minimised (convex, quadratic, nonlinear, etc.), its regularity and the dimension of the space studied. Derivative-free optimization (DFO) methods are typically considered for the minimization/maximization of functions for which the corresponding derivatives neither are available for use nor can be directly approximated by numerical techniques. Problem of this type are common in engineering optimization where the value of the cost function is often computed by simulation and may be subject to statistical noise or other form of inaccuracy. In fact, expensive function evaluations would prevent approximation of derivatives, and, even when computed, noise would make such approximations less reliable. Thus, the objective of this work is to implement an efficient heuristic-designed procedure in order to find optimal solution when using TELEMAC-2D to assess a hydrodynamic performance.

Section II and III introduce the principle of the Derivative-free optimization algorithm and the software tools used for this work respectively. Section IV is dedicated to model results obtained from several different hydraulic applications: calibration and shape optimization. Finally, Section V, offers some conclusions and outlook.

II. CONTEXT AND PRINCIPLE

A. Context

Parameter estimation, a subset of the so-called inverse problem, consists of evaluating the underlying input data of a problem from its solution. The Derivative-free optimization is used here for demonstration purpose on two different hydraulic inverse problems:

- *Parameter Calibration.* Numerical models are nowadays commonly used in fluvial and maritime hydraulics as forecasting and assessment tools for example. Model results have to be compared against measured data in order to assess their accuracy in operational conditions. Amongst others, this process touches on the calibration, verification and validation. In particular, calibration aims at simulating a series of reference events by adjusting some uncertain physically-based parameters until the comparison is as accurate as possible. Calibration is critical to all projects based on numerical models as it takes a very large proportion of the project lifetime. Thus, in this work, a real estuary configuration is presented and calibrated using measurement data.
- *Shape optimization configuration.* Applications of shape optimization to hydraulic engineering are rare, especially for the cases where optimization is used to inform actual engineering design. The Derivative-free

optimization is used here to present a methodology that can be applied by end users working on their own shape optimization problems in the fields of river and coastal hydraulics. For example, applications of shape optimization could include determining the optimal layout of a groyne field along a coastline that could address sedimentation and navigation issues, the shape and orientation of a breakwater protecting a harbour or a marina subject to various environmental and economic constraints, as well as many others.

B. Cost function formulation

Thereafter, all model parameters constitute the n-components of the control vector $X = (X_i)^T, \forall \mathrm{i} \in [1, \dots \mathrm{n}]$.

The optimization of hydraulic problems is a parameter estimation or reverse method used to simulate a series of reference events by adjusting uncertain physically-based parameters contained in the control vector X to produce a solution that is as accurate as possible. Therefore, the optimal search for the control vector takes the form of an objective or cost function $J(X)$ given in (1).

$$\mathrm{J(X)} = \frac{1}{2}\big(\mathrm{Y} - \mathrm{H(X)}\big)^{\mathrm{T}}\mathrm{R}^{-1}\big(\mathrm{Y} - \mathrm{H(X)}\big) \qquad (1)$$

where the components of X represents parameters to be designed / calibrated, Y is the target state/observation vector, H is an operator enabling the passage of the parameter space (where the vector X lives) to the target state/observation space (where Y lives) such that $Y = H(X)$ and R is a weighted covariance matrix. This is a formulation of the optimal search of control vector X adopted in this work.

Many deterministic optimisation methods are known as gradient descent methods. However, sometimes derivatives neither are available for use nor can be directly approximated by numerical techniques. Problem of this type are common in engineering optimization where the value of the cost function is often computed by simulation and may be subject to statistical noise or other form of inaccuracy. In fact, expensive function evaluations would prevent approximation of derivatives, and, even when computed, noise would make such approximations less reliable. In such cases, Derivative-free optimization methods are particularly useful.

In this paper, the Particle Swarm Optimizer (PSO) has been used to solve the hydraulic optimization problem.

C. Particle Swarm Optimizer

1) Informal description

Particle swarm optimization is a population-based stochastic optimization technique developed by [2], inspired by social behaviour of bird flocking or fish schooling. PSO shares many similarities with evolutionary computational techniques such as Genetic Algorithms [3]. The system is initialized with a population of random solutions and searches for optima by updating generations. In PSO, the potential solutions, called particles, fly through the search space by following the current optimum particle. In fact, for each particle, it is possible to evaluate the cost function value given by Eq.1. Then, the global optimum point of the particle swarm, i.e. the one having the smallest cost function value is looked for. This is useful to compute a velocity for each particle. The particle swarm optimization concept consists of, at each iteration of the algorithm, changing the velocity of each particle towards the best solution. A particle is made of:

- a position inside the search space
- the cost function value at this position
- a velocity (in fact a displacement), which is used to compute the next position
- a memory, that contains the best position (called the previous best) found by the particle
- the cost function value of this previous best

2) Mathematical formulation

In a search space of dimension d, the swarm particle i has a location and velocity (in fact a displacement) vector $\overrightarrow{x_i} = (x_{i,1}, x_{i,2}, \dots, x_{i,d})$ and $\overrightarrow{v_i} = (v_{i,1}, v_{i,2}, \dots, v_{i,d})$ respectively. The quality of its position is determined by the value of the objective function at this point. Moreover, the best position by which the particle has already passed, denoted $\overrightarrow{Pbest_i} = (Pbest_{i,1}, Pbest_{i,2}, \dots, Pbest_{i,d})$, is kept in memory. Another "best" value that is tracked by the particle swarm optimizer is the best value, obtained by any particle of the swarm is denoted as

$$\overrightarrow{Gbest} = (Gbest_1, Gbest_2, \dots, Gbest_d).$$

At the iteration $t+1$, the new particle position $\overrightarrow{x_i^{t+1}}$ is computed as expressed in Eq. 2.

$$\begin{cases} x_{i,j}^{t+1} = x_{i,j}^t + v_{i,j}^{t+1} \\ v_{i,j}^{t+1} = \omega v_{i,j}^t + c_1 r_1 \big(Pbest_{i,j}^t - x_{i,j}^t\big) \\ \qquad \dots + c_2 r_2 \big(Gbest_j - x_{i,j}^t\big) \end{cases} \qquad (2)$$

where ω is a constant called inertia coefficient, c_1 and c_2 are two constants representing acceleration coefficients, r_1 and r_2 are two numbers randomly generated at each iteration and dimension from the uniform distribution $U[0;1]$. In this work, the parameters ω, c_1 and c_2 are set to the default value 0.5.

As presented in Eq.2 and displayed in Figure 1, the particle displacement is governed by the following components: inertia term (ωv_i^j), cognitive and social component respectively $c_1 r_1 \big(Pbest_i^j - x_i^j\big)$ and $c_2 r_2 \big(Gbest^j - x_i^j\big)$.

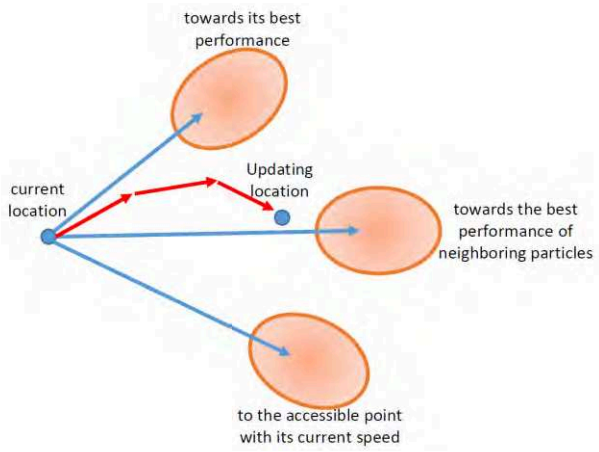

Figure 1. Particle displacement.

Then, the variables $\overrightarrow{Pbest_i}$ and, $\overrightarrow{Gbest}$ are determined using Eq. 3 and 4.

$$\overrightarrow{Gbest} = arg \min_{\overrightarrow{Pbest_i}} J(\overrightarrow{Pbest_i}), \forall\, i \in [1, N] \quad (3)$$

$$\overrightarrow{Pbest^{t+1}} = \begin{cases} \overrightarrow{Pbest_i}, \text{if } J\left(\overrightarrow{x_i^{t+1}}\right) \geq \overrightarrow{Pbest_i} \\ \overrightarrow{x_i^{t+1}} \text{ else} \end{cases} \quad (4)$$

where J denote the cost function defined in Eq. 1.

This process is summarized in the algorithm presented in Table 1.

1-Initialisation of the swarm composed by $\boldsymbol{N}$ particles: pick a random position and velocity
2-Compute the particle positions
3-For each particle $\boldsymbol{i}$, $\overrightarrow{\boldsymbol{Pbest_i}} = \overrightarrow{\boldsymbol{x_i}}$
4-Compute $\overrightarrow{\boldsymbol{Gbest}}$
5-While the stop criterion is not satisfied do:
6- Compute the particle displacement (Eq. 2)
7- Evaluate the particle positions (call of hydraulic solver)
8- update , $\overrightarrow{\boldsymbol{Pbest_i}}$ and , $\overrightarrow{\boldsymbol{Gbest}}$ (Eq. 3 and Eq. 4)
9-End

Table 1. Particle Swarm Optimization Algorithm

III. SOFTWARE TOOLS

The particle swarm optimization algorithm presented in the previous section (section II) combines different fields such as optimisation, numerical analysis, parameter estimation, and free surface flow hydraulics. The software implementation of the algorithm has to be designed for different architectures with reusable components. This study is performed by coupling the hydrodynamic solver TELEMAC-2D and the toolkit library PYSWARM for particle swarm optimization in python within the SALOME platform, through the component TelApy of the TELEMAC system.

A. The SALOME platform

SALOME is an open source platform (www.salome-platform.org) for pre and post processing of numerical simulations, enabling the chaining or the coupling of various software tools and codes. SALOME is developed by EDF, the CEA and OPENCASCADE S.A.S. under the GNU LGPL license. It is based on an open and flexible architecture with reusable components, which can be used together to build a computation scheme assembling each module or external codes together through specific communication protocols. In our case, the TELEMAC-2D model is driven through the TelApy component and dynamically linked to PYSWARM library within SALOME (See Fig. 2). In fact, all the components within SALOME can be used together with the YACS module which builds a computation scheme and call each module and makes them communicate. In our case TELEMAC-2D and PYSWARM are working together within this platform. Moreover, the platform supports advanced generation of numerical model geometry through it extensive CAD modelling computational engine, thus making it applicable to a wide variety of studies and applications. Its meshing capabilities are also extensive, allowing a user to generate meshes using common 2D and 3D formats. Moreover, the SALOME platform has provided its users access to all of its functionalities through an integrated Python interface. These features make for the SALOME platform an ideal choice for a tool set used shape optimization studies where meshes need to be generated automatically for each new designed parameters.

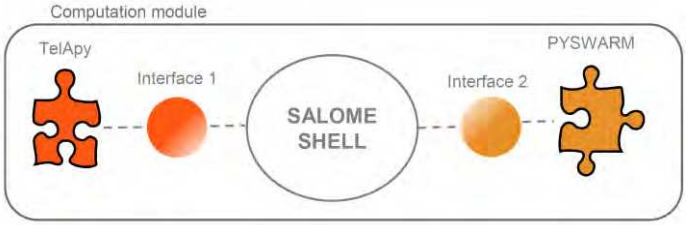

Figure 2. The SALOME composition linking TelApy to PYSWARM library

B. The TelApy component of the TELEMAC system

The recently implemented TelApy component is distributed with the open source TELEMAC system (www.opentelemac.org). It aims at providing python source code that wraps and controls a TELEMAC simulation through a Fortran API (Application Program Interface) [1]. The API's main goal is to have control over a simulation while running a case. For example, it allows the user to hold the simulation at any time step, retrieve some variables and / or change them. The links between the various interoperable scientific libraries available within the Python language allows the creation of an ever more efficient computing chain able to more finely respond to various complex problems. The TelApy component has the capability to be expended to new types of TELEMAC simulations including high performance computing for the computation of uncertainties, other optimization methods, coupling, etc.

C. The particle swarm optimization PYSWARM

The population-based metaheuristic algorithm used for this work is a Particle Swarm Optimizer written in Python that

is a fork of the open source module PYSWARM[1]. PSO defines and iteratively improves a set of candidates (particles) towards optimality. Theoretically, PSO does not ensure to find optimal solutions but in practice it performs very well. Moreover it does not rely on gradient computations as it does not assume the problem to be differentiable.

IV. APPLICATIONS

A. Shape Optimization application

1) Numerical configuration

The shape optimization problem used in this work consists of finding an optimum position of the slots of a typical fish passage. The geometry of the fish passage used in this example is obtained from [4], where a similar problem is solved (albeit in a different way). The fish passage consists of ten identical compartments, with each having two slots (See Fig. 3). The slots are referred to in this work as upper and lower. The position of the slots for any given shape is specified with four variables representing the center point of the upper (x_U, y_U) and lower (x_L, y_L) slot, respectively (See Fig. 3). A combination of the four values thus defines a particular shape of the flume. Thus, the objective is to design the fish passage shape by changing the position of the slots (x_U, y_U, x_L, y_L) in order to obtain a desired target velocity in the channel. The optimization problem is to select the position and length of the upper and lower slots, such that it optimizes the objective function while satisfying the problem constraints. In fact, in the numerical optimization the search space is restricted to a rectangular zone bounded by (x_a, y_a) on the lower left, and (x_b, y_b) on the upper right. A constraint is specified in the optimization to ensure the slots are spaced at least $\Delta x = x_L - x_U$ apart horizontally, and at least $\Delta y = y_L - y_U$ vertically. This constraint is required in order to prevent the numeric optimizer from selecting invalid and physically irrelevant geometries (such as one where the upper and lower slots touch or overlap).

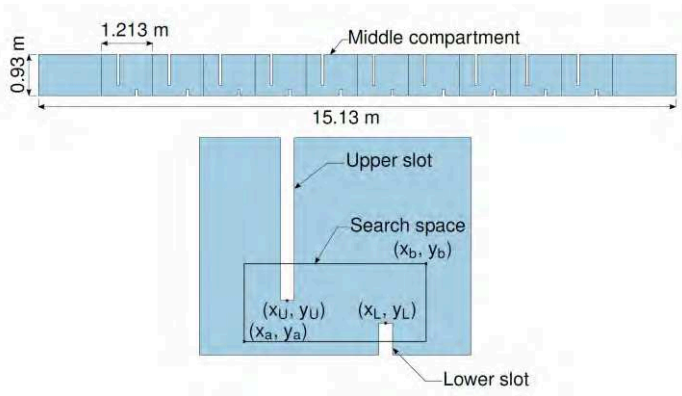

Figure 3. Geometry definition of the fish flume test case

The particulars of the problem simulated here are (units in meters, unless otherwise specified): Search space $x_a = 6.653$, $x_b = 7.260$, $y_a = 0.050$, and $y_b = 0.243$, width of the slots $w = 0.063$; channel slope $S_0 = 0.05$; bottom Chezy friction coefficient $f = 57.36\ m^{1/2}/s$; initial water depth $h_0 = 0.50$; discharge in the flume $Q_0 = 0.065\ m^3/s$; constraint values $\Delta x = 0.1$, and $\Delta y = 0.05$.

2) Optimization problem definition

One way to validate the tool chain developed in this work is to artificially set up a desired state. The aim of this optimization configuration is to find optimal shape design based on a numerically generated synthetic data from the so-called "identical-twin-experiment", in which true state is known. The initial (starting shape) used in the optimization process is defined as, $(x_U, y_U, x_L, y_L)_i = (6.7, 0.23, 7.23, 0.15)$, while the target shape to recover is defined as $(x_U, y_U, x_L, y_L)_t = (6.927, 0.147, 7.168, 0.054)$, where the subscript i, t denotes the initial and target shape respectively. The optimization process is then started with some initial state, with an end goal to recover the specified (or desired) shape. In order to solve the shape optimization problem applied in hydraulic engineering the end user is required to possess a set of tools that can:

- i) simulate a given shape and obtain a simulated system state,
- ii) extract results from the simulated system state and obtain a value of a pre-defined objective function,
- iii) try a new shape, and simulate its system state,
- iv) carry out as many new iterations until a global optimum is found.

3) Cost function formulation

In the cost function formulation given in Eq. 1, the target state vector is the x and y components of the flow velocity, in the middle compartment (See Fig. 3), extracted from the steady state solution of the target shape such as $Y = \begin{bmatrix} u_t \\ v_t \end{bmatrix} = H(x_U, y_U, x_L, y_L)$.

The operator H enabling the passage of the parameter space (slots coordinates) to the target state space (velocity fields) consists of a tool chain that can automatically:

- generate new shapes (which requires create a new mesh, assigning bathymetry/topography to the mesh, assigning initial and boundary conditions) that are ready to be used in a numerical model,
- call the hydraulic solver TELEMAC-2D,
- and extract from the steady state solution of the shape the x and y components of the flow velocity (u, v) in the middle compartment.

Thus, the main issue for the shape optimization is to have a tool allowing to mesh automatically new shapes. The SALOME platform supports advanced generation of numerical model geometry through its extensive CAD modelling computational engine, thus making it applicable to a wide variety of studies and applications. The SALOME platform has provided its users access to all of its functionalities through an integrated Python interface. These

[1] https://github.com/fzao/pyswarm

features make the SALOME platform an ideal choice for a tool set used in the shape optimization studies where meshes need to be generated automatically for each new designed parameters.

And finally, R is diagonal matrix containing node weighting according to their area.

4) Numerical results

In this work, the optimizer selects and tries new shapes during its course of execution. Each iteration of the optimizer requires a TELEMAC-2D solution of a shape where positions of the slots are evaluated for each considered particle. In this example, the swarm of PSO optimizer is composed of 10 particles and the maximum number of iterations is set to 20. After specifying initial and target shapes the optimization simulations are carried out. Table 2 shows the results of the simulations.

Simulation shape	x_U [m]	y_U [m]	x_L [m]	y_L [m]	$J(x)$ [-]
Initial	6.700	0.230	7.230	0.150	0.137
Target	6.927	0.147	7.168	0.054	0.0
optima	6.924	0.152	7.193	0.052	0.0033

Table 2. Slot positions and cost function at initial, target and optima configurations

Figure 4 presents the generated optimum graphically and optimizer convergence plots is shown in Figure 5.

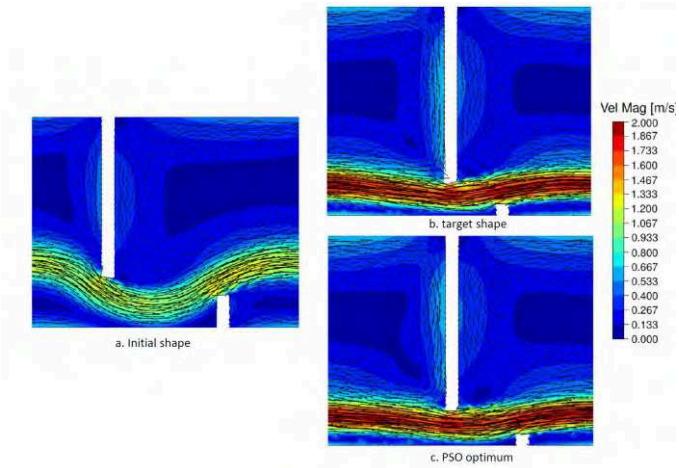

Figure 4. Fish flume at initial (a), target (b) and optima (c) configurations

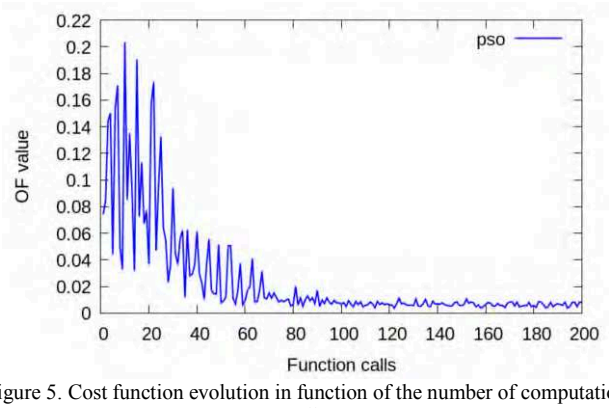

Figure 5. Cost function evolution in function of the number of computation calls

As shown in Figure 4, the fish flume optimum structure is much closer to the target shape than the initial one. As expected, the final results emphasises the efficiency of the parametric shape optimization tool which is able to deliver optimal structure design for hydraulic engineering applications. However, some slot position differences can be observed (see Tab. 2). The defined objective function does not seem to be sensitive to small fluctuation in the position of the slots. Given the shape optimization tool kit is working as intended, a relevant question to pose is what are the effects of the four design variables on the previously defined optimization problem. This question is answered by carrying out a global sensitivity analysis using Morris's method [5] on the four design variables (x_U, y_U, x_L, y_L), and to analyze how they influence the defined objective function $J(x)$ in the fish flume case.

5) Sensitivity Analysis

The sensivity analysis aims at quantifying the relative importance of each input parameter of a model. The variance-based methods aim at decomposing the variance of the output to quantify the participation of each variable when these ones are considered as independents. Generally, these techniques compute sensitivity indices called Sobol Indices [6]. The definition of Sobol indices is a result of the ANOVA (ANalysis Of VAriance) variance decomposition. Morris's method, unlike Sobol's method, only provides qualitative answers regarding parameter interactions but it does so with much less model evaluations. In fact, Morris's method measures global sensitivity using a set of local derivatives (elementary effects) taken at discrete points sampled through the parameter space. Each parameter is perturbed along a pre-defined grid to create a trajectory through the parameter space. For a given model with d parameters, one trajectory will contain d perturbations. Each trajectory yields an estimate of the elementary effect for each parameter (ratio of the change in model output to the change in parameter). Once trajectories are sampled, the resulting set of elementary effects are then averaged to give an estimate of total order effects [5]. The standard deviation of the elementary effects describes the variability through the parameter space, and thus describes the degree to which interactions are present. Total order effects are described with a parameter μ; the higher the value for a particular parameter, the more influential that parameter is. The degree of interaction is captured with a parameter σ; the higher the value for a particular parameter, the more the parameter in question interacts with other parameters.

Thus, in this work, the variables (or parameters) considered in the Morris's method are the four design variables of the shape optimization problem (x_U, y_U, x_L, y_L). The bounds of each design variable had to be individually specified such that $(x_U, y_U) \epsilon [6.653, 6.994] \times [0.129, 0.242]$ and $(x_L, y_L) \epsilon [7.097, 7.250] \times [0.010, 0.079]$, to make sure the set of samples generated by Morris's method actually meets the constraints of the optimization problem. For the sampling of the parameter space using Morris's method, the

number of trajectories, r, is set at 10. The number of grid points, p, to sample the parameter space in each dimension is also set at 10. From the theory embedded in Morris's method, the number of parameter samples that is generated is $r \times (d+1) = 10 \times (4+1) = 50$. Application of Morris's method, in combination with the tool chain built in this work, produce the Morris's effects plot shown in Figure 6.

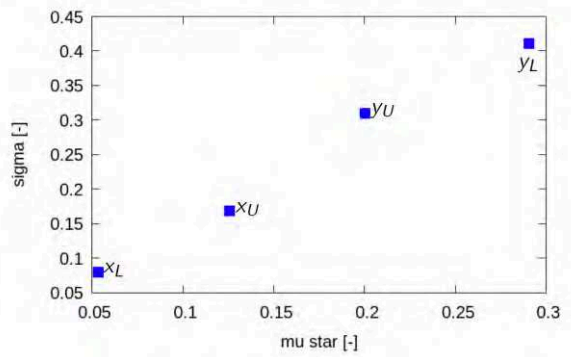

Figure 6. Global sensitivity analysis of design variables using Morris's method

From Morris's effects plot shown in Figure 6, it is readily discernible that the y coordinates of the fish slots are the most influential variables, together with the fact that they are also the ones that are most likely to interact with each other. This conclusion is consistent with the findings discovered through the numerical results presented in Figure 4, where it was found that varying the x coordinates of the slots have less influence on the velocity magnitude.

B. Calibration application

1) Context

The Bordeaux harbour, located in the largest estuary in Western Europe, faces many challenges of development in the Gironde estuary area. It must simultaneously manage the estuary natural constraints and improve its capacity of reception of larger ships in the next two years to answer the growing international market demand. In fact, the increasing use of maritime transport leads to an increase in ship size in order to minimize the transport costs in terms of budget and time. On the other hand the dimension of access channels and harbours cannot follow the expansion rate of the vessels. Thus, in order to satisfy the demand of the market for increasing ships size, while ensuring navigation safety, the water-depth evolution in the estuary needs to be predicted with a maximal accuracy. Numerical models are nowadays commonly used in fluvial and maritime hydraulics as forecasting and assessment tools for example. Model results have to be compared against measured data in order to assess their accuracy in operational conditions. Amongst others, this process touches on the calibration, verification and validation. In particular, calibration aims at simulating a series of reference events by adjusting some uncertain physically based parameters until the comparison is as accurate as possible. Calibration is critical to all projects based on numerical models as it requires a very large proportion of the project lifetime. The objective of this work is to implement an efficient calibration algorithm, capable of processing measurements optimally, to estimate the partially known or missing parameters (bathymetry, bed friction, inflow discharge, tidal parameter, initial state, etc.).

2) Numerical configuration and available data

The Gironde is a navigable estuary in southwest France and is formed from the meeting of the rivers Dordogne and Garonne just downstream of the centre of Bordeaux, it is the largest estuary in western Europe. The hydraulic model used in this work covers approximately 195 km between the fluvial upstream and the maritime downstream boundaries conditions representing an area of around 635 km^2. The finite element mesh is composed of 173781 nodes (see Fig. 7). The mesh size varies from 40 m within the area of interest, the navigation channel, to 750 m offshore (western and northern sectors of the model). As shown in Figure 7, six friction areas are considered in the hydraulic model.

The boundary conditions along the marine border of the model have been set up using depth-averaged velocities and water levels from the Legos numerical model TUGO dataset (46 harmonic constants). Surge data, describing the difference between the tidal signal and the observed water level, are taken into account using a data file that comes from Hycom2D model of the SHOM [7]. Surface wind data is also considered in the model to simulate the flow under wind blowing conditions. A flow discharge is imposed upstream of the Gironde estuary model on the Garonne and the Dordogne rivers. Time series are available for these two liquid boundaries.

Several observation stations are available in the region of interest. These stations measure the free surface flow evolution every 60 seconds at the The Verdon, Richard, Lamena, Pauillac, Fort Médoc, Ambes, The Marquis, Bassens and Bordeaux locations (see Fig. 7). For this study, observation results are used over a 36 hours period from August 12th to 14th, 2015.

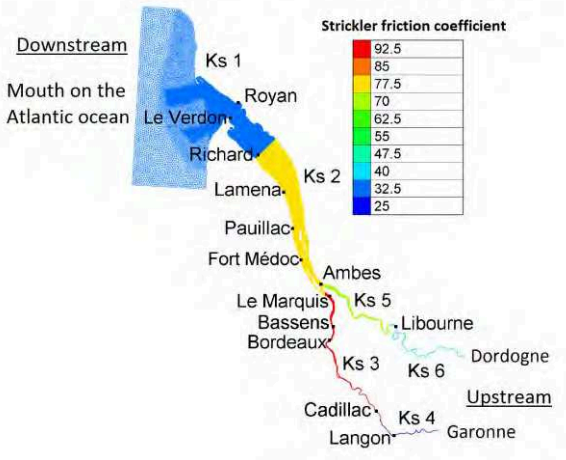

Figure 7. Model mesh with friction coefficient areas and observation station locations

3) Sensitivity analysis

Calibrating a hydrodynamic model (here for a real tidal site) is typically an engaged and difficult process due to the complexity of the flows and their interaction with the shoreline, the bathymetry, islands, etc. Thus, it is essential to understand in depth the relationship between the modelling calibration parameters and the simulated state variables which are compared to the observations. In this case, the identification of the most influential input parameters by sensitivity analysis has been led to target the calibration parameters when observations are available. In particular, both friction and tidal amplification were highlighted.

a) friction coefficient

Friction comes into the momentum equations of the shallow water equations and is treated in a semi-implicit form within TELEMAC-2D [8]. The two components of friction force are given in Eq. (6).

$$\begin{cases} \mathrm{F_x} = -\frac{\mathrm{u}}{2\mathrm{h}}\mathrm{C_f}\sqrt{\mathrm{u}^2+\mathrm{v}^2} \\ \mathrm{F_y} = -\frac{\mathrm{v}}{2\mathrm{h}}\mathrm{C_f}\sqrt{\mathrm{u}^2+\mathrm{v}^2} \end{cases} \quad (3)$$

where h is the water depth, C_f a dimensionless friction coefficient and u and v are the horizontal x and y components of the current velocity.

The roughness coefficient often takes into account the friction by the walls on the fluid or other phenomena such as turbulence. Thus it is difficult to define directly from available data and must be adjusted using the water surface profiles measured for a given flow rate.

b) Tidal amplification parameter

Tidal characteristics are imposed using a database of harmonic constituents to force the open boundary conditions. For each harmonic constituent, the water depth h and horizontal components of velocity u and v are calculated, at point M and time t by Eq. (7).

$$\begin{cases} \mathrm{F(M,t)} = \sum_\mathrm{i} \mathrm{F_i(M,t)} \\ \mathrm{F_i(M,t)} = \\ \qquad \mathrm{f_i(t)A_{F_i}(M)\cos\left(\frac{2\pi t}{T_i} - \varphi_{F_i}(M) + u_i^0 + v_i(t)\right)} \end{cases} \quad (7)$$

where F is either the water level (referenced to mean sea level) z_S or one of the horizontal components of velocity u or v, i refers to the considered constituent, T_i is the period of the constituent, A_{F_i} is the amplitude of the water level or one of the horizontal components of velocity, $\phi_{F_i}$is the phase, $f_i(t)$ and $v_i(t)$ are the nodal factors and u_i^0 is the phase at the original time of the simulation. The water level and velocities of each constituent are then summed to obtain the water depths and velocities for the open boundary conditions (8).

$$\begin{cases} \mathrm{h} = \alpha\sum \mathrm{z_{Si}} - \mathrm{z_f} + \mathrm{z_{mean}} + \gamma \\ u = \beta\sum u_i \\ v = \beta\sum v_i \end{cases} \quad (4)$$

where z_f is the bottom elevation and $\mathrm{z_{mean}}$the mean reference level. In Eq. (8), the tidal amplitudes multiplier coefficient of tidal range and velocity, respectively α and β, at boundary locations and the sea level correction γ are assumed to be the tidal calibration parameters [9].

c) Analysis of variance

The sensivity analysis has been carried out based on the computation of Sobol sensitivity indices according to the methodology presented in [11]. In this paper, we investigate the effect of three sources of uncertainty, the friction coefficients, the tidal amplification coefficients along the marine boundaries (α and β) and the mean water level correction coefficient γ. The source quantification of the uncertain variables, arbitrarily chosen, is summarized in Table 3.

Parameter	Probability density function
K_1 [$m^{1/3}s^{-1}$]	$U[30.4; 45.6]$
K_2 [$m^{1/3}s^{-1}$]	$U[64; 96]$
K_3 [$m^{1/3}s^{-1}$]	$U[80; 100]$
K_4 [$m^{1/3}s^{-1}$]	$U[20; 30]$
K_5 [$m^{1/3}s^{-1}$]	$U[64; 96]$
K_6 [$m^{1/3}s^{-1}$]	$U[36; 54]$
α and β [-]	$N(1; 0.07) \in [0.8; 1.2]$
γ [m]	$N(0.4438; 0.0295) \in [0.355; 0.532]$

Table 3. Source Quantification of uncertain variables

To handle the sensitivity analysis, it is important to run a lot of simulations in order to have reliable results. In this work, around 15,000 Monte-Carlo computations have been carried out based on TELEMAC-2D through the SALOME platform described in [10].

Figure 8 displays the total Sobol sensitivity indices obtained at the Bordeaux observation station.

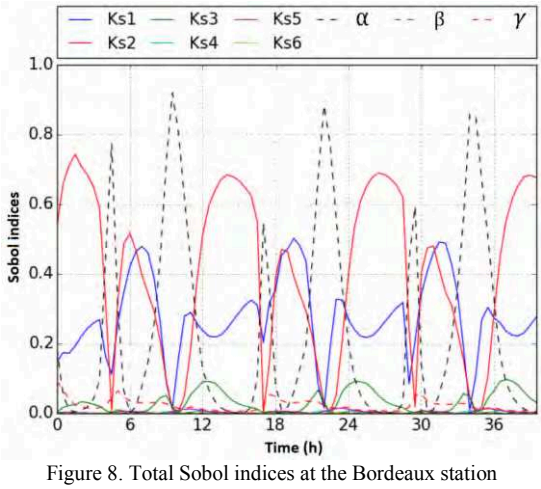

Figure 8. Total Sobol indices at the Bordeaux station

As shown by the sensitivity analysis, the most influent variables on the water depth variation are the friction coefficients (K_1, K_2, K_3) (in $m^{1/3}s^{-1}$), the tidal amplitudes multiplier coefficient of tidal range α and the sea level

correction γ (in m). The other variables can be considered negligible in comparison. These results depend, of course, on the hypothesis on the input random variables and especially on the choice of their distributions. Consequently, the calibration of the model is focused on these parameters.

4) Parameter calibration

In the cost function formulation given in Eq. 1, the observation vector is the free surface flow evolution extracted every 60 seconds at the The Verdon, Lamena, Pauillac, Fort Médoc, Bassens and Bordeaux locations. The observation operator H represents a call to the hydraulic solver and the observation covariance matrix R contains small value terms leading to represent a huge confidence on the observation value. At each iteration of the optimization algorithm, 448 particles fly through the search domain. The algorithm is stopped after 10 iterations. Moreover, the PSO algorithm results are compared with the results obtain from the gradient based method described in [11]. The obtained results are summarized in the Table 4.

parameters	K_1	K_2	K_3	α	γ	$J(X)$
Initial	19	50	50	0.75	-0.0562	6,34e6
PSO optimum	40.8	58.3	107	1.00	0.502	1,63e5
Gradient optimum	39.2	60.5	98.5	0.99	0.497	1,64e5

Table 4. parameter values and cost function at initial, gradient based and derivative free optima configurations

Calibrated parameters (see Tab. 4) with derivative free and gradient based approaches are not so far. The number of function calls is 224 for the gradient based method and 4480 for the PSO algorithm. In fact, the derivative information in optimization process allows to drastically reduce the number computations.

Figure 9 displays the results of the automatic calibration over a 36 hours period.

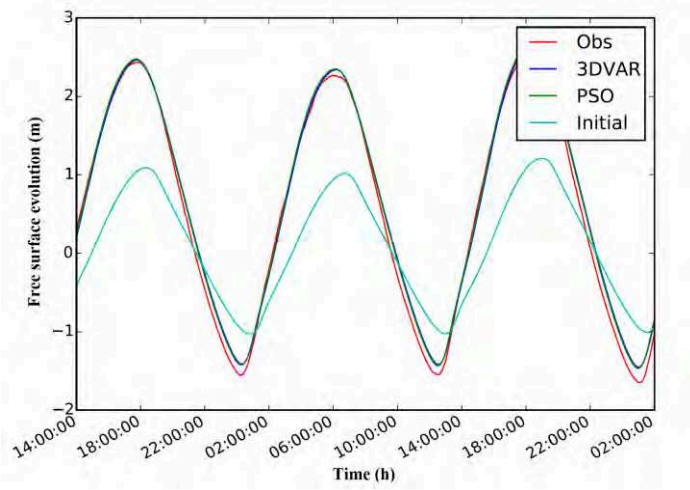

Figure 9. Free surface evolution at the Lamena station

As shown in Figure 9, the water surface profiles calculated are much closer to the measurements than the initial model calibration. The final results emphasises the efficiency of the automatic calibration tool in the framework of a maritime configuration. Moreover, the computation time is a crucial point from operational point of view. Thus, the algorithmic optimization tool implemented in this work has been written to make use of multiprocessor parallelism in order to be efficient and compatible with industrial needs. In fact, at each PSO iteration, the computation of each particle is an independent hydraulic state. Thus, the particle swarm can be evaluated in parallel. As TELEMAC is also a MPI-based parallel code, different configurations for parallelism are possible. In this work, the particle swarm is distributed on cluster to run in parallel and the particle computation is sequential.

V. CONCLUSIONS

Derivative-free optimization methods are typically considered for the minimization/maximization of functions for which the corresponding derivatives neither are available for use nor can be directly approximated by numerical techniques. Problem of this type are common in engineering optimization where the value of the cost function is often computed by simulation and may be subject to statistical noise or other form of inaccuracy. In fact, expensive function evaluations would prevent approximation of derivatives, and, even when computed, noise would make such approximations less reliable. Thus, the objective of this work is to implement an efficient heuristic designed procedure in order to find optimal solution when using TELEMAC-2D to assess a hydrodynamic performance. Two examples are given dealing with a model calibration and a shape optimization. In both cases the underlying optimization problems are solved by coupling a population-based metaheuristic to the numerical model with the help of TelApy [1]. The population-based metaheuristic is a Particle Swarm Optimizer written in Python that is a fork of the open source module PYSWARM. PSO defines and iteratively improves a set of candidates (particles) towards optimality. Theoretically, PSO does not ensure to find optimal solutions but in practice it performs very well. Moreover it does not rely on gradient computations as it does not assume the problem to be differentiable. Finally its convergence is fast enough in comparison with other algorithms even when coupled with TELEMAC-2D. Future works will include the multicriteria optimization and combination of DFO and gradient based algorithms to take advantage of both approaches.

REFERENCES

[1] C. Gœury, Y. Audouin, and F. Zaoui, "User documentation v7p3 of TelApy module," 2017

[2] R. C. Eberhart, J. Kennedy. "A new optimizer using particle swarm theory," 6 th International Symposium on Micromachine and Human Science, Nagoya, Japan, pp. 39-43, 1995

[3] W.F. Abd-El-Wahed, A.A. Mousa, M.A. El-Shorbagy, "Integrating particle swarm optimization with genetic algorithms for solving nonlinear optimization problems", Journal of Computational and Applied Mathematics, 235(5), 1446-1453, 2011.

[4] L. Alvarez-Vasquez, A. Martinez, M. Valquez-Mendez, M. Villar, "Numerical resolution of a shape optimization problem in hydraulic engineering", European Conference on Computational Fluid Dynamics, P. Wesseling and J. Periaux, eds., TU-Delft, pp. 1-13.

[5] J. Herman, J. Kollat, P. Reed, T. Wegener, "Technical Note: Method of Morris effectively reduces the computation demands of global sensitivity analysis for distributed watershed models." Hydrology and earth system sciences, 17, pp.2893–2903.

[6] I.M Sobol′, "Global sensitivity indices for nonlinear mathematical models and their Monte Carlo estimates", Mathematics and Computers in Simulation, 55(1-3), 271-280, 2001.

[7] E. P. Chassignet, H. E. Hurlburt, O. M. Smedstad, G. R. Halliwell, P. J. Hogan, A. J. Wallcraft, R. Baraille, and R. Bleck, "The hycom (hybrid coordinate ocean model) data assimilative system", Journal of Marine Systems, 65(1) :60-83, 2007.

[8] J-M. Hervouet, "Hydrodynamics of Free Surface Flows", Wiley, 2007, pp. 83–130.

[9] C. T. Pham, F. Lyard, "Use of tidal harmonic constants databases to force open boundary conditions in TELEMAC", Proceedings of the 19th Telemac-Mascaret User Club, 2012.

[10] C. Goeury, T. David, R. Ata, S. Boyaval, Y. Audouin, N. Goutal, A.-L. Popelin, M. Couplet, M. Baudin, R. Barate, "Uncertainty Quantification on a real case with TELEMAC-2D", Proceedings of the 22nd Telemac-Mascaret User Club, 2015.

[11] C. Gœury, A. Ponçot, J.-P. Argaud, F. Zaoui, R. Ata, and Y. Audouin, "Optimal calibration of TELEMAC-2D models based on a data assimilation algorithm", 24th Telemac-Mascaret User Conference, Graz, Austria, pp. 73- 80, October 2017

Ensemble Integrations of Telemac-Mascaret for the optimal model calibration

F. Zaoui[1], C. Goeury[1], Y. Audouin[1]
[1] EDF R&D – National Laboratory for Hydraulics and Environment (LNHE), 6 quai Watier, 78401 Chatou, France
E-mail: fabrice.zaoui@edf.fr

***Abstract*— This paper is focused on the use of a filtering method with Telemac-Mascaret in order to calibrate the most influent modelling parameters to their optimal values when the observation data is acquired. Optimality remains an objective that tends to reduce uncertainty a posteriori by finding trade-offs between model results and observations. This can be done by explicitly considering the uncertainties associated with the modelling process and the measurement chain. Two main families of mathematical methods are developed by the community of Data Assimilation to achieve this task. The first is a variational approach based on the mathematical minimization of a two parts error function. The second is a filtering approach where only linear algebra formula are used. The paper presents two real test cases with the Ensemble Kalman Filtering (EnKF) method for the error reduction of parameter estimation of the Telemac-Mascaret system.**

I. INTRODUCTION

Data Assimilation (DA) is a family of mathematical methods for the state estimation of a physical dynamic system commonly used in geosciences [1][2]. Observations and prior information are optimally combined with the results of a numerical model in order to minimize the uncertainty on the state of a system. Different techniques can help to compensate for the errors. The two most popular are the variational approach and the filtering methods. In this paper, the DA-based estimation relies on the Ensemble Kalman Filter (EnKF) [3]. This filter is close to a Monte Carlo sampling method but it does not require in practice a large number of state vectors to define a converging ensemble. It will apply to find the best estimations for some physical parameters of Telemac-Mascaret during the calibration phase.

The application of EnKF to Telemac-Mascaret is not new, see for instance [4] for a Telemac 2D application in the late 2000s on twin experiments or more recently [5] for a Mascaret-based operational application. The objective of this paper is to show on two real test cases how the same EnKF algorithm [6] can successfully calibrate Telemac-Mascaret models with little implementation effort and a reasonable computational cost. After a short presentation of DA and EnkF, the paper introduces the Python tools [7] used for the implementation of this automatic filter-based calibration. These tools are open-source and easy to learn.

A Mascaret test case is firstly presented and calibrated on the value of the friction coefficients of the Rhône River in France. As this test has a low computational cost, it is used for a small study of sensitivity in order to better understand the convergence of the filter with respect to some of its parameters. A Telemac 2D maritime case is also filtered with EnKF in order to calibrate some coefficients of a tidal wave. This case allowed us to compare the method with a variational approach and clearly demonstrates the interest of the filter as competitor for future real test cases using a complex representation.

II. DATA ASSIMILATION

A. Background

The aim of a Data Assimilation (DA) method is to find the best estimation of a state using two sources of information, model results and observational data. These information sources are supposed to be complementary and recorded over time. Both have errors that can be seen as random variables and modeled as probability density functions. Applying the Bayes' theorem:

$$p(x|y) = \frac{p(y|x)p(x)}{p(y)} \quad (1)$$

the estimation of an unknown state x is the distribution $p(x|y)$ given a prior knowledge $p(x)$ on the state, the observations $p(y)$ not depending on x and the probability $p(y|x)$ of having y if x was known, i.e. the likelihood. The uncertainty on x is reduced with rule (1) compared to the observations and a-priori estimation, see Fig. 1.

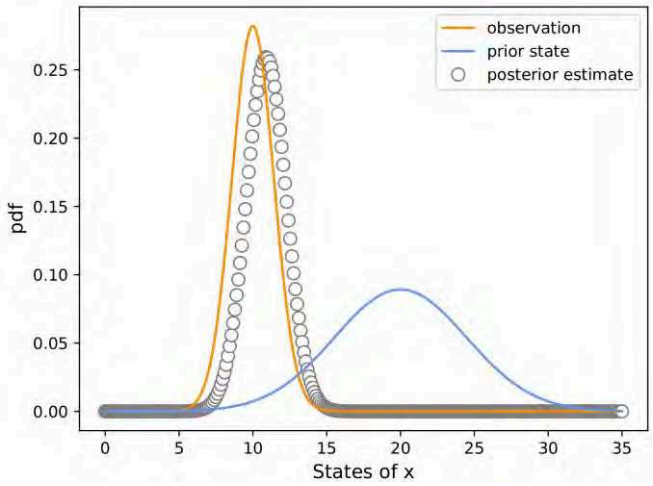

Figure 1. Coupling prediction and measurement

In most applications involving DA, a Gaussian distribution is used for the probability density functions of errors of each information source. This hypothesis, although it may be far from reality, simplifies the definition of uncertainties and opens many perspectives in the theory of estimation. A discrete state space model can be written as:

$$x_{k+1} = M_k(x_k) + w_k \qquad w_k \sim \mathcal{N}(0, Q_k) \qquad (2)$$

where x_{k+1} is the predicted system state at time step $k+1$, M_k is a linear or non-linear model and w_k a Gaussian noise representing the modelling errors with a covariance matrix Q_k. If x_k stands for the parameters to calibrate then it is convenient to take $M_k = I$. Similarly, the observations can be modelled as:

$$y_k = H_k(x_k) + v_k \qquad v_k \sim \mathcal{N}(0, R_k) \qquad (3)$$

where H_k is the observation model (shallow water) that relates the values of parameters x_k to the measurements y_k and v_k the observational noise with the covariance R_k.

DA aims to estimate $\hat{x}$ as a solution of a mismatch problem to the observations. If the observations are simultaneously considered for a prescribed time window, the solution is a global model trajectory $\hat{x}_{0:N} = (\hat{x}_0, \hat{x}_1, .., \hat{x}_N)^T$ where $\hat{x}_k$ is for the time $t_k \in [t_0, t_N]$ a local solution influenced by all the observations $y_{0:N}$. By supposing identical time steps for the model and the availability of observations, the DA problem in a variational approach can be written as the minimization of the error function $J(\hat{x}_{0:N})$:

$$J(\hat{x}_{0:N}) = \frac{1}{2}\|\hat{x}_0 - x_b\|^2_{B^{-1}} + \frac{1}{2}\sum_{k=1}^{N}\|\hat{x}_k - M_{k-1}(\hat{x}_{k-1})\|^2_{Q_k^{-1}} + \frac{1}{2}\sum_{k=0}^{N}\|y_k - H_k(\hat{x}_k)\|^2_{R_k^{-1}} \qquad (4)$$

The first two terms in (4) penalize the gaps to the prior (background) solution x_b at t_0 and to modelling solutions from t_1 to t_N. The third term is the penalization to observations. All terms are weighted by the error covariance matrices B, Q and R.

B. Ensemble Kalman Filtering

The Kalman filters are not global but sequential DA techniques where observations are gradually assimilated by evolving the uncertainty in the state from one observation time to the next. The original version of Kalman filter [8] assumes that operators M and H are linear. To work around this problem, the extended Kalman filter (EKF) has been developed but it still needs a linearization part that can pose computational cost and/or convergence problems (tangent linear and adjoint models required).

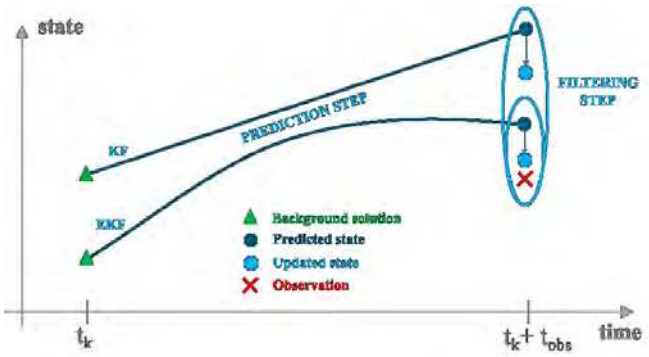

Figure 2. Sketch of KF and EKF algorithms

EnKF is an alternative method to estimate the covariance matrix using as a first approximation a sample of random states (ensemble). Each state (member) evolves forward in time using M_k and the covariance is approximated with the new ensemble (prediction step). Then the ensemble is updated using perturbed observations (filtering step). In practice for most applications EnKF does not require a large number of members to converge.

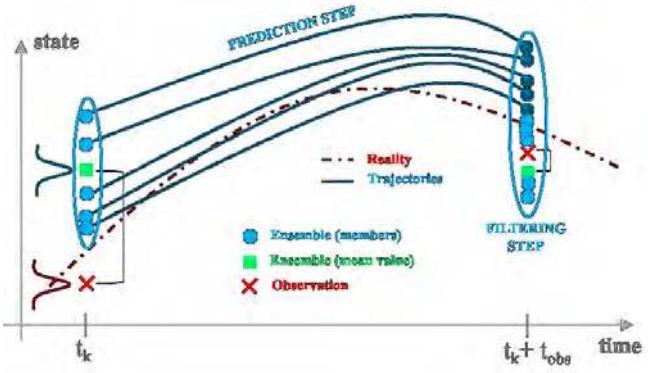

Figure 3. Sketch of EnKF algorithm

Prediction step

- Propagation of each member i of ensemble N_e from time t_k to $t_k + t_{obs}$ where t_{obs} is the period of observations:

$$x^i_{k+obs} = M_{k:k+obs}(x^i_k) + w^i_k \qquad (5)$$

- Estimation of the covariance matrix:

$$P_{k+obs} = \frac{1}{N_e - 1}\sum_{i=1}^{N_e}(x^i_{k+obs} - \overline{x}_{k+obs})(x^i_{k+obs} - \overline{x}_{k+obs})^T$$

with the mean ensemble: $\overline{x}_{k+obs} = \frac{1}{N_e}\sum_{i=1}^{N_e} x^i_{k+obs}$ (6)

Filtering step

- Computation of the Kalman gain:

$$K_{k+obs} = P_{k+obs}H^T(HP_{k+obs}H^T + O_{k+obs})^{-1} \qquad (7)$$

where O_{k+obs} is the covariance computed from the perturbed observations.

- Update the ensemble:

$$x^{i*}_{k+obs} = x^i_{k+obs} + K_{k+obs}(y_{k+obs} + v^i_k - Hx^i_{k+obs}) \qquad (8)$$

III. IMPLEMENTATION

A. FilterPy

FilterPy is an open source (MIT License) Python module that implements some Kalman and Bayesian filters [9]. The module is rather oriented for engineering studies and offers documentation and basic examples for each filter. See [6] for the EnKF algorithm implemented in FilterPy as there exits many versions of this filter. In this program there is no particular improvement of the classic algorithm based on (5)-(8). Most advanced algorithms can implement for instance methods like localisation and/or inflation to make EnKF working in high dimension or being less cost computational. For the time being, these techniques have not been considered for solving data assimilation problems with the Telemac-Mascaret examples of this paper.

B. TelApy

All the computations with the modules of the Telemac-Mascaret system can now be done directly in Python with TelApy [7]. TelApy is a package for using APIs of the system. It allows a fine interaction with the code while running. For instance it is possible to ask for values of variables or set some new values for parameters at any time of the simulation. The list of variable names and functions that can be used with TelApy are documented and tutorials exist in the source of the system [10].

TelApy is generic enough to not restrict the use of Telemac-Mascaret to some use cases or simulation platform. In particular it allows to easily couple Telemac-Mascaret with an optimizer or a filter like FilterPy for the DA.

C. Coupling

The coupling between FilterPy and TelApy is quite easy. The user has only to write a supervisor script to firstly initialize the two modules and then call TelApy for $t \in [t_k, t_k + t_{obs}]$ followed by a call to FilterPy.

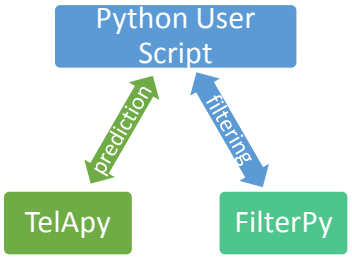

Figure 4. Python example for EnKF with Telemac-Mascaret

Pseudo code

algorithm telemac-enkf is
  input: the size of the ensemble N_e
    the Telemac steering file ***cname***
    initial values p_0 for the parameters
    model covariance matrix Q
    observation covariance matrix R
    observation operator H
  output: ensemble of optimal Telemac states T_{opt}
    optimal values for parameters P_{opt}

  define an ensemble of parameters p_f from (p_0, N_e)
  define an ensemble of Telemac states S from (***cname***, p_f)
  while the time t is **in** the assimilation window **do**
    if observation is available:
      $p_f \leftarrow$ FilterPy(S, p_f, H, R) # filtering
    else:
      $S \leftarrow$ TelApy(S, p_f) # prediction
      $p_f \leftarrow p_f + Q$
    $t \leftarrow t + 1$

  return ($T_{opt} = S$, $P_{opt} = p_f$)

D. Parallelism

Since each member i of N_e is an independent hydraulic state, the ensemble can be predicted in parallel. As Telemac is also a MPI-based parallel code, different configurations for parallelism are possible. TelApy requires the mpi4py module for solving the physics and one can add in the user script the support of the multiprocessing if needed for predictions. For the filtering equations (7)-(8), FilterPy is sequential. This is not an issue when N_e and $dim(x)$ are low values.

IV. Results and Discussion

A. Mascaret

EnKF is used to calibrate nine friction coefficients of the Rhône river in France on a reach of 22 km long. The geometry is not described as it is not the purpose of the present study. The mesh is made of 1,259 1D nodes. The boundary conditions are an imposed flow rate of 156 m^3/s at the upstream and an imposed water level of 187.3 m at downstream. One observation of the water level per friction zone is available for this non-overtopping flow regime.

The background x_b is a vector of nine Strickler coefficients of 40 $m^{1/3}/s$. The initial ensemble will be a normal distribution around this mean value. The initial error (L^2-norm) on the water levels computed by Mascaret and corresponding to x_b is equal to 0.6125 m.

As a reference for the appreciation of EnKF results, a variational approach has been tested for the minimization of (4) by an L-BFGS algorithm [11]. This has given a solution $\hat{x}_{L-BFGS}$ corresponding to an error of 0.0894 m.

Many configurations with EnKF have been tested for different values of N_e repeated 100 times over 10 assimilation cycles (filtering). The choice for 100 repetitive runs of EnKF is done for trying to get some basic but confident statistics on the behaviour of the filter. The choice to stop EnKF after only 10 assimilation cycles is arbitrary but identical for all the values of N_e.

Fig. 5 shows the statistics of these errors. The best solution (minimal error) was found for $N_e = 64$ with a value equal to 0.0159 m. This is an improvement corresponding to a ratio ≈ 38 in comparison with the initial error (background solution) and to a ratio ≈ 5 in comparison with the reference solution (variational solution). It is noticeable that the reference solution in terms of error value can be reached by EnKF with a low value of N_e, typically $N_e = 8$. To be certain to get the same performance as the reference solution it would be better to work with $N_e \geq 64$.

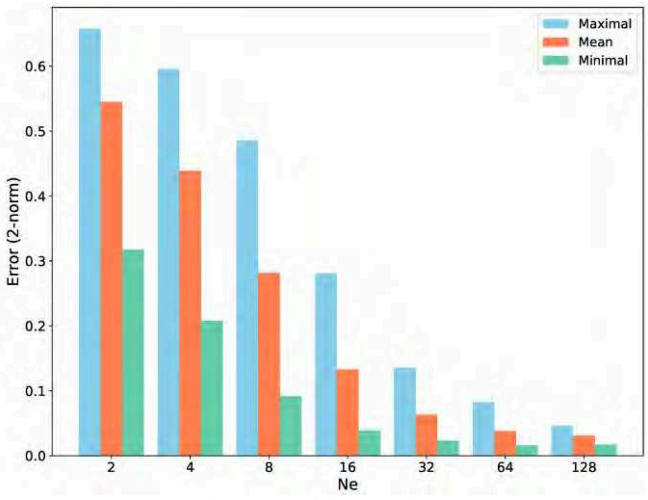

Figure 5. Statistic errors for EnKF

The longitudinal profile of the river with the water levels corresponding to the background solution x_b and to the EnKF best solution are depicted in Fig. 6.

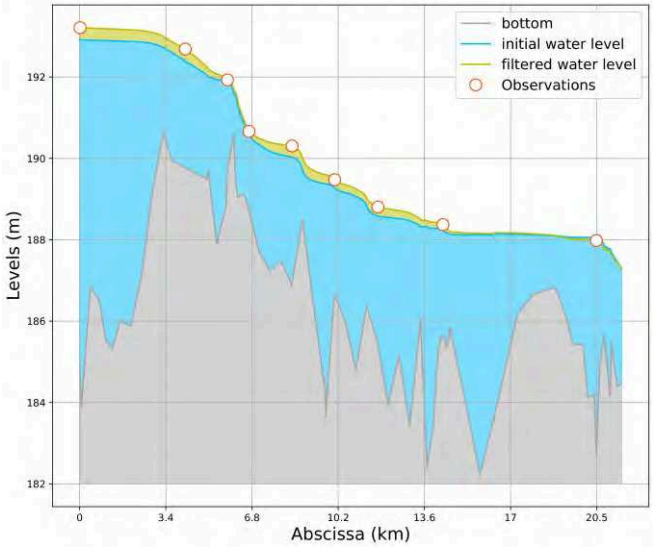

Figure 6. Results for the water levels (background and EnKF-based calibration)

Tab. 1 and Fig. 7 presents the optimal values for the friction parameters in the different zones of the river for the variational and filtering approaches. Results in Tab. 1 are rounded with no decimal part for reading convenience.

TABLE 1. FRICTION COEFFICIENTS RESULTS ($m^{1/3}/s$)

Zone	1	2	3	4	5	6	7	8	9
x_b	40	40	40	40	40	40	40	40	40
$\hat{x}_{L-BFGS}$	32	25	36	39	29	32	33	27	40
$\hat{x}_{EnKF}$	31	26	35	42	28	34	32	25	45

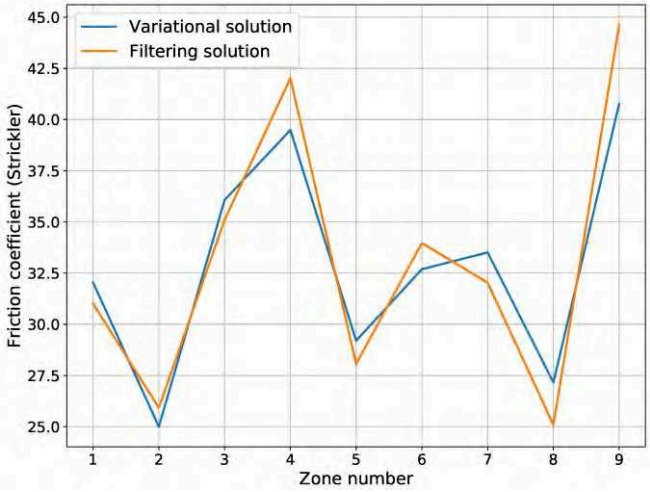

Figure 7. Optimal parameters with two DA methods

Calibrated parameters (Fig. 7) with variational and filtering approaches are not so far apart, although the resulting errors differ (0.0894 m vs 0.0159 m). Both results are in the same space where the filtering method was able to achieve a better accuracy. It is noticeable that if the convergence tolerance of the L-BFGS algorithm is decreased, the differences with EnKF vanish.

Fig. 8 presents some convergences of EnKF for 100 assimilation cycles and different values of N_e. Since EnKF is a stochastic algorithm, the curves in Fig. 8 may slightly change but not so much in practice for this Mascaret calibration problem.

Anyway the EnKF convergence is clearly correlated with the value of N_e. It is not surprising to see how the errors are sensitive to the ensemble size. Too low values can lead to an undersampling of the search space of the parameters and consequently to the divergence of the filter. As expected best results are obtained for the largest ensemble sizes. The difference between $N_e = 64$ and $N_e = 128$ is small and here the best ratio between the calculation cost and the convergence error lies between these two values.

Whatever the tests here, the convergences have always been quite regular and monotonic.

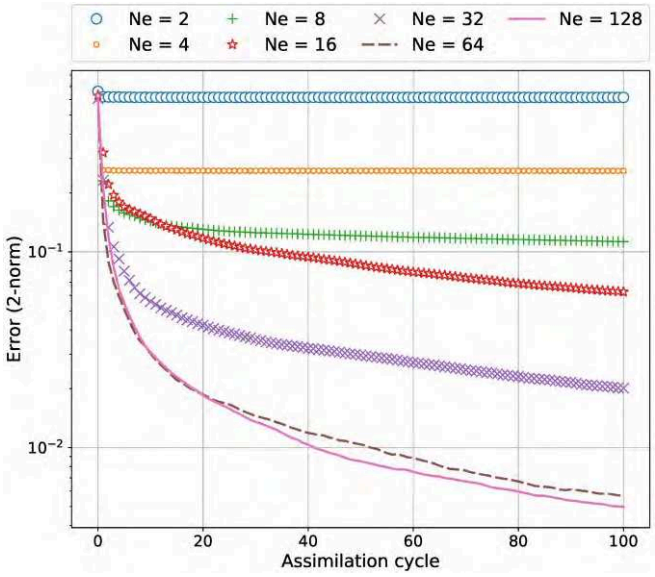

Figure 8. Typical convergence of EnKF for different values of N_e

In this calibration problem the computational cost is extremely low as it is the steady state computational kernel of Mascaret that is used by TelApy. Consequently, the filtering with FilterPy is systematically done: $t_{k+obs} = t_{k+1}$ for all k as Mascaret is able to compute the steady state in one step. Hence the number of Mascaret simulations needed by the EnKF calibration is equal to N_e multiplied by the number of assimilation cycles.

In order to see the relative importance of covariance matrices Q (2) and R (3) on the convergence of EnKF, many calibrations have been tested considering those matrices as diagonal with an identical variance value for all the terms and ranging from 10^{-2} to 10^{-8} m^2. Tests have been performed for $N_e = 64$ and the convergence was stopped after 10 assimilation cycles. Fig. 9 shows the corresponding results with a representation of the error function in the variance space $[10^{-2}, 10^{-8}] \times [10^{-2}, 10^{-8}]$ for two levels of fine and coarse discretization.

The two graphs in Fig. 9 give concordant information. One striking feature is that EnKF is almost independent on the values of $diag(Q)$ and $diag(R)$ in a wide range extending from 10^{-3} to 10^{-8}. The interaction effects between Q and R on the error function are practically non-existent. Q only increases the error function for a large variance value and only when $diag(R)$ is small. As complement, large values for R have always the same impact whatever Q covariance is.

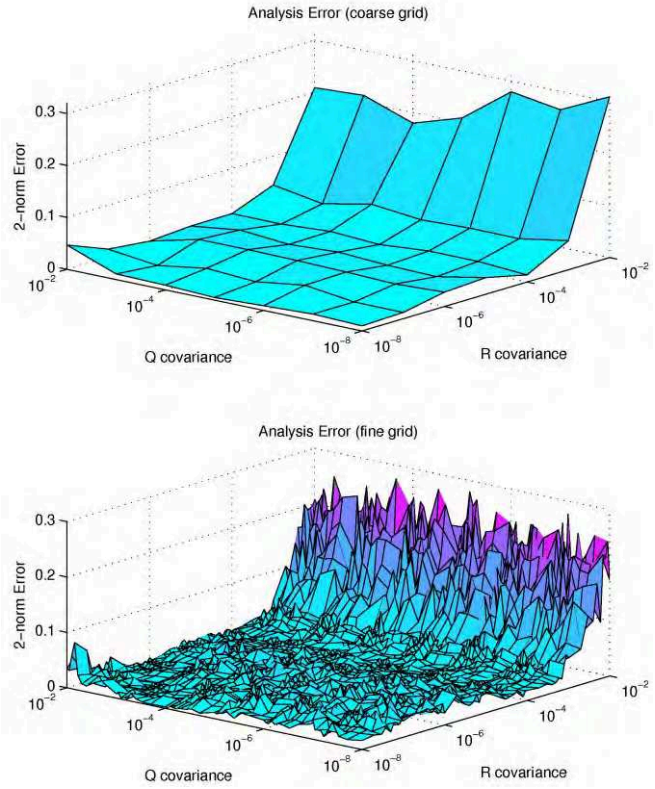

Figure 9. EnKF errors as a function of diagonal elements of Q and R

The rapid convergence and the relatively low importance of the prediction model error indicate that the physics of the case while being non-linear is not so difficult to capture with the basic version of the EnKF algorithm. However, as the best solutions are only reached for the largest N_e values, the ensemble spread might be increased by a covariance inflation to mitigate the undersampling of low N_e values. Inflation or localisation techniques are not implemented in the actual version of FilterPy but they could be tested in the future with minimal changes in the module.

The covariance matrix for the convergence of the ensemble $N_e = 128$ after 100 assimilation cycles is presented in Fig. 10. As expected the matrix is diagonal dominant with few interactions except for the three last zones where a negative covariance appears. Actually, this part of the river is the most difficult one to calibrate as the flow regime is sub-critical and constrained by an imposed water level at the end of the reach. Other off-diagonal elements are negligible indicating that there is no spurious correlation.

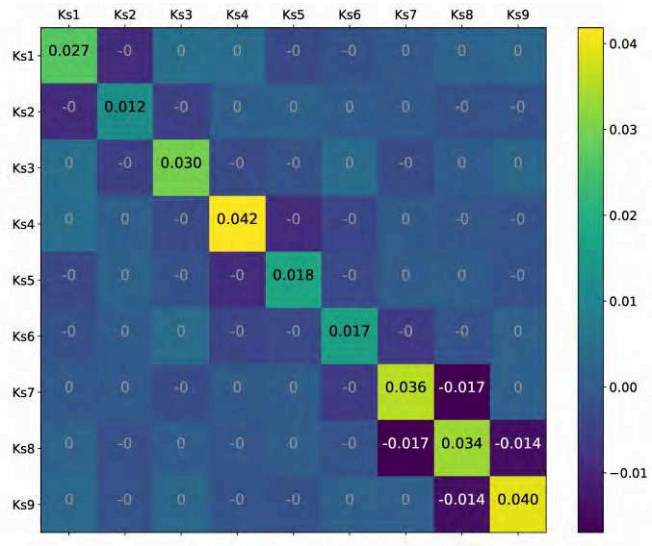

Figure 10. Covariance matrix for the Strickler's coefficients K_s

B. *Telemac*

Any model using the Telemac-Mascaret system can be calibrated according to Fig. 4. The implementation is relatively easy. The reader is invited to test the approach on a simple Telemac 2D case if interested [12].

To perform on a real test case, EnKF is used to calibrate three tidal parameters of a maritime configuration. The study concerns the Alderney Race that is located between the island of Alderney, UK, and the western tip of the Cotentin peninsula in Normandy, France. Details of this Telemac study are presented in [13]. The modelling covers an area of roughly 55 km × 35 km and the finite element discretization is composed of a triangular mesh with 17,983 nodes and 35,361 elements. The mesh size varies from 100 m on the shoreline and within the areas of interest to 1.8 km offshore, western and northern sectors.

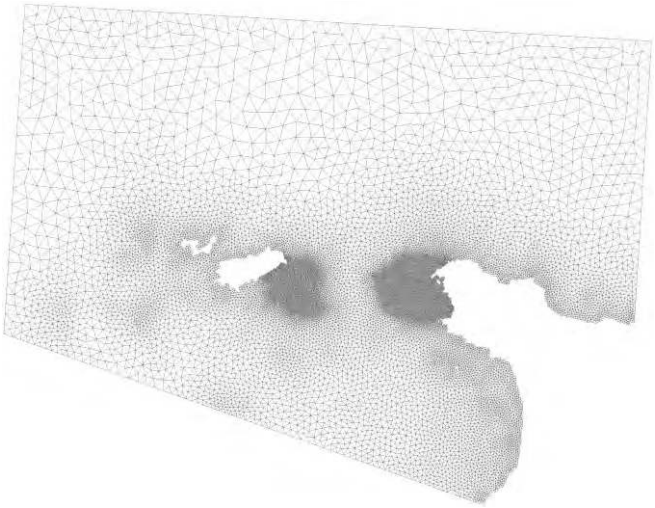

Figure 11. Model mesh

The boundary conditions of the model have been set up using depth-averaged velocities and water levels from the TPXO dataset (8 primary, 2 long-period and 3 nonlinear

constituents). The TPXO dataset is an accurate global models of ocean tides based on a best-fit of tidal levels measured along remote sensing tracks from the TOPEX/POSEIDON satellite project in operation since 2002. Moreover, velocities and water depths are imposed along the marine borders of the model using Thompson-type boundary conditions that allows internal waves to leave the domain with little or no reflection.

Several measurement campaigns were carried out to the west of Cap de la Hague. For this study, only the results of one of these (a campaign lasting six months) are used over a 5 days period from October 15th to 20th. This six-month campaign was carried out during summer of 2009 (from the end of July to the end of January). Two ADCPs were deployed to measure flow velocity (magnitude and direction) and water depth with 1 measurement every 10 minutes and one hour respectively.

The model calibration is done by estimating three tidal parameters that were proved to be the most influent ones on the Telemac results after a sensitivity analysis [13]. Tidal characteristics are imposed using a database of harmonic constituents to force the open boundary conditions. For each harmonic constituent, the water depth h and horizontal components of velocity u and v are calculated, at point M and time t by:

$$F(M,t) = \sum_i F_i(M,t) \tag{9}$$

$$\left\{ F_i(M,t) = f_i(t) A_{F_i}(M) \cos\left(\frac{2\pi t}{T_i} - \varphi_{F_i}(M) + u_i^0 + v_i(t) \right) \right.$$

where F is either the water level (referenced to mean sea level) z_s or one of the horizontal components of velocity u or v, i refers to the considered constituent, T_i is the period of the constituent, A_{F_i} is the amplitude of the water level or one of the horizontal components of velocity, ϕ_{F_i} is the phase, $f_i(t)$ and $v_i(t)$ are the nodal factors and u_i^0 is the phase at the original time of the simulation.

The water level and velocities of each constituent are then summed to obtain the water depths and velocities for the open boundary conditions:

$$\begin{aligned} h &= \alpha \sum_i z_{s_i} - z_f + z_{mean} \\ u &= \beta \sum_i u_i \\ v &= \beta \sum_i v_i \end{aligned} \tag{10}$$

where z_f is the bottom elevation and z_{mean} the mean reference level.

In (10), the multiplier coefficients of the tidal range and velocity, respectively α and β, at boundary locations and the sea level z_{mean} are the tidal parameters to be calibrated with EnKF.

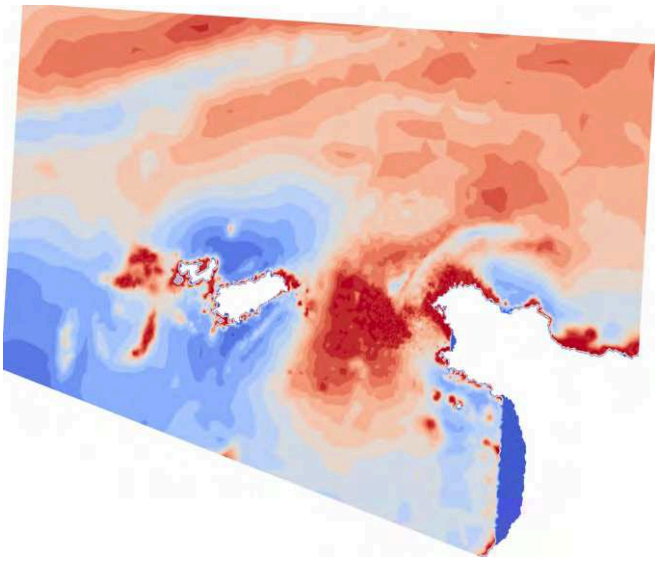

Figure 12. Example of the velocity distribution (magnitude)

The initial mean values for the ensemble of tidal parameters are set to $z_{mean} = -1.6$, $\alpha = 1$ and $\beta = 1$ as prescribed by the original study of this model [13]. Fig. 13 shows the water depths on 24 hours (the first day of a five-day period) and at a point of observation, calculated before and after the calibration of tidal parameters by EnKF.

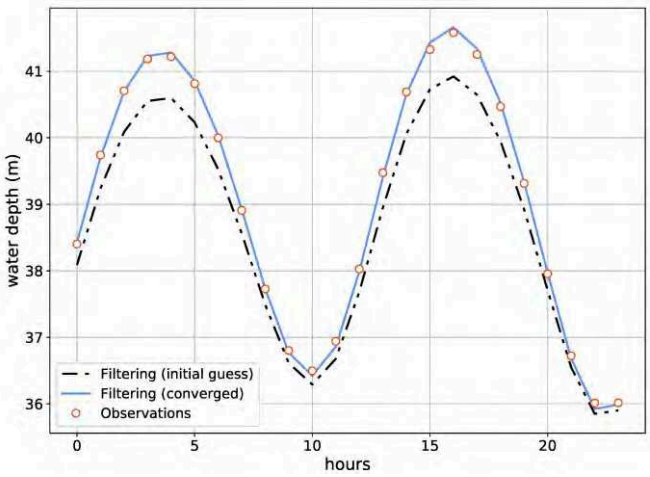

Figure 13. Water depths before and after EnKF convergence

The results on the water depth in Fig. 13 match very well with the observations. The error between the simulation and the observation is approximately four times lower than that obtained with a variational approach [13]. Indeed, the error 2-norm for the optimal solution of 3D-VAR is 0.83 m ($z_{mean} = -0.995, \alpha = 1.112, \beta = 1.106$) and 0.22 m for the EnKF ($z_{mean} = -1.149, \alpha = 1.112, \beta = 1.106$). Except for the seal level z_{mean} the two others solutions on the tidal range and velocity are identical.

The number of members N_e required to obtain the best EnKF estimate was only 5. In practice, the solution was not found the first time but it required few tests. In total the computational cost was less important than working with a much larger ensemble.

The filtering step was applied every hour all along the five-day period. Fig. 14 presents the convergence for the three tidal parameters (mean values) together with the decrease of the error norm between observations and estimations

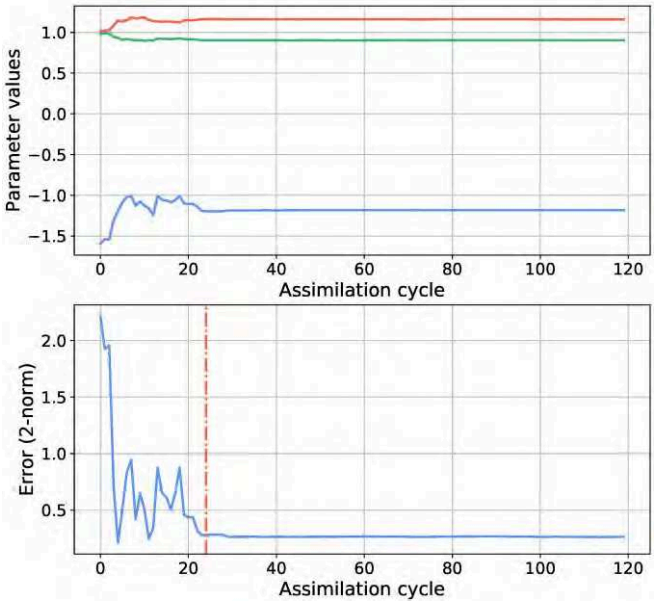

Figure 14. Convergence reached in 24 hours

It should be noted that only 24 assimilations (24 hours with one assimilation per hour) are necessary to reach the best estimates. For the remainder of the period, no further changes are identified. The entire five-day window is not necessary in this example, but that does not mean that the parameters can not change over time beyond this period. This will surely depend on the time of year and weather conditions.

The computational cost here is very acceptable and less important than those of the variational approach [13]. For example on a standard PC workstation of four cores (Intel® Xeon® CPU E3-1240@3.4 GHz), the time required to lead the assimilation in Fig. 14 to its end was about 40 minutes.

V. Conclusions

This article presents a Python-based framework for data assimilation with the Telemac system. The data assimilation technique studied is the Ensemble Kalman Filter. It is shown how this filter can work well with the Telemac system for optimal model calibration with a small number of parameters. The filter is also considered competitive compared to other methods for its ease of implementation and its quick convergence on fairly simple problems.

In perspective, this first use of EnKF with the Telemac system at EDF R&D will certainly be continued on more complex models, that is to say with a greater dimensionality or a different physics. This will be an opportunity to test filter improvement techniques such as localisation and inflation, to use HPC as EnKF is easily parallelisable, or to compare the performance on surrogate models.

Acknowledgement

The authors gratefully acknowledge the open source community and especially that of Python. Many thanks to Dr. Sophie Ricci (CERFACS) and Vanessya Laborie (CEREMA) for the motivating discussions on EnKF and the Telemac-Mascaret system.

References

[1] E. Blayo, M. Bocquet, E. Cosme, and L.F. Cugliandolo, “Advanced Data Assimilation for Geosciences,” Lecture Notes of the Les Houches School of Physics: Special Issue, Oxford University Press, June 2012

[2] A. Carrassi, M. Bocquet, L. Bertino, and G. Evensen, “Data Assimilation in the Geosciences - An overview on methods, issues and perspectives,” unpublished

[3] G. Evensen, “Sequential data assimilation with a nonlinear quasi-geographic model suing Monte Carlo methods to forecast error statistics,” J. Geophys. Res., vol. 99, pp. 10143-10162, 1994

[4] I.S. Strub, J. Percelay, O.-P. Tossavainen, and A.M. Bayen, “Comparison of two data assimilation algorithms for shallow water flows,” Networks and Heterogeneous Media, ©American Institute of Mathematical Sciences, vol. 4, Num. 2, pp. 409–430, June 2009.

[5] S. Barthélémy, S. Ricci, M.C. Rochoux, E. Le Pape, and O. Thual, “Ensemble-based data assimilation for operational flood forecasting – On the merits of state estimation for 1D hydrodynamic forecasting through the example of the ‘Adour Maritime’ river,” Journal of Hydrology, vol. 552., pp. 210-224, 2017.

[6] J.L. Crassidis and J.L. Junkins, “Optimal Estimation of Dynamic Systems,” CRC Press, pp. 257-9, Second Edition 2012

[7] Y. Audouin, C. Gœury, F. Zaoui, R. Ata, S. El Idrissi Essebtey, A. Torossian, and D. Rouge, “Interoperability Applications of TELEMAC-MASCARET System,” 24th Telemac-Mascaret User Conference, Graz, Austria, pp. 57- 64, October 2017

[8] R.E. Kalman, “A new approach to linear filtering and prediction problems,” Journal of Basic Engineering, vol. 82, pp. 35-45, 1960

[9] R. Labbe, “Kalman and Bayesian Filters in Python,” https://github.com/rlabbe/Kalman-and-Bayesian-Filters-in-Python

[10] C. Gœury, Y. Audouin, and F. Zaoui, “User documentation v7p3 of TelApy module,” 2017

[11] F. Demangeon, C. Gœury, F. Zaoui, N. Goutal, V. Pascual, and L. Hascoët, “Algorithmic differentiation for the optimal calibration of a shallow water model,” La Houille Blanche, vol. 4, pp. 53-61, 2016

[12] F. Zaoui, Ensemble Kalman filter example for Telemac-Mascaret, https://github.com/fzao/telenkf

[13] C. Gœury, A. Ponçot, J.-P. Argaud, F. Zaoui, R. Ata, and Y. Audouin, “Optimal calibration of TELEMAC-2D models based on a data assimilation algorithm”, 24th Telemac-Mascaret User Conference, Graz, Austria, pp. 73- 80, October 2017

The effect of mesh size and bed roughness on the simulation of sediment transport off the east coast of Norfolk

Dr Catherine VILLARET[1], Dr Alexandros Avdis[2], David Rushton[1], Dr. Andy Mills[1]
[1] East Point Geo, [2] Imperial College, London. Primary contact: cathvillaret@eastpointgeo.com

Abstract
The choice of mesh size and friction factors have been shown to be major sources of uncertainty in flow and morphodynamic modelling (See for example Villaret et al, TUC 2014). In order to reduce this uncertainty, we propose to use the robust finite element mesh generator qmesh (www.qmesh.org) developed by Avdis and Hill. (Renewable Energy, 2018) to test different mesh sizes and assess their influence on both flow and sediment transport rates. We also propose here a new approach based on physical ground to estimate the bed roughness from a high resolution dataset.

The Norfolk coastal area
The region of interest extends 100 km offshore of the east coast of Norfolk, including the elongated Norfolk sand banks (Cross Sands/ Cockle Gateway). This highly dynamic area is an ideal modelling test case for reasons which include:

- A considerable amount of publicly available hydrodynamic and sediment transport data exist, including flow and velocity data from the SNS2 2001 survey, that can be used for model validation.
- Morphodynamic features are reported with interactions at different scales and include the Norfolk banks parallel to the shore line with characteristic length scales of 5-10 km and smaller bedforms down to mega-ripples ripples in the near shore zone.
- Finally, an understanding of flow and sediment transport processes has commercial applications of relevance to this area, which include offshore renewables, oil & gas and power infrastructure and decommissioning operations.

Bathymetry data – DEM construction
Two different sources of raw bathymetry were used: (1) EMODnet (portal.emodnet-bathymetry.eu) regionally continuous data gridded at approximately 180m, and (2) Several higher resolution but smaller extent bathymetric datasets were mosaiced into a 25m grid using data from the UKHO data portal (aws2.caris.com/ukho) which ranged from 1981 to 2017. Initial preparation requires interpolation to avoid inconsistencies between the different data sets.

Meshing tool
The model domain includes the shoreline portion between Cromer and Lowestoft and extends approximately 50 km offshore to include the Norfolk offshore banks. We built a Telemac model using qmesh in a QGIS representation. In addition to the coarse mesh (baseline model) we built a high-resolution model (170 000 elements and 80 000 grid nodes).
The mean bed level and bed roughness were estimated from the EMODnet data sets for the coarse mesh and using the high-resolution DEM for the fine mesh. The mean bathymetry was obtained by applying a filtering length (ideally of the order of the mesh size) representative of the mean bed level, averaged over the mesh scale. In a second step, the bed roughness is determined as proportional to the bedforms heights, simply by applying the same filtering length to the differential DEM (local filtered). As a final step, both geometry files (coarse and fine mesh) were constructed using pputils, to include the mesh, mean bed level and bed roughness. The grain diameter was also included as a function of water depth, based on expert knowledge.

Tidal flow
The TPXO database was used to impose the flow (free surface and velocity) at the boundary nodes. Harmonics analysis of the flow model over 4 months were compared for the 4 main tidal gauges (M2, S2, N2 and M4). Both the coarse and fine mesh were able to capture the tidal flow variation in comparison with the tidal gauges although a more detailed calibration is needed (by varying the tidal amplitude at the offshore node). However, the general agreement is best with the fine mesh.

Morphodynamic Assessment
Morphodynamic model results obtained after 1 year of bed evolution are extremely different between the coarse and fine mesh. Only the fine mesh resolution is able to capture the mesoscale features (sand waves). A comparison between the high resolution model and the high resolution datasets gives an indication on the direction and celerity of sand waves by following individual crest lines across repeat surveys. Although the picture is complex there appears a north/south divide offshore Caister and Winterton.

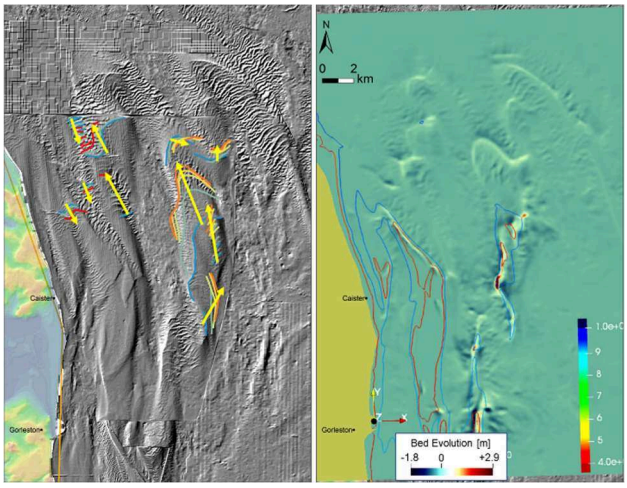

Figure 1: repeat survey analysis of bedforms (left) and comparison with 300 day bed evolution modelling (right)

Conclusion
This paper discusses the role of the mesh and initial treatment of the bathymetry datasets in the construction of the geometry file. We propose a new method to directly estimate the bed roughness from high resolution bathymetry. Although a coarse mesh gives a relatively rough estimate of the tidal flow, the morphodynamics results are completely unrealistic. The preliminary morphodynamics model results using the fine mesh resolution show realistic features (with greater evolution ranges along the crest of sand banks) and emerging sand waves. The approach proposed for the bed roughness estimation based on physical ground (from bathymetry analysis) needs to be further improved using a variable filtering length (consistent with the spatially varying mesh size). Results are however globally consistent with the bed roughness predictions using Van Rijn (2001) decomposition of bed roughness in terms of megaripples and dunes.

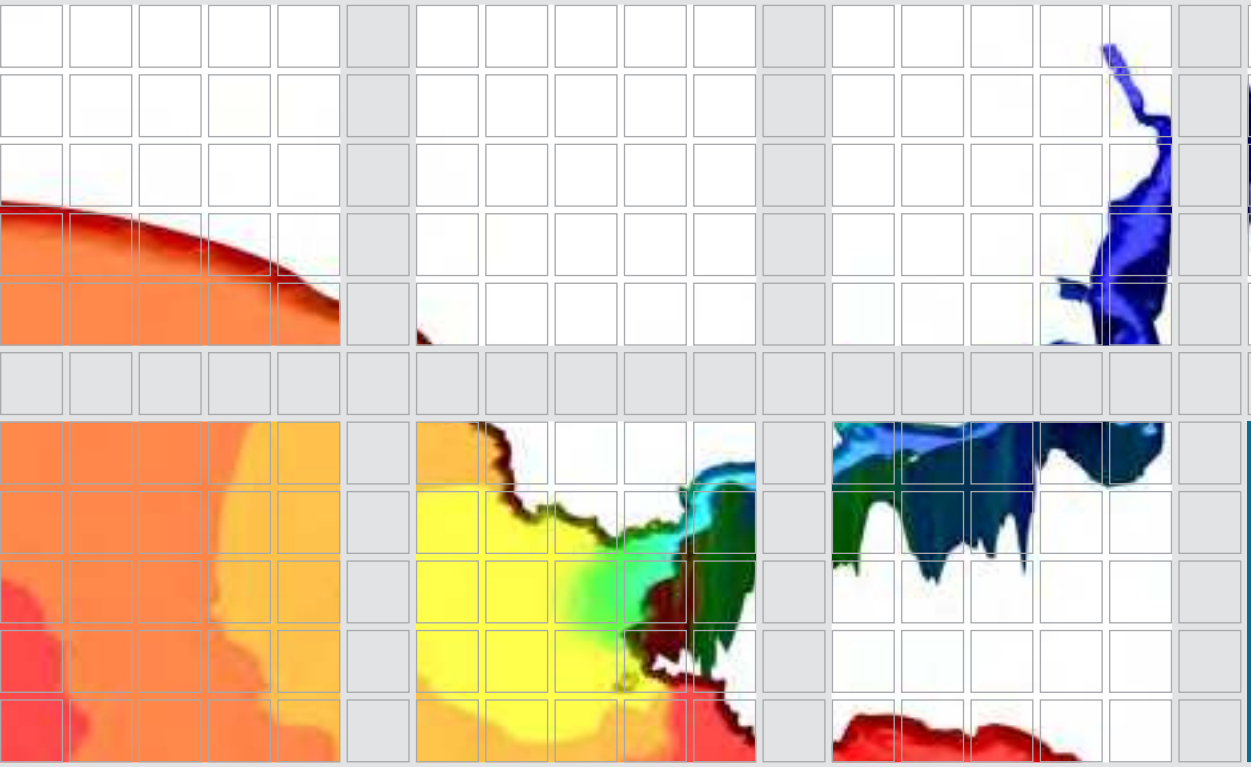

Norwich
UK

Collaborative Centre for the Sustainable Use of the Seas (CCSUS)
Centre for Environment, Fisheries and Aquaculture Science (Cefas)
Pakefield Road,
Lowestoft, NR33 0HT, UK
telemac2018@gmail.com
► **www.telemac2018.org.uk**

ISBN 978-0-907545-75-0
DOI 10.14465/2018.tucxxv.nrw